Improved Optical Trapping of SrOH to Probe Ultralight Dark Matter

A DISSERTATION PRESENTED
BY
ABDULLAH NASIR
TO
THE DEPARTMENT OF PHYSICS

IN PARTIAL FULFILLMENT OF THE REQUIREMENTS
FOR THE DEGREE OF
DOCTOR OF PHILOSOPHY
IN THE SUBJECT OF
PHYSICS

HARVARD UNIVERSITY
CAMBRIDGE, MASSACHUSETTS

MAY 2026

Improved Optical Trapping of SrOH to Probe Ultralight Dark Matter

Abstract

Polyatomic molecules are promising platforms for conducting precision measurements to probe the Standard Model, owing to their unique degrees of freedom including vibrations and rotations. In particular, ultracold SrOH has sensitivity to the variation of the proton to electron mass ratio μ and subsequently to scalar ultralight dark matter (UDM) fields. We discuss the laser slowing, sub-Doppler cooling, and trapping of SrOH and present an order-of-magnitude improved trap number through the use of transverse cooling of the molecular beam resulting in $\sim 10^4$ optically trapped molecules. This would allow for a two-order-of-magnitude improvement on the current best sensitivities to UDM over four decades of mass. Probing μ-variation is not only important for UDM studies, but has more general implications for a variety of fundamental physics searches. Additionally, this increase in trapped molecule number makes SrOH a viable candidate in the search for the electron's electric dipole moment (eEDM) for fundamental symmetry violations. These techniques are broadly applicable, and make cooling and trapping heavier and more complex molecules with greater sensitivity to fundamental physics more viable.

Citations to Previous Work

Portions of this thesis or results described herein have previously been published in the references below. Where appropriate, citations and acknowledgments are also provided in the body of the thesis for derivative or collaborative work.

1. Z. D. Lasner, A. Frenett, H. Sawaoka, L. Anderegg, B. L. Augenbraun, H. Lampson, M. Li, A. Lunstad, J. Mango, A. Nasir, T. Ono, T. Sakamoto, and J. M. Doyle, "Magneto-optical trapping of a heavy polyatomic molecule for precision measurement," *Phys. Rev. Lett.* **134**, 083401 (2025).

2. H. Sawaoka, A. Nasir, A. Lunstad, M. Li, J. Mango, Z. D. Lasner, and J. M. Doyle, "Optical Trapping of SrOH Molecules for Dark Matter and T-violation Searches," *Phys. Rev. Research* **8**, 013100 (2026).

3. A. Lunstad, H. Sawaoka, Z. D. Lasner, A. Nasir, M. Li, J. Mango, R. Fields, and J. M. Doyle, "High-sensitivity molecular spectroscopy of SrOH using magneto-optical trapping," *Phys. Rev. A* **113**, 042820 (2026).

4. H. Sawaoka, A. Frenett, A. Nasir, T. Ono, B. L. Augenbraun, T. C. Steimle, and J. M. Doyle, "Zeeman-Sisyphus deceleration for heavy molecules with perturbed excited-state structure," *Phys. Rev. A* **107**, 022810 (2023).

5. A. Nasir, A. Lunstad, M. Li, S. Salim, S. Liu, C. Hallas, J. Doyle, "Order of Magnitude Improved Optical Trapping of Molecules Through Transverse Cooling," *arXiv:2607.16913.* (2026)

Contents

List of Figures

List of Tables

To my favorite scientist

Acknowledgements

I would first like to thank my advisor, John Doyle. I really didn't know anything about molecules before joining John's group but I ended up loving everything we did in the lab with his direction. He makes a great effort to develop a personal relationship with his students, and is unbelievably composed in times of crises such as the COVID pandemic or the current "we have no more money" pandemic. It has been a treat to be part of his group.

My committee members have also been instrumental throughout graduate school. Markus has aided my understanding with his deep questions getting at the fundamentals of what we do and his remarkable technical expertise. Susanne has always ensured that I understand the long term implications of my research and provided pivotal insight for the transverse cooling simulation project I undertook. I am extremely grateful for the both of them.

My mentors in college are why I decided to pursue a physics PhD in the first place. Tiku, my thesis advisor, mentored me with patience, kindness, and introduced me to the world of AMO. Despite me flooding the lab with (possible) Thallium water, he always pushed me in the right direction and is the reason I am here today. Charlie with his self-deprecating humor and youthful energy was always there to lend an ear, drive me to Rhode Island, and be someone that I could confide in. Catherine is the best teacher I have ever had, and will ever have because I don't intend to go back to school. She made me love physics and want to pursue it and am very thankful to her.

I first started in the Doyle group on the now deprecated YbOH experiment, where I was lucky enough to work under an exceptional collection of post-docs and graduate students.

Zack Lasner is one of the best, most well-rounded physicists I have ever met. He taught me everything about molecular structure, experimental techniques, and fundamental physics. His humility and work

ethic are an inspiration and I look up to him greatly.

Ben Augenbraun, who was practically a celebrity in the Williams physics department, would take the time every Friday to answer all my questions about what we did. I have never seen anyone give presentations as good as his, or explain difficult concepts with such ease and clarity.

Alex Frenett, who I now consider a friend, showed me how the experiment worked at a time when I lacked experience. I always felt comfortable confiding in him about things I was struggling with both in and out of lab. I really loved playing soccer with him and trying to get him to appreciate Declan Rice's prowess on the field.

I learned a lot from Hiro Sawaoka's meticulous approach to the experiment and enjoyed discussing his models and ideas. We probably wouldn't have an SrOH MOT today had he not thought about the Doppler shifts of our slowing beams.

Loic Anderegg is the definition of a long-distance running open-water swimming experimental powerhouse. I have never met someone who is so efficient at doing what needs to be done on the experiment, and so technically competent. I would also like to thank all the Doyle group members I have had the pleasure to interact with including Nathaniel, Debayan, Yicheng, Xing and many others.

I have been very lucky to have such a good relationship with my lab mates on SrOH, and although this thesis has my name on the front, it is a reflection of all the hard work that we have done as a collective.

Annika Lunstad is the person I have worked with and overlapped with the most in graduate school. I remember the time where we had to set up three dye lasers in Lyman 29. It was her first time doing so, and by the end of the day, she had put together all three on her own working far better than anything I could manage. She took that experience to SrOH and constructed the most impressive and complicated daisy chained SFG system, something we always show off to visitors. In fact, no SFG system in the lab is untouched by her. I don't know if I have ever met someone with the combination of her incredible technical ability, bigger picture thinking, and sharp debugging skills. Through working with her, I always knew she

would become an incredible scientist and the go-to person in lab for almost everything. Today, however, she has somehow exceeded those already lofty expectations. She also possesses a warmth, friendliness, and empathy that is frankly rare in this field. We have developed a wonderful friendship together, where her kindness not only makes mundane lab days much better, but makes everyone in the group much more comfortable. If she had not joined, I would most likely not have made it this far and would not be writing this thesis today. This degree is as much hers as it is mine.

Mingda Li is one of the funniest, most compassionate and technically gifted students I've worked with. He is always thinking about how he can help the experiment and his labmates and has a lot of credit cards, like myself. His sincere care for all of us, and just how much fun he is to talk to about everything, has made this experiment a true joy to work on. I consider him my little brother.

Jack Mango, after whom the fruit was named, was one of the first young students I was in charge of. His diligence on the experiment, coding proficiency, and love for milky always brighten my mood, especially as we share Instagram reels in our office instead of designing a buffer gas cell.

Saif Salim joined last year and is one of the most sincere people I have ever met. His warmth and enthusiasm embraces me in the cold depth of the Lyman basement (I don't work there), and his attempts at a coup although fruitless have been endearing.

It turns out there are non-SrOH people in the Doyle group. One of them is my good friend Paige Robichaud who has achieved remarkable things on the CaOH experiment. Despite her proficiency, she is one of the most approachable and humble people I know. She has a professional attitude which is incredibly admirable, and is always willing to lend a hand or answer any questions. I have enjoyed, and will continue to enjoy, our conversations ranging from the Minnesota Vikings to piping hot physics tea, and will always appreciate the mark she made on the group in making it so much more welcoming and fun. From hanging out during morning coffees with Annika, eating salmon and beans for dinner, walking to and fro the machine learning class I stopped attending, this experience would truly not be the same

without Paige.

To Christian Hallas, I almost feel like you with how much I've said in this acknowledgment section. Christian has an enthusiasm and a gentle kindness that has helped me get through the most difficult of lab days. Our friendship also serves as a welcome break from lab, where I feel comfortable talking to him about future job prospects, how to navigate lab dynamics, or just nonsensical things about soccer or his favorite Danish desserts.

Avikar Periwal got away without a compliment on my defense, but I can't help but say how important he has been for me and the group. His friendship, sheer skill at pretty much everything he does, willingness to listen to my Vyvanse fueled rants and rambles, and generosity have made the last year or two quite wonderful. He's sitting next to me right now wondering how I got this far without knowing any LaTeX. I think the group is extremely lucky and better off with him in it.

Grace Li has always helped me understand what to do next in Silksong and gives me massive fomo with her extremely cute cat. She is unbelievably good at what she does and I am excited to see her continue to push the $CaNH^2$ experiment forward. The work she has done thus far has been remarkable with her amazing team.

Part of that team is Giseok Li has always been critical of my lack of motivation to go to the gym, but always brightens my time in the office. Watching him become confident in his work has been incredibly heartwarming and I hope he continues to recognize just how wonderful a scientist he is.

Scarlett Yu and Jiaqi You reside in the depths of the CaF experiment and have never hesitated to engage in banter with me. Scarlett's extremely tasteful Instagram reels fill my day with an unspecified but quite strong feeling, and I appreciate Jiaqi for letting me hide at his desk, never judging me for not knowing what the most basic RF components are.

Junheng Tao has always been extremely friendly and kind to me, and I'm really sorry to him about the milk receipts. The fact that he never seems that upset about it is a testament to his patience.

I would like to thank everyone on RaX, particularly Arian who has been a mainstay from the YbOH days, always willing to discuss ideas or help out with our experiment.

I owe a lot to the amazing friends I have made along the way. Trisha has always enjoyed making fun of my squat depth but is incredibly empathetic and kind. I have enjoyed all our conversations about serious things, ridiculous things, and everything in between. It has always been a joy to share foods that we love from our childhood homes, and she always brings together people through planned outings to places on the Northeast or to extremely good restaurants. She has truly made the department a better place.

Karter is an absolutely sweet man who loves whipped cream and is such a joy to be around. Playing Mario Kart, getting Scoop 'n Scootery (yuck) and just talking about our lives, our jobs, and trying to predict what happens in movies are all things that have made the last few years so fulfilling. He has a sincerity that is rare and has really, really helped and supported me in most aspects of my life.

Together, Trisha and Karter have treated me like family and often drive me to suburbia where I spend all my money on random kitchen items.

Noah has helped ground me in graduate school. It might sound surprising given these acknowledgments, but Noah might be the funniest person in the department. His humor and gentleness have made my time in graduate school so worthwhile, and I don't think there exists a more brilliant but kind and gentle person. Lucie, who is French, has been a breath of fresh air ever since she arrived to *America*. I have truly appreciated chatting with her and complaining about the various hardships related to being an immigrant here, and she is always extremely attentive and willing to listen.

Katya and I started life in Cambridge about a year apart, and have spent a lot of time gossiping, dreading immigration issues and recounting stories from the troubling times in rural Massachusetts. I would have genuinely dropped out if she wasn't here to be okay with me flaking on her but still hanging out with me. She has such a calming presence and is unbelievably considerate and incredible at what she does. Her defense (congratulations!) was an inspiration and served as an example of what hard work and great

scientific communication looks like.

Jamie is the type of person that is very comfortable to be around because of her consideration and kindness. If she ever meets someone new, she always goes out of her way to be friendly and open. Between video games, cats, and Bonchon, she is a big reason why Cambridge has been so enjoyable and I am looking forward to returning from the dead to hang out with her.

Nicole was probably my first friend in the US and is the type of person who does not judge you for vanishing off the face of the Earth. She asks incredible questions about anything, and is incredibly attentive and genuine in the way that she listens. I have cherished all of our conversations together and am looking forward to hanging in New York.

Speaking of New York, Emily has made herself at home among all the rats and is probably baking something extremely delicious. We have cooked many things together and have reminisced on our time in college. I have been very inspired by her various talents and the fact that she is still such a down-to-Earth person. I feel very lucky to have her as a friend and she has always welcomed me into her home with open arms.

Much to the concern of, perhaps every single person in the US, from Pakistan emerged a trio that would take football twitter by storm.

I have known Taimur for over a decade, and he strikes an incredible balance between winding me up about Arsenal but also being incredibly sweet and supportive. It always feels like the good old days when we hang out and I cherish his friendship a lot. He has always been incredibly supportive of me and what I've wanted to pursue, and he has always treated me with so much kindness and care even when perhaps I have not deserved it.

Suroor has always been a grounding force for me, and is always enthusiastic about everything I do in my life even when it's really, honestly, not that interesting. I have enjoyed seeing her journey into music and hope she continues to pursue her passions. She has taught me a lot about things outside of my physics

bubble, and has inspired me to broaden my interests.

This is actually way too long so I just want to give my thanks to so many people including Rabia, Aurelien, Zubia, Conner, Ryan, Caelen, Alex (all of them), Sorcha, Sabrina, Nate, Derrick, Ashay, Heather, Mariam, and many, many others.

About 28 years ago, I was born. The people responsible for this, namely my parents, have always shown unconditional support for me and my dreams. Despite the fact that I have been gone so long and never come back, they have always made sure that I do what I love and am happy. I am incredibly lucky to have had such an attentive, loving, and caring support system in my corner who have always sincerely wanted what is best for me.

My sisters Nadia, Sara, and Anum are huge sources of inspiration for me. Their work ethic and ability to put up with me have made my life extremely fulfilling and they mean a whole lot to me. Even when I'm difficult or disappear, they always approach me with open arms and zero judgement. Shayan entered the family and seamlessly fit into the whirlwind, treating me like his younger brother, and providing a shield from the chaos.

"Unity, Faith, Dis[persed fluorescence]"

Muhammad Ali Jinnah [Altered]

1 Introduction

In 2010, the laser cooling of molecules was demonstrated for the first time using the diatomic species Strontium Fluoride (SrF) [1], nearly three decades following the laser slowing of a Sodium atomic beam [2]. The additional complexity present in molecular structure compared to atomic structure, as well as the wide range of species available, gives molecules remarkable potential in the field of quantum science. That very complexity, however, is what makes it so challenging to harness these capabilities using cooling, trapping, and complete quantum control. The laser cooling of SrF proved that such a task was difficult but not impossible. The first three-dimensional molecular trap, again in SrF, was demonstrated soon after in 2014 [3] and signified a paradigm shift in modern Atomic, Molecular, and Optical (AMO) physics. Rapid progress was made to implement with molecules the routine techniques used to control atoms, including

chirped slowing [4], sub-Doppler cooling [5–7], optical traps [8–12], lattices [13, 14], and optical tweezers [15, 16]. Today, ultracold molecules are amenable to the full range of quantum control technologies, resulting in several breakthrough results demonstrating their promise, such as measurements of dipolar entanglement [16], very long ground state lifetimes [11], and protocols for precision measurements in an optical trap [17, 18]. In this work, we leverage these techniques and apply them to the SrOH molecule.

In this chapter, we develop the foundation to explain how ultracold SrOH (in an optical trap) holds significant promise for precision searches for beyond the Standard Model (BSM) physics. We first describe the importance of ultracold SrOH for dark matter and BSM particles. Following this, we introduce the SM and how certain unanswered questions within its framework motivate such measurements. We then discuss the motivation for searches of ultralight dark matter in Sec. 1.3 and the electron's electric dipole moment in Sec. 1.4, developing a theoretical framework from the perspective of an AMO experimentalist. We ultimately show how SrOH is a strong candidate for such measurements. Lastly in Sec. 1.5, we touch upon the importance of laser cooling and how conducting such measurements in an optical trap is advantageous.

1.1 Ultracold SrOH for Fundamental Physics Searches

Precision measurements in atoms and molecules can probe unanswered fundamental physics questions related to the Standard Model and cosmology, testing theoretical models for new physics. Molecules are particularly amenable systems to this end. Compared to atoms, their richer degrees of freedom including vibrations and rotations make them, in certain important cases, intrinsically more sensitive to new fundamental physics. The two most sensitive measurements of the electron's electric dipole moment (eEDM) to search for T-violating physics have been conducted using molecules. These include the ACME collaboration which uses a beam of ThO molecules [19], and the trapped molecular ion experiment at JILA [20],

which uses HfF^+. The current state-of-the-art methods, however, are approaching a bottleneck in sensitivity. The generic, unentangled statistical uncertainty for a precision measurement is given by:

$$d_{\text{bsm}} \propto \frac{1}{X_{\text{sys}}\tau\sqrt{N}}, \tag{1.1}$$

where X_{sys} is the "intrinsic" sensitivity that the molecule provides, N is the number of molecules you measure and τ is the measurement interaction time. The bottleneck for a molecular beam experiment is often τ, where obtaining increasingly longer interaction lengths L has diminishing returns as the detectable flux of molecules goes down as $1/L^2$. For molecular ions, drastically increasing N is also challenging due to Coulomb repulsion. In both cases, adding this additional complexity to circumvent these limitations results in greater challenges in controlling systematic errors.

A promising platform that could alleviate some of these issues is an ultracold, optically trapped neutral molecular species. This would allow for long trap lifetimes to provide much larger τ, as well as the ability to scale N with a higher ceiling than in a molecular ion experiment. Additionally, control over systematic effects would be made much simpler due to exceedingly small confinement volumes of ~100 μm. One can take inspiration for potential future directions in precision measurement from the technological developments in other areas of the AMO community, especially optical clocks. Early clocks were developed using atomic beams [21] and fountains, eventually leading to a ground-breaking redefinition of the SI second [22]. However, in the last several decades, technology has evolved such that the current best clocks utilize either the high numbers and long coherence times in optically trapped neutral atoms or the long term confinement and reduced environmental noise of trapped atomic ions. These improvements have been remarkably successful, showing how to achieve tightly controlled environments with high number and long coherence times. The difficulty in applying these methods to precision measurement for fundamental physics (searches for BSM particles) lies in the complexity of the systems with highest sensitivity, namely molecules.

In general, full quantum control of ultracold atoms allows for better systematic control, reducing the effects of Doppler widths and photon recoil [23, 24], dramatically improving the performance of clocks. As such, it would be ideal to pair this kind of control with the intrinsic sensitivity to fundamental physics that molecules possess. Unfortunately, the complex structure that makes molecules so sought after for such studies make them challenging to laser cool. SrOH thus holds significance in the context of precision measurement, as it is the only molecular species with high sensitivity to new physics that has been laser cooled and optically trapped.

In particular, the vibrational modes in molecules including SrOH make them probes of the oscillation of $\mu = m_p/m_e$, the proton-to-electron mass ratio, allowing for constraints on certain models of ultralight dark matter (UDM) [25, 26]. Although all molecules are sensitive to this oscillation, SrOH has a fortuitous pair of closely spaced vibrational modes that make sensing μ-variation technologically convenient, with easy access to multistate systematic error suppression protocols. More generally, μ-variation is model independent and can help test a wide variety of new physics through constraints on its oscillation or drift [25, 27], including tests of the equivalence principle [27, 28], "fifth force" theories [28], the cosmological evolution of fundamental constants [27], and the existence of generic BSM scalar or pseudoscalar fields [25, 29]. Additionally, the parity doublet structure in the bending mode in conjunction with SrOH's high mass makes it an excellent candidate for improving the sensitivity of the eEDM, thus extending its already far reach into T-violating physics. From Eq. 1.1, this high intrinsic sensitivity X_{stat}, large τ due to optical trapping (Chapter 6), and improved N through the advent of novel techniques including the transverse cooling of the molecular beam illustrate the potential of SrOH for such studies. The development of these techniques for a heavy polyatomic species also has broader implications for other fundamental searches. Their implementation makes trapped molecule experiments with heavier or more complex species with even greater potential for fundamental physics searches more viable.

1.2 Precision Measurements for Beyond the Standard Model Physics

In this section, we describe the necessary background to motivate precision measurement searches with SrOH. This includes first a description of the Standard Model (SM) in Sec. 1.2 a) and how it is currently incomplete. Then, in Sec. 1.2 b) we briefly discuss common experimental methods employed to help solve some of the mysteries in the SM, potentially leading to new physics.

1.2 a) The Standard Model

Precision measurements of atomic or molecular structure are deep experimental probes in particle physics. The Standard model (SM) is the quantum field theory that describes all known elementary particles and their interactions [30] and has been remarkably successful at explaining and predicting much - but not all - of the observed behavior in the Universe. For example, the most precise measurement of the electron's magnetic moment [31] agrees with the SM prediction to one part in 10^{12}.

Despite the fact that the SM has remained self-consistent and has withstood nearly every laboratory-based experimental test to date, it is still unable to explain major observed phenomena in the universe. Below are a few pertinent open questions that the SM has failed to explain:

- **Gravity**: Currently, only three of the four fundamental forces of nature are accounted for in the framework of the SM: the weak and strong interactions and the electromagnetic force, while gravity is excluded.

- **Matter-Antimatter Asymmetry**: Based on astrophysical observations of the cosmic microwave background (CMB), cosmic rays, and the makeup of stars and galaxies, we know that the Universe is made of almost entirely matter with little antimatter. This asymmetry is not accounted for in the SM as we elaborate upon in Sec. 1.4, when we discuss the search for the electron's electric dipole

moment.

- **Dark Matter:** The SM does not have a description of the true nature of dark matter, which comprises 27% of the total mass-energy density of the Universe. Sec. 1.3 focuses on probing the effects of dark matter on molecular states within a certain predicted DM mass range.

These mysteries along with many others have driven efforts towards developing theoretical models which either add extensions to the SM, or that come up with non-SM frameworks. This can include the introduction of new particles, interactions, or whole sectors. Discoveries of new particles or tighter bounds on parameters of interest can help add constraints to theories and inform the true worth of future directions.

1.2 b) Experiments to Probe the Standard Model

Fundamental physics can be probed in a variety of complementary ways. Below, we provide a few examples before going into detail about precision measurements in the next section.

Direct Detection

Several groups have designed experiments aimed towards directly measuring the effects of phenomena found naturally in the Universe, using the environment around us as a "laboratory". This work often involves building advanced state-of-the-art detectors with low noise floors and high sensitivities to the physics of interest. For example, the Super-Kamiokande Collaboration measured the oscillation of atmospheric neutrinos in 1998 [32] using an array of 11,146 photomultiplier tubes (PMTs). This result was significant as it implied that neutrinos had mass which is not accounted for in the SM. Additionally, the LUX-ZEPLIN (LZ) collaborations design and utilize a liquid Xenon detector to search for Weakly Interacting Massive Particles (WIMPs), which have been proposed as a dark matter candidate [33].

Collider Physics

Colliders work by producing high energy collisions in particle beams and detecting the byproducts. These byproducts have energies at the 100 GeV − 1 TeV scale, have very short lifetimes, and cannot be produced in any other way. The Large Hadron Collider (LHC) at CERN is an example of a collider and is where the ATLAS and CMS collaborations detected the Higgs boson in 2012 [34, 35]. While demonstrably successful, such projects face technological limitations towards pursuing higher energy regimes including monetary cost, sheer size, and detector capabilities [36].

Precision Measurements of Atomic and Molecular Structure

Atoms and molecules can be used as testbeds for the SM to measure the effects of BSM physics or test certain SM predictions. Thus far, AMO experiments have established precise measurements of the electron's magnetic moment in agreement with the SM prediction [31], as well as leading sensitivities on the *e*EDM to probe time reversal symmetry violation (T-violation) and test new physics at the 3 − 30 TeV scale [19, 20, 37]. The advantage of such systems is that they can probe a wide range of energy scales using well established techniques in table-top systems, often relying on common spectroscopic methods. Additionally, these tests can be quite broad through 2-loop interactions with BSM particles.

1.3 Dark Matter

In this section, we aim to show why SrOH is a strong candidate to probe ultralight dark matter (UDM). We first motivate the existence of dark matter through a discussion of various astrophysical observations, showing its gravitational effects with ordinary matter. We then discuss a certain class of DM known as ultralight dark matter (UDM) to which the SrOH experiment is sensitive. Next, we elucidate how predicted

dark matter candidates arise out of certain particle physics theories through a specific example involving the strong CP problem and the postulation of the axion. We then link this to the SM and show how certain candidates can give rise to oscillations in fundamental constants which we can measure. In particular, we are interested in dilatonic UDM which is predicted to cause oscillations in the proton-to-electron mass ratio μ. Having established this foundation, we show how the vibrational structure of SrOH makes it particularly sensitive to such an oscillation.

1.3 a) Astrophysical Evidence for the Existence of DM

Despite the fact that DM does not interact with electromagnetic fields, there is a plethora of evidence for its existence through astrophysical observations: unaccounted for mass permeates the Universe and accumulates on the edges of galaxies. Astrophysical observations from the middle of the 20th century laid the foundation for the evidence of DM. We follow Ref. [38] closely and summarize some of the significant results.

In 1933, Fritz Zwicky analyzed a cluster of galaxies and calculated the velocity dispersions based on the observed mass of all the stars and luminous matter [39]. The measured values however disagreed by an order of magnitude, implying the existence of some hidden mass that could not be directly observed. It was later discovered that these galaxies contained halos of massive, hot gas which helped reduce the discrepancy but did not completely eliminate it. While Zwicky's observations alone are not a direct confirmation that dark matter exists, they were foundational for more compelling discoveries decades later. Perhaps the most famous and direct piece of evidence pointing towards dark matter's existence comes from Vera Rubin's work in 1970 [40] studying galaxy rotation curves. By mapping out the rotational velocity v_{rot} of some galaxy at a given radius r from the center, one can infer what the mass distribution of the galaxy is via the expression

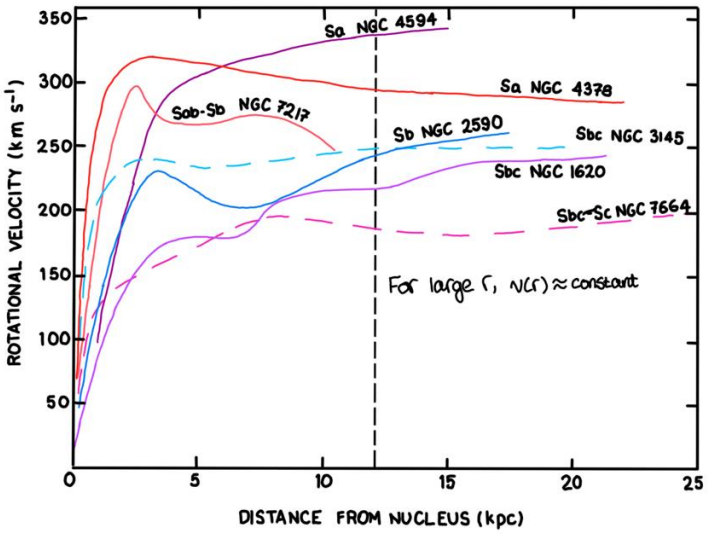

Figure 1.1: Galaxy rotation curves from Vera Rubin's observations. Based on the observed matter distribution in these galaxies, we expect $v(r) \propto \frac{1}{\sqrt{r}}$ resulting in the curves dropping off at high r. Instead, $v(r)$ is approximately constant at large distances from the center, suggesting that some unaccounted for mass extends past the boundaries of visible galaxies. Figure recreated from [40].

$$v_{\text{rot}}(r) = \sqrt{\frac{GM(r)}{r}}, \tag{1.2}$$

where $M(r)$ is the mass density of the galaxy and G is the gravitational constant. Based on the distribution of luminous matter in galaxies, $M(r)$ should be approximately constant resulting in $v_{\text{rot}}(r) \propto 1/\sqrt{r}$ [41]. However, Rubin showed that $v_{\text{rot}}(r)$ is constant, implying that $M(r) \propto r$ and that there exists unobserved matter concentrated on the edge of galaxies.

In 2006 gravitational lensing observations of the Bullet Cluster, a pair of galaxies that merged hundreds of millions of years ago, fortified the already compelling evidence laid out by Rubin [42]. Gravitational lensing is the phenomenon where light is bent in the presence of a high gravitational field due to a massive object, which can shift the apparent position of other objects nearby. Shown in Fig. 1.2, the implied mass distribution of the Bullet Cluster from gravitational lensing studies is distinct from the luminous matter distribution, where large amounts of mass collect beyond the edges of the observed galaxies, similar to what Rubin observed. Additionally, the violent collision processes following the merging of the galaxies

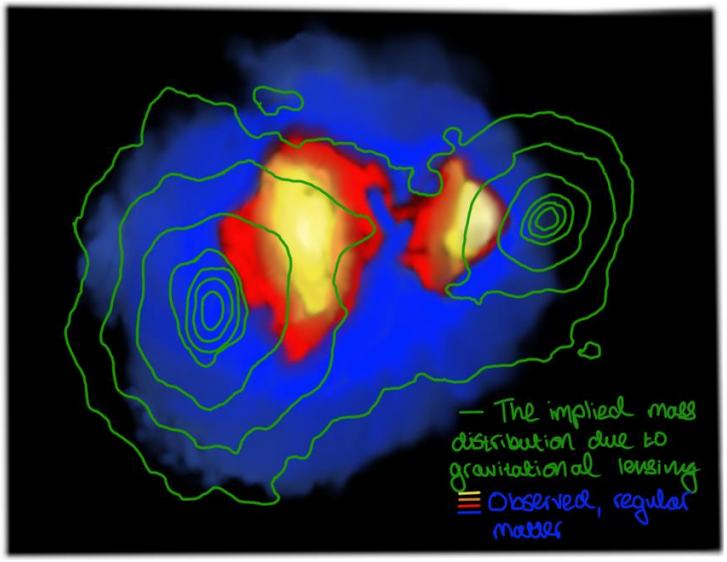

Figure 1.2: Gravitational lensing of the Bullet Cluster. The green contour plots show the implied mass distribution from gravitational lensing, where the colored heatmap shows the observed matter. The contours spread out beyond the observed matter with their centers shifted. They also seem to have passed through each other relatively unscathed, suggesting the existence of unreactive dark matter. Figure recreated from [42]

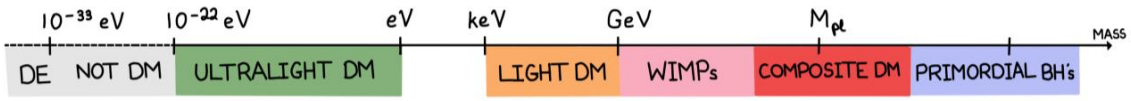

Figure 1.3: The parameter space for DM, showing the potential masses of the proposed candidates spanning almost 100 orders of magnitude. Figure recreated from [43].

resulted in hot baryonic matter that interacted in the way we would expect. The purported dark matter shown by the contour plots however seems to have passed through rather uneventfully, providing evidence that it does not react with ordinary matter.

1.3 b) Ultralight Dark Matter

The unknown nature of dark matter is illustrated, almost comically, in Fig. 1.3 which shows the mass range for potential dark matter candidates, scaling nearly 100 orders of magnitude from the subatomic scale to galaxies and primordial black holes. Several experiments utilize different techniques and aim to probe

some fraction of this mass range, where the predicted particle and underlying physics can vary drastically between regimes.

As discussed in Ref. [38], a "well motivated" theory of dark matter includes a creation mechanism that matches the current observed density. These theories predict long lived, stable particles that have survived since the early Universe. Additionally, such theories also solve some other mystery that the SM cannot explain; since the parameter space for what dark matter could be is so large, these criteria help add necessary constraints to dark matter models.

The SrOH experiment probes the ultralight dark matter (UDM) regime for masses between 10^{-22} – 10^{-18} eV. In this regime, UDM is treated like a classical bosonic field, and measurements aim to measure its coherent, wavelike properties with its Compton frequency

$$\omega_c = \frac{mc^2}{\hbar}, \tag{1.3}$$

where c is the speed of light, m is the mass of the dark matter particle and $\hbar$ is the reduced Planck constant. The UDM field must be bosonic as the high mode occupation number required to produce this classical field is forbidden for fermions due to the Pauli exclusion principle. Moreover, there is a minimum particle mass as lighter UDM particles result in longer wavelengths which eventually match the scale of dwarf galaxies, resulting in "fuzzy" dark matter which no longer behaves like a coherently oscillating wave. Even for a given mass range, several theories can predict various different coupling mechanisms to the SM, some of which we explore below.

1.3 c) Axions

Although not directly relevant for the SrOH UDM search, a well known candidate for the UDM field is the axion [44–46]. This example is pertinent as it sheds light on how high energy theory attempts to

reconcile issues with the SM and how this can, in turn, result in a well-motivated dark matter candidate. Additionally, the relevant mechanisms for our experiment in the dilaton and the "Higgs portal" require a level of theoretical description that is out of the scope of this thesis.

An axion is a hypothetical particle initially proposed to solve what is known as the strong-CP problem in quantum chromodynamics (QCD) [44–47], where CP stands for charge-parity. In the QCD Lagrangian, CP-violation is contained in the operator [47]

$$\mathscr{L}_\theta = -\frac{\bar{\theta}}{32\pi^2} G^a_{\mu\nu} \tilde{G}^{a\mu\nu}, \tag{1.4}$$

where $G^a_{\mu\nu}$ and $\tilde{G}^{a\mu\nu}$ represent the gluon strength and its dual. More importantly for our motivation of axions, the phase $\bar{\theta}$ is some tunable parameter between 0 and 2π which sets the size of CP violating effects in QCD. The explicit details of this formula are not important for this discussion and only serve to show how one can predict a physical observable from such a theory. For example, this phase term gives rise to a neutron EDM [47]

$$d_n \approx 3.6 \times 10^{-16} \bar{\theta}\ e\ \text{cm}, \tag{1.5}$$

where e is the elementary charge. From precision measurements [48], $|d_n| < 1.1 \times 10^{-25}\ e$ cm which implies $\bar{\theta} \lesssim 10^{-10}$. This value gives rise to the strong-CP problem: since $\bar{\theta}$ is actually the sum of two independent parameters in QCD, it seems far too coincidental that they miraculously cancel to such high precision. This issue was circumvented through the introduction of a dynamical field which can give rise to a theoretical particle known as the axion, where specific details can be found in [44–46]. In addition to helping solve the strong CP problem, axions are predicted to be ultralight, cold, and stable, while their production and abundances are consistent with the amount of dark matter that exists, thus forming the basis of a well motivated DM theory. As such, attempts to solve a puzzle in QCD and extend the SM serendipitously gave

birth to a viable dark matter candidate.

1.3 d) Fundamental Constant Variation

Having provided an example of how dark matter candidates can arise from theory, it is important to know the various ways in which we can measure their effects. From Ref. [38], one can show quantitatively how DM particles interact with the SM. This is pivotal, as to understand the true nature of DM there needs to be some potentially (very weak) coupling to the SM to allow for our atoms, molecules, or detectors to have any chance of revealing a signal. The general form of these so-called "portals" can be written in a model-independent way for a time-dependent scalar or pseudo-scalar dark matter field ϕ such that

$$\mathscr{L}_{\text{portal}} = \left(-\sum \Gamma_f^{(1)} m_{f,0} c^2 \bar{\psi}_f \psi_f + \frac{\Gamma_\alpha^{(1)}}{4} F_{\mu\nu} F^{\mu\nu} \right) \sqrt{\hbar c}\phi, \tag{1.6}$$

where m_f and ψ_f represent the SM fermionic fields and masses, $F^{\mu\nu}$ is the electromagnetic Faraday tensor, $\hbar$ is the reduced Planck constant, c is the speed of light, ϕ is the dark matter field, and $\Gamma_{f/\alpha}$ is some coupling constant between the SM and that dark sector. The overall effect of this portal when added as a correction to the SM lagrangian is to shift, say, the fermionic mass [29]

$$m_{f,0}^{\text{eff}} = m_{f,0} \left(1 + \Gamma_f^{(1)} \sqrt{\hbar c}\phi \right). \tag{1.7}$$

If ϕ then has some time dependence such that we have $\phi(t)$, this results in an oscillation at the Compton frequency of the dark matter field.

Having established how UDM fields can give rise to variations in fundamental constants, we can now specify the models that the SrOH experiment aims to probe. The oscillations we described can arise due to higher order effects from pure axions [49, 50], axion-like particles (ALPs) [51, 52], or dilatons [53, 54]. Specifically, a dilaton is a scalar field that arises commonly in string theory and extensions to gravity that

has also been identified as a potential dark matter candidate [55]. In the spirit of Eqs. 1.7 and 1.6, one can write down a dilaton-mediated oscillation of the fundamental constant μ, the proton-to-electron mass ratio from Ref. [28]

$$\frac{d\mu}{\mu} = \left(d_{m_e} + d_g + M_A d_{\hat{m}}\right)\kappa\phi(t), \tag{1.8}$$

where for some time-dependent dilaton scalar field, there is some coupling d_{m_e} to the electron, d_g to the gluon, and $d_{\hat{m}}$ to the quarks where κ is some normalization factor and M_A is a dimensionless scaling factor. This provides us with a signal we can search for using our molecular system, and is what the SrOH molecule is particularly sensitive to. In general, probing μ-variation allows us to be sensitive to a range of possible models, allowing for a broader reach into BSM physics.

1.3 e) Probing UDM and μ-Variation with SrOH

Polyatomic molecules, with SrOH being an exemplar species, are powerful probes of μ-variation. Since atomic and molecular energy levels depend on the mass of the proton and electron, they also depend on μ. As such, their energy levels could oscillate with the UDM field which can be measured via simple spectroscopic techniques. For a given transition between two energy levels, the sensitivity of the measurement depends on the differential sensitivity that each state has to μ. For an atom, where each energy level "wiggles" approximately the same amount with μ, a spectroscopic measurement would yield a flat line. Linear triatomic molecules like SrOH however have three distinct vibrational modes, as elaborated more in Chapter 2. These can be written as (v_1, v_2^l, v_3) where v_1 represents the number of vibrational quanta in the Sr-O stretching mode, v_2 the Sr-O-H bending mode with l quanta of angular momentum, and v_3 the O-H stretching mode. The different characteristics of the bending mode in particular make a UDM measurement viable. Following Ref. [25], consider ground and excited state energy levels E_g and E_e with some

energy difference $\omega = E_e - E_g$. Then,

$$\frac{\delta\omega}{\omega} = \frac{1}{E_e - E_g}\left(\frac{\partial E_e}{\partial \mu} - \frac{\partial E_g}{\partial \mu}\right)\delta\mu, \tag{1.9}$$

$$\frac{\delta\omega}{\omega} = Q_\mu \frac{\delta\mu}{\mu}, \tag{1.10}$$

where Q_μ is known as the relative enhancement factor. Furthermore, one can show that for harmonic and anharmonic frequencies ω_{harm} and ω_{anharm}

$$\omega_{\text{harm}} \propto \mu^{-1/2}, \tag{1.11}$$

$$\omega_{\text{anharm}} \propto \mu^{-1}. \tag{1.12}$$

Thus, picking a vibrational transition where the levels have different degrees of harmonicity leads to enhanced sensitivity to μ-variation. We can then modify Q_μ to reflect this dependence by first, defining

$$\Delta E = \Delta E_{\text{harm}} - \Delta E_{\text{anharm}}, \tag{1.13}$$

and taking the derivatives

$$\frac{\delta E_e}{\delta \mu} - \frac{\delta E_g}{\delta \mu} = -\frac{1}{2\mu}\Delta E_{\text{harm}} - \frac{1}{\mu}\Delta E_{\text{anharm}}. \tag{1.14}$$

Putting this all together,

$$Q_\mu = \frac{1}{2}\left(1 + \frac{\Delta E_{\text{anharm}}}{\Delta E_{\text{harm}} + \Delta E_{\text{anharm}}}\right), \tag{1.15}$$

producing the result from Ref. [25]. Thus, our sensitivity to the oscillating UDM field depends on us selecting energy levels with different degrees of harmonicity and anharmonicity and thus differential sen-

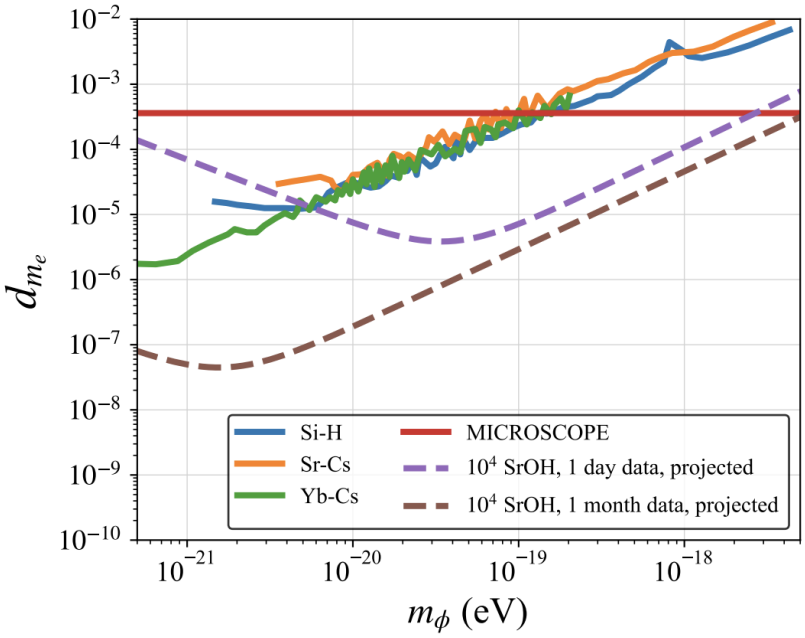

Figure 1.4: Exclusion plot showing the projected sensitivity of SrOH to UDM compared to experiments described in Refs. [56–59]. Depending on the total integration time, 10^4 optically trapped SrOH molecules can improve UDM limits by ~2 orders of magnitude over 4 decades of mass.

sitivities to μ. A natural choice is choosing a transition between a state with only an excited stretching mode and another with only an excited bending mode, where as described in more detail in Chapter 2, the former has more harmonicity and the latter more anharmonicity. In SrOH as shown in Fig. 1.5, the identified states of interest are $\tilde{X}^2\Sigma^+(200) \rightarrow \tilde{X}^2\Sigma^+(03^10)$, which have already been studied with high-resolution spectroscopy. One can calculate that $|Q_\mu| > 100$ for this transition, which means for an SrOH trap with 10^5 molecules with a coherence time of $\tau \approx 140$ ms and a month of integration time, we can improve the sensitivity on the coupling of the UDM field to the electron by two orders of magnitude over three decades of mass (which can be converted to Compton frequency). This is reflected in the exclusion plot in Fig. 1.4 which includes experiments with leading UDM sensitivities in Refs. [56–59]. Another advantage of the $\tilde{X}^2\Sigma^+(200) \rightarrow \tilde{X}^2\Sigma^+(03^10)$ is that the states are nearly degenerate and can be driven with microwaves which are simpler and more robust than optical frequencies. In particular, addressing multiple rotational

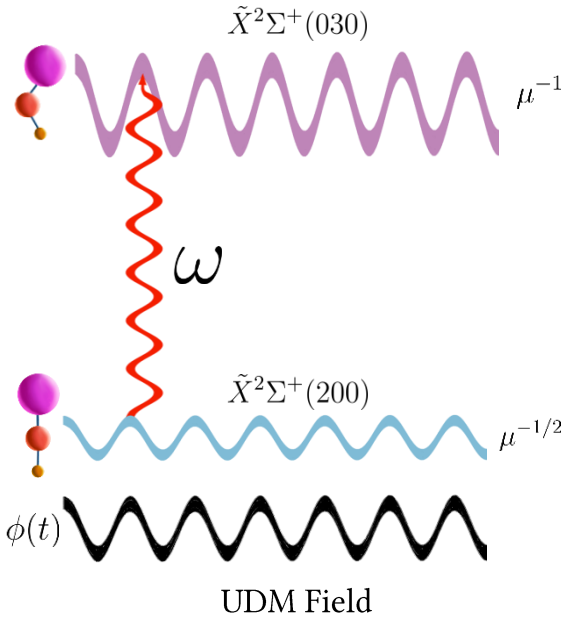

Figure 1.5: The differential sensitivities of the $\tilde{X}^2\Sigma^+(200)$ and $\tilde{X}^2\Sigma^+(03^10)$ states in SrOH, allowing for precision spectroscopy to probe μ-variation. The states oscillate with different dependencies on μ due to their different degrees of harmonicity and anharmonicity.

states in this manifold is trivial, enhancing systematic rejection. Moreover, the $\tilde{X}^2\Sigma^+(200) \rightarrow \tilde{X}^2\Sigma^+(03^10)$ transition is estimated to have a weak transition dipole matrix element of 0.02 D [25]. It is much easier to engineer microwave systems with much higher effective powers compared to optical lasers, which makes them pivotal for the success of such a measurement. We have thus shown that SrOH is a strong candidate to probe UDM through the measurement of the oscillation of μ. Its polyatomic structure generically contains states with differential μ-sensitivity, where the sheer density of states also increases the likelihood of them being near-degenerate. Moreover, we discuss in Sec. 1.5 how conducting this measurement with ultracold SrOH in a conservative trap is advantageous.

1.4 The Electron's Electric Dipole Moment

The goal of this section is to show how polyatomic molecules like SrOH are promising candidates to probe the electron's electric dipole moment (*e*EDM). We first motivate such a measurement by discussing how the observed matter anti-matter asymmetry in the Universe requires more T-violation than the SM predicts, after which we describe how BSM theories may give rise to additional T-violating effects which can manifest as *e*EDMs. Following this, we provide some background as to how an *e*EDM can manifest as an observable energy shift and use this fact to show how it is an example of T (and P) violation, where the below discussions follow Refs. [60, 61] closely.

1.4 a) Searching for T-Violating Physics

As mentioned in Sec. 1.3, a key question unanswered by the SM is why matter dominates over antimatter in the Universe. This is known as the Baryon Asymmetry of the Universe (BAU), and it is argued by Sakharov that four criteria must be satisfied for it to be explained as also described in Ref. [62]:

1. Assuming baryonic symmetry at the start of the Big Bang, there must be some process that then violates Baryon number.

2. There must be C (charge) violation, such that if a process converts $\psi \rightarrow \bar{\psi}$ at some rate $\rho(\psi \rightarrow \bar{\psi})$, the reverse process occurs at a larger rate such that $\Gamma(\bar{\psi} \rightarrow \psi) > \Gamma(\psi \rightarrow \bar{\psi})$.

3. C violation is not enough. For example, if a process prefers baryons with some positive parity $\Gamma(\bar{\psi^+} \rightarrow \psi^+)$, then CP results in $\Gamma(\psi^+ \rightarrow \bar{\psi}^+)$ when C is reversed followed by $\Gamma(\bar{\psi}^+ \rightarrow \bar{\psi}^-)$ when P is reversed. Thus, the preference for baryons is compensated for by CP symmetry and so CP violation is necessary. From the CPT theorem [63], this whole quantity is conserved and thus CP violation is

equivalent to T violation.

4. The early Universe was not in thermal equilibrium as matter and antimatter share the same mass, and their number densities given by the Boltzmann factor e^{-mc^2/k_BT} would need to be different.

The criterion relevant to the *e*EDM is that of T-violation. Though there exists T-violation in the SM, there is not enough to explain the BAU. We discussed earlier a phase in QCD which encodes some of this T-violation. Additionally, there exists a phase in the Cabibbo-Kobayashi-Maskawa (CKM) matrix which encodes quark transition probabilities in the presence of the weak interaction. The CKM matrix phase also accounts for a small amount of T-violation which predicts a value for the *e*EDM to be $|d_e| \sim 10^{-44}$ e cm, currently fourteen orders of magnitude smaller than the current state-of-the-art measurement [64, 65]. We discussed in the previous section that the measurement of the neutron EDM gave rise to the strong CP problem which motivated many BSM theories. In a similar way, constraints on the *e*EDM can inform and probe the SM.

As such, extensions to the SM at the TeV level may give rise to particles whose interactions with SM particles, such as the electron, result in T-violating effects including a permanent electric dipole moment. For example, as shown in Fig. 1.6, assume the simplest case for an *e*EDM. Taking an analog of the one-loop Feynman diagram for the anomalous magnetic moment, supersymmetry predicts that in the presence of a CP violating phase, an *e*EDM could be generated on the order of [66]

$$d_{edm} \approx 10^{-3} \left(\frac{m_e}{m_X}\right)^2 \mu_B. \tag{1.16}$$

This is a convenient way to understand how the mass of new particles depends on the value of the *e*EDM at the one-loop level.

We have established why the search for the *e*EDM is vital to probe, but what exactly do we look for? Take an electron with a permanent dipole moment $\vec{d}_{\text{edm}}$. We can then write the Hamiltonian for this

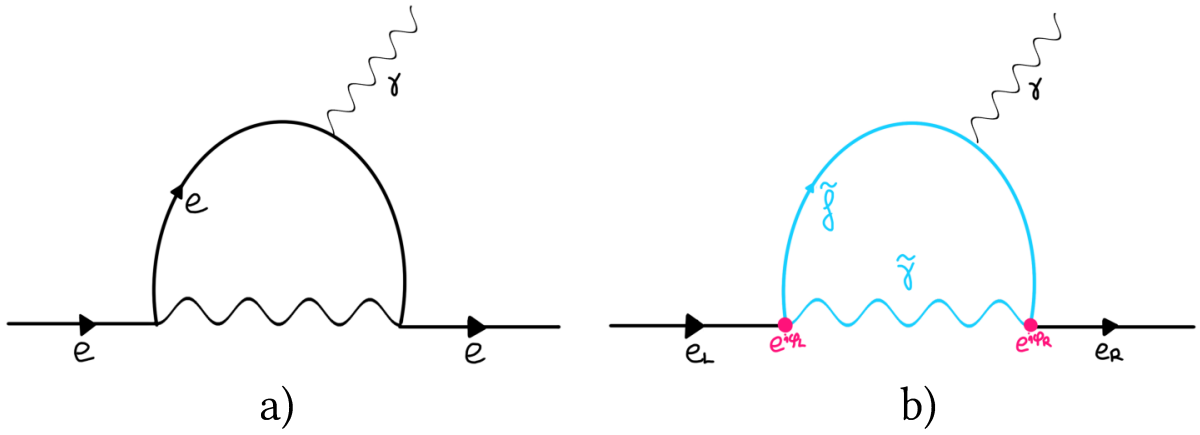

Figure 1.6: a) One-loop diagram showing the anomalous magnetic moment. b) One-loop Feynman diagram analogous to what is shown in a) predicting an *e*EDM from a SUSY model. Here, $\tilde{f}$ is a sfermion and $\tilde{\gamma}$ is a virtual photino which picks up some complex phase φ_L.

*e*EDM in an electric field, given that the electron is a spin-1/2 particle. Although this fact seems obvious, it is a key assumption that determines how *e*EDM measurements are made. Several experiments justify the certainty with which we state this fact, including the Stern-Gerlach experiment [67] , strict limits on the Pauli exclusion principle by looking for anomalous X-ray transitions in Copper atoms [68], and the excellent agreement of the $g-2$ measurement [31] with the SM prediction. Given this, the only relevant vector quantity in question is the spin of the electron which the *e*EDM must point in the direction of. For a given electric field $\vec{\mathscr{E}}$, the Hamiltonian is given by

$$H_{\text{edm}} = -2d_{\text{edm}}(\vec{S}\cdot\vec{\mathscr{E}}) \tag{1.17}$$

$$= \pm d_{\text{edm}}\mathscr{E}_z, \tag{1.18}$$

where the $\vec{S}$ is the electron spin. Fig. 1.7 shows with the help of this Hamiltonian how the *e*EDM is a T and P-violating effect. This involves understanding how an external electric field and the electron spin change under T and P reversal. First, for an electric field one can write the force on some charged particle q in some electric field $\vec{\mathscr{E}}$

$$\vec{F} = q\vec{\mathscr{E}}. \tag{1.19}$$

Newton's laws must hold under time reversal, which means $\vec{\mathscr{E}}$ is unchanged. Moreover, since an electric field can generally be written as

$$\vec{\mathscr{E}} \propto \frac{\vec{r}}{|\vec{r}|^3}. \tag{1.20}$$

A parity inversion changes $\vec{r} \to -\vec{r}$ and thus inverts $\vec{\mathscr{E}} \to -\vec{\mathscr{E}}$, which shows that electric fields are parity odd. Next, we show how the electron spin transforms under P and T reversal by using orbital angular momentum. Since the spin is also an angular momentum, the same logic applies. For a particle with some position vector $\vec{r}$ and momentum $\vec{p}$, the orbital angular momentum is given by

$$\vec{L} = \vec{r} \times \vec{p}, \tag{1.21}$$

$$= \vec{r} \times m\vec{v} \tag{1.22}$$

for mass m and velocity $\vec{v}$. Under T-reversal, we have $\vec{v} \to -\vec{v}$ where $\vec{r}$ remains unchanged, giving $\vec{L} \to -\vec{L}$. Under parity inversion, reflection about the coordinate axis results in both $\vec{p} \to -\vec{p}$ and $\vec{v} \to -\vec{v}$ such that $\vec{L}$ remains unchanged. As a result, angular momentum in general and thus the electron spin is T-odd and P-even. The resulting Hamiltonians become

$$H_{\text{edm}} \xrightarrow[\text{T-reversal}]{\text{P-inversion}} -2d_{\text{edm}}\left(\pm\vec{S}\right)\left(\mp\vec{\mathscr{E}}\right) = -H_{\text{edm}}. \tag{1.23}$$

Since the Hamiltonian changes sign in this way, we conclude that the *e*EDM violates both T and P symmetries. This ties together with the fact that the SM, which contains little T-violation, predicts such a small *e*EDM value. Moreover, it explains how BSM models that incorporate more T-violation generically contain higher magnitude *e*EDMs [64, 65].

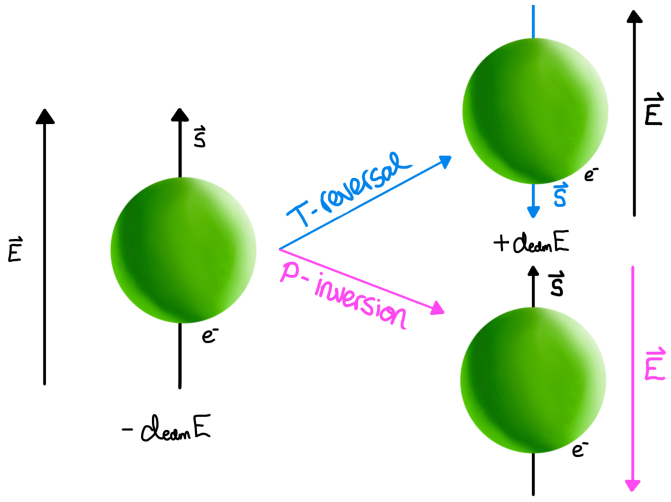

Figure 1.7: T and P violation due to the *e*EDM, where the Hamiltonian changes sign under T reversal and P inversion.

1.4 b) *e*EDM Searches in Atoms and Molecules

A bound electron in an atom or molecule is an ideal system to carry out an *e*EDM measurement. For a free electron, an applied electric field necessary to induce a Stark shift would also accelerate an electron away from any detection region, making a measurement with a long interaction time difficult. On the other hand, one potential caveat to having a bound system relates to Schiff's theorem, which states that there can be no first order Stark effect in the *e*EDM in the limit of nonrelativistic quantum mechanics [69, 70]. To show this, take $\vec{d}_{\text{edm}} = d_{\text{edm}}\vec{S}$ such that averaging the Hamiltonian over an electron orbit gives

$$\langle H_{\text{edm}} \rangle \propto -\langle \vec{d}_{\text{edm}} \cdot \vec{\mathscr{E}} \rangle \tag{1.24}$$

$$\propto -\langle \vec{d}_{\text{edm}} \rangle \cdot \langle \vec{\mathscr{E}} \rangle, \tag{1.25}$$

where we have used the fact that over one orbit, the electron spin remains unchanged. Then, for some general Hamiltonian $H = \frac{p^2}{2m} + V$ for a particle with momentum p and mass m in some potential V,

electrostatics tells us that

$$\langle \vec{\mathscr{E}} \rangle = -\nabla V. \tag{1.26}$$

Rewriting in terms of the momentum operator $\hat{p} = -i\hbar\nabla$,

$$\frac{1}{i\hbar}[\hat{H}, \hat{p}]\psi = \frac{1}{i\hbar}\left[\frac{\hat{p}^2}{2m}, \hat{p}\right]\psi + \frac{1}{i\hbar}[V, \hat{p}]\psi \tag{1.27}$$

$$= 0 - \frac{i\hbar}{i\hbar}(V\nabla\psi - \nabla V\psi) \tag{1.28}$$

$$= -(V\nabla\psi - \psi\nabla V - V\nabla\psi) \tag{1.29}$$

$$= -\nabla V, \tag{1.30}$$

such that

$$\mathscr{E} = \frac{1}{i\hbar}[\hat{H}, \hat{p}], \tag{1.31}$$

$$\langle \mathscr{E} \rangle = \frac{1}{i\hbar}\langle\psi|\hat{H}\hat{p} - \hat{p}\hat{H}|\psi\rangle \tag{1.32}$$

$$= \frac{\lambda}{\hbar}\langle\psi|\hat{p} - \hat{p}|\psi\rangle \tag{1.33}$$

$$= 0. \tag{1.34}$$

Thus, our song and dance ends up showing that if we assume an unchanged spin, the expectation value of the Hamiltonian ends up zero and we cannot measure the eEDM. In reality, the motion of the electron particularly in the presence of a heavy nucleus is subject to relativistic effects. Thus, the electron spin is length contracted by an amount depending on the relative positions of the electron and nucleus. As such,

$$\langle H_{\text{edm}} \rangle \propto \langle \vec{d}_{\text{edm}} \cdot \vec{\mathscr{E}} \rangle \neq \langle \vec{d}_{\text{edm}} \rangle \cdot \langle \vec{\mathscr{E}} \rangle, \tag{1.35}$$

such that the Hamiltonian can be written in terms of an effective electric field $\mathscr{E}_{\text{eff}}$

$$H_{\text{edm}} \propto -d_{\text{edm}} \mathscr{E}_{\text{eff}}. \tag{1.36}$$

It turns out that due to relativistic effects, $\mathscr{E}_{\text{eff}} \propto Z^3$ for high Z which is the nucleon number in an atom or molecule. This means picking species with heavier nuclei is advantageous. In fact, an SrOH molecule has $\mathscr{E}_{\text{eff}} = 2.14$ GV/cm which is several orders of magnitude higher than what can be reasonably applied in a laboratory setting, highlighting the power of the bound atomic or molecular system.

1.4 c) Parity Doublets

We have established why atoms and molecules are ideal tools to conduct an *e*EDM search. Polyatomic molecules are particularly advantageous systems in this regard due to their vibrational structure which includes closely spaced parity doublets. As we will show in this section, these parity doublets allow for sensitivity to the *e*EDM and allow for robust systematic rejection [17, 71]. In order to measure a Stark shift due to the *e*EDM, it is necessary to apply an external electric field $\vec{\mathscr{E}}_{\text{ext}}$ and mix states of opposite parity. To see why, we see that in free space the Hamiltonian is parity invariant and thus, if two parity eigenstates are mixed we obtain for the parity odd dipole moment $\vec{d}$ an expectation value

$$\begin{aligned}
\langle\psi|\vec{d}\cdot\vec{\mathscr{E}}_{\text{lab}}|\psi\rangle &= \langle\psi|\vec{d}|\psi\rangle\vec{\mathscr{E}}_{\text{lab}} && (1.37)\\
&= \langle\psi|P^\dagger P\vec{d}P^\dagger P|\psi\rangle\vec{\mathscr{E}}_{\text{lab}} && (1.38)\\
&= \langle\psi|(\pm)P\vec{d}P^\dagger(\pm)|\psi\rangle\vec{\mathscr{E}}_{\text{lab}} && (1.39)\\
&= \langle\psi|-\vec{d}|\psi\rangle\vec{\mathscr{E}}_{\text{lab}} && (1.40)\\
&= -\langle\psi|\vec{d}|\psi\rangle\vec{\mathscr{E}}_{\text{lab}} && (1.41)\\
&= 0. && (1.42)
\end{aligned}$$

As a result, a state with definite parity cannot have a permanent dipole moment as it is parity-odd: the

symmetry of the system does not allow it. If we have two states of opposite parity however, we can write a Hamiltonian with non-zero off diagonal terms such that

$$H = \begin{pmatrix} -\frac{\hbar\Delta}{2} & -d\mathscr{E} \\ -d\mathscr{E} & \frac{\hbar\Delta}{2} \end{pmatrix} \tag{1.43}$$

where the states are separated by energy Δ in the presence of an electric field $\mathscr{E}$ where the transition dipole moment is d. Diagonalizing this Hamiltonian leads to

$$E_\pm = \pm\sqrt{\left(\frac{\hbar\Delta}{2}\right)^2 + (d\mathscr{E})^2} \qquad \text{(energy eigenvalues)}, \tag{1.44}$$

$$|\psi_-\rangle = \cos\theta\,|+\rangle + \sin\theta\,|-\rangle \qquad \text{(lower eigenstate)}, \tag{1.45}$$

$$|\psi_+\rangle = -\sin\theta\,|+\rangle + \cos\theta\,|-\rangle \qquad \text{(upper eigenstate)}, \tag{1.46}$$

$$P_\pm \equiv \frac{\partial E_\pm}{\partial(d\mathscr{E})} = \pm\frac{d\mathscr{E}}{\sqrt{\left(\frac{\hbar\Delta}{2}\right)^2 + (d\mathscr{E})^2}} = \pm\sin(2\theta) \qquad \text{(polarization)}, \tag{1.47}$$

$$\langle H_{\text{edm}}\rangle_\pm = \pm d_{\text{edm}}\mathscr{E}_{\text{eff}}P_\pm \qquad (e\text{EDM energy shift}). \tag{1.48}$$

Here, $\tan(2\theta) = \frac{2d\mathscr{E}}{\hbar\Delta}$ and $|\pm\rangle$ are the parity eigenstates which form the basis for H. From these expressions, we see that complete mixing of the parity eigenstates is achieved when $P = 1$ as that results in $|\cos\theta| = |\sin\theta| = \frac{1}{\sqrt{2}}$ from Eqs. (1.49) and (1.50). This then corresponds to a maximum possible differential eEDM energy shift of $2d_{\text{edm}}$ from Eq. (1.52).

From Eq. 1.47, we see that the degree of polarization increases when Δ is reduced for a fixed dipole moment and electric field, where Δ is the energy difference between states of opposite parity. In atoms, these are separated by ~100 THz between electronic states. Molecules however due to their complex structure including rotational and vibrational states can have "parity doublets" (PDs) often spaced by ~10 MHz which allows for complete mixing in modest electric fields and more sensitivity to the eEDM. While such

structure exists in certain diatomic species, they generically exist in the electronic ground states of polyatomic molecules.

Molecules are thus more attractive systems than atoms to conduct such a measurement and in fact have set the best limits to date. We have mentioned that closely spaced parity doublets allow for molecules to be easily polarized in modest lab fields. Given that this orients the molecule in the direction of the applied field, we must also ensure that the molecular internuclear axis $\hat{n}$ which is parallel to $\vec{\mathscr{E}}_{\text{eff}}$ is also parallel to the electron spin $\vec{S}$, such that

$$H_{\text{edm}} = -d_{\text{edm}}\mathscr{E}_{\text{eff}}\left(\vec{S}\cdot\hat{n}\right). \tag{1.49}$$

This means that we must orient both the internuclear axis and the spin to the same axis. As mentioned above, polarizing the molecule takes care of the first criterion where we can calculate using Eq. 1.47 that $\langle\vec{d}\rangle = dP_{\pm}\hat{z}$ for an electric field applied in the z direction. Then, since the dipole moment is aligned with the internuclear axis, this implies that $\hat{n}$ lies along $\hat{z}$. Thus, we simply need to align the spin in the same direction which can be done via a magnetic field in the $\hat{z}$ direction.

The ability to orient the molecule in space also allows for greater robustness to systematic effects. As shown in Fig. 1.8, one can conduct a spin precession measurement to measure the *e*EDM. Systematic effects may give rise to a false signal, however. Having multiple "switches" is then advantageous: for example, flipping the orientation of the molecule either spectroscopically or through reversing the electric field results in an *e*EDM shift with a different sign. If there then exists a systematic effect that is invariant in one of those switches, simply subtracting the two conditions subtracts out that systematic while preserving a non-zero *e*EDM. Since anything in the lab can present as a systematic, it is possible that some are invariant only under certain switches. Thus, having various switches allows for a robust precision measurement.

From Eq. 1.50, for a Ramsey type measurement proposed for an *e*EDM search, the statistical sensitivity scales as

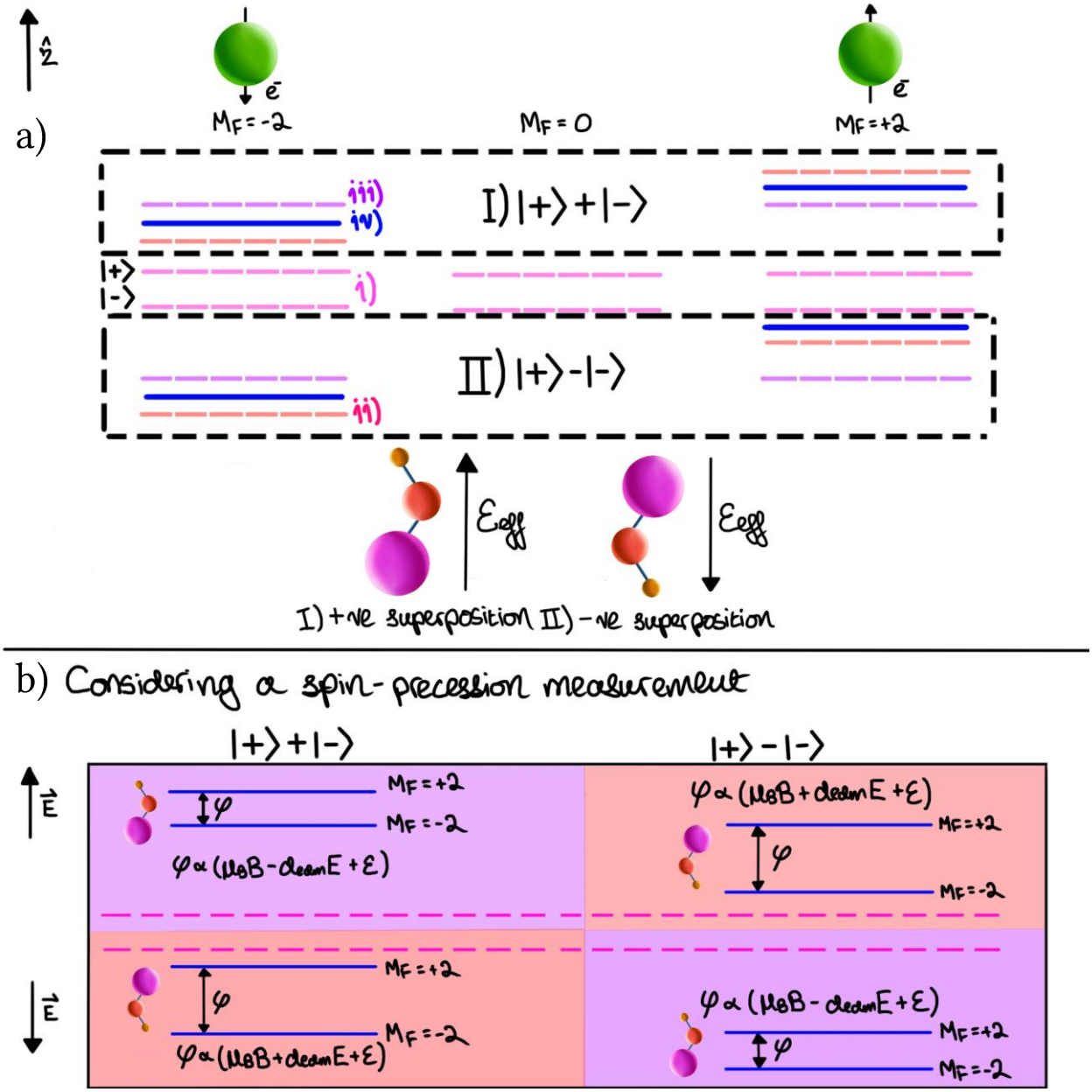

Figure 1.8: a) Energy levels in a $F = 2$ state with parity doublets denoted by $|+\rangle$ and $|-\rangle$. i) The free space parity doublet structure. ii) An electric field is applied in the $+\hat{z}$ direction, mixing the parity doublet states and inducing a Stark shift. iii) A magnetic field is applied to orient the spin resulting in a Zeeman shift on top of the already applied Stark Shift. iv) The eEDM is turned on, adding another Stark shift on top of the previously mentioned effects. Case I) is the energy eigenstate when the molecules are in a positive superposition of the parity eigenstates and case II) is when they are in a negative superposition. b) Cases to consider when conducting a spin precession measurement. The accumulated phase depends on the eEDM shift, the Zeeman shift, and some systematic effect ε. The effect of the eEDM can be switched by flipping the molecular orientation via flipping the electric field or spectroscopically. As such, systematic effects that are invariant in one, but not the other, can be canceled out via the appropriate switch through a linear combination of the two conditions.

$$d_{\mathrm{edm}} = \frac{\hbar}{2\mathscr{E}_{\mathrm{eff}}\sqrt{\tau_{\mathrm{int}}}\sqrt{N\tau}}, \tag{1.50}$$

where $\mathscr{E}_{\mathrm{eff}}$ is the effective electric field, τ_{int} is the total integration time, N is the number of measurements and τ is the coherence time. Although SrOH does not have the highest $\mathscr{E}_{\mathrm{eff}}$ out of the laser coolable alkaline earth metal triatomic molecules, it is the heaviest trapped polyatomic molecule to date, and rapid progress is being made to increase trap numbers and potentially make it a viable candidate to probe the *e*EDM as discussed in Chapter 7.

1.5 Laser Cooling

Being able to laser cool and optically trap molecules is advantageous for precision measurements. Conservative optical traps minimally alter the ground state energy structure, allowing for spectroscopy techniques with high coherence times due to the high trap lifetime. Additionally, systematic effects need only be considered over the small trap size. Unfortunately, the complexity that makes molecules such attractive prospects for precision measurements also makes them difficult to laser cool. Despite this, an ever-growing list of molecules has been optically trapped and cooled with novel techniques being developed to improve numbers, densities, and decrease temperatures, some of which are discussed in later chapters. Fig. 1.9 summarizes the advances in direct laser cooling. In this thesis, we discuss and show results for direct laser cooling from a cryogenic buffer gas beam (CBGB) [72].

1.5 a) Improving Trap Numbers

Although SrOH is a useful tool for precision measurements, much of the work described in this thesis toward improving trapped molecule numbers can also aid in the laser cooling of heavier and more complex species with higher sensitivities to BSM physics. SrOH exists in an intermediate zone: it is perhaps not

heavy enough to be the frontrunner to probe CP-violating physics, nor is it too heavy or complex to be unfeasible for laser cooling although its mass adds difficulty when compared to CaOH. As such, the experiment serves as a useful testbed for even heavier species, much like the CaOH experiment served as a blueprint [11, 73] for the laser cooling of SrOH.

1.6 Thesis Overview

This thesis describes the improved optical trapping of SrOH by nearly an order of magnitude through transverse cooling of the molecular beam. We first discuss the molecular structure of SrOH in Chapter 2 including details regarding photon cycling and the ability to laser cool. Following this, in Chapter 3 we discuss the production and laser slowing of SrOH leading up to initial trapping in a MOT in Chapter 4. In Chapter 5, we elaborate on the techniques employed once a MOT is demonstrated, including further sub-Doppler cooling of the trapped molecular cloud followed by compression in a conveyor-belt (CB) MOT. Moreover, we show measurements of the science state lifetimes in the optical dipole trap (ODT) for both the UDM and *e*EDM measurements. Then, in Chapter 6 we discuss the transverse cooling of the SrOH molecular beam to improve the trapped molecule number. Last, we briefly touch upon the Ytterbium Monohydroxide (YbOH) experiment in Chapter 7 where we show results related to the Zeeman-Sisyphus deceleration of the molecular beam, as well as spectroscopy characterizing f-orbital decays which make laser cooling YbOH so challenging.

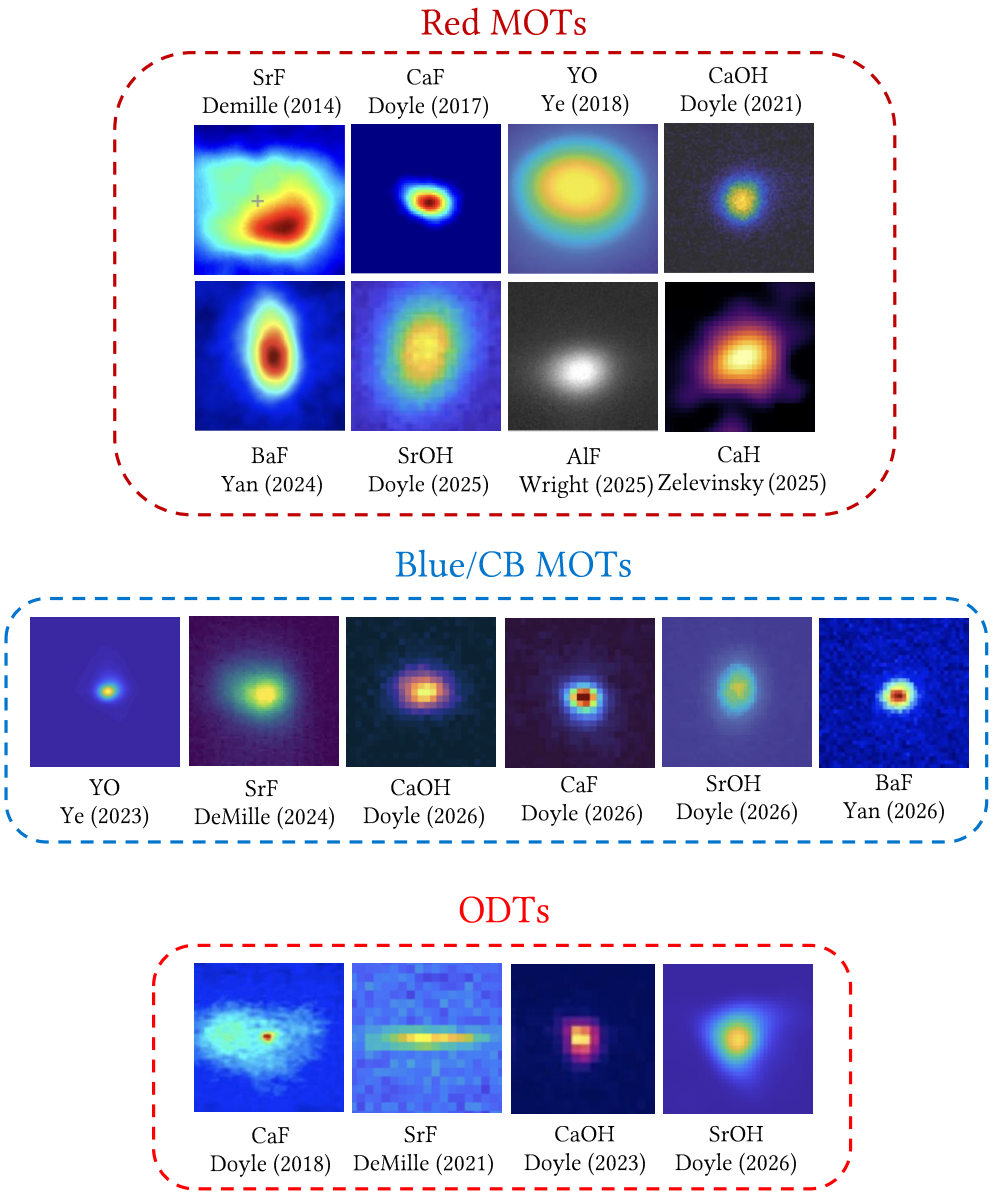

Figure 1.9: Examples of molecular MOTs, blue and CB MOTs, and ODTs over the last decade [3, 8, 9, 11, 12, 73–84].

A diatomic molecule is one atom too [few]

Arthur Schawlow [Altered]

2

SrOH Molecular Structure

The rich and complex internal structure of molecules is what makes them unique tools in quantum science, but is also the reason they are difficult to control. In this Chapter, we describe this structure in detail by first discussing the Born Oppenheimer Approximation in Sec. 2.1 which allows us to discuss the necessary Hamiltonians and energy levels. The electronic, vibrational, and rotational energy structures are described in Sec. 2.2-2.5, after which we study the perturbations due to various coupling mechanisms in Sec. 2.6. Finally, we conclude in Sec. 2.7 by illustrating the energy levels in SrOH based on the framework we establish in this Chapter.

2.1 Born Oppenheimer Approximation

In order to understand the vibrational and rotational structure of a molecule, we first need to write down a Hamiltonian in a tractable way. This means making some simplifying assumptions based on the underlying physics that govern the nucleons and electrons. The full, nonrelativistic molecular Hamiltonian can be found in several resources including [85] and is written as

$$\hat{H} = -\sum_i \frac{\hbar^2}{2m_e}\nabla_i^2 - \sum_A \frac{\hbar^2}{2M_A}\nabla_A^2 - \sum_{i,A} \frac{Z_A e^2}{4\pi\varepsilon_0\, r_{iA}} + \sum_{i<j} \frac{e^2}{4\pi\varepsilon_0\, r_{ij}} + \sum_{A<B} \frac{Z_A Z_B e^2}{4\pi\varepsilon_0\, R_{AB}}, \tag{2.1}$$

$$= \hat{T}_N + \hat{T}_e + \hat{V}_{NN} + \hat{V}_{eN} + \hat{V}_{ee}, \tag{2.2}$$

where i indexes the electron positions, A the nuclei positions, $\hat{T}_N$ is the nuclear kinetic energy, $\hat{T}_e$ is the electronic kinetic energy, $\hat{V}_{NN}$ is the nuclear-nuclear repulsion energy, $\hat{V}_{eN}$ is the electron-nuclear attraction energy, and $\hat{V}_{ee}$ is the electron-electron repulsion energy.

In order to learn anything from this Hamiltonian, we must invoke what is known as the Born-Oppenheimer (BO) approximation. As shown in Eq. 2.2, the potentials that govern the electrons and nuclei are similar in magnitude. This means that the electrons move much faster than the nuclei as they have much smaller mass. As a result, we can freeze out the motion of the nuclei and separate the nuclear and electronic wavefunctions such that

$$\psi = \psi_{el}(\mathbf{r}_i; \mathbf{r}_A)\psi_N(\mathbf{r}_A). \tag{2.3}$$

The intermediate steps for this derivation, as well as much of the information in this chapter, can be found in several resources [85–89]. The total wavefunction is then

$$\psi = \psi_{el}\psi_{rot}\psi_{vib}, \tag{2.4}$$

where the nuclear wavefunction has been decomposed into rotational ψ_{rot} and vibrational ψ_{vib} components, assuming any rotation-vibration couplings are small. We can now treat each of these components separately and develop intuition to show how they affect our ability to laser cool our molecules.

2.2 Electronic Structure

The electronic wavefunction in Eq. 2.1 depends on the electronic kinetic energy, the electron-electron interaction energy and the electron-nucleon energy. Even with the BO approximation, dealing with and diagonalizing the electronic Hamiltonian is still difficult and requires further careful treatment. For a molecule like SrOH which contains an alkaline-earth metal atom and a ligand, we can utilize what is known as Ligand Field Theory to qualitatively understand the electronic structure through a perturbative approach.

As discussed in [90, 91], take the Hamiltonian

$$H_{LFT} = H_{Sr^+} + H_{OH^-} + H_{e^-}, \tag{2.5}$$

where the three terms on the right represent the Hamiltonians for the Sr^+ ion, the ligand, and the interaction between the optically active valence electron from the Sr atom and the ligand. A perturbation from the ligand assuming a point charge structure, which is valid if we have a linear molecule, has three qualitative effects

1. The energy levels of the atomic ion orbitals are rearranged.

2. The degeneracy of the *nl* atomic orbitals is lifted and the states are split into *ml* components.

3. Orbitals with the same m_l are allowed to mix, resulting in each molecular orbital being a linear combination of atomic orbitals.

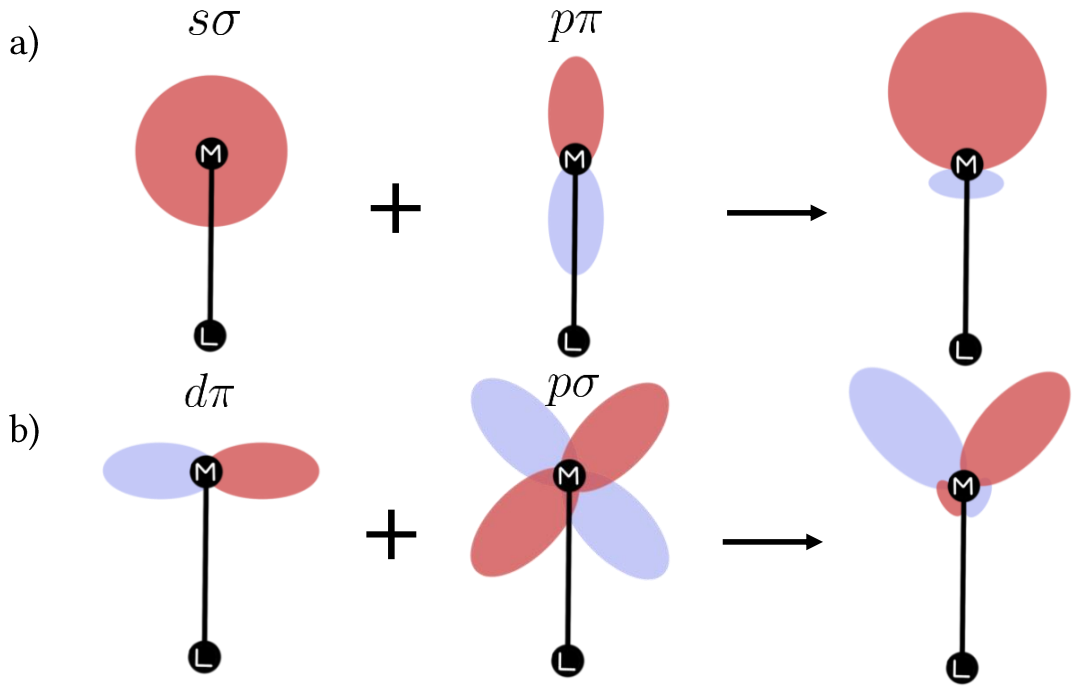

Figure 2.1: a) Orbital distribution for the $\tilde{X}^2\Sigma^+$ state in a linear triatomic molecule, where the $s\sigma$ and $p\pi$-like orbitals hybridize to form an s-like orbital. b) Orbital distribution for the $\tilde{A}^2\Pi_{1/2}$ state in a linear triatomic molecule where the $d\pi$ and $p\sigma$-like orbitals hybridize to form a p-like orbital.

Fig. 2.1 helps illustrate these effects. Electronic states of linear triatomic molecules can be written as

$$\widetilde{X}^{2S+1}\Lambda, \tag{2.6}$$

where $\widetilde{X}$ denotes the ground electronic state and each subsequent excitation is labeled $\widetilde{A}$, $\widetilde{B}$, $\widetilde{C}$ etc. The superscript $2S+1$ denotes the spin multiplicity and Λ is the projection of the electronic angular momentum onto the molecule axis where Σ, Π, Δ, Φ correspond to $\Lambda = 0, 1, 2, 3$. SrOH with Sr^{88} is a doublet molecule such that $2S+1 = 2$, where the ground electronic state is labeled $\tilde{X}^2\Sigma^+$ and is symmetric under reflections about a plane that passes through the internuclear axis (is s-like). Moreover, the first excited electronic state is labeled $\tilde{A}^2\Pi_{1/2}$ and contains parity doublets arising from the non-zero orbital angular momentum.

2.3 Vibrational Structure

The vibrational energy levels of molecules can be described in terms of the normal modes of the system. In general, an N-body system has $3N$ degrees of freedom where translations and rotations in all three axes account for three modes each, and the remaining $3N-6$ correspond to vibrational modes. For linear triatomic molecules like SrOH, the rotation about the internuclear axis has zero moment of inertia, which results in the molecule having two rotational modes which represent end-over-end rotations in the two axes perpendicular to the internuclear axis. The remaining $3N-5=4$ modes are vibrational and are labeled $\left(v_1, v_2^l, v_3\right)$, where v_i represents the number of quanta in each corresponding mode for $i=1,2,3$. Here, v_1 describes the Sr-O stretching mode, v_2 the doubly degenerate Sr-O-H bending mode with vibrational angular momentum l, and v_3 the O-H stretching mode.

2.3 a) Harmonicity and Anharmonicity in the Vibrational Modes

As we mentioned in Chapter 1, the stretching and bending modes differ in the amount of anharmonicity they contain, which results in sensitivity to μ-variation. The wavefunctions of the stretching (bending) vibrational modes are represented by 1D (2D) harmonic oscillators, where the energies are [25]

$$G(v_1,v_2,v_3)=\underbrace{\sum_{i=1}^{3}\omega_i\left(v_i+\frac{d_i}{2}\right)}_{\text{harmonic}}+\underbrace{\sum_{i=1}^{3}\sum_{k>i}x_{ik}\left(v_i+\frac{d_i}{2}\right)\left(v_k+\frac{d_k}{2}\right)+g_{22}l^2}_{\text{anharmonic}}. \tag{2.7}$$

The first term represents the energies of a classic harmonic oscillator with frequency ω_i with the degeneracies represented by $d_i=1$ for stretching modes and $d_i=2$ for bending modes. In reality, the molecular potentials are not perfectly linear and there exists some anharmonicity which contribute to the energies as shown in the second term in Eq. 2.7, where x_{ik} and g_{22} are anharmonic constants and l is the vibrational quantum number associated with the bending mode. Specifically, a vibrational mode is essentially har-

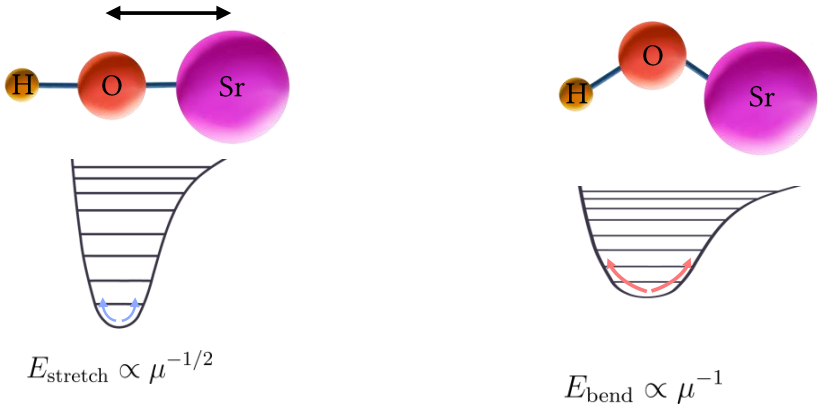

Figure 2.2: The potential energy surfaces associated with a) The SrOH stretching mode where the first order change in the bond length results in a steeper potential. As such, the stretching mode has more harmonic character and has energies $\propto \mu^{-1/2}$. b) The SrOH bending mode where the second order change in the bond length produces a shallower potential, resulting in more anharmonicity with energies $\propto \mu^{-1}$.

monic if the motion remains near the potential minimum and samples only the part of the potential that is nearly quadratic. Anharmonicity is increased as larger parts of the potential are sampled, rendering it less parabolic. Stretching modes are more harmonic than bending modes, as displacing an atom by some small distance δ from equilibrium along the symmetry axis results in the bond length changing by the same amount. In the bending mode, however, when the molecule is displaced in the direction orthogonal to the symmetry axis by δ, the bond angle changes to first order but the bond length to second order in δ. This results in a smaller restoring force, weaker spring constant, and lower vibrational frequency than the stretching case. As such, the bending mode has a shallower potential, where for the same δ a wider distance over the potential is sampled, resulting in more anharmonicity. This result is summarized in Fig. 2.2.

2.3 b) Franck-Condon Factors and Vibrational Branching Ratios

Franck-Condon factors (FCFs) play a crucial role in determining whether a molecule is laser-coolable. They are defined as the degree of wavefunction overlap between two states such that

$$q_{v_e \to v_g} = \left| \int \psi_e^* \psi_g \, d\tau \right|^2 . \tag{2.8}$$

such that $\sum_{v_g} q_{v_e \to v_g} = 1$. In reality, the more physically meaningful parameters are the vibrational branching ratios (VBRs) given by

$$\mathrm{VBR}_{v_e \to v_g} = \frac{q_{v_e \to v_g} \, \omega_{v_e, v_g}^3}{\sum_{v_g'} q_{v_e \to v_g'} \, \omega_{v_e, v_g'}^3} . \tag{2.9}$$

where ω is the transition frequency, and a normalization condition $\sum_{v_g} \mathrm{VBR}_{v_e \to v_g} = 1$ is satisfied. These values were measured for SrOH using dispersed laser-induced fluorescence (DLIF) spectroscopy [92] and encode the probability that an excited state spontaneously decays to a particular v_g. Practically, if a transition has a VBR that is close to 1, it is said to be "diagonal" as any off-diagonal couplings to other unaddressed states are small compared to the main transition. The plethora of ground vibrational states in polyatomic molecules means that having a highly diagonal cooling transition is not possible: indeed, the same complex structure that makes molecules such attractive systems also renders them difficult to laser cool. As discussed in more detail in Chapter 3, any transition with a VBR < 1 means vibrational states unaddressed by the cooling laser are populated, and photon cycling ceases once a molecule decays to one of these "dark states". This is circumvented through repumping these states with a separate laser, and so lower VBRs for a given set of transitions result in a larger number of lasers needed which increases experimental complexity[2.1]. A "laser-coolable" molecule is one where the VBRs for a set of transitions is ~1 such that a reasonable number of repump lasers are needed. The VBR for the main cycling transition as well as other diagonal vibrational transitions in SrOH is ~0.95 [92].

[2.1] And monetary cost. In the year 2026, we worry more about our money budget than our photon budget.

2.3 c) "Designing" a Laser-Coolable Molecule

As described in the work of Di Rosa [93], a laser-coolable molecule is one with strong enough single photon transitions to allow for high scattering rates, has diagonal FCFs, and contains no intermediate electronic states that could present as loss channels. It is in fact possible to choose a class of molecules with near-diagonal FCFs, making laser cooling viable. If, for a particular transition, the ground- and excited-state vibrational wavefunctions have similar curvatures, then they will have a high degree of overlap and consequently a high FCF. The shape of the vibrational wavefunctions depends predominantly on the bond geometry between the atoms in the molecule. Thus, a transition that does not significantly alter the bond lengths or angles in the molecule will yield favorable FCFs. From [94], this can be achieved by producing a molecule comprising an alkaline-earth metal M and an electronegative ligand such as OH. The OH group attracts electron density toward itself to form the chemical bond, resulting in a single optically active valence electron being centered on the metal atom. Because this electron does not significantly participate in the molecular bonding, excitations involving it do not drastically change the bond geometry, resulting in transitions between states with a high degree of vibrational overlap. Thus, we can design a class of molecules of the form M–O–H that are amenable to laser cooling. This principle can be generalized to a wide range of ligands including F, NH_2, OCH_3 and SH to name a few, allowing for laser-coolable molecules with different symmetries [95].

2.4 Rotational Structure

To good approximation, the rotational Hamiltonian of a molecule can be described as a rigid rotor. This results in energies of the form

$$E_{\text{rot}} = BJ(J+1), \tag{2.10}$$

where B is the spectroscopically assigned rotational constant and represents the moment of inertia, and J is the quantum number associated with the end over end rotation of the nuclei. In reality, the molecule is not fully rigid and the rotation results in a centrifugal force that slightly lengthens the bonds. This results in an additional term

$$E_{\text{rot}} = BJ(J+1) + D\left[J(J+1)\right]^2 \tag{2.11}$$

where D is the centrifugal distortion parameter.

2.4 a) Rotational and Electronic Coupling

In reality, the end over end rotation of the molecule is not entirely divorced from the electronic motion. Although we used the BO approximation to fully separate the motion of the nuclei from the electron, there still exist small interactions between the two. We can contextualize these interactions by identifying the various angular momentum couplings that arise due to rotation of the constituent particles in the molecule. Table 2.1 shows the labelings for the relevant angular momenta we will consider.

Table 2.1: Relevant angular momentum vectors and their projections.

Description	Vector	Projection
Rigid body rotation	$\vec{R}$	–
Vibrational angular momentum	$\vec{G}$	ℓ
Electronic orbital angular momentum	$\vec{L}$	Λ
Total spinless angular momentum	$\vec{N} = \vec{J} - \vec{S}$	$K = \ell + \Lambda$
Electron spin angular momentum	$\vec{S}$	Σ
Total angular momentum (no hf)	$\vec{J}$	$P = \ell + \Lambda + \Sigma$
Total angular momentum (hf)	$\vec{F} = \vec{J} + \vec{I}$	–

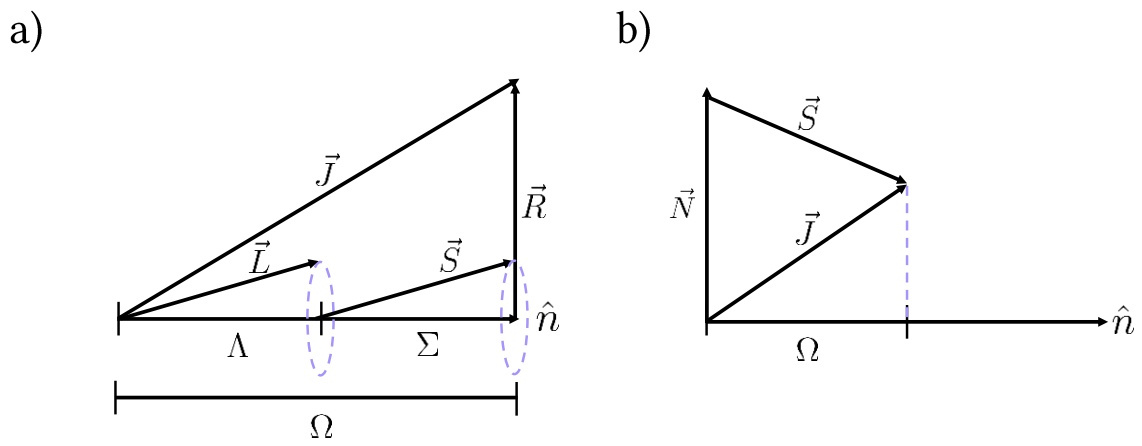

Figure 2.3: Angular momentum coupling in Hund's cases a) and b) for a linear triatomic molecule.

2.4 b) Hund's Cases

In SrOH, the electronic state determines which angular momentum couplings dominate. For example, the ground electronic state is a Σ state and the first excited electronic state is a Π state. The angular momentum and its projections are approximately conserved in these states and are referred to as "good quantum numbers". Instead of dealing with the full complexity of the exact Hamiltonian, we can form a basis corresponding to these approximately conserved quantities. Hund's cases describe different regimes of angular momentum coupling, allowing us to choose a basis depending on the dominant effects in the molecule. Although there exist five such cases, we show the two that are relevant for the lower electronic states in a linear triatomic doublet molecule in Fig. 2.3. In Hund's case (a), the electronic orbital angular momentum L and the electron spin S couple strongly to the molecular axis and precess rapidly about it. Their projections, Λ and Σ, are good quantum numbers. The SrOH first excited electronic state $\tilde{A}^2\Pi_{1/2}$ is best described by this basis as it has non-zero orbital angular momentum. In Hund's case (b), the electron spin does not couple strongly to the molecular axis which means the electron spin projection is not a good quantum number. The total angular momentum excluding spin is approximately conserved, such that

$\vec{N} = \vec{J} - \vec{S} = \vec{R} + \vec{L} + \vec{G}$. The SrOH ground electronic state $\tilde{X}^2\Sigma^+$ is written in this basis as it has zero orbital angular momentum.

2.4 c) The Complete Rotational Hamiltonian

Having discussed the various angular momentum coupling mechanisms, we can now incorporate them into the rotational Hamiltonian. We previously expressed this Hamiltonian in terms of some quantum number J in Eq. 2.4, which only accounted for the end over end rotation. In reality, the rotational angular momentum $\vec{R}$ can be written in terms of the total angular momentum $\vec{J}$ and the orbital and spin angular momenta $\vec{L}$ and $\vec{S}$, keeping in mind the rotational and electronic couplings. Thus, the rotational Hamiltonian can be rewritten as

$$\hat{H} = B\left(\hat{R}_x^2 + \hat{R}_y^2\right) \tag{2.12}$$

$$= B\left[\left(\hat{J}_x - \hat{L}_x - \hat{S}_x\right)^2 + \left(\hat{J}_y - \hat{L}_y - \hat{S}_y\right)^2\right] \tag{2.13}$$

$$= \underbrace{B\left(\hat{J}^2 - \hat{J}_z^2\right) + B\left(\hat{L}^2 - \hat{L}_z^2\right) + B\left(\hat{S}^2 - \hat{S}_z^2\right)}_{\text{diagonal terms}}$$

$$+ \underbrace{B\left(\hat{L}_+\hat{S}_- + \hat{L}_-\hat{S}_+\right)}_{1} - \underbrace{B\left(\hat{J}_+\hat{L}_- + \hat{J}_-\hat{L}_+\right)}_{2} - \underbrace{B\left(\hat{J}_+\hat{S}_- + \hat{J}_-\hat{S}_+\right)}_{3}. \tag{2.14}$$

where we have used raising and lowering operators for the cross terms. This Hamiltonian is not quantitatively useful for, say, fitting spectroscopic lines as the coefficient in front of each of the cross terms labeled 1, 2, and 3 does not correctly represent the magnitude of these interactions. This is due to what we described in Sec. 2.5, where the explicit mechanisms that give rise to these angular momentum couplings are brought about by interactions with electronic states that are not explicitly accounted for in this expression. This Hamiltonian is qualitatively useful, however, in that it illustrates all the possible angular momentum coupling combinations. Consequently, based on the appropriate Hund's case for a given electronic state,

we can treat the predominant coupling mechanism as a perturbation on the zeroth order rotational motion of the state and derive an expression for the expected energies. Below, we show examples of such perturbations and how they give rise to splittings in the rotational structure of SrOH.

2.5 Perturbations

Through the BO approximation, we have separated the electronic, vibrational, and rotational wavefunctions. This allows us to treat small couplings between these degrees of freedom as perturbations, revealing the various splittings and shifts of the zeroth-order SrOH structure. In this section, we discuss the higher-order effects that remain consistent with the BO approximation and that are related to the cross terms in Eq. 2.14. The purpose of describing these perturbations is to understand the magnitude of these splittings which in turn informs us of how to address them when laser cooling SrOH. These splittings are addressed below.

2.5 a) Spin-Rotation Splitting

For the $\tilde{X}^2\Sigma^+$ state in Hund's case (b), the electron spin couples more strongly to the rotation of the molecule than to the internuclear axis. Thus, the electron experiences an effective magnetic field in the rotating molecular frame due to the orbiting nuclei. This is known as the spin-rotation interaction, and is qualitatively captured in cross term 3 in Eq. 2.14. We can write

$$\hat{H}_{\mathrm{SR}} = \gamma\, \hat{\mathbf{N}} \cdot \hat{\mathbf{S}} = \frac{1}{2}\gamma \left(\hat{\mathbf{J}}^2 - \hat{\mathbf{N}}^2 - \hat{\mathbf{S}}^2\right), \tag{2.15}$$

where γ is the spin-rotation constant and represents the coupling strength resulting in an energy

$$E_{\mathrm{SR}} = \gamma\left[J(J+1) - N(N+1) - S(S+1)\right] \tag{2.16}$$

$$= \gamma\left[J(J+1) - N(N+1) - \frac{3}{4}\right]. \tag{2.17}$$

Given that $S = \pm\frac{1}{2}$, we have two SR components labeled F_1 and F_2 such that

$$E_{\mathrm{SR}}(F_1) = \frac{1}{2}\gamma\left[\left(N+\frac{1}{2}\right)\left(N+\frac{3}{2}\right) - N(N+1) - \frac{3}{4}\right] = \frac{1}{2}\gamma N \tag{2.18}$$

$$E_{\mathrm{SR}}(F_2) = \frac{1}{2}\gamma\left[\left(N-\frac{1}{2}\right)\left(N+\frac{1}{2}\right) - N(N+1) - \frac{3}{4}\right] = -\frac{1}{2}\gamma(N+1), \tag{2.19}$$

which manifests as a two-fold splitting of the rotational levels. From Table 2.2, we see that the spin-rotation constant $\gamma = 72.8$ MHz. If we have a ground state rotational level and want to address both spin-rotation states, we use an acousto-optic modulator (AOM) to apply frequency sidebands to cover this splitting.

2.5 b) Spin-Orbit Coupling

In the $\widetilde{A}$ state, which is well described by Hund's case (a), the electron spin is more strongly coupled to the internuclear axis than it is to the molecular rotation. An electron orbiting the internuclear axis experiences a strong electric field due to the charged nuclei. As a result, it experiences an effective magnetic field in its own frame, which couples to its spin through relativistic effects. This is known as the spin-orbit interaction and is described by

$$H_{\mathrm{SO}} = A_{\mathrm{SO}}\,\hat{L}\cdot\hat{S}, \tag{2.20}$$

where A_{SO} is the spin-orbit constant. In Hund's case (a), the orbital and spin angular momenta are strongly coupled to the internuclear axis, resulting in Λ and Σ being good quantum numbers. As such, the dominant contribution to H_{SO} comes from the $\hat{L}_z$ and $\hat{S}_z$ operators, such that

$$E_{\mathrm{SO}} = A\Lambda\Sigma, \tag{2.21}$$

resulting in the energies

$$E_{\mathrm{SO}}\left(\Omega = \frac{1}{2}\right) = A_{\mathrm{SO}}(1)\left(-\frac{1}{2}\right) = -\frac{1}{2}A_{\mathrm{SO}}, \tag{2.22}$$

$$E_{\mathrm{SO}}\left(\Omega = \frac{3}{2}\right) = A_{\mathrm{SO}}(1)\left(\frac{1}{2}\right) = \frac{1}{2}A_{\mathrm{SO}}. \tag{2.23}$$

Here, the total electronic projection is given by $\Omega = \Lambda + \Sigma$. The off-diagonal contributions

$$\frac{A_{\mathrm{SO}}}{2}\left(\hat{L}_+\hat{S}_- + \hat{L}_-\hat{S}_+\right) \tag{2.24}$$

do not contribute to the spin-orbit energy to first order, but do contribute at second order, which is encapsulated in the discussion of Λ-doubling below. The effect of spin-orbit coupling is to split the $\tilde{A}$ state into two manifolds separated by energy A_{SO}, each with its own rotational ladder. The lower spin-orbit manifold is labeled $\tilde{A}^2\Pi_{1/2}$ and the upper $\tilde{A}^2\Pi_{3/2}$. From Table 2.3, the spin-orbit constant $A_{\mathrm{SO}} = 7.9$ THz, such that if we want to address the upper spin-orbit manifold we must significantly increase our laser frequency.

2.5 c) Λ-Doubling

In Hund's case (a) for the $\tilde{A}^2\Pi_{1/2}$ state of SrOH, Λ represents the projection of the electron's orbital angular momentum onto the internuclear axis. In free space, the Hamiltonian is invariant under parity which means that the field-free eigenstates must also be eigenstates of the parity operator. Because states with projections $+\Lambda$ and $-\Lambda$ are degenerate, the parity eigenstates are formed as linear combinations of these two oppositely signed Λ states

$$|\psi_{e/f}\rangle = \frac{|\Lambda\rangle \pm |-\Lambda\rangle}{\sqrt{2}}. \tag{2.25}$$

which when transformed under parity gives

$$\hat{P}|\pm\Lambda\rangle = |\mp\Lambda\rangle, \tag{2.26}$$

$$\hat{P}|\psi_{e/f}\rangle = \frac{|-\Lambda\rangle \pm |\Lambda\rangle}{\sqrt{2}} = \pm|\psi_{e/f}\rangle. \tag{2.27}$$

We can use these parity states as the basis functions for a linear triatomic. There are a few contributions towards the lifting of this degeneracy related to second order couplings between the Σ and Π states which is known as Λ-doubling. For SrOH, Λ-doubling occurs predominantly in the $\tilde{A}^2\Pi_{1/2}$ state due to mixing from the $\tilde{B}^2\Sigma^+$ state. We can look back at the relevant cross terms in Eq. 2.14 to show how this happens:

1. $\hat{\mathbf{L}}_+\hat{\mathbf{S}}_- + \hat{\mathbf{L}}_-\hat{\mathbf{S}}_+$: The terms that couple the orbital and spin angular momenta result in a coupling between electronic states that differ in Λ and Σ by ±1 and ∓1, respectively. Each term also preserves the total electronic angular momentum $\Delta\Omega = 0$. Thus, they result in a mixing between the ground electronic state and the lower spin-orbit manifold of the first excited electronic state such that ${}^2\Sigma^+_{1/2} \leftrightarrow {}^2\Pi_{1/2}$. The contribution of this term comes from both the rotational Hamiltonian in Eq. 2.14 $\propto B_{\text{rot}}$, as well as from the off diagonal terms present when describing the spin-orbit interaction in Eq. 2.24 $\propto A_{\text{SO}}$.

2. $\hat{\mathbf{J}}_+\hat{\mathbf{L}}_- + \hat{\mathbf{L}}_+\hat{\mathbf{J}}_-$: The terms that couple the total and electron orbital angular momentum result in interactions between electronic states with Λ and Ω differing by ±1 with $\Delta\Sigma = 0$. This results in a mixing between ${}^2\Pi_{1/2} \leftrightarrow {}^2\Sigma^+_{1/2}$ and ${}^2\Pi_{3/2} \leftrightarrow {}^2\Sigma^+_{1/2}$ and is $\propto B_{\text{rot}}$ only.

These off diagonal mixings can result in second order energy shifts, resulting in splittings of the ${}^2\Pi$ manifolds by coupling through an intermediate Σ state such that $\Pi \rightarrow \Sigma \rightarrow \Pi$. We previously discussed

the symmetry of the $^2\Sigma^+$ state under a reflection in a plane intersecting with the nuclear axis. Since the Hamiltonian is symmetry conserving, only states with the same type of symmetry can mix. This means that only the Π component with the same reflection symmetry can mix with the electronic ground state, corresponding to shifts of the $|\psi_e\rangle$ in Eq. 2.25. Since $|\psi_f\rangle$ has the opposite symmetry, it is not shifted which results in the degeneracy breaking and an energy splitting between the two states of opposite parity.

In SrOH, the $^2\Pi_{3/2}$ state has negligible Λ-doubling when compared to $^2\Pi_{1/2}$. The $^2\Pi_{1/2}$ state has a direct coupling that mixes with the $^2\Sigma^+$ state through both rotational and spin-orbit effects, unlike the $^2\Pi_{3/2}$ state which is only mixed through rotation. The rotation can uncouple and "loosen" the electronic orbital angular momentum from the internuclear axis. In the SrOH $^2\Pi$ state however, $A_{\mathrm{SO}} \gg B_{\mathrm{rot}}$ as the spin-orbit effect is the dominant coupling mechanism. As such, the contribution to Λ-doubling from the molecular rotation is less significant. Solving for the energy expressions in the symmetrized basis:

$$\psi(^2\Pi_{1/2}(e/f)) = \frac{1}{\sqrt{2}}\left[\psi(^2\Pi_{1/2}) \pm \psi(^2\Pi_{-1/2})\right] \tag{2.28}$$

$$\psi(^2\Pi_{3/2}(e/f)) = \frac{1}{\sqrt{2}}\left[\psi(^2\Pi_{3/2}) \pm \psi(^2\Pi_{-3/2})\right] \tag{2.29}$$

$$\psi(^2\Sigma^+_{1/2}(e/f)) = \frac{1}{\sqrt{2}}\left[\psi(^2\Sigma^+_{1/2}) \pm \psi(^2\Sigma^+_{-1/2})\right] \tag{2.30}$$

Then, the energy splittings are given by:

$$\Delta E_{\Lambda d}\left(^2\Pi_{1/2}(f-e)\right) = (p+2q)\left(J+\frac{1}{2}\right) \tag{2.31}$$

$$\Delta E_{\Lambda d}\left(^2\Pi_{3/2}(f-e)\right) = \frac{2Bq}{A_{\mathrm{SO}}}\left(J+\frac{1}{2}\right)\left[\left(J+\frac{1}{2}\right)^2 - 1\right] \tag{2.32}$$

$$p = \sum_{|^2\Sigma^+\rangle} \frac{2B \langle ^2\Pi|L_+|^2\Sigma^+\rangle \langle ^2\Pi|G_+|^2\Sigma^+\rangle}{(E_{^2\Pi} - E_{^2\Sigma^+})} \tag{2.33}$$

$$q = \sum_{|^2\Sigma^+\rangle} \frac{2B^2 \langle ^2\Pi|G_+|^2\Sigma^+\rangle^2}{(E_{^2\Pi} - E_{^2\Sigma^+})} \tag{2.34}$$

As such, it is justified to ignore the Λ-doubling in the $^2\Pi_{3/2}$ state as q is small compared to p and $\frac{B}{A_{SO}} \ll 1$.

2.5 d) The Bending Mode and Parity Doublet Structure

As mentioned in Chapter 1, the bending mode in linear triatomic molecules contains closely spaced parity doublets. The ability to fully mix these states in modest electric fields can orient the molecule in the lab frame, unlocking its potential to probe CP-violating physics such as the *e*EDM with high systematic rejection. We describe here the energy structure of a particular bending vibrational state in the ground electronic state after which we discuss how Coriolis effects break the degeneracy between states of opposite parity. As shown in Table 2.3, $p = -4.3$ GHz. When doing spectroscopy, this means that it is important to keep track of the excited state parity and adjust the laser frequency accordingly.

Ground Electronic State Bending Vibrations

The $\tilde{X}^2\Sigma^+(01^10)$ state behaves similarly to $\tilde{X}^2\Sigma^+(000)$, but with a few corrections to account for the change in geometry. The cylindrical symmetry of the molecule is now broken as the molecule is bent, which results in a non-zero moment of inertia along the internuclear axis. The end over end rotational angular momentum is then $\vec{R} = \vec{N} - \vec{G}$, where $\vec{N}$ is the spin-free angular momentum and $\vec{G}$ is the vibrational

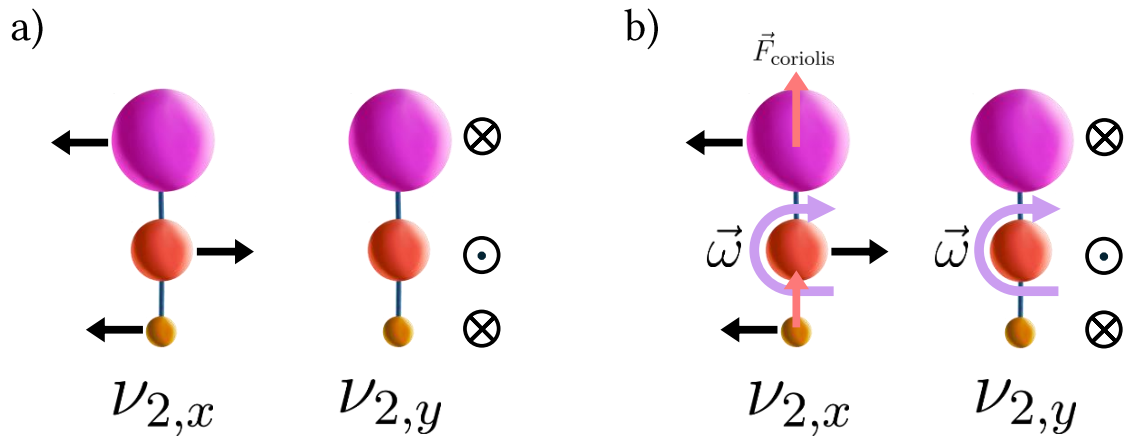

Figure 2.4: Parity doublet splitting in the bending mode due to the end over end rotation of the molecule. The Coriolis force affects only one of the two degenerate states, resulting in a breaking of this degeneracy.

angular momentum with projection l on the internuclear axis. Thus,

$$E_{\text{rot}} = B(\vec{R}^2) \tag{2.35}$$

$$= B(\vec{N}^2 - \vec{G}^2) \tag{2.36}$$

$$= B\left[N(N+1) - l^2\right], \tag{2.37}$$

resulting in an offset of the rotational ladder where $N > |l|$.

Next, we describe the spin-rotation interaction. To achieve this for the bending mode, we model the molecule as a symmetric top with non-zero moment of inertia along the internuclear axis. From [89], the spin-rotation Hamiltonian is given by

$$H_{\text{SR}} = \frac{1}{2}\epsilon_{xx}\left(N_+S_- + N_-S_+\right) + \epsilon_{aa}N_zS_z \tag{2.38}$$

$$= \frac{1}{2}\gamma\left(N_+S_- + N_-S_+\right) \tag{2.39}$$

where ϵ_{ij} are the non-vanishing components of a general spin-rotation tensor. We find that the spin-rotation energies are

$$E_{\mathrm{SR}}(F_1) = \frac{\gamma}{2}\left[1 - \frac{\ell^2}{N(N+1)}\right]N \tag{2.40}$$

$$E_{\mathrm{SR}}(F_2) = -\frac{\gamma}{2}\left[1 - \frac{\ell^2}{N(N+1)}\right](N+1). \tag{2.41}$$

Although this approximate treatment of the spin-rotation effect in the bending mode helps provide some intuition for the magnitude of the splitting, spectroscopic measurements in these states differ significantly from what is expressed in Eq. 2.41 [96].

Coriolis Effects and ℓ-Doubling

The parity eigenstates in the bending mode are given by

$$|\pm\rangle = \frac{|\ell\rangle \pm |-\ell\rangle}{\sqrt{2}}. \tag{2.42}$$

The degeneracy between these parity eigenstates is lifted by a Coriolis interaction arising from the end-over-end rotation of the molecule, as shown in Fig. 2.4. These parity eigenstates are linear combinations of the $\pm\ell$ states and describe the molecule bending into and out of a fixed plane. This gives rise to ℓ-type doubling, with energy shifts

$$E_{\ell d} = \pm(-1)^{N+\ell}\,\frac{q_\ell}{2}\,N(N+1), \tag{2.43}$$

where (q_ℓ) is a fitted constant that decreases with increasing ℓ. As discussed in Chapter 1, mixing these parity doublets yields oriented states $|\pm\ell\rangle$, which describe the bent molecule rotating about its internuclear axis.

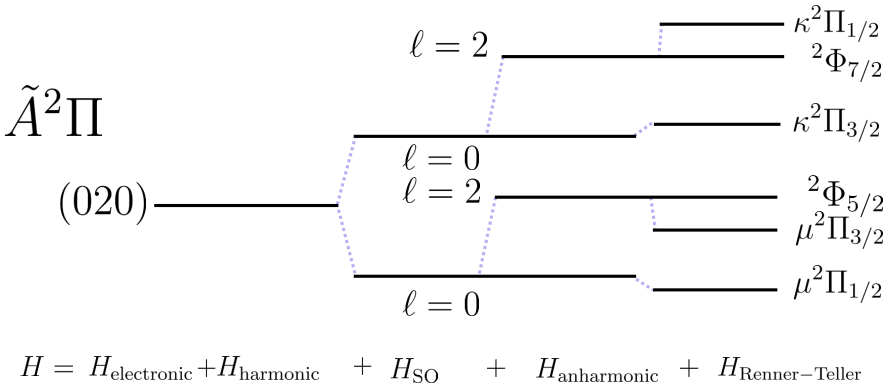

Figure 2.5: Additional splittings in the $\tilde{A}^2\Pi(020)$ state due to Renner-Teller coupling, recreated from Ref. [96].

2.6 Renner–Teller Coupling

In a $^2\Pi$ state with orbital angular momentum projection $\Lambda = \pm 1$ and bending vibrational angular momentum projection $\ell = \pm 1$, there can exist a coupling between these two quantities, resulting in a modification of the electronic energy levels. If the electronic state is degenerate in the linear configuration, bending can split it into two potential curves $E^+(\varphi)$ and $E^-(\varphi)$, where φ is the bond angle. The unperturbed bending potential is described by a quartic function:

$$E^0(\varphi) = a\varphi^2 + b\varphi^4. \tag{2.44}$$

Bending breaks the cylindrical symmetry and gives rise to a nonzero difference between the two bending potential curves:

$$E^+(\varphi) - E^-(\varphi) = \alpha\varphi^2 + \beta\varphi^4. \tag{2.45}$$

Hence, the electronic energy is modified by the bending vibration. The resulting vibronic angular momentum about the molecular axis in Hund's case (a) is $K\hbar$, where

$$K = |\Lambda \pm \ell|, \tag{2.46}$$

with $K = 0, 1, 2, \ldots$ labelled by $\Sigma, \Pi, \Delta, \ldots$, respectively. Renner–Teller coupling therefore splits each vibrational level into different vibronic sublevels. For a $^2\Pi$ state with $\Lambda = \pm 1$, $v_2 = 1$, and $\ell = \pm 1$, the four possible (Λ, ℓ) combinations give rise to two $K = 0$ components and two $K = 2$ components. This discussion applies to a $^2\Pi$ state because its p-like orbitals are degenerate in the linear configuration, whereas this is not the case for a $^2\Sigma$ state. Renner-Teller coupling is an example of a breakdown of the BO approximation as it arises from the interaction between the electronic and vibrational degrees of freedom. Thus, to describe it, we can no longer treat the motion of the nuclei and electrons as separate. The Renner-Teller splitting in the (020) vibrational state in the $\tilde{A}^2\Pi$ state is shown in Fig. 2.5. From Ref. [97], the Renner-Teller Hamiltonian can be written in terms of a multipole expansion such that

$$H_{\text{Renner–Teller}} = V_{11}\left(Q_+ e^{-i\theta} + Q_- e^{+i\theta}\right) + V_{22}\left(Q_+^2 e^{-2i\theta} + Q_-^2 e^{+2i\theta}\right) + \cdots \tag{2.47}$$

where $Q_\pm$ are raising and lowering operators that act on the vibrational angular momentum ℓ. Additionally, the $e^{i\theta}$ terms act as raising and lowering operators on Λ, the orbital angular momentum, where θ is the azimuthal angle of the electron's orbit. Lastly, V_{11} and V_{22} represent the mixing strengths between angular momentum states. Following [97], these terms have the following effects:

1. V_{11}: The dipolar term in the interaction which mixes states with $\Delta v_2 = \pm 1$, $\Delta\ell = \pm 1$, $\Delta\Lambda = \mp 1$, $\Delta K = 0$.

2. V_{22}: The quadrupolar term in the interaction which mixes states with $\Delta v_2 = \pm 2$, $\Delta\ell = \pm 2$, $\Delta\Lambda = \mp 2$, $\Delta K = 0$.

The Renner-Teller interaction however couples the bending and stretching modes, where V_{11} couples the $\tilde{A}$ and $\tilde{B}$ states and V_{22} couples the oriented states $|\Lambda\rangle$ and $|-\Lambda\rangle$. As a result, there is vibrational

Table 2.2: Molecular constants for the SrOH $\tilde{X}^2\Sigma^+$ state.

Molecular Constant	Description	Angular Momentum Coupling	Frequency
$T_{000}(\tilde{X})$	Ground state electronic energy	–	0
$B_{000}(\tilde{X})$	Rotational constant	–	7.770 GHz
$D_{000}(\tilde{X})$	Centrifugal distortion constant	–	6.536 kHz
$\gamma_{000}(\tilde{X})$	Spin-rotation constant	$\hat{N}$ and $\hat{S}$	72.768 MHz

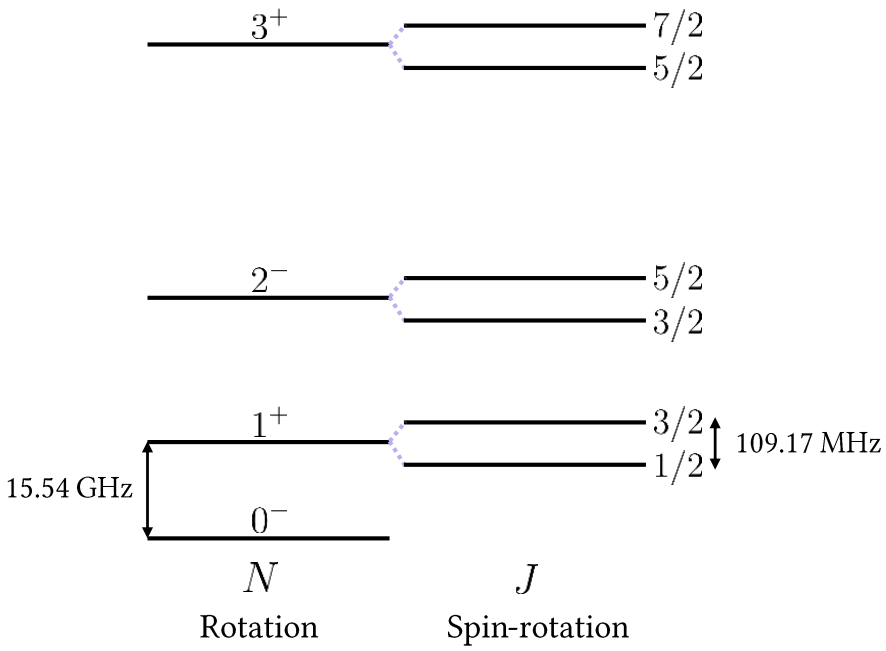

Figure 2.6: $\tilde{X}^2\Sigma^+$ state level structure.

leakage from the $\tilde{A}^2\Pi_{1/2}(000)$ state to the $\tilde{X}^2\Sigma^+(010)$ and $\tilde{X}^2\Sigma^+(020)$ which require repumping in our laser cooling scheme, where these transitions are nominally forbidden to zeroth order due to angular momentum selection rules enforcing $\Delta\ell = 0$. Additionally, the Renner-Teller interaction causes energy shifts which must be taken into consideration when doing repumper spectroscopy as described in [97].

Table 2.3: Molecular constants for the SrOH $\tilde{A}^2\Pi_{1/2}$ state.

Molecular Constant	Description	Angular Momentum Coupling	Frequency
$T_{000}(\tilde{A}^2\Pi_{1/2})$	First excited electronic state	–	435.975 THz
$B_{000}(\tilde{A})$	Rotational constant	–	7.611 GHz
$D_{000}(\tilde{A}))$	Centrifugal distortion constant	–	6.516 kHz
$p_{000}(\tilde{A}))$	Λ-doubling constant	$\hat{J}$ and $\hat{S}$, $\hat{J}$ and $\hat{L}$	−4.293 GHz
$q_{000}(\tilde{A}))$	Λ-doubling constant	$\hat{J}$ and $\hat{L}$	−5.996 MHz
$A_{SO}(\tilde{A}))$	Spin-orbit constant	$\hat{L}$ and $\hat{S}$	7.900 THz

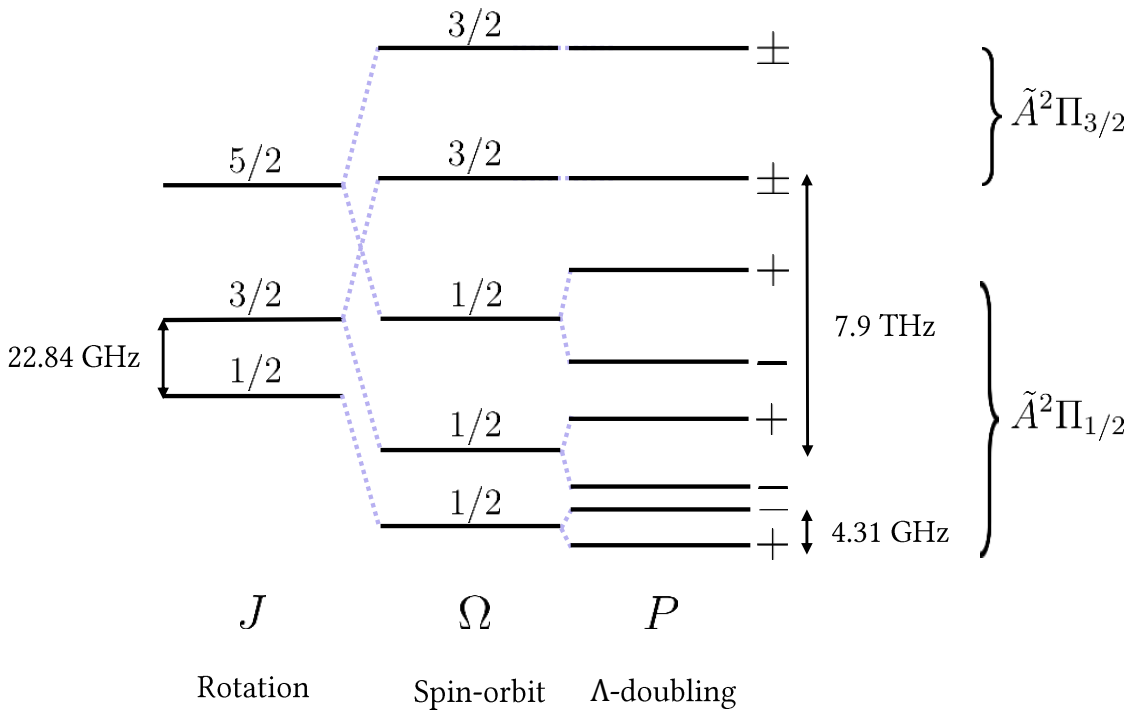

Figure 2.7: $\widetilde{A}^2\Pi$ state level structure.

2.7 SrOH Energy Levels

We consolidate here the information from this Chapter to summarize the energy structure in SrOH between the ground and excited electronic state used for our laser cooling transition as well as the bending mode. The molecular constants and their energies for this state are summarized in Table 2.2.

2.7 a) $\tilde{X}^2\Sigma^+$: Ground Electronic State Structure

The effective Hamiltonian for the $\tilde{X}^2\Sigma^+$ state for a low level vibrational stretching state is given by

$$H_{\text{eff}}(\tilde{X}^2\Sigma^+) \approx B_{\text{X}_{\text{rot}}} N^2 + \gamma \vec{N} \cdot \vec{S}, \tag{2.48}$$

where $B_{\text{X}_{\text{rot}}}$ is the rotational constant and γ is the spin-rotation constant. This result in energies that we derived in Sec. 2.5 a)

$$E(^2\Sigma^+ F_1(e)) = BN(N+1) + \frac{1}{2}\gamma N \tag{2.49}$$

$$E(^2\Sigma^+ F_2(f)) = BN(N+1) - \frac{1}{2}\gamma(N+1) \tag{2.50}$$

which describe a ladder of rotational state each split into two opposite parity states due to the spin-rotation effect as shown in Fig. 2.6.

2.7 b) $\widetilde{A}^2\Pi$: First Excited Electronic State Structure

As we did for the ground electronic state, the effective Hamiltonian for the $\tilde{A}^2\Pi_{1/2}$ and $A^2\Pi_{3/2}$ stretching states are given by

$$E\left(^2\Pi_{1/2}, e/f\right) = -\frac{A_{\text{SO}}}{2} + B_{\text{A}_{\text{rot}}}\left[J(J+1) - \frac{1}{4}\right] \pm \frac{1}{2}(p+2q)\left[J+\frac{1}{2}\right], \tag{2.51}$$

$$E\left(^2\Pi_{3/2}\right) = +\frac{A_{\text{SO}}}{2} + B_{\text{A}_{\text{rot}}}\left[J(J+1) - \frac{9}{4}\right], \tag{2.52}$$

where $B_{\text{A}_{\text{rot}}}$ is the rotational constant, A_{SO} is the spin orbit splitting, and $p+2q$ describes the Λ-doubling between opposite parity states as shown in Fig. 2.7. Table 2.3 shows the molecular constants for this state.

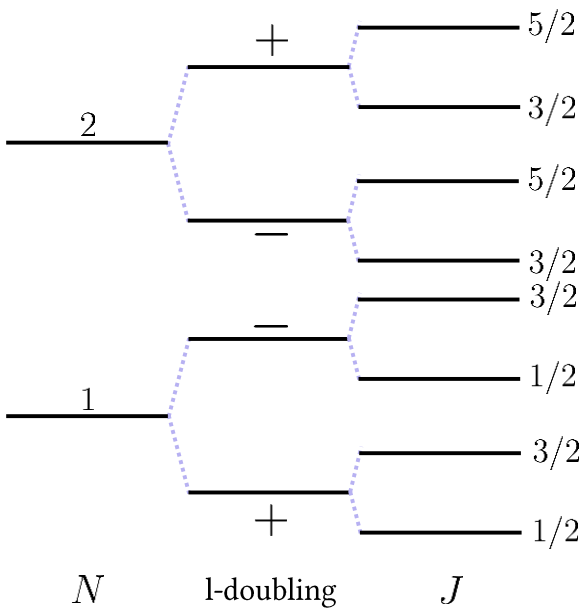

Figure 2.8: Bending mode level structure.

2.7 c) $\tilde{X}^2\Sigma^+(01^10)$: Bending Mode States

For the $\tilde{X}^2\Sigma^+(01^10)$ bending mode state, we can write the energies as

$$E\big(\tilde{X}(01^10), F_1, \pm\big) = B_{\mathrm{X_{rot}}}\big[N(N+1)-1\big] + \frac{\gamma}{2}\left(1 - \frac{1}{N(N+1)}\right)N \pm (-1)^{N+1}\frac{q_\ell}{2}N(N+1), \tag{2.53}$$

$$E\big(\tilde{X}(01^10), F_2, \pm\big) = B_{\mathrm{X_{rot}}}\big[N(N+1)-1\big] - \frac{\gamma}{2}\left(1 - \frac{1}{N(N+1)}\right)(N+1) \pm (-1)^{N+1}\frac{q_\ell}{2}N(N+1). \tag{2.54}$$

where F_1, F_2 represent the parity doublet states, $B_{\mathrm{X_{rot}}}$ is the rotational constant, γ is the spin-rotation constant and q_ℓ is the ℓ-doubling constant. The energy structure is depicted in Fig. 2.8.

"There are [months] where [not a single word of my dissertation is written] and there are days where [3 chapters of my dissertation are written]."

Vladimir Lenin [Altered] [Apocryphal]

3

Molecular Production and Laser Slowing

The SrOH molecular beam has a peak forward velocity of ~100 m/s, whereas magneto-optical traps have finite capture velocities which are appreciably lower. As such, a deceleration step using laser slowing is required to bridge the gap. For laser cooling experiments in general, this slowing step is often the most complex and technically challenging: this is especially true in molecular experiments where many repump lasers may be required to cycle enough photons in order to remove energy.

In this Chapter, we first discuss the production and laser cooling sequence of SrOH in Sec. 3.1 after which we discuss how to build a laser cooling scheme for SrOH in Sec. 3.2 including a brief spectroscopic background and considerations when deciding which repumping pathways to use. We then outline in

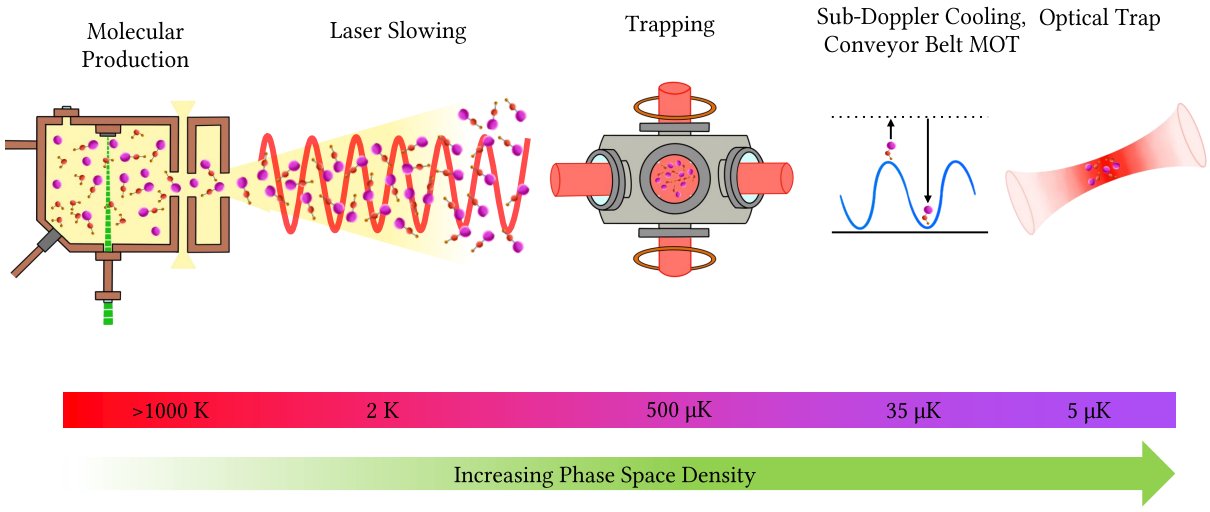

Figure 3.1: SrOH laser cooling experimental sequence. The molecules are first produced in a cryogenic buffer gas cell, after which they are entrained in a beam via collisions with Helium buffer gas. Following this, the molecular beam is laser slowed, magneto-optically trapped, sub-Doppler cooled and compressed, and finally trapped in an optical dipole trap.

Sec. 3.3 how lasers can impart forces on molecules. Following this, we discuss the laser slowing for SrOH in Sec. 3.4 where we present experimental parameters and results.

3.1 Molecular Production and Laser Cooling Scheme

The SrOH experiment, schematically shown in Fig. 3.1, utilizes a cryogenically cooled buffer gas beam (CBGB) of SrOH, a well-established technique used in many other direct laser cooling experiments [72–74]. The details of this production can be found in previous theses [98, 99]; here, we provide a brief summary. A strontium metal target housed in a copper cell held at a temperature of ~2 K is ablated using an ND:Yag pulsed laser with a wavelength of 532 nm and a pulse energy of ~15 mJ. The cell resides in an evacuated "beambox" comprising a sequence of copper shields which provide radiation shielding, where the beambox is cooled via a Cryomech PT420 pulse tube. The ensuing atoms then react with room-temperature water vapor to form gas-phase SrOH. An 800 mW, 688 nm laser is used to drive the $5s^2\ {}^1S_0 \rightarrow 5s5p\ {}^3P_1$ atomic

transition in Sr and enhance the reaction rate by an order of magnitude. During this process, Helium buffer gas is introduced into the cell, where it thermalizes with the cold walls and rotationally cools the molecules through collisions. The buffer gas entrains the molecules into a cold, slow molecular beam with a forward velocity of 110 ± 20 m/s. Following production, the molecular beam is radiatively slowed, as we describe in this Chapter, while the rest of this thesis describes the other trapping and cooling steps shown in Fig. 3.1.

3.2 Designing a Laser Cooling Scheme

Laser cooling relies on the continuous absorption and emission of photons in what is known as photon cycling. Before discussing how this results in deceleration in Sec. 3.3, we elaborate on how achieving photon cycling in molecules is challenging as a result of their complex internal structure, after which we describe the SrOH laser cooling scheme.

3.2 a) Photon Budget

The ability to continuously scatter photons is vital for successful laser cooling. This process of "photon cycling" can occur indefinitely for an ideal two-level system, where the molecule can only return to the ground state that is addressed by the cooling laser. Unfortunately, such a system does not exist in reality for the molecular species we work with, as illustrated in Fig. 3.6. As described in 2 in our discussion of vibrational branching ratios, molecules must be carefully selected to have "diagonal" transitions which decay back down to the original vibrational ground state the majority of the time.[3.1]. Although the main cooling transition $\tilde{X}^2\Sigma^+(000) \rightarrow \tilde{A}^2\Pi_{1/2}(000)$ in SrOH has a promising sounding VBR of 95.63(20)% [92],

[3.1]The term "diagonal" is somewhat misleading. If one considers only the vibrational quantum numbers, the corresponding transition may appear diagonal. In reality, however, the Hamiltonian contains off-diagonal elements through couplings between different vibrational modes and electronic states. Here, "diagonal" is used to mean that the Franck–Condon factor is largest for decay back to the initially addressed vibrational state.

having a single laser for laser cooling would be grossly insufficient. From $v_{\text{recoil}} = 0.55$ cm/s, the number of photons n_γ needed to impart a velocity change of Δv_{slow} is expressed as

$$n_\gamma = v_{\text{slow}}/\Delta v_{\text{recoil}}, \tag{3.1}$$

where slowing an SrOH beam starting at 100 m/s to 0 m/s would require $n_\gamma \approx 18000$ photon scatters. Given this, if we only had the main cooling laser on during slowing, we would on average be able to scatter only ~20 photons before exiting the optical cycle, which is several orders of magnitude below our requirement. As such, it is important to identify the major contributing losses to other vibrational dark states, and "plug" each channel with another laser known as a "repump". This process is described in Sec. 3.2. The photon scattering process can be described as a Bernoulli process. Suppose, for a given number of repump lasers, the molecule decays to an unaddressed dark state with probability p. The probability P_n for a molecule to scatter n photons is

$$P_n = (1-p)^n, \tag{3.2}$$

where the average number of photon scatters $n_{\gamma_{\text{budget}}}$ can be expressed as

$$n_{\gamma_{\text{budget}}} = \frac{1}{1-p}, \tag{3.3}$$

and $n_{\gamma_{\text{budget}}}$ is referred to as the "photon budget". Explicitly, the photon budget is determined by the number of repump lasers is the average number of photons scattered before $1/e$ of the molecules are lost to unaddressed vibrational ground states. This provides a much more quantitative description of the loss incurred by having a finite photon budget. For example, if we need to scatter 20,000 to slow to the MOT capture velocity, but have a photon budget of 10,000, we end up with $\exp(-20{,}000/10{,}000) = \exp(-2) \sim 10\%$ of our original molecules still in the optical cycle. As such, the question of available photons turns into a

measure of available molecule number, which as discussed in Chapter 1, is crucial to the success of precision measurements. Such a simple mathematical treatment of molecule loss allows for us to predict how carefully we need to understand the vibrational losses in our system. For example, if we want to keep 60% of our population after scattering 20,000 photons, we can plug into Eq. 3.2

$$0.6 = (1-p)^{20{,}000},$$
$$p = \frac{\ln 0.6}{20{,}000} \approx 10^{-5}.$$

This means that we would need to be able to identify a scheme where vibrational dark states are visited only 0.001% of the time. In Sec. 3.2 we describe how to implement such a laser cooling scheme.

A "laser cooling scheme" for a molecule is simply a description of various transitions required in slowing and trapping, starting with the "mainline" transition where the first excitation occurs which is responsible for momentum removal, followed by the "repumping" transitions required to close the optical cycle, setting the photon budget. These transitions need to be carefully considered to ensure that a high enough scattering rate can be achieved while using technologically convenient wavelengths at reasonable powers.

3.2 b) Identifying Loss Channels through Spectroscopy

Before a cooling scheme can be developed and implemented, it is necessary to identify the decay channels at the required sensitivity, which is at the 10^{-5} level for our experiment. For SrOH, this characterization begins with dispersed light induced fluorescence spectroscopy (DLIF), described in detail in [92]. In short, the $\tilde{X}^2\Sigma^+(000) \rightarrow \tilde{A}^2\Pi_{1/2}(000)$ transition in SrOH is driven by a 688 nm laser. The molecules then decay predominantly back down to the $\tilde{X}^2\Sigma^+(000)$ state, in addition to other vibrational states in the ground electronic manifold with non-negligible probabilities. Each of these decays results in the emission of a

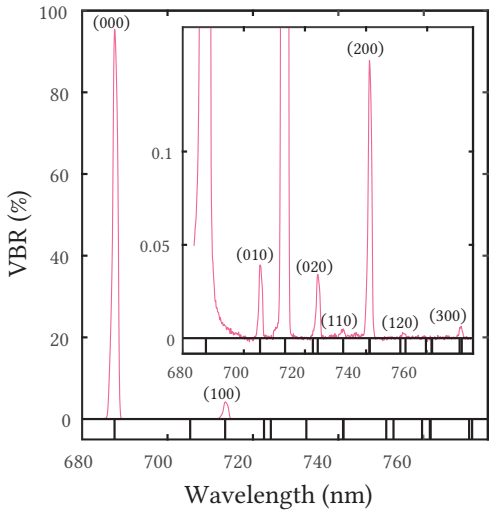

Figure 3.2: DLIF data from Ref. [92], showing the predominant decays to vibrational ground states in SrOH, which are now addressed with repumping lasers on the experiment.

photon with a distinct wavelength, which can then be collected on a spectrometer. As such, one can obtain spectra similar to Fig. 3.2. The graph shows peaks at particular wavelengths, where the y-axis is normalized and the peak heights represent the probability of decaying to a specific vibrational state.

DLIF is only able to identify these decay wavelengths to resolutions of ~1 cm^{-1}, which corresponds to a frequency of 30 GHz. Successful repumping requires the ability to drive such transitions close to the MHz level, necessitating a higher resolution spectroscopy method for states not resolved to within ~10 MHz. The nature of the spectroscopy needed depends on the transition of interest, as well as the prior knowledge of other states. Examples of some techniques are described in Refs. [96, 99] and shown in Fig. 3.3.

3.2 c) Choosing the Repumping Pathways

Once the relevant vibrational ground states are identified through DLIF, the repumping pathways must be chosen. The selected excited states to repump through must also be identified via spectroscopy in a manner similar to what was described earlier. The following considerations are taken into account when developing the final laser cooling scheme, such as the SrOH scheme shown in Fig. 3.4:

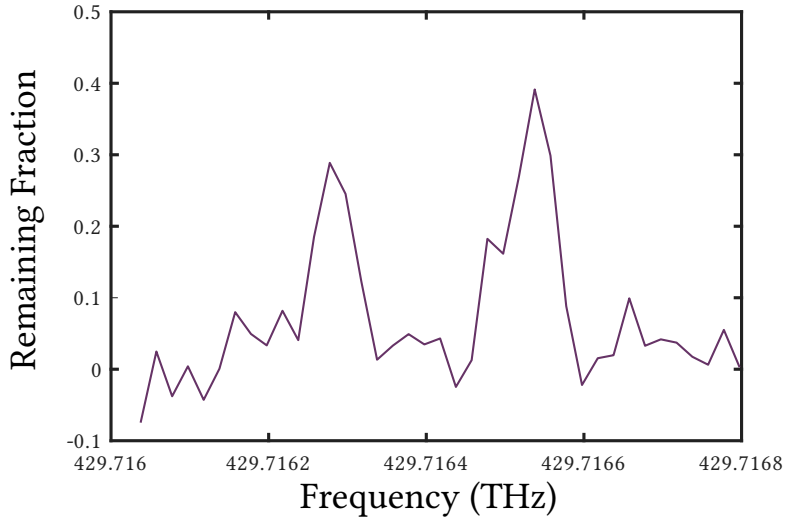

Figure 3.3: High resolution spectra using the MOT fluorescence as the signal from Ref. [96]. This plot shows the spin-rotation splitting in the excited state for the $\tilde{X}^2\Sigma^+(12^20) \rightarrow \tilde{A}(020)\kappa^2\Pi_{1/2}$ repumping transition.

1. **Avoid sharing excited states**: From Refs. [100, 101], the maximum achievable scattering rate for a multi-level system can be approximated as

$$R_{\text{scatter}}^{\text{max}} = \frac{n_{\text{e}}}{n_{\text{e}} + n_{\text{g}}}\Gamma \tag{3.4}$$

where n_e is the number of excited states and n_g is the number of ground states, assuming each transition is driven with equal strength. To understand this, we use from Ref. [101] the fact that R_{scatt} relates to the excited state population ρ_{ee} where

$$R_{\text{scatt}} = \Gamma\rho_{\text{ee}}. \tag{3.5}$$

For a two-level system in the highly saturated regime, $\rho_{\text{ee}} = 0.5$. However, in a multilevel system with several ground states and one excited state, the maximum population in the excited state decreases proportionally with the total number of levels, resulting in the above scattering rate shown in Eq. 3.4. As such, it is important to select a unique excited state for each ground state to maintain

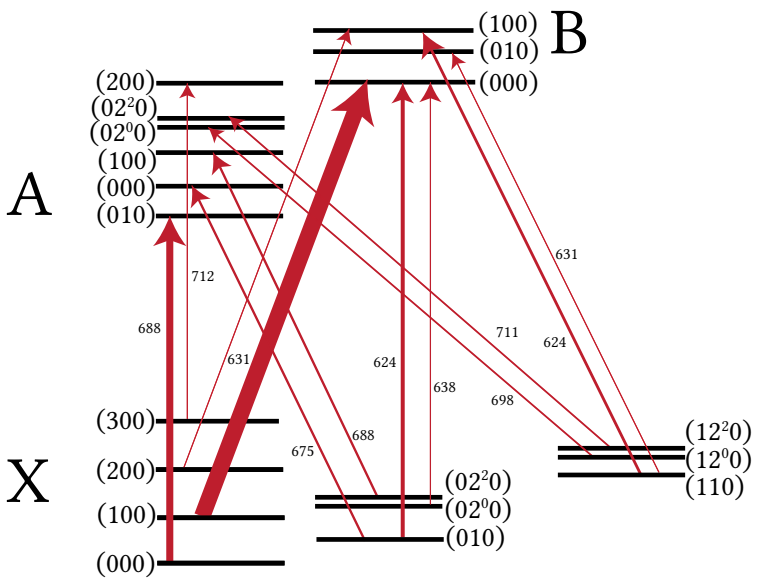

Figure 3.4: Laser cooling scheme for SrOH, where line thicknesses represent power requirements for each laser.

the highest possible scattering rate.

2. **Select excited states that have strong decays to the target ground state**: When selecting excited states, especially for earlier repumpers, it is important to return to the target ground state, $\tilde{X}^2\Sigma^+(000)$, as quickly as possible. In our discussion of VBRs, we have characterized the probability of decaying from $\tilde{A}^2\Pi_{1/2}(v_1, v_2^l, v_3) \rightarrow \tilde{X}^2\Sigma^+(v_1, v_2^l, v_3)$; in general, that decay strength translates to the transition strength of the reverse process $\tilde{X}^2\Sigma^+(v_1, v_2^l, v_3) \rightarrow \tilde{A}^2\Pi_{1/2}(v_1, v_2^l, v_3)$. Thus, for the first repumping transition, we select $\tilde{X}^2\Sigma^+(100) \rightarrow \tilde{B}^2\Sigma^+(000)$ which predominantly decays back to $\tilde{X}^2\Sigma^+(000)$. For the second repump, we then drive $\tilde{X}^2\Sigma^+(200) \rightarrow \tilde{B}^2\Sigma^+(100)$ which predominantly decays back to $\tilde{X}^2\Sigma^+(100)$. This cascading effect allows for efficient optical cycling with a high scattering rate, and similar logic can be applied to later repumping transitions.

3. **Choose reasonably strong transitions**: Although not an intrinsic limitation, repumping efficacy can be limited by available laser power. As such, it is important to select strongly allowed tran-

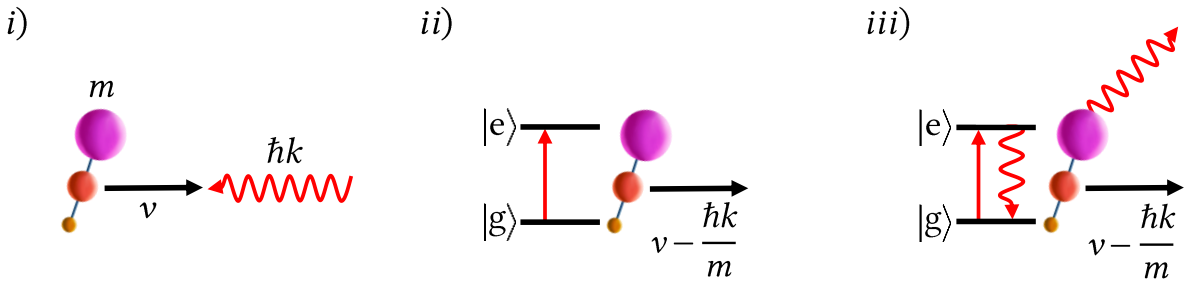

Figure 3.5: Simple cartoon picture of a photon absorption and emission event during radiative slowing. i) The molecule has some forward velocity v and interacts with a counter-propagating laser. ii) Photon absorption results in excitation, and a reduction in forward velocity through the conservation of momentum. iii) The molecule de-excites, emitting a photon in a random direction. Here, k is the wavevector of the laser light, $\hbar$ is the reduced Planck constant, and m is the mass of the molecule.

sitions to relax such requirements, especially when dealing with several repumping lasers where high power requirements can add to technical complexity and cost. As addressed in the first consideration as well as in Chapter 2, the wavefunction overlap between two states determines the transition dipole matrix element between them. As such, stronger transitions are those which involve minimal changes to vibrational quantum numbers. This then informs the choice of excited state in conjunction with Condition 1.

3.3 Imparting Forces on Molecules Using Light

Before describing how to construct a laser cooling scheme for a molecule, we discuss the basics of what laser cooling entails and why applying such techniques to molecules can be challenging. Laser cooling in atoms was theorized in the mid 1970's [102] and implemented soon thereafter [2, 103]. From these initial demonstrations, the field has evolved to develop more sophisticated methods to obtain colder temperatures and extend these techniques to more complex species. Despite these advances, simple, well established methods such as Doppler cooling remain relevant today and are crucial components of molecular laser cooling experiments, particularly in slowing a molecular beam.

3.3 a) Radiative Slowing

The theory of Doppler cooling, discussed in Ref. [100] and shown in Fig. 3.5, begins with a molecule with some velocity $\vec{v}_{\text{initial}}$ travelling in the $+\hat{x}$ direction. If the molecule encounters a resonant laser beam traveling in the $-\hat{x}$ direction, it can absorb a photon and receive a momentum kick in the $-\hat{x}$ direction, slowing the molecule down such that

$$\begin{aligned} m v_{\text{final}} &= m v_{\text{initial}} - \hbar k, \\ v_{\text{recoil}} &= v_{\text{final}} - v_{\text{initial}} = \frac{\hbar k}{m}. \end{aligned} \tag{3.6}$$

Here, m is the mass of the molecule being slowed, where the mass of SrOH is $m_{\text{SrOH}} = 105$ amu, $\hbar$ is the reduced Planck constant, k is the photon wavenumber, v_{initial} and v_{final} are the initial and final velocities of the molecule, respectively, and the recoil velocity v_{recoil} is the velocity kick experienced by a molecule through the absorption of one photon. For SrOH, $v_{\text{recoil}} = 0.55$ cm/s. The recoil velocity for a species is an important metric, as it determines how many photon absorptions are needed to obtain the target net velocity change. Table 3.1 shows recoil velocities for some select atoms and molecules, where the forward beam velocities are taken from Refs. [104, 105]. For a molecule with mass m and a given cooling wavelength, the speed scales $\propto \frac{1}{\sqrt{m}}$ whereas the recoil velocity scales $\propto \frac{1}{m}$. This means that direct laser cooling of a heavier species requires a longer slowing length.

Once a molecule experiences a momentum kick due to a photon absorption event, it then emits a photon in a random direction. As such, enough of these absorption and emission events known as "photon scatters" result in an overall net force in the propagation direction of the laser, whereas the emission occurs isotropically and results in zero average momentum change, but some diffusive heating. Following Ref. [100], one can describe this force as the product of the absorbed photon momentum p_γ and the scattering rate R_{scatter} such that

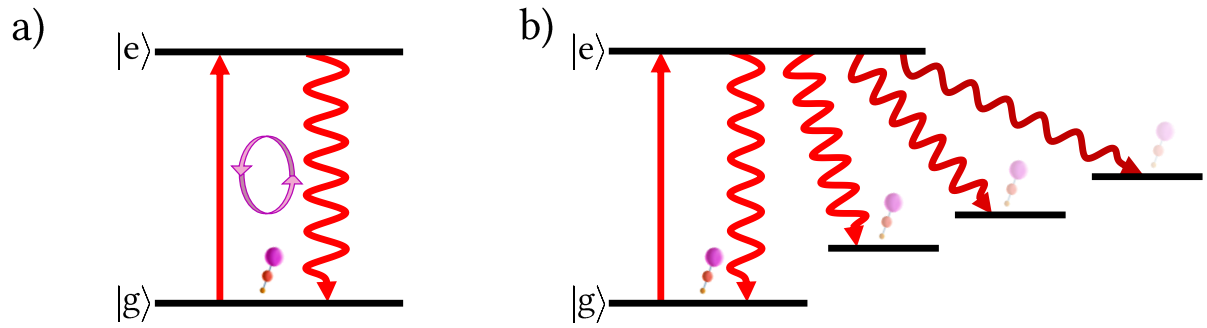

Figure 3.6: Simple schematic depicting the different regimes of photon cycling. a) Photon cycling in an ideal two-level system, where every decay goes back to the original ground state. b) A multi-level system in a molecule where the decays can happen to a number of dark ground states.

$$F_{\text{scatter}} = \underbrace{\hbar k}_{p_\gamma} \underbrace{\frac{\Gamma}{2}\frac{s}{1+s+4\delta^2/\Gamma^2}}_{R_{\text{scatter}}}. \tag{3.7}$$

Here, Γ is the natural linewidth of the transition, $s = I/I_{\text{sat}}$ is the saturation parameter for a given laser intensity I and saturation intensity I_{sat} of a transition, and $\delta = \omega_0 - \omega$ is the relative detuning between the resonance frequency for a transition, ω_0 and the laser frequency ω. When $s \to \infty$, this expression reduces to give a maximum force and acceleration

$$\begin{aligned} F_{\text{max}} &= \frac{\hbar k \Gamma}{2}, \\ a_{\text{max}} = F_{\text{max}}/m &= \frac{v_{\text{recoil}}\Gamma}{2}, \end{aligned} \tag{3.8}$$

where we have nicely recovered an expression that depends on parameters fully specified by the species used. Although we painted a mostly innocuous picture of the photon absorption and emission process, in reality the isotropic photon decay results in random fluctuations of the molecule velocities, setting a limit on the minimum temperature this method can achieve. In the overall frame of the slowed molecular beam, the Doppler force can be written as

$$\vec{F}_{\text{Doppler}} = \vec{F}_{\text{abs}} + \delta\vec{F}_{\text{abs}} + \vec{F}_{\text{em}} + \delta\vec{F}_{\text{em}}. \tag{3.9}$$

Table 3.1: Recoil velocities for select atoms and molecules. Heavier species and longer cooling wavelengths lead to smaller recoil velocities, making direct laser slowing more challenging. The forward velocities are taken from [104, 105], where the velocities for molecules denoted with $*$ are extrapolated from CaOH based on their mass and cooling wavelength.

Species	Cooling Wavelength (nm)	Mass (amu)	CBGB Velocity (m/s)	Recoil Velocity (cm/s)
Ca	423	40	–	2.36
Sr	461	88	–	0.98
CaF	606	59	~150	1.12
CaOH	626	57	~150	1.12
SrOH	688	105	~110	0.55
$CaOCH_3$	629	71	~150*	0.89
$CaNH_2$	630	56	~150*	1.13
CaOPh	610	133	~110*	0.49

We have already described the effects of $\vec{F}_{\text{abs}} + \vec{F}_{\text{em}}$ above. The remaining δ terms contribute to the aforementioned fluctuations, where $\delta\vec{F}_{\text{abs}}$ and $\delta\vec{F}_{\text{em}}$ arise from the randomness in the absorption and emission processes. The absorption term is related to the fact that the number of photons absorbed in a particular time is not always the same, whereas the emission term can be thought of as the variance due to a molecule's velocity undergoing a random walk through several emission events. The balance between these fluctuations and the overall cooling force results in a minimum obtainable temperature T_{D} known as the Doppler limit such that

$$T_{\text{D}} = \frac{\hbar\Gamma}{2k_{\text{B}}}, \tag{3.10}$$

where k_B is the Boltzmann constant. For SrOH, $T_D \approx 150\ \mu$K. We will discuss in next subsection technical details of different slowing techniques, including ways to remain resonant with the relevant cooling lasers as the molecular velocities change and result in Doppler shifting out of resonance. In Chapter 6, we describe techniques to cool below this limit using sub-Doppler cooling techniques.

3.3 b) Doppler Shifts

We must account for the Doppler shift when slowing to ensure that the molecules are always close to resonance and are continuously cycling photons. For a transition with resonance frequency ω_0 at rest, the Doppler shift is written as

$$\omega = \omega_0 \left(1 - \frac{v}{c}\right), \tag{3.11}$$

where, for a molecule traveling with velocity v parallel to the laser wave vector, the resonance frequency shifts to ω. Here we assume $v \ll c$ where c is the speed of light, a condition well satisfied in laser-cooling experiments. From this equation, we see that molecules traveling against a laser will see a blue-shifted resonance such that $\omega > \omega_0$. Consequently, the slowing light must be red-detuned from the nominal zero velocity resonance frequency, and should be set to cover the necessary velocity classes as the molecular beam is slowed. Below, we describe a few well established techniques used to achieve radiative slowing, after which we discuss how they are experimentally implemented in the SrOH experiment.

3.3 c) White-light Slowing

As the name suggests, white-light slowing circumvents the Doppler-shift issue by broadening the slowing laser frequency to cover all possible velocity classes, from the peak molecular beam velocity to approximately 0 m/s. Initial demonstrations of slowing a molecular beam to MOT capture velocities involved this technique [3, 74]. The broadening is achieved by an overdriven electro-optic modulator (EOM), which utilizes the electro-optic effect to modulate the phase, amplitude, or polarization of light. This can be done by applying a radio-frequency (RF) electric field to a non-linear crystal to change its refractive index. For white-light slowing, phase modulation is used to add frequency sidebands to the carrier frequency (the slowing laser). The total spectrum can be summarized as

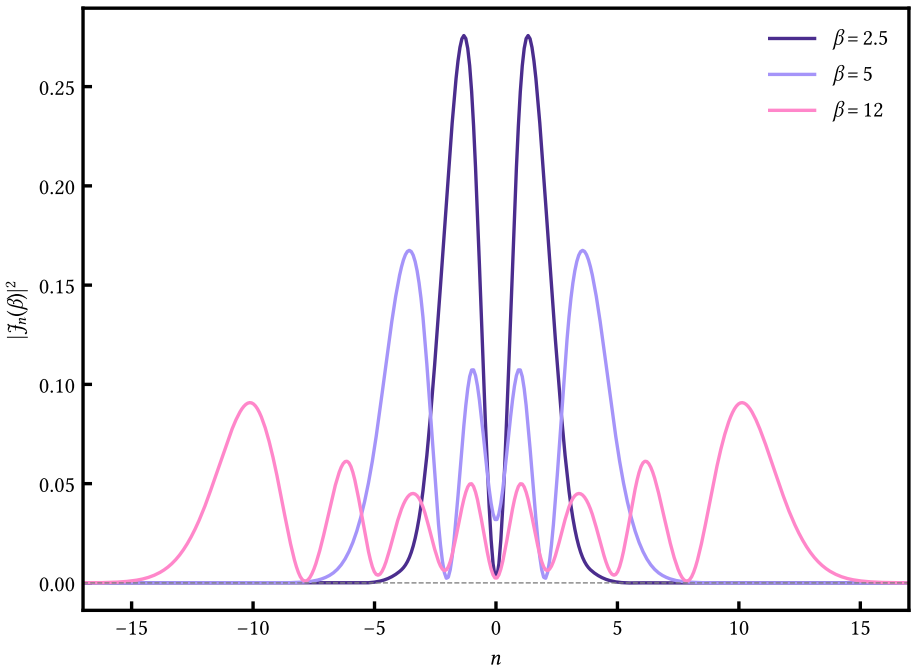

Figure 3.7: Amplitude of Bessel functions for different values of β. In order to get sidebands up to some order n, we require $\beta > n$.

$$E(t) = E_0 \sum_{n=-\infty}^{\infty} J_n(\beta)\, e^{i(\omega + n\Omega)t}, \tag{3.12}$$

where E_0 is the carrier amplitude, ω is the carrier frequency, Ω is the modulation frequency of the RF input which determines how much each sideband is shifted, $J_n(\beta)$ is a Bessel function defining the amplitude of each sideband component, and β is modulation amplitude which is proportional to the RF input drive strength. In white-light slowing, the modulation frequency is chosen to be smaller than the natural linewidth of the molecular transition to ensure that the molecules are always close to resonance with a sideband for any given velocity class. Although the above equation shows that phase modulation results in an infinite number of sidebands, for $n \gg \beta$,

$$J_n(\beta) \sim \frac{1}{\sqrt{2\pi n}} \left(\frac{e\beta}{2n}\right)^n. \tag{3.13}$$

Practically, this means that the sideband amplitude for large n decreases very rapidly. As such, a broad spectrum is obtained by increasing β via a large RF drive, to obtain enough sidebands to cover the full velocity spread. Often, an LC tank circuit is used to provide the voltage gain needed to resonantly drive the given EOM crystal. Although white-light slowing is simple to implement, it can be inefficient. First, it is difficult to very precisely select a sharp slowing cutoff at the MOT capture velocity, potentially resulting in molecules being turned around as discussed in Ref. [106]. Additionally, the power per sideband P_n is expressed as

$$P_n = P_{\text{slow}} |J_n(\beta)|^2, \tag{3.14}$$

where P_{slow} is the carrier, or slowing laser, power. Since $|J_n(\beta)| < 1$, this means that the total power of the laser is distributed among the sidebands, resulting in lower power per velocity class. This is problematic as the cooling scattering rate is proportional to the laser intensity. As such, low laser power will result in lower deceleration and a smaller change in velocity over a fixed beamline distance.

3.3 d) Chirped Slowing

Instead of covering every necessary velocity class from the start, one can sweep the frequency of the slowing laser to match the velocity of the molecule as it is slowed. This is known as chirped slowing and is generally more efficient than white-light slowing as the total laser power is utilized for each velocity class. One potential limitation, as discussed in Ref. [107], is related to the speed of the sweep. Depending on the scattering rate of the slowing transitions and the number of photon scatters required, it may be required to sweep 100 MHz $-$ 1 GHz in as little as 1 $-$ 10 ms. While this posed a problem in early laser cooling experiments, modern-day solid-state laser technology makes this slowing technique viable and widely used.

3.3 e) Zeeman Slowing

While the previous two slowing techniques are used widely in molecule laser cooling experiments, Zeeman slowing, the most efficient and ubiquitously used in atomic experiments is yet to be implemented. Before discussing the reason for this, we first describe the principles of the technique. Following from Ref. [100], one way to deal with the Doppler shift is by inducing a position dependent internal energy shift along z, such that

$$\omega_0 + f(z) = \omega + kv, \tag{3.15}$$

in terms of the $k-$vector of the laser, where some spatially varying energy shift $f(z)$ adds to the resonance frequency ω_0 to compensate for the Doppler shift on the laser frequency ω. One way to engineer $f(z)$ is to use a spatially varying magnetic field $B(z)$ to Zeeman shift the internal states, such that $f(z) = \mu_B B(z)/\hbar$, where μ_B is the magnetic moment. Then, for an initial velocity v_0, the velocity as a function of position becomes

$$v(z) = v_0 \left(1 - \frac{z}{L}\right)^{1/2}, \tag{3.16}$$

where L is the stopping distance for a given constant deceleration. From this, we obtain the magnetic field profile

$$B(z) = \frac{\hbar k v_0}{\mu_B} \left(1 - \frac{z}{L}\right)^{1/2} + B_{\text{bias}}, \tag{3.17}$$

where B_{bias} allows for tuning of the final velocity. This technique combines the benefits of the previous two: similar to white-light slowing, the atoms are slowed from some initial velocity v_i to some final velocity v_f regardless of their spatial distribution, so long as v_i is below the maximum velocity cutoff. However, as

is the case with chirped slowing, the atoms see the intensity of the laser light itself, and not some fraction of it in a frequency sideband. Although this combination makes this technique the theoretical ideal, it is currently not viable for molecule laser cooling experiments. As discussed in Chapter 4, molecules are cooled on Type-II transitions, where there exist more ground states than excited states. This, combined with the fact that species like CaF, CaOH, and SrOH have negligible excited state g-factors, means that slowing would rely on the ground state Zeeman shift. This can be troublesome as the ground states would split into multiple manifolds, each of which can be populated when the molecules decay from the excited state. Since each manifold has a different Zeeman shift, a different frequency of light is needed to address each transition. Depending on the magnitude of the shift, this would require either multiplying the number of slowing lasers by the number of manifolds, or reverting back to white-light broadening. Despite these issues, there is ongoing work to demonstrate a Zeeman slower with CaF molecules [108].

3.4 Slowing SrOH: Experimental Details

The initial demonstration of radiative slowing of the SrOH molecular beam was done entirely with white-light broadened lasers. Since then, the slowing techniques have matured, including chirped lasers and a transverse cooling region prior to slowing. In this section, we describe the slowing infrastructure and some key results. Additional information on these experimental details can be found in Refs. [98, 99].

3.4 a) Beamline and Vacuum Apparatus

As described in Sec. 3.1, SrOH molecules are produced inside a copper cell in the beam box, after which Helium buffer gas entrains them in a beam which propagates down a $L = 1.45$ m long evacuated beamline towards the final trapping region as shown in Fig. 3.8. This length was determined by theoretically scaling from the CaOH experiment [73], accounting for the different slowing laser wavelength and molecular

mass. Establishing and maintaining good vacuum is vital for the successful laser cooling of SrOH. Because the SrOH molecule is a radical as is the case with all directly cooled molecular beam experiments, it is extremely unstable and rapidly reacts in regular atmospheric conditions. The beam box itself is evacuated with a Roots pump (Leybold nXR40i) which backs two Turbo pumps (Pfeiffer HiPace 80), which results in a pressure of 2×10^{-7} Torr at cryogenic temperatures as read on an ion gauge (Kurt J. Lesker KJLC 354). Additionally, charcoal sorbs inside the beambox allow for adsorption of the Helium buffer gas. Under standard experimental conditions, this pressure can rise to as high as 1×10^{-6} Torr when flowing the Helium buffer gas and water to produce the SrOH molecules. Once the molecules leave the beam box, they enter a custom made chamber with a square cross-section where transverse cooling is implemented as shown in Chapter 7. An ultra-high vacuum (UHV) shutter (VS25S1T0) is installed at the end of this region, where we determine the time when it is closed to allow for sufficient time for the molecular beam to propagate while minimizing Helium build up in the beamline.

The second region of the beamline follows a gate valve (Kurt J Lesker 10840-UE01) and is pumped by a Hi-Cube (Pfeiffer HiCube 80) backing a Turbo pump (Pfeiffer HiPace 300), as well as a titanium sublimation pump (TSP) (Agilent 9160050 TSP filament cartridge) driven by a Gamma Vacuum DIGITEL TSPq controller (TSPQ2U1SSN). This region is designed to have several view ports for ample optical access on the sides, top, and bottom to allow for measurements of the characteristics of the molecular beam. When pumped down separately from the beam box, the pressure in this region reaches 1×10^{-8} Torr as monitored by a nude Bayard-Alpert ion gauge (Agilent 572) read out by an XGS-600 gauge controller. Following another gate valve, trapping is done inside a UHV MOT chamber (Kimball Physics, MCF800-SphSq-G2E4C4A16) held at $\sim 10^{-10}$ Torr when pumped separately. The same HiCube used for the middle part of the beamline backs a large Turbo (Pfefiffer HiPace 700), which pumps down the MOT chamber with the help of a TSP (Agilent 9160050 TSP filament cartridge).

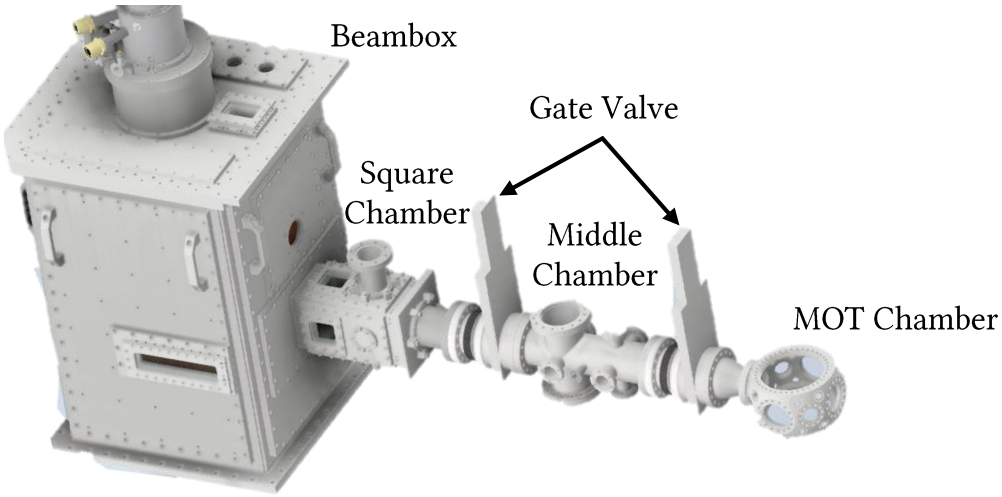

Figure 3.8: Beambox and beamline for SrOH slowing and trapping.

3.4 b) Slowing Lasers

As summarized in 3.2, a total of 12 lasers are used for slowing, including the mainline and 11 additional repump lasers resulting in a photon budget of $\gamma_{\text{budget}} \sim 15000$. With the exception of the first repump driving the $\tilde{X}^2\Sigma^+(100) \rightarrow \tilde{B}^2\Sigma^+(000)$ transition, every laser is white-light broadened via an EOM which comprises of a lithium niobate crystal (AdvR MgLN z-cut crystal; 1x1x60mm; Uniform copper plated electrode on gold) in custom made aluminum housing (based on Digikey P/N 501-2054-ND), as well as an LC circuit (iron powder core Amidon T106-2) and transformer with ferrite core (Digikey P/N 495-5064-ND). A function generator (Siglent SDG2042X) supplies the RF input through an RF amplifier (Mini-Circuits ZHL-1-2W+), with the LC circuit providing voltage gain to phase modulate the crystal. The first repump laser has higher power requirements and is thus frequency chirped. Details of this as well as each laser system, how they are grouped to share EOMs and eventually combined down the beamline are given immediately below.

Table 3.2: Main and repumping transitions used to cool SrOH, including wavelengths, the type of laser used, and the laser power.

Ground State ($X^2\Sigma$)	Excited State	Wavelength (nm)	Technology	Power
(000)	$\tilde{A}^2\Pi_{1/2}(000)$	687.6	SFG	800 mW
(100)	$\tilde{B}^2\Sigma^+(000)$	630.9	SFG	1 W
(200)	$\tilde{B}^2\Sigma^+(100)$	630.5	SFG	100 mW
$(010; N = 1)$	$\tilde{B}^2\Sigma^+(000)$	624.5	SFG	3 W
(02^00)	$\tilde{B}^2\Sigma^+(000)$	638.0	SFG	600 mW
(02^20)	$\tilde{A}(020)\mu^2\Pi_{1/2}$	687.7	VECSEL	40 mW
$(010; N = 2)$	$\tilde{A}(010)\kappa^2\Sigma_{1/2}$	674.5	ECDL	5 mW
(300)	$\tilde{A}^2\Pi_{1/2}(200)$	711.5	ECDL	6 mW
$(110; N = 1)$	$\tilde{B}^2\Sigma^+(010)$	629.1	SFG*	20 mW
(12^00)	$\tilde{A}(020)\mu^2\Pi_{1/2}$	711.4	ECDL	5 mW
(12^20)	$\tilde{A}(020)\kappa^2\Pi_{1/2}$	697.7	ECDL	5 mW
$(110; N = 2)$	$\tilde{B}^2\Sigma^+(010)$	629.2	SFG*	5 mW

Mainline and Friends: $\tilde{X}^2\Sigma^+(000)$, $\tilde{X}^2\Sigma^+(010; \mathrm{N} = 2)$, $\tilde{X}^2\Sigma^+(12^00)$

As shown in Fig. 3.9, the light for the main cooling transition, $\tilde{X}^2\Sigma^+(000) \rightarrow \tilde{A}^2\Pi_{1/2}(000)$, is provided by a sum-frequency generation laser (SFG) made by PreciLasers (YTFL-SSFG-687-5-CW). The system directly provides the required visible output at 688 nm at a peak power of 5 W, whereas for the other SFGs on the experiment, we combine and sum the infrared (IR) inputs on a periodically poled lithium niobate (PPLN) crystal to generate the visible light. This is challenging to do for the mainline wavelength which combines light from a 1064 nm and 1980 nm fiber amplifier, the latter of which is difficult to align and overlap as its high wavelength is outside the range of many readily available IR viewers and optics.

The initial mainline laser path is common to every repumper, such that the light is split on a polarizing beamsplitter (PBS) (Thorlabs PBS122) where the majority of the light is directed to slowing, and $\sim 0.1 - 1\%$ of it is sent through a fiber to be locked on a wavemeter. Since the output polarization of the laser is vertical, a half waveplate (HWP) (Foctek WP0225H) prior to the PBS is turned to maximize the vertical (reflected) arm of the PBS to the experiment. Following this, the light is aligned through an acousto-optic modulator (AOM) (G&H AOMO 3080-125) which acts as a switch, as shown in Fig. 3.9. In short, the first

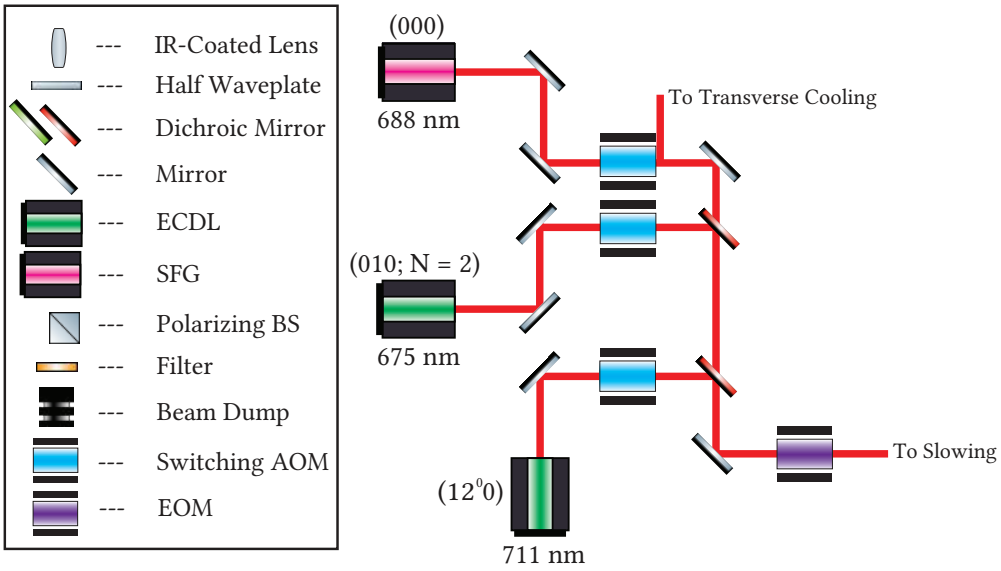

Figure 3.9: SFG and ECDL systems for the $\tilde{X}^2\Sigma^+(000)$, $\tilde{X}^2\Sigma^+(010;\mathrm{N}=2)$ and $\tilde{X}^2\Sigma^+(12^00)$ repumping transitions.

diffraction order of the AOM is maximized and coupled to the experiment, and the zeroth order is dumped. As such, switching the RF input to the AOM on and off allows us to subsequently switch the light in under 1 ms.

The mainline is then combined with the 7th and 10th repumps addressing the $\tilde{X}^2\Sigma^+(010;\mathrm{N}=2) \rightarrow \tilde{A}(010)\kappa^2\Sigma_{1/2}$ and $\tilde{X}^2\Sigma^+(12^00) \rightarrow \tilde{A}\mu^2\Pi_{1/2}(020)$ transitions, respectively. Both of these repumps are supplied by external cavity diode lasers (ECDLs) (MOGlabs LDL) providing ~20 mW of power each, with wavelengths of 675 nm for $\tilde{X}^2\Sigma^+(010;\mathrm{N}=2)$ and 711 nm for $\tilde{X}^2\Sigma^+(12^00)$. The mainline and $\tilde{X}^2\Sigma^+(010;\mathrm{N}=2)$ lasers are then combined using a dichroic mirror (Semrock FF685-Di02), after which they are combined again with the $\tilde{X}^2\Sigma^+(12^00)$ light in identical fashion (Semrock FF685-Di02). The combined laser beam is then aligned through an EOM to provide white-light broadening of ~300 MHz, after which it is fiber coupled to the slowing via a photonic-crystal fiber (PCF) (ALPhANOV LMA-PM-15), designed to efficiently transfer high optical power.

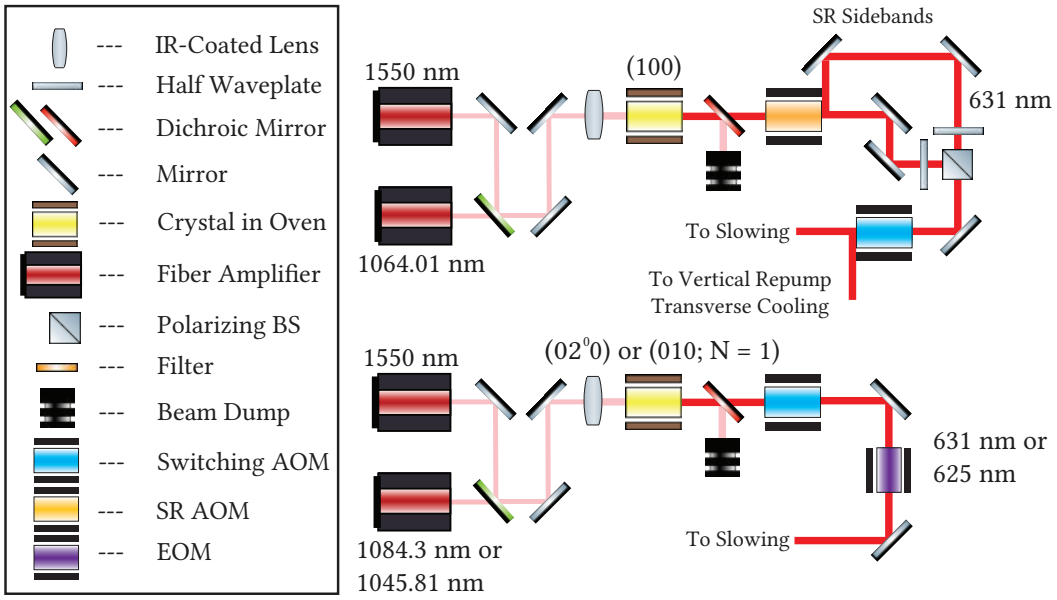

Figure 3.10: SFG setups for the $\tilde{X}^2\Sigma^+(100)$, $\tilde{X}^2\Sigma^+(02^00)$ and $\tilde{X}^2\Sigma^+(010;\mathrm{N}=1)$ lasers.

Stand Alone SFG Systems: Chirped $\tilde{X}^2\Sigma^+(100)$, $\tilde{X}^2\Sigma^+(02^00)$, $\tilde{X}^2\Sigma^+(010;\mathrm{N}=1)$

The first repumping transition light, $\tilde{X}^2\Sigma^+(100) \rightarrow \tilde{B}^2\Sigma^+(000)$, is generated by an SFG at 631 nm. For this laser, two Precilaser fiber amplifiers (EFA-SF-1550-10-CW; YFA-SF-1064-10-CW) centered at 1550 nm (Erbium doped) and 1064 nm (Ytterbium doped) are seeded by narrow linewidth semiconductor lasers from Precilaser (EFL-1550-0.04-S) and Innolume (DFB-1064-PM-30-OI). Unlike for the mainline, we overlap the IR wavelengths ourselves through a Periodically Poled Lithium Niobate (PPLN) crystal (HCP Photonics SFVIS-MB-50) housed inside an oven that comes with Precilaser, where we use temperature tuning to achieve phase matching and subsequent sum-frequency generation. The IR frequencies are summed to produce ~6 W of visible light as shown in Fig. 3.10 from 10 W of power in each IR wavelength. After a wavemeter pick off and alignment through a switching AOM, the light is aligned through another AOM driven at 110 MHz to account for the ground state SR splitting, since it is not white-light broadened. The zeroth and first diffraction orders are set to opposite linear polarizations using HWPs and are then combined on a PBS. The combined light then goes through the switching AOM, where the first order diffraction

is sent via a PCF to the slowing region, and the zeroth order continues to propagate to repump the MOT and transverse cooling regions, as we discuss in Chapters. 4 and 7.

The first repump is frequency chirped to account for the Doppler shift in slowing. Initial slowing was demonstrated with it being white-light broadened, but once a weak MOT signal was observed, it was changed to the current chirped configuration. To achieve this, a voltage ramp is applied to the current controller of the seed laser supplying the 1064 nm fiber amplifier, with the help of a sample-and-hold circuit (LF398). The wavemeter locking software was modified to disregard large frequency jumps when chirping, to prevent disrupting the sweep.

The $\tilde{X}^2\Sigma^+(02^00) \rightarrow \tilde{B}^2\Sigma^+(000)$ transition at 638 nm and $\tilde{X}^2\Sigma^+(010;\mathrm{N}=1) \rightarrow \tilde{B}^2\Sigma^+(000)$ transition at 625 nm are also driven by SFGs built identically to the $\tilde{X}^2\Sigma^+(100)$ laser, but with different seed wavelengths. They are both individually white-light broadened using EOMs, where the $\tilde{X}^2\Sigma^+(010;\mathrm{N}=1)$ laser is delivered to the slowing region by a PCF compared to a standard PM fiber for the $\tilde{X}^2\Sigma^+(02^00)$ as it requires more power. The SFGs can produce > 5 W of power each, but not all of this is used in slowing for the $\tilde{X}^2\Sigma^+(02^00)$.

Daisy Chained SFGs: $\tilde{X}^2\Sigma^+(200)$, $\tilde{X}^2\Sigma^+(110;\mathrm{N}=1)$, $\tilde{X}^2\Sigma^+(110;\mathrm{N}=2)$

Late repumps have lower power requirements as their ground states are visited comparatively less often compared to earlier repumps, which means that they don't need to be pumped out of as rapidly. One can take advantage of this fact by multi-seeding the fiber amplifiers, preventing the need for two dedicated systems for each visible wavelength. The combined IR can then pass through multiple crystals in series, where temperature tuning can selectively phase match to preferentially sum the relevant wavelength. The visible light is then separated from the remaining IR, which goes to another crystal and the process is repeated to form a "daisy chain". Due to the reduced power in one of the IR wavelengths, as well as a worse beam shape after the first crystal, the power after subsequent crystals tends to decrease, making

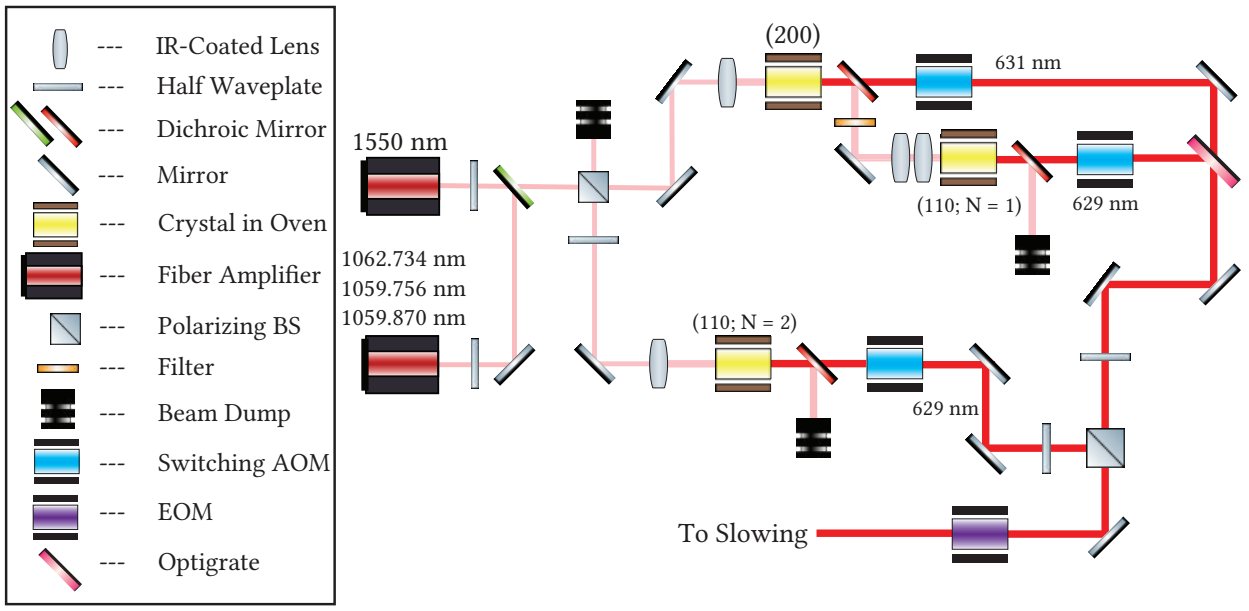

Figure 3.11: Daisy chain SFG setup for the $\tilde{X}^2\Sigma^+(200)$, $\tilde{X}^2\Sigma^+(110;\mathrm{N}=1)$ and $\tilde{X}^2\Sigma^+(110;\mathrm{N}=2)$ repumping transitions.

this technique only viable for late repumpers as they are effective even with low powers. This requires lasers with similar wavelengths, such that they are within the bandwidth of the amplifiers.

This approach is implemented for the $\tilde{X}^2\Sigma^+(200) \rightarrow \tilde{B}^2\Sigma^+(100)$, $\tilde{X}^2\Sigma^+(110;\mathrm{N}=1) \rightarrow \tilde{B}^2\Sigma^+(010)$ and $\tilde{X}^2\Sigma^+(110;\mathrm{N}=2) \rightarrow \tilde{B}^2\Sigma^+(010)$ transitions, each close to 630 nm. The setup consists of an Er-doped 1550 nm amplifier with a single seed laser. A Yb-doped 1064 nm amp is then multi-seeded with the relevant wavelengths before the IR is combined and daisy chained as shown in Fig. 3.11, where the $\tilde{X}^2\Sigma^+(200)$ repump has ~500 mW of power right after the crystal, the $\tilde{X}^2\Sigma^+(110;\mathrm{N}=1)$ has ~100 mW, and the $\tilde{X}^2\Sigma^+(110;\mathrm{N}=2)$ has ~20 mW. Because the wavelengths are so close, a regular dichroic mirror cannot be used to combine the lasers. Instead, a volume Bragg grating (OptiGrate BP630) with a resolution of ~0.1 nm is used to combine the $\tilde{X}^2\Sigma^+(200)$ and $\tilde{X}^2\Sigma^+(110;\mathrm{N}=1)$ lasers, which are then passed through an EOM then combined with the $\tilde{X}^2\Sigma^+(110;\mathrm{N}=2)$ laser (also white-light broadened via an EOM) on a PBS and being fiber coupled to the experiment.

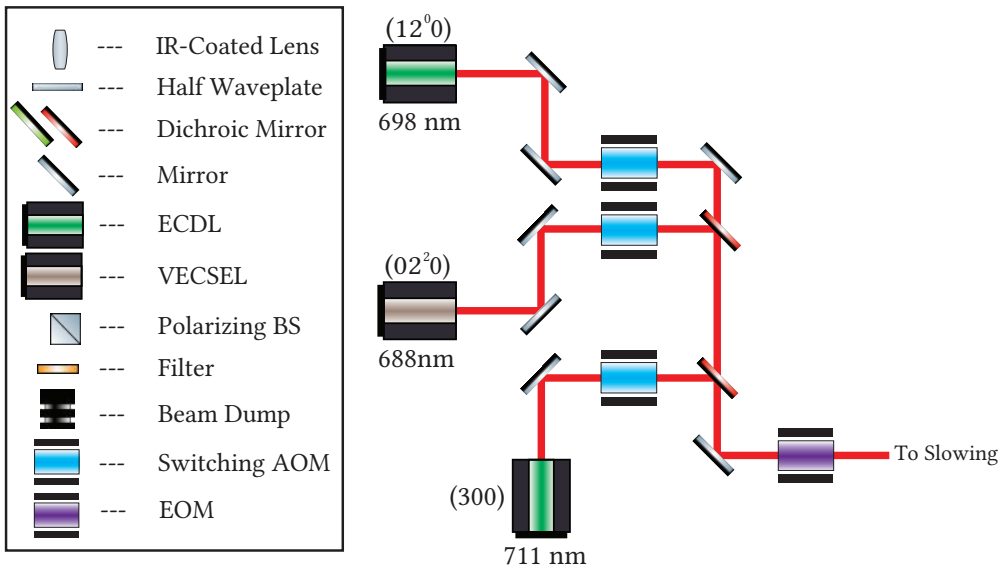

Figure 3.12: ECDLs and VECSEL for the $\tilde{X}^2\Sigma^+(300)$, $\tilde{X}^2\Sigma^+(12^20)$ and $\tilde{X}^2\Sigma^+(02^20)$ repumping transitions.

Remaining Repumps: $\tilde{X}^2\Sigma^+(300)$, $\tilde{X}^2\Sigma^+(12^20)$, $\tilde{X}^2\Sigma^+(02^20)$

The $\tilde{X}^2\Sigma^+(300) \rightarrow \tilde{A}^2\Pi_{1/2}(200)$ and $\tilde{X}^2\Sigma^+(12^20) \rightarrow \tilde{A}(020)\kappa^2\Pi_{1/2}$ transitions are addressed by ECDLs (MOGlabs LDL) at 711 nm and 698 nm respectively, with up to 20 mW of power each. As illustrated by Fig. 3.12, these are then combined with the laser addressing $\tilde{X}^2\Sigma^+(02^20) \rightarrow \tilde{A}(020)\mu^2\Pi_{1/2}$ at 688 nm supplied by a vertical-external-cavity surface-emitting-laser (VECSEL) (Vexlum VALO SHG) with ~500 mW of power before being white-light broadened and fiber coupled to the experiment.

3.4 c) Laser Slowing Results

The slowing laser light is routed to the optics table that houses the MOT chamber, where every repumper is combined with the main slowing light into one beam using a combination of dichroic mirrors, PBSs, and Optigrates, depending on their wavelengths. The combined slowing beam passes through a Pockels cell (Conoptics 350-50) which switches the light between orthogonal polarizations at a frequency of 1.5 MHz. The light then passes through an adjustable-focus lens assembly, after which it is expanded via ThorLabs

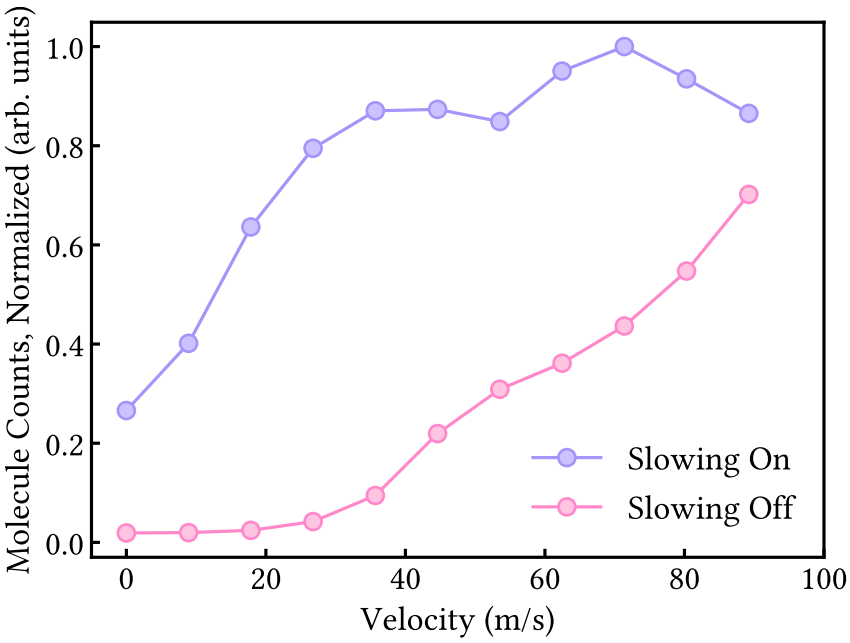

Figure 3.13: Velocity sensitive traces of the molecular beam with slowing on and off. The slowing light was turned on for 22 ms where the purple trace shows a large fraction of molecules with velocities of > 30 m/s. The unslowed pink trace has almost no molecules in this velocity class, which provides conclusive evidence that the velocity distribution of the beam was shifted by the slowing light. The peak velocity of ~110 m/s of the unslowed trace is cut off in this figure.

beam expander (GBE10-A) to roughly a 2 cm $1/e^2$ diameter. It is sent down the beamline and carefully aligned, centered through the MOT chamber window. The combined beam is focused right before the cell exit aperture, and is aligned to pass through the back snorkel window to ensure that it is centered relative to the molecular beam.

Initial slowing measurements involved collecting velocity sensitive data of the molecular beam, where additional details can be found in Ref. [99]. In this configuration, every laser was white-light broadened to ~300 MHz. Slowing was directly demonstrated for higher velocities than the MOT capture velocity, as it was difficult to resolve lower velocities due to the detection laser power broadening. Fig. 3.13 shows that when the slowing lasers are turned on, there is an increase in the proportion of molecules at lower velocity classes compared to the unslowed beam. Furthermore, Fig. 3.14 shows time-of-flight data of the slowed and unslowed beams, where the difference between them is clearly non zero. After successful slowing, the

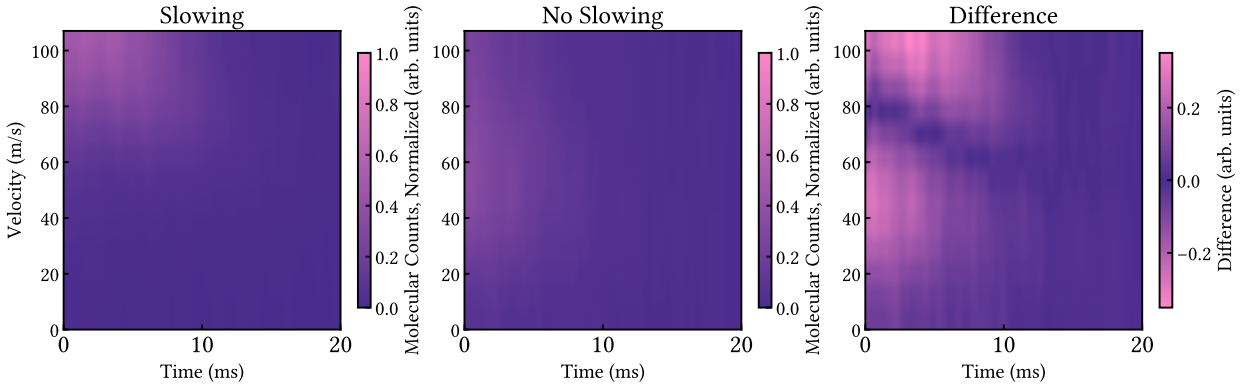

Figure 3.14: Time-of-flight data of the molecular beam, with slowing off, slowing on, and the difference between the two. The x-axis shows the arrival time of the molecules and the y-axis their velocity. There is a clear difference between the traces indicating that slowing has been achieved.

remaining optimization was done by observing the MOT itself described in Chapter 4, where details of chirped slowing will also be discussed.

3.5 Conclusion

In this Chapter, we discussed the laser slowing of the SrOH molecular beam. Decelerating over a long beamline as well as using and optimizing many repump lasers makes this step nontrivial. However, achieving these results allows us to load a magneto-optical trap (MOT) which is a key step towards full quantum control. In the next Chapter, we discuss this trapping while also presenting results that show how the MOT performance depends on the chirped slowing parameters.

""Because at the end is electricity, that through heat creates light and life. Because if not it would be ***[Redacted]*** *dark if this guy [Edison] doesn't have the idea to do that. "*

Mikel Arteta

4

Magneto-Optical Trapping

Magneto-Optical Traps (MOTs) are crucial in laser cooling, allowing for initial confinement, cooling, and subsequent spatial and phase space compression of atomic or molecular species emerging from a relatively hot source. Once the hurdle of acquiring a stable MOT is overcome, several diverse science applications become tenable, including loading optical traps, lattices, and tweezers [11, 13–16, 109]. In this Chapter, we first discuss the principles of an RF MOT, after which we discuss the experimental implementation and results for trapped SrOH.

4.1 Principles of Magneto-Optical Trapping

A MOT of SrOH is described in Ref. [77]; we expand upon those results below. The number of molecules initially captured was 2,000(600), which was increased to a peak MOT number of 32,400(4700) through the implementation of the two latest repumpers, as well as various improvements to slowing beam powers and production, discussed in Ref. [96]. Additional work to transverse cool the molecule beam as described in Chapter 7 has increased this number to 380,000(50,000).

4.1 a) Scattering Forces

A MOT in three dimensions consists of three orthogonal sets of retro-reflected beams and the presence of a three-dimensional magnetic field gradient to provide trapping. We first turn our attention to the effect of the laser light. Closely following Ref. [100], we recall from Eq. 3.3 a) in Chapter 3 that photon scattering from a laser provides some force F_{scatter} to a molecule in one dimension. Take a molecule with forward velocity v in a one-dimensional molasses defined by two counter-propagating lasers each with wavenumber k to form an "optical molasses". The molecule sees both lasers Doppler shifted, but with different signs depending on their relative directions, such that

$$F_{\text{molasses}} = F_{\text{scatter}}\left(\omega - \omega_0 - kv\right) - F_{\text{scatter}}\left(\omega - \omega_0 + kv\right). \tag{4.1}$$

As done in the [100], assuming a low velocity $kv \ll \Gamma$, we can Taylor expand each term to first order to obtain

$$F_{\text{molasses}} \approx F_{\text{scatter}} - kv\frac{\partial F_{\text{scatter}}}{\partial \omega} - F_{\text{scatter}} - kv\frac{\partial F_{\text{scatter}}}{\partial \omega}, \tag{4.2}$$

$$F_{\text{molasses}} = -2kv\frac{\partial F_{\text{scatter}}}{\partial \omega}, \tag{4.3}$$

$$F_{\text{molasses}} \approx -4\hbar k^2 \frac{I}{I_{\text{sat}}} \frac{2\delta/\Gamma}{\left(1 + (2\delta/\Gamma)^2\right)^2} v, \tag{4.4}$$

$$F_{\text{molasses}} \approx -\alpha v. \tag{4.5}$$

The lasers provide a damping force which slows molecules down to some small, finite velocity, but does not confine them. Trapping requires an additional step, which is adding position dependence to create a restoring force, where molecules are always pulled towards some region. This can be achieved by applying a magnetic field gradient and assigning the laser beams opposite circular polarizations , where we again refer to Ref. [100] to obtain

$$F_{\text{MOT}} = F^{\sigma^+}_{\text{scatter}}\left(\omega - kv - (\omega_0 + \beta z)\right) - F^{\sigma^-}_{\text{scatter}}\left(\omega - kv - (\omega_0 + \beta z)\right), \tag{4.6}$$

$$F_{\text{MOT}} \approx -\alpha v - \frac{\alpha\beta}{k} z, \tag{4.7}$$

where α is defined as above and $\beta = (g\mu_B/\hbar)(dB/dz)$ comes from the magnetic field gradient. F_{MOT} now resembles a damped harmonic oscillator with the same damping force from the molasses, but with a restoring force due to the magnetic field gradient which enforces a position dependence.

To more intuitively discuss how a MOT works, we look to Fig. 4.1 as an example. Take a "Type-I" transition, one where the angular momentum in the excited state is greater than in the ground state, the simplest of which comprises of $J = 0 \rightarrow J = 1$. Assume a magnetic field gradient in the $+z$ direction with a laser with σ^+ polarization propagating along the same direction, and one with σ^+ polarization going the opposite direction, both detuned red from the zero field resonance. The restoring force can be explained as follows: for a molecule positioned at some $+z$ from the center of the trap, the magnetic field gradient Zeeman shifts the $M_J = -1$ level closer to resonance. Due to angular momentum selection rules, this

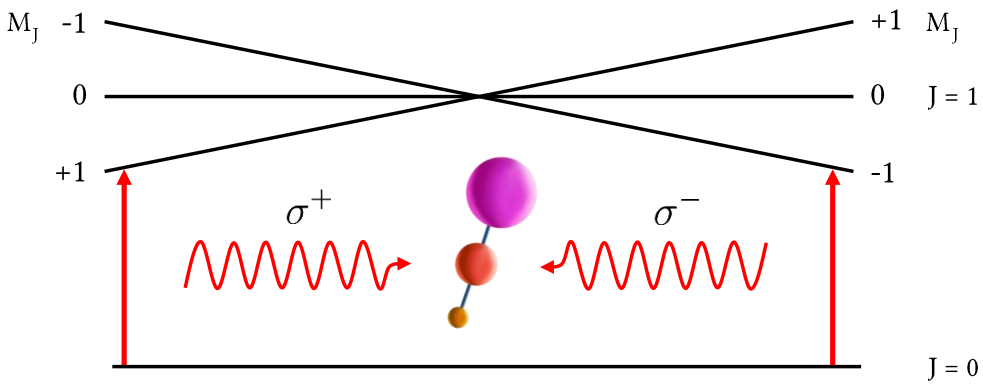

Figure 4.1: Cartoon picture of a "type-I" MOT on a $J = 0 \rightarrow J = 1$ transition.

results in preferential photon scattering from the laser with σ_- polarization, which pushes the molecule back to $z = 0$. Additionally, the red detuning of the laser means that the further away the molecules are from the trap center, the closer they are to resonance, resulting in a position dependent force. By symmetry, this description is identical for when the molecule is at position $-z$. The damping is explained by the Doppler shift, whereby faster molecules see the red detuned laser beams in the rest frame closer to resonance, resulting in a velocity dependent force. The combination of these effects results in damped oscillations, leading to trapping. To attain trapping in three-dimensions, we use a pair of orthogonal beams as described above in each of the $\hat{x}, \hat{y}$ and $\hat{z}$ directions. The trapping mechanism in three dimensions is more complicated as the molecules sees each laser polarization at once. Ref. [110] goes into great detail and simulates what these trapping forces look like, but practically, three-dimensional MOTs work as expected.

4.2 RF MOTs for Type-II Transitions

Typical molecular MOTs use type-II transitions and rely on the rapid, simultaneous switching of the magnetic field gradient and polarization. These RF MOTs are ubiquitously used for diatomic and triatomic molecular species [3, 73–78]. In this section, we discuss the need for these type-II transitions to provide rotational closed cooling transitions, and briefly discuss how RF MOTs are implemented.

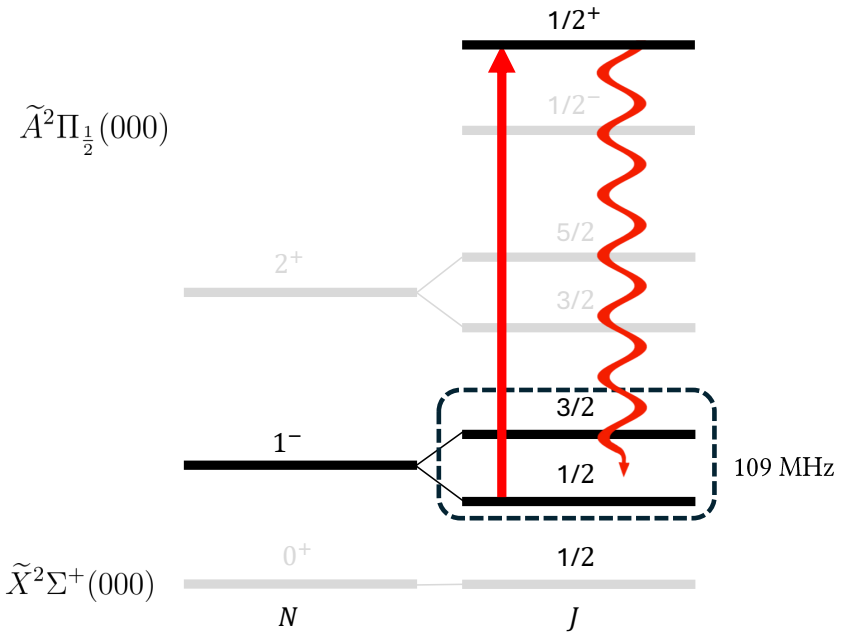

Figure 4.2: Rotational closure for the SrOH laser cooling transition.

4.2 a) Rotational Closure

Rotational transitions are governed by strict angular momentum selection rules, unlike vibrations. As such, we can carefully select the rotational ground and excited states for a laser cooling scheme to prevent rotational loss. Allowed rotational transitions obey the selection rules $\Delta J = \pm 1, 0$. Moreover, transitions may only occur between states of opposite parity. We can naively design a laser cooling scheme starting from the lowest rotational state $N = 0^+,\ J = 1/2$ in $\tilde{X}^2\Sigma^+(000)$, where J is the spin-rotation level and the superscript + denotes positive parity. If this is excited to the $J = 1/2^-$ state in the $\tilde{A}^2\Pi_{1/2}$ manifold, the molecule can decay to the original ground state, but also to a higher rotational state $N = 2^+,\ J = 3/2$, which is 16.2 GHz off resonance from the main cooling light. Instead, as shown in Fig. 4.2, we choose to drive the $N = 1^-$ to $J = 1/2^+$ transition, as the molecule can only decay to the $N = 1^-,\ J = 1/2, 3/2$ ground states, which are separated by the spin-rotation splitting of ~109 MHz and can be easily addressed with an acousto-optic modulator (AOM). Thus, starting at $N = 1^-$ allows for a rotationally closed transition.

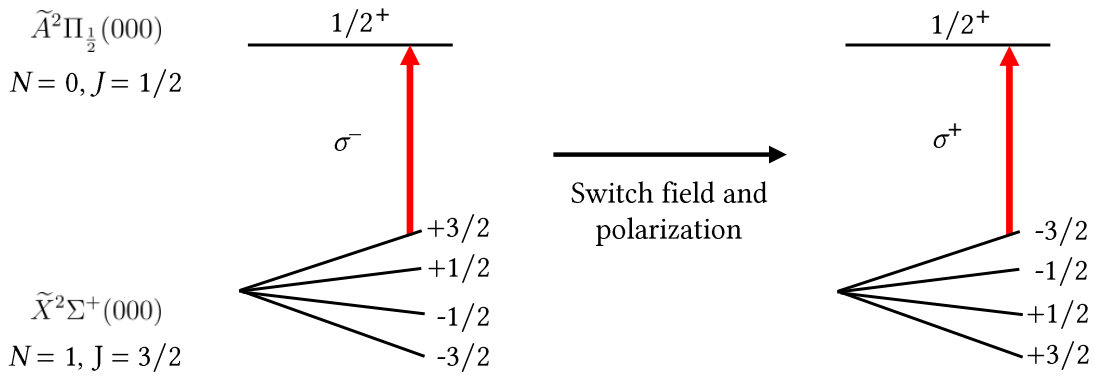

Figure 4.3: Polarization and magnetic field gradient switching in a "type-II" system to form an RF MOT.

These transitions are known as type-II as the ground state has larger angular momentum than the excited state.

4.2 b) RF MOTs

The type-II transitions needed to maintain rotational closure make trapping more difficult as decays can occur to dark ground states, which are unaddressable by the cooling light. For example, Fig. 4.3 shows the $J = 3/2$ spin-rotation manifold in the cooling transition in SrOH. If a σ^- transition is drive between the $M_J = +3/2 \rightarrow M'_J = +1/2$ states, selection rules allow for a decay down to the unaddressed $M_J = -1/2$ state, which thwarts the ability to scatter photons and apply a trapping force. To circumvent this issue, we rapidly switch the laser polarization and the direction of the magnetic field gradient on the order of the scattering rate at ~1 MHz.

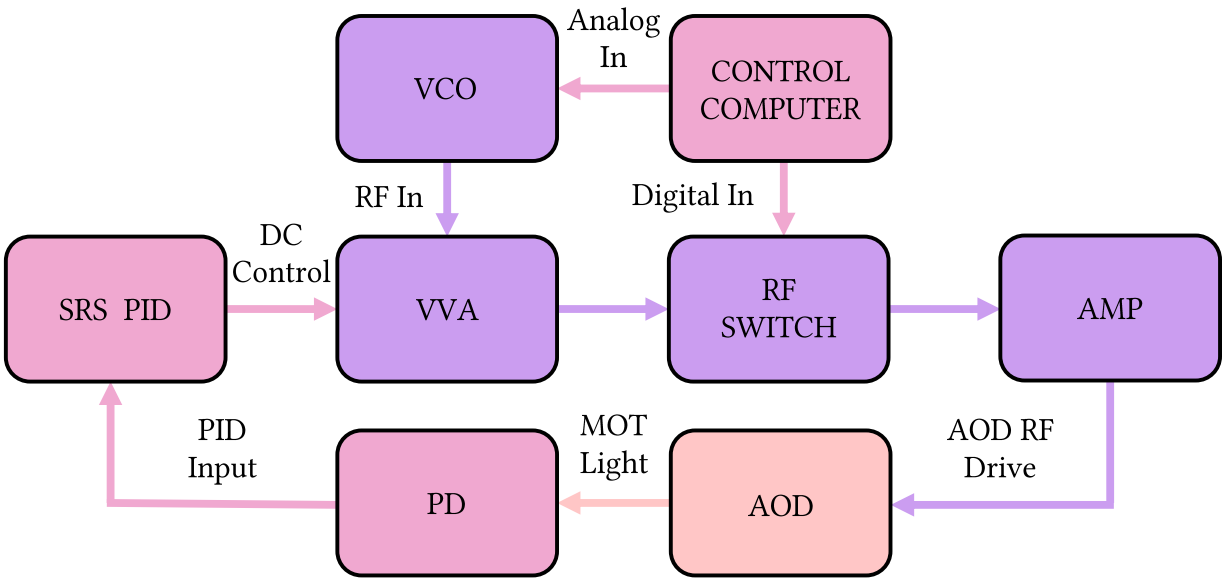

Figure 4.4: RF Circuit used to adjust the MOT beam detunings and PID their intensities.

4.3 MOT Experimental Details

4.3 a) Optics Setup

The MOT light is supplied by a Precilasers system (FL-SF-688-5-CW) identical to the one used for slowing. The light from this laser is sent through a double-pass acousto-optic deflector (AOD) (XSoptix AODF 4105) and is aligned through several AOMs to allow for switching between the RF MOT, sub-Doppler cooling, and the conveyor belt (CB) MOT. The AOD is set up using the catseye alignment method, the description of which is given in Chapter 6 along with the switching sequence used for each mentioned technique. An RF circuit comprising a voltage controlled oscillator (VCO) (Mini-Circuits ZOS-150) and a voltage variable attenuator (VVA) (Mini-Circuits ZX73-2500-S+), shown in Fig. 4.4 is used to drive the AOD. A voltage is supplied via Cicero to vary the AOD drive, and thus, the detuning of the MOT light. Its intensity is controlled through a proportional-integral-derivative (PID) loop, whereby a Stanford Research Systems (SRS)

PID module reads a voltage from a photodiode (Thorlabs PDA36A2) measuring the MOT beam intensity, and stabilizes it via the VVA to the voltage set point given by Cicero. The MOT light passes through a Pockels cell (Conoptics 350-210-01-RP) driven by a high-voltage amplifier (Conoptics Model 25D) for polarization switching, after which it is aligned through an AOM (IntraAction AOM-110) to add spin-rotation sidebands. The SR components are coupled through two ports of a 4×4 fiber splitter (Evanescent Optics 4x4 splice-less PM coupler array), where three of the outputs are for each of the MOT axes, and one is to monitor the power for the intensity PID. A HWP before each fiber collimator is used to ensure that the polarization of the light is aligned with the fast axis of the fiber, which can be verified on a polarimeter (Thorlabs PAX1000IR1). Before entering the MOT chamber, the light is expanded using a Thorlabs telescope (GBE10-B) out of the fiber, and aligned through a quarter waveplate (QWP) (WPQ20ME-633) into the MOT chamber. It passes through a HWP to rotate the circular polarization before being reflected back.

4.3 b) Magnetic Field Gradient

The magnetic field gradient is provided by a pair of in-vacuum anti-Helmholtz coils fabricated on a custom gold-plated direct-bonded copper (DBC) substrate with an aluminum nitride (AlN) ceramic base (Remtec DBC Products, DWG D1698), which are sprayed with black paint to minimize light scattering. They are driven by two individual channels on a function generator (Siglent SDG2042X) with a sinusoidal wave at a frequency of ~1 MHz, which then goes through a pair of commercially bought amplifiers (ENI550L50W). An RF tank circuit is then used to efficiently transfer this signal to the MOT coils, consisting of a tunable capacitor with a capacitance between $150 - 1500$ pF (Comet CVUN-1500AC/3-JHJA-Z), allowing us to easily impedance match each individual coil. Vacuum feedthrough rods mechanically attach the coils to the MOT chamber; these are externally accessible and water cooled to prevent excessive heating. The Pockels cell responsible for switching the polarization and oscillating magnetic field are synced with each other using a function generator (Siglent SDG2042X). .

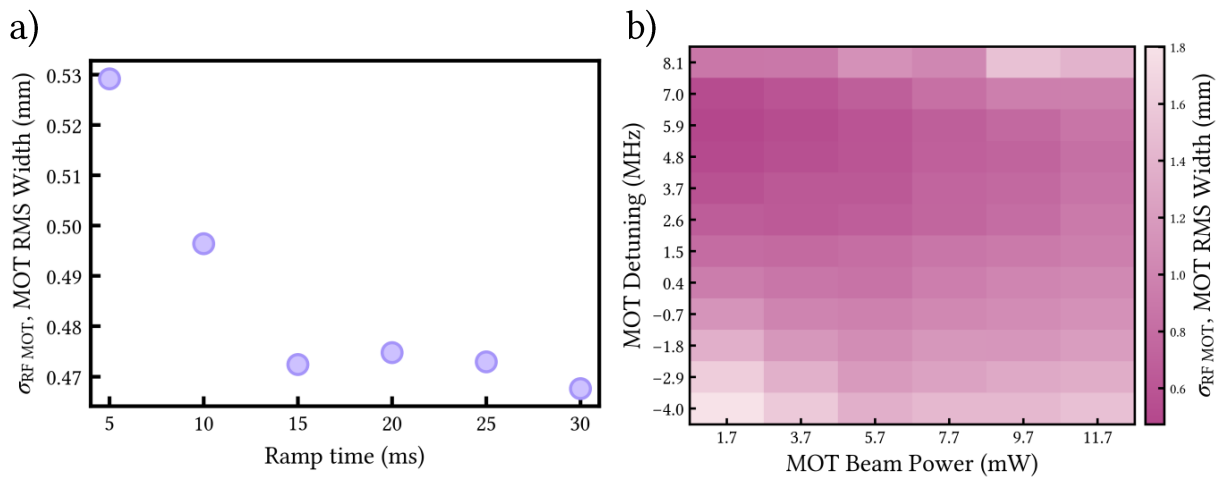

Figure 4.5: MOT size as a function of ramp parameters. a) RMS MOT width $\sigma_{\mathrm{RF\,MOT}}$ vs ramp time in milliseconds. Experimentally, the ramp time is set to 15 ms where maximum compression is achieved at the earliest. We avoid ramping for longer as this results in more molecules lost due to the finite MOT lifetime. b) 2D colormap of $\sigma_{\mathrm{RF\,MOT}}$ as a function of the MOT light detuning and power. The optimal configuration involves a lower power but the same frequency at the end of the ramp.

4.3 c) Initial Capture and Ramp

Molecules are captured in the MOT immediately after slowing ends, after which it is imaged for 100 ms on an EMCCD camera (Andor iXon Ultra 897). During capture and imaging, every repump except the first is left on, and the mainline slowing light is turned off. An AOM switches off the first repump light, and the zeroth order light is frequency shifted 110 MHz through another AOM (G&H AOMO 3080-125) and is combined via a dichroic mirror with the vertical MOT arm. The first repump scatters enough photons at a high enough rate to displace the MOT, which can be avoided by having the light be retroreflected and orthogonal to the slowing light.

The molecules are captured with an initial MOT laser power of $P = 3.7$ mW red-detuned by 7 MHz from resonance as shown in Fig. 4.6 and initial magnetic field gradient of $\mathscr{B} = 12$ G/cm. After a 15 ms capture period, the power and magnetic field gradient are ramped over an additional 15 ms to values of $P = 0.5$ mW and $\mathscr{B} = 16$ G/cm, compressing the molecular cloud size from 1.3 mm to ~ 0.5 mm. As

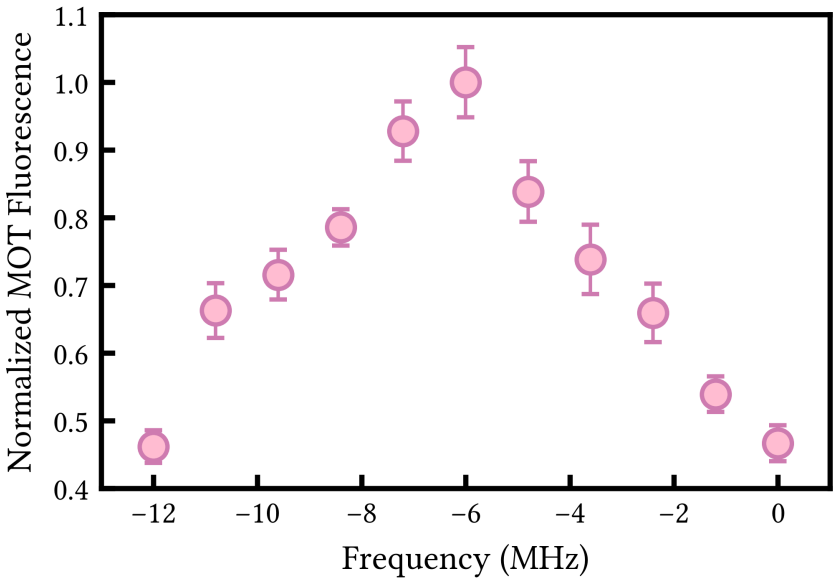

Figure 4.6: MOT fluorescence as a function of overall detuning done by directly scanning the frequency of the MOT laser. The slope on the blue-detuned side relative to the optimum is steeper due to increased heating.

we will discuss in Chapter 6, reducing the size of the trapped molecule cloud using a conveyor-belt (CB) MOT after this stage is important for efficient ODT loading. Fig. 4.5 shows the MOT cloud diameter as a function of various ramp parameters. The initial parameters are optimized to capture as many molecules as possible, where a high P enables a high scattering rate and a low $\mathscr{B}$ results in a large MOT capture volume. During the ramp, lowering the scattering rate through decreasing P reduces the heating effect from photon scattering, resulting in compression. Additionally, ramping $\mathscr{B}$ to higher values increases the slope of the Zeeman shift, thus reducing the capture volume. The highest achieved trapped number in the MOT from Ref. [96] was 32,400(3700) with a photon budget of 14,500(700).

4.3 d) Chirped Slowing and Larger Beams

Initial implementation of the MOT, as discussed in Refs. [77], involved white light slowing. Although fluorescence was observed, the molecules were never truly captured and were damped without being turned around. Unlike the true MOT trapping data we show below, the MOT lifetime in that initial work

showed no dependence on experimental parameters, suggesting that the molecules were not confined and were simply being damped as they passed through the MOT region. Moving from the earlier "MOT-like" conditions involved first increasing the beam size by a factor of 2 to $\sigma = 2$ cm. We note that this σ is larger than what is used on the CaOH and CaF experiments in our group. Although the exact nature of the initial system is not fully understood, we predict that its behavior can be attributed to the higher mass of SrOH. To see why this is, using Ref. [111], one can estimate the capture velocity of a MOT using kinematics where

$$v_{\text{cap}}^2 + 2aL = 0, \tag{4.8}$$

$$v_{\text{cap}}^2 = -2aL, \tag{4.9}$$

$$v_{\text{cap}}^2 = \frac{2\hbar k}{m}\frac{\Gamma}{2}L, \tag{4.10}$$

$$v_{\text{cap}} = \sqrt{\frac{\hbar k \Gamma L}{m}}, \tag{4.11}$$

for a molecule with mass m and natural lifetime Γ at a maximum scattering rate $\Gamma/2$, with a trap diameter of L. We assumed here that L is the distance at which the light becomes resonant with the molecule, after which the detuning flips and we can no longer apply a restoring force. Although its expression is reasonably simple, estimating the true MOT capture velocity is difficult as both Γ and L are difficult to know very precisely. Regardless, the scaling of v_{cap} is insightful as it shows that for heavier molecules, the capture velocity decreases but can in principle be recovered by proportionally increasing the MOT size. Fig. 4.7 shows the difference between the MOT-like forces and the current MOT.

In conjunction with the implementation of this improvement, chirped slowing allows for more laser power per velocity class for the first repumper, resulting in a MOT where molecules undergo many oscillations before the molecules are lost to vibrational dark states. Fig. 4.8 shows the dependence of the number of trapped molecules on various chirped slowing parameters.

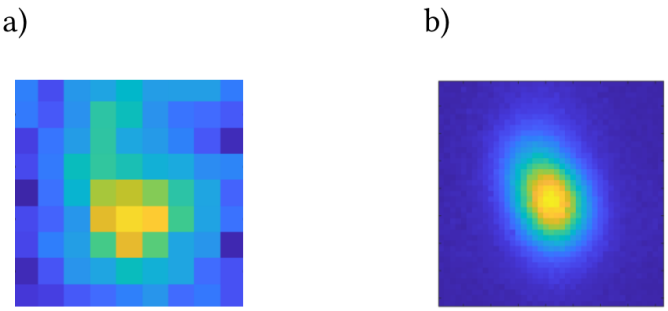

Figure 4.7: MOT fluorescence signal a) "MOT-like forces" with white light slowing and a $1/e^2$ diameter $d_{\mathrm{MOT}} = 1$ cm and b) with chirped slowing and $d_{\mathrm{MOT}} = 2$ cm.

4.3 e) Lifetimes

The MOT lifetime is predominantly limited by the finite photon budget as it relies on a consistent, high scattering rate to maintain its trapping force. The MOT lifetimes for different total powers from all three orthogonal, retro reflected MOT arms, as well as varying photon budgets, are shown in Fig. 4.9. These measurements are taken by imaging the MOT with variable hold times after initial capture and plotting the number of trapped molecules as a function of time. A decaying exponential is then fit to the data where we designate the lifetime τ as the fitted time constant. The longest measured lifetime has a value of 210(30) ms, where additional details about this data can be found in Refs. [77, 96].

In Fig. 4.9 a), τ is plotted as a function of power and is seen to follow the relation

$$\tau(P) = \tau_0 \frac{P + P_0}{P}, \tag{4.12}$$

where τ_0 is the lifetime in the fully saturated regime as shown in Fig. 4.9 a ii), P is the total power of the MOT beams, and P_0 is the saturation power. At low powers, the curve looks roughly linear as the

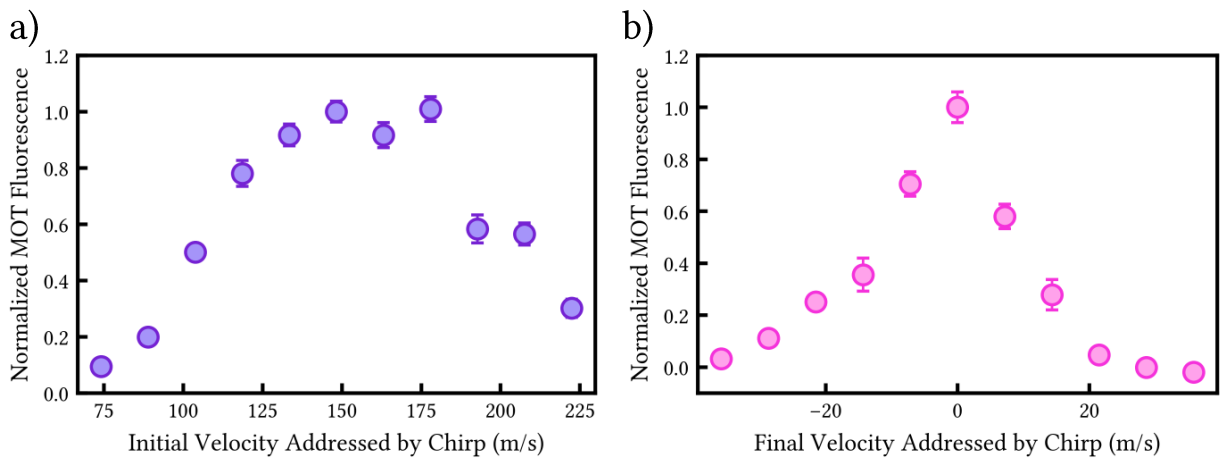

Figure 4.8: MOT fluorescence as a function of chirped slowing parameters. a) Scanning the initial velocity class addressed by chirped slowing. b) Scanning the final velocity class addressed by chirped slowing. The optimal starting velocity is around 130 m/s, which is higher than the beam velocity of 110 m/s, showing that we slow past the peak of the distribution. Each of these points was taken for a total slowing time of 22 ms, but changing this value would result in the above peak shifting for the initial chirp velocity. The final velocity is sharply peaked at 0 m/s.

increasing scattering rate decreases the MOT lifetime. As power is increased, τ appears to asymptote to τ_0 as the optical transition approaches saturation. From the fit, $\tau_0 = 15.5(1.68)$ ms and $P_0 = 18.5(2.7)$ mW.

Fig. 4.9 b ii) shows τ as a function of the photon budget n_γ. The photon budget is reduced by sequentially turning off repumping lasers after initial capture of molecules in the MOT. For large enough n_γ, τ is roughly linear as expected. One can use the measured τ to estimate the peak number of trapped molecules, as discussed in Refs. [77, 112].

4.3 f) Temperature

The temperature T of the MOT is measured by releasing the cloud and fitting its diameter σ at different times, also known as a time-of-flight measurement. For a particular spatial axis, the Gaussian width of the MOT relates to the temperature and expansion time as

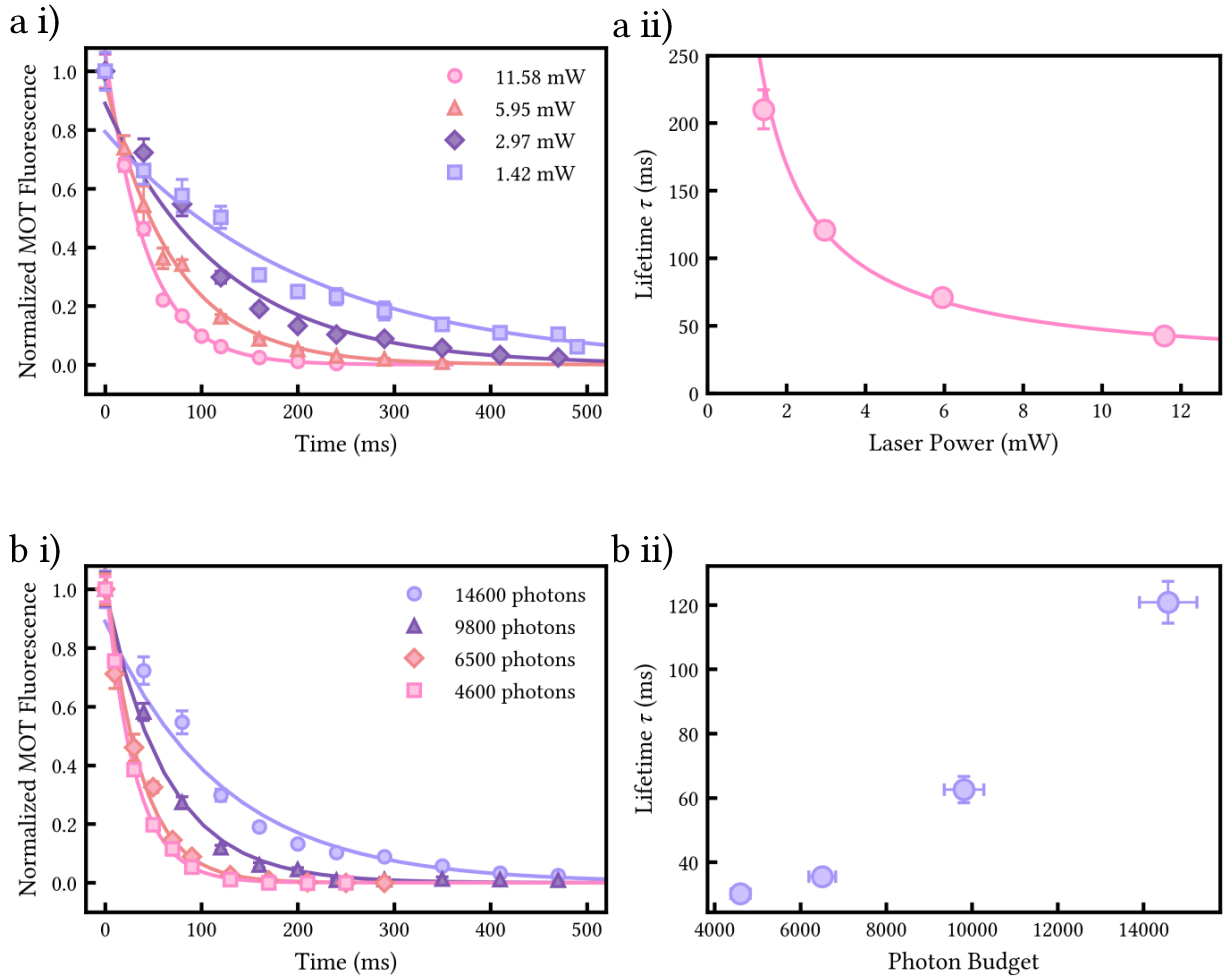

Figure 4.9: MOT lifetime data as a function of a) i) MOT beam power and ii) individual lifetimes plotted as a function of power and b) i) Photon budget and ii) individual plotted lifetimes as a function of photon budget.

$$\sigma(t) = \sqrt{\sigma_0^2 + (k_B T/m)t^2}, \tag{4.13}$$

where σ_0 is the initial size and t is the expansion time. We fit this function to our time of flight data to extract $T = T_{\parallel}^{1/3} T_{\perp}^{2/3}$ such that for $T_{\parallel}$ and $T_{\perp}$, $\sigma_{\parallel}$ and $\sigma_{\perp}$ are the sizes along the axial and transverse directions, respectively. The form of T arises from the fact that there are two transverse directions but only one axial direction. At a total beam power of $P = 1.1$ mW, $T = 1.2(3)$ mK and is seen to increase with

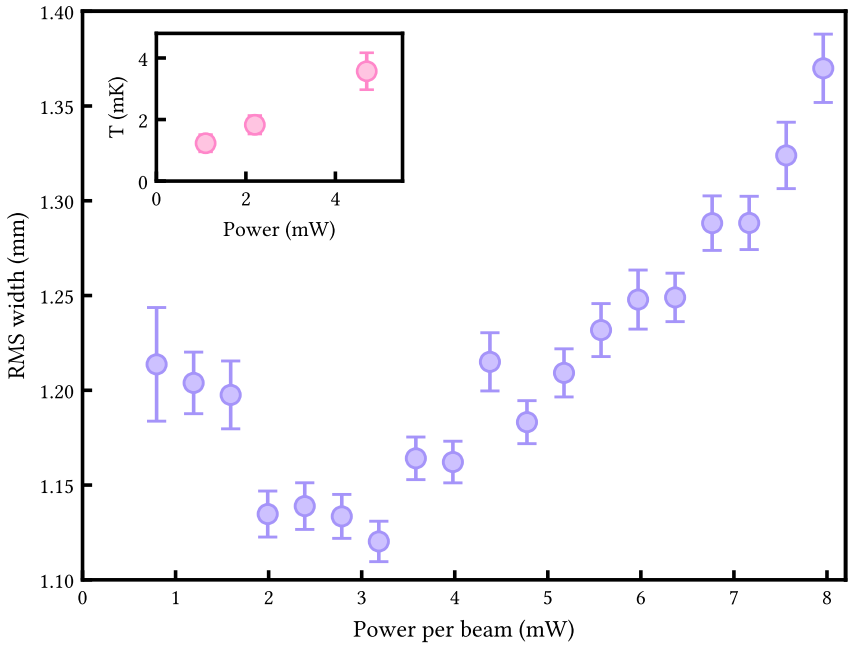

Figure 4.10: MOT size as a function of power, with the inset showing temperature as a function of power. At low powers, the size increases as the loading and capturing in the MOT is compromised.

higher P. This T is significantly higher than typical atomic MOTs due to the fact that the type-II trapping configuration results in sub-Doppler heating when the trapping light is red-detuned, as we describe in Chapter 6. Fig. 4.10 shows how the temperature and size varies as a function of power.

4.3 g) Oscillations

We measured the oscillations in the MOT as shown in Fig. 4.11, showing clear damped oscillations as expected. This is done by turning the main slowing laser on for 1 ms and providing an impulse to the MOT, after which it is imaged at several time increments and its mean position is measured and plotted. The data is fit to an expression describing the position of a damped harmonic oscillator

$$r(t) = Ae^{-\beta t/2}\cos\left(\sqrt{\omega^2 - (\beta/2)^2}t + \phi\right), \tag{4.14}$$

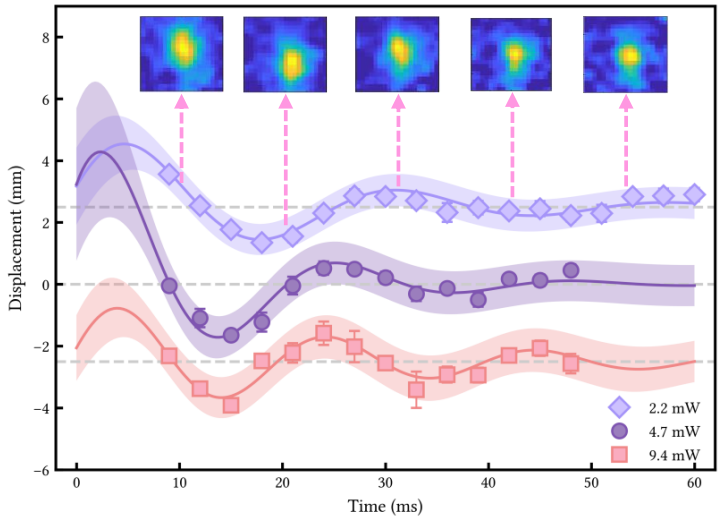

Figure 4.11: Mean MOT position as a function of time after being pushed. The three curves are taken at different powers, which does not change the damping constant or oscillation frequency, but only the amplitude of oscillations. Camera images of the MOT at the correspondingly labeled positions are shown on the top of the figure.

where the damping constant $\beta \sim 100\ \mathrm{s}^{-10}$ and the natural oscillation frequency $\omega \sim 2\pi \times 45$ MHz based on the fitted curves.

4.4 Conclusion

In summary, we have presented and discussed the magneto-optical trapping of SrOH. Under optimal trapping conditions, ~30,000 molecules were trapped with a lifetime τ of up to ~200 ms and a cloud size σ of ~0.5 mm with a temperature $T = 1$ mK. The realization of a MOT is a key stepping stone towards our eventual goal of a precision measurement inside an optical trap. In the next chapter, we will discuss the additional cooling and compressing steps taken towards achieving that goal.

This used to be part

Of the next chapter, you see

So the quote now sucks

A Haiku by me (Abdullah)

5

Sub-Doppler Cooling and Conveyor-Belt MOT Compression

To achieve the goal of loading an ODT of SrOH, we must implement additional experimental techniques after loading the MOT. As discussed below, loading an ODT directly from an RF MOT is inefficient due to the high temperature and large size of the trapped molecule cloud. As such, the development of sub-Doppler cooling techniques and compression through a blue-detuned "Conveyor-Belt" (CB) MOT have greatly improved ODT loading efficiencies. In this chapter, we begin by illustrating the principles of sub-Doppler cooling in Sec. 5.1, describing various techniques, experimental implementations and final results.

We then move to treating CB MOTs in a similar way in Sec. 5.2.

5.1 Sub-Doppler Cooling

Sub-Doppler cooling bridged the gap between the lowest achievable MOT temperature and the temperature required to load an ODT. Several techniques, namely Λ-enhanced Gray Molasses (Λ-GM) and Single Frequency (SF) cooling, are now mainstays in molecular laser cooling experiments, resulting in temperatures of $1-10$ μK. As elaborated on below, sub-Doppler (SD) cooling relies on blue-detuned light in Type-II systems, as opposed to red-detuned light used for Doppler cooling, which means typical molecular MOTs are hotter compared to atomic MOTs where Type-I approaches can be used. The SrOH MOT temperature of 1 mK is too hot to reliably load an optical dipole trap directly, necessitating an extra cooling step to achieve desired temperatures of ~100 μK. To understand why this is the case, consider an optical trap with depth U_0 such that any particles with energy $E > U_0$ escape it. We can write the probability of this occurring for a molecular cloud with temperature T as

$$P(E > U_0) \propto e^{-\frac{U_0}{k_B T}}, \tag{5.1}$$

where k_B is the Boltzmann constant. We define the dimensionless quantity η such that

$$\eta = \frac{U_0}{k_B T}, \tag{5.2}$$

which we want to maximize to efficiently load the ODT. Trap depths for ODTs are typically on the order of $k_B * (500\ \mu\text{K})$. This results in $\eta \sim 0.5$ when considering the MOT temperature, which means on average ~60% of molecules would be too hot to be trapped. The situation becomes worse if the molecular cloud has collisions, either with other molecules or with the photon field of the MOT. In this case, molecules above

the threshold of the trap quickly "boil over the edge". Thus, it is imperative to bring this temperature down to achieve values of $\eta \sim 10$, where even with rethermalization losses are low.

5.1 a) Cooling Mechanisms

As mentioned before, Type-II laser cooling transitions are necessary to maintain a closed photon cycle, but result in additional experimental complexity when loading a MOT due to the need to switch polarizations and magnetic field gradients and destabilize dark states. Furthermore, at low temperatures Type-II systems experience SD heating with red-detuned light. Atomic MOTs are often far colder [113] as the situation is flipped in the Type-I case, where red-detuned light provides both Doppler and SD cooling.

Before detailing experimental parameters and results, we discuss some relevant mechanisms to develop intuition for SD cooling processes. First, we generally outline Sisyphus cooling using a toy model in one dimension. Although not a perfect explanation for the type of cooling we implement, it provides a simple understanding for how SD and Doppler cooling are distinct, and elucidates the difference between blue and red-detuned type-II systems. It also demonstrates the important role that dark states play for SD cooling, where colder temperatures can be achieved as molecules in such states are not heated as a result of photon emission and absorption events. We then discuss the experimentally relevant mechanisms in Λ and SF cooling which help highlight how careful dark state tuning can result in excellent cooling performance.

Sisyphus Cooling

A toy model for this mechanism is shown in Fig. 5.1 to aid in the upcoming explanation. In general, Sisyphus cooling works in the following way:

1. A standing wave of laser light is created and is blue (red) detuned relative to some excited state to provide cooling (heating). Depending on the optical setup, this can result in a spatially varying

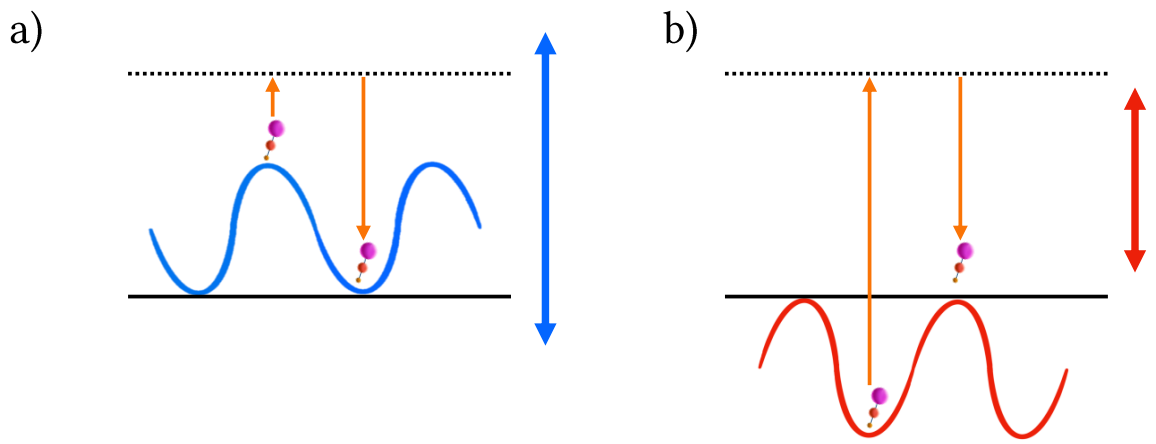

Figure 5.1: Sisyphus mechanisms in a) A blue-detuned system where the orientation of the bright and dark states results in optical pumping at the peak of the bright state energy distribution, resulting in cooling. b) A red-detuned system where optical pumping occurs at the trough of the bright state energy distribution, resulting in heating

intensity or polarization landscape.

2. Since the system is Type-II, there also exists a stable dark state in the ground state.

3. Molecules traverse the standing wave and experience a spatially varying coupling to the excited state.

4. The gradient and detunings are engineered such that the molecules are most likely to be excited at an energy maximum. This means a molecule will ride up a slope, lose kinetic energy, and then undergo a transition. For red-detuning, the opposite process occurs where molecules are optically pumped at the bottom of a hill after gaining kinetic energy.

5. In the blue-detuned case, the molecule decays into the dark state where it is unable to ride back down the slope and recover its kinetic energy. At an energy minimum for the bright state, it is either spatially remixed (often with the assistance of a magnetic field or polarization switching).

Table 5.1: Recoil temperatures for select atoms and molecules. SrOH has both the longest wavelength and the heaviest mass, and therefore the lowest recoil limit.

Species	Cooling Wavelength (nm)	Mass (amu)	Recoil Limit (nK)
Ca	423	40	1340
Sr	461	88	512
CaF	606	59	442
CaOH	626	57	429
SrOH	688	105	193

Thus, at every step, the energy removed is equal to the energy difference between the peaks and troughs. For some energy difference U_0, this corresponds to a temperature T:

$$k_B T = U_0. \tag{5.3}$$

As shown in Fig. 5.1, the orientation of the bright and dark states changes, which determines whether the excitation occurs at a peak (trough) to give cooling (heating). The limit to the cooling occurs when U_0 is equal to the recoil energy gained when a photon is spontaneously emitted. For a species with mass m and cooling wavelength λ, this corresponds to a temperature T_{Sisyphus} of

$$T_{\text{Sisyphus}} = \frac{\hbar^2}{M\lambda^2}. \tag{5.4}$$

Table 5.1 shows the recoil limits for a selection of species.

Λ-Enhanced Gray Molasses

One of the experimental techniques we use to sub-Doppler molecules is Λ-Enhanced Gray Molasses (Λ-GM), which is a special kind of Gray Molasses cooling using velocity selective coherent population transfer (VSCPT). A schematic of the cooling is shown in Fig. 5.2 a), where the cooling light forms a $\sigma^+\sigma^-$ polarization gradient implemented in a Type-II configuration and the detunings are adjusted to form a Λ-system.

For the Λ-system, we can write the eigenstates in the momentum basis such that the ground states are $|g_1, p\rangle$, $|g_2, p\rangle$ and the excited state is $|e, p\rangle$. Each ground state is coupled to the excited state by a particular laser frequency that imparts momentum $\hbar k$ in the propagation direction of the light. This results in eigenstates of the form $|g_1, p + \hbar k\rangle$ and $|g_2, p - \hbar k\rangle$ depending on how the relative detunings are chosen. Through the Λ-system, the light couples the excited state to a bright superposition given by

$$|\psi_B\rangle = \frac{1}{\sqrt{2}} \left(|g_1, p + \hbar k\rangle - |g_2, p - \hbar k\rangle \right), \tag{5.5}$$

which results in photon scattering, while the orthogonal state which is dark to the laser light is given by

$$|\psi_D\rangle = \frac{1}{\sqrt{2}} \left(|g_1, p + \hbar k\rangle + |g_2, p - \hbar k\rangle \right). \tag{5.6}$$

Now, take the kinetic energy operator

$$H_{\text{kinetic}} = \frac{\hat{p}^2}{2M}, \tag{5.7}$$

which acts on the dark state to give

$$H_{\text{kinetic}}|\psi_D\rangle = \frac{1}{\sqrt{2}} \left[\frac{(p + \hbar k)^2}{2M} |g_1, p + \hbar k\rangle + \frac{(p - \hbar k)^2}{2M} |g_2, p - \hbar k\rangle \right], \tag{5.8}$$

$$H_{\text{kinetic}}|\psi_D\rangle \not\propto |\psi_D\rangle. \tag{5.9}$$

This shows that the dark state is not generally an eigenstate of the kinetic energy operator since it is composed of two different momentum states. Consequently, as molecules move with finite velocity v, the dark superposition evolves and gains some bright-state character. Moreover, the two-photon detuning δ_Λ shifts the relative energy of the two ground-state components in the rotating frame as shown in [114]. As

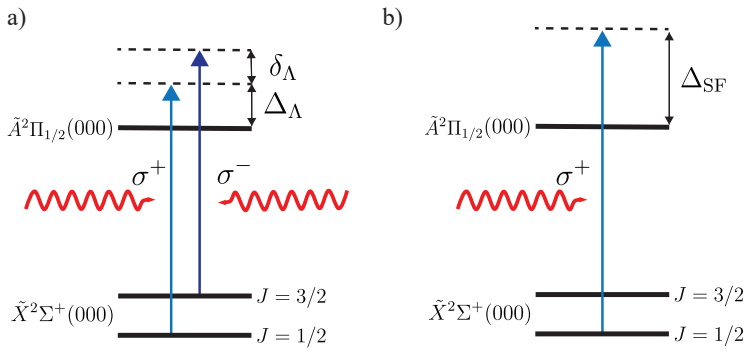

Figure 5.2: Sub-Doppler cooling level diagrams in SrOH. a) Λ-GM cooling, where two frequencies are present to create a Λ-system with a $\sigma^+\sigma^-$ polarization gradient. b) SF cooling, where the frequency component addressing the upper spin-rotation level is removed to prevent inadvertent heating.

a result of this shift, we obtain

$$H_{\delta_\Lambda} = \frac{\hbar\delta_\Lambda}{2}\left(|g_1, p+\hbar k\rangle\langle g_1, p+\hbar k| - |g_2, p-\hbar k\rangle\langle g_2, p-\hbar k|\right). \tag{5.10}$$

The overlap between the bright and dark states is then given by

$$\langle\psi_B|H_{\text{kinetic}} + H_{\delta_\Lambda}|\psi_D\rangle = \frac{1}{2}\left[\frac{(p+\hbar k)^2}{2M} - \frac{(p-\hbar k)^2}{2M}\right] + \frac{\hbar\delta_\Lambda}{2} \tag{5.11}$$

$$= \frac{1}{4M}\left[(p+\hbar k)^2 - (p-\hbar k)^2\right] + \frac{\hbar\delta_\Lambda}{2} \tag{5.12}$$

$$= \frac{\hbar k p}{M} + \frac{\hbar\delta_\Lambda}{2}. \tag{5.13}$$

For a given Λ-configuration, molecules scatter photons from the counter-propagating frequency component if the above expression is non-zero, resulting in cooling. The molecules then become fully dark to the lasers for some momentum p_{dark} such that

$$\frac{\hbar k p_{\text{dark}}}{M} + \frac{\hbar\delta_\Lambda}{2} = 0. \tag{5.14}$$

For a given molecular mass M, we can express this momentum in terms of a velocity

$$v_{\text{dark}} = -\frac{\delta_\Lambda}{2k}. \tag{5.15}$$

For optimal cooling, the molecules stop scattering photons when they are fully cold and at rest. This is achieved by setting the two-photon detuning $\delta_\Lambda = 0$ such that $v_{\text{dark}} = 0$ m/s. We have thus shown that we can utilize the dark state structure present in a type-II system to achieve sub-Doppler cooling through Λ-GM.

Single Frequency Cooling

Single frequency (SF) as shown in Fig. 5.2 b) is similar to Λ-GM, but with the frequency component that addresses the $J = 3/2$ spin-rotation level turned off. The cooling mechanism can be derived and explained in a similar manner to what we described above for Λ-GM, except now the σ^+ component which was previously red-detuned relative to the $J = 1/2$ level is removed to prevent any heating. In some species, SF cooling allows for much colder temperatures [11, 12] when compared to Λ-cooling. In SrOH and CaOH, however, both cooling techniques result in similar temperatures. SF cooling has the advantage that it is simple to account for light shifts in the presence of a high-power infrared laser used to provide optical trapping as described later. However, it is implemented with a much higher detuning $\Delta_{\text{SF}} > \Delta_\Lambda$ and lower scattering rate, which means its performance relies on an already cold cloud of molecules that have had Λ-GM applied to them.

5.1 b) Sub-Doppler Cooling of SrOH

Experimentally, sub-Doppler cooling is implemented right after the MOT is captured and compressed. The magnetic field gradient is turned off and the overall detunings of the MOT light are shifted blue, where a series of AOMs switch to produce the necessary frequency components and polarizations of light. Details of this process are described using Figs. 5.9-5.12 later in the chapter. The figure of merit for the effectiveness

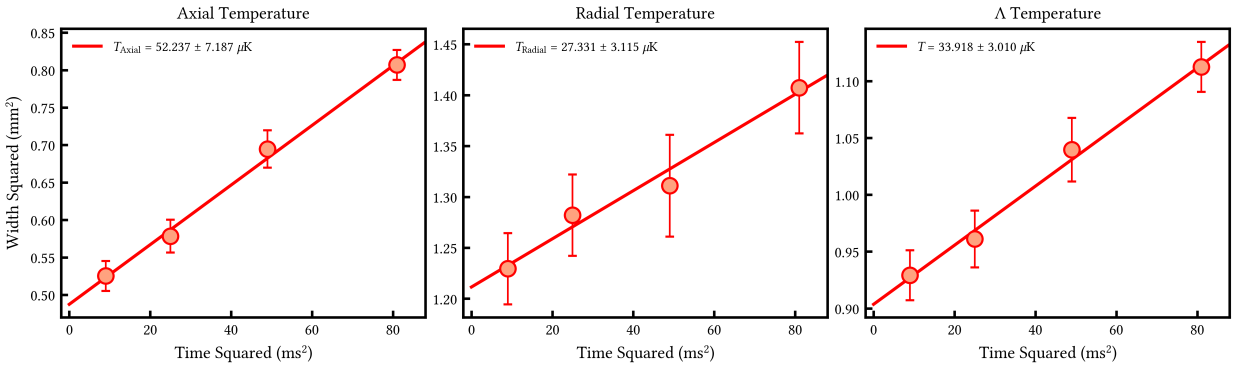

Figure 5.3: Time-of-flight data for Λ-GM showing the minimum obtained temperature.

of the cooling is the final temperature of the molecular cloud after the cooling is applied. We first describe how these temperatures are measured via time-of-flight (TOF) before presenting the relevant data.

Time-of-flight Measurements

The temperature of the molecular cloud can be measured by allowing it to ballistically expand for different time periods and measuring its size. Once SD cooling is applied, any cooling or trapping light is turned off and the molecules are allowed to expand for some time. Following this, the cloud is "resonantly imaged" using the light resonantly addressing the $\tilde{X}^2\Sigma^+(000) \rightarrow \tilde{A}^2\Pi_{1/2}(000)$ transition along with every repumper. For temperature measurements, it is crucial to image for as little time as possible as the photon-scatters can further heat the molecules and result in inaccurate data. The imaging occurs for 2 ms, where an EMCCD detects 611 nm photons decaying from $\tilde{B}^2\Sigma^+(000) \rightarrow \tilde{X}^2\Sigma^+(000)$. This is the decay that is addressed by our first repumper, and corresponds to 1 in every 20 emitted photons. Following this, the root mean square (RMS) widths are extracted in the radial and axial directions. Using kinematics, one finds the temperature of the cloud T to be related to its RMS width σ as

$$\sigma(t)^2 = \sigma_0^2 + k_B T t^2/m, \tag{5.16}$$

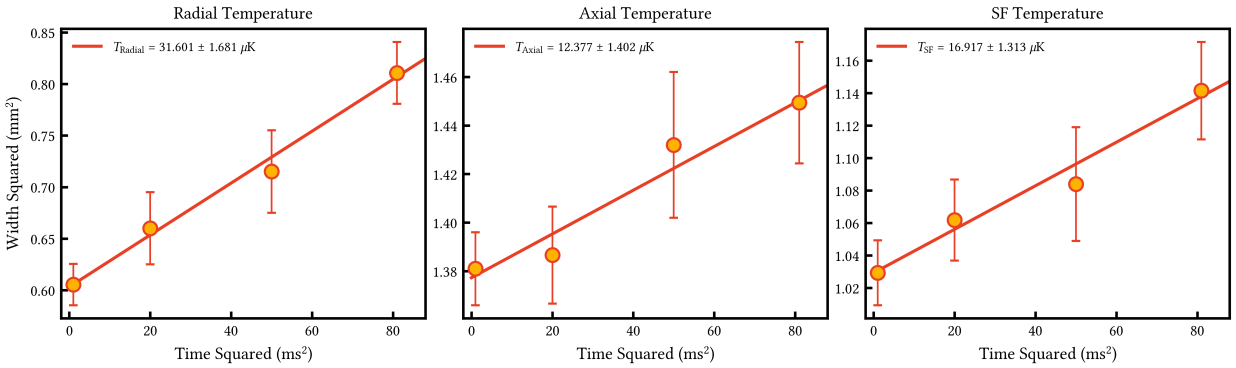

Figure 5.4: Time-of-flight data for SF cooling showing the minimum obtained temperature.

where σ_0^2 is the initial cloud size, T is the fitted temperature, t is the expansion time, k_B is the Boltzmann constant, and m is the mass of the particle. The above equation is linearized by squaring the dependent and independent terms such that extracting the temperature becomes as simple as fitting the slope of a straight line to the data. The radial and axial widths $\sigma_\perp$ and $\sigma_\parallel$ are fit to give a final temperature $T = T_\parallel^{2/3} T_\perp^{1/3}$.

Λ-GM and SF Results

Fig. 5.3 shows time-of-flight data to measure the lowest achieved temperature through Λ-GM, and Fig. 5.5 shows the temperature dependence on the two-photon detuning δ_Λ and overall detuning Δ_Λ varied with the cooling light intensity I_Λ and the temperature T_Λ as a function of cooling time t_Λ. Under optimal conditions the cooling light is applied for $t_\Lambda = 2$ ms, considerably longer than the characteristic cooling time of $\tau_\Lambda = 0.19(1)$ ms, shown in Fig. 5.5 c). A minimum temperature of 34(3) μK is achieved with $\Delta_\Lambda = 13.2$ MHz, $\delta_\Lambda = -0.4$ MHz and an intensity $I_\Lambda = 3.7$ mW/cm^2. Fig. 5.4 shows time-of-flight data for SF cooling, where we achieve a minimum temperature of $T_{SF} = 16.9(1.3)$ μK with $\Delta_{SF} = 96$ MHz and an intensity $I_{SF} = 9.5$ mW/cm^2. The SF cooling performance plateaus at high intensity and detuning.

Although sub-Doppler cooling results in nearly a two-order-of-magnitude reduction in molecular cloud temperature, it does not result in temperatures that approach the recoil limit of $T_{recoil} = 193$ nK for SrOH. In reality, the dark states are not perfect as the molecule is not an ideal three-level system,

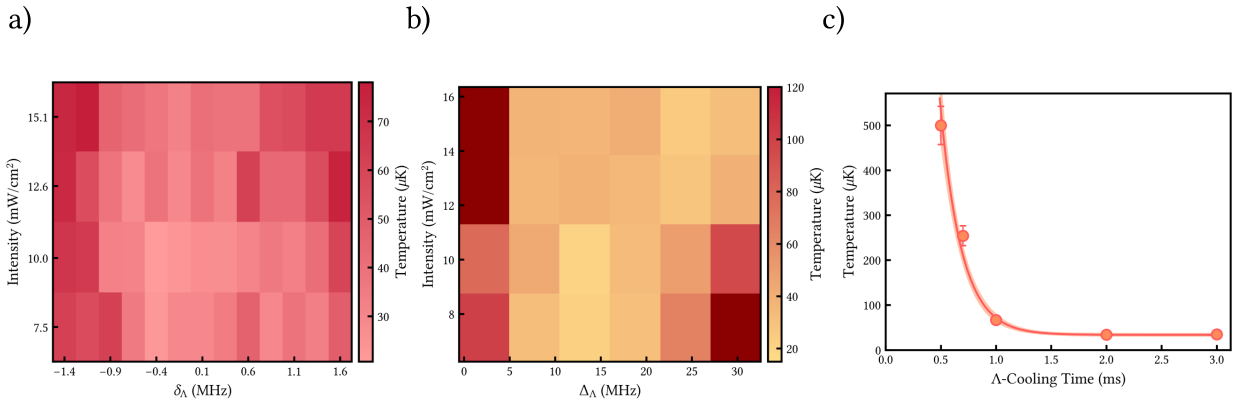

Figure 5.5: Scans of various Λ-GM parameters while optimizing molecular temperature. a) 2D scan of the two-photon detuning δ_Λ and intensity. b) 2D scan of the overall detuning Δ_Λ and intensity. c) Temperature as a function of cooling time.

which results in some heating due to photon scattering.

5.2 Blue-Detuned Conveyor Belt MOT

Having cooled the molecules down to ensure a high enough η to load the ODT, the loading efficiency can be further improved by shrinking the trapped molecular cloud to better spatially mode match with the optical trap. For an ODT with a 50 μm waist, a cloud size $\sigma = 500$ μm occupies too high a volume to capture an appreciable fraction of the molecules. This issue is addressed by using a blue-detuned conveyor belt MOT (CB MOT) which provides rapid compression without appreciable loss or heating. While blue-detuned MOTs have been employed in molecular systems in the past [80], the "1+2" frequency configuration of the CB MOT was recently discovered and enabled record molecular MOT densities and ODT transfer efficiencies [82, 83].

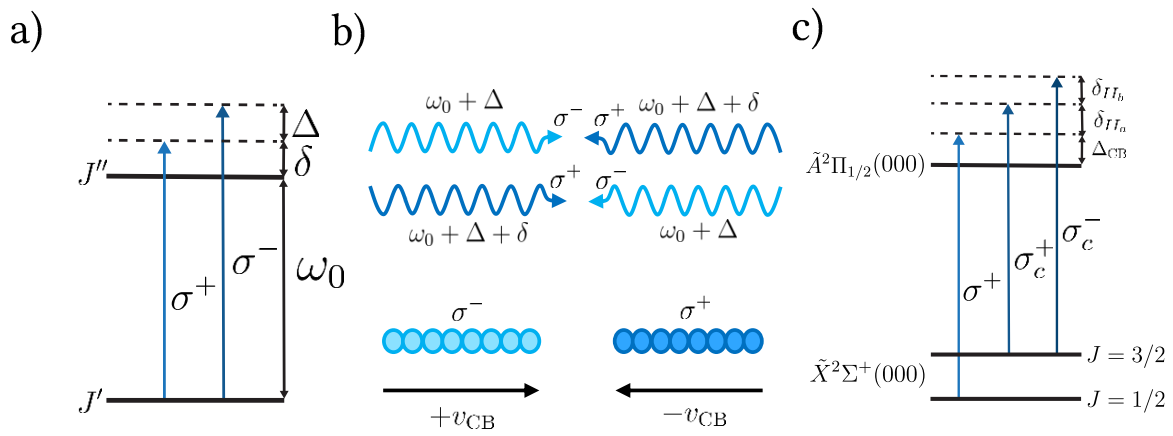

Figure 5.6: CB MOT Mechanism. a) Toy model used to describe the combining of circularly polarized light to form the moving lattices. b) Illustration of the formation of the two conveyor belts which shuttle the molecules to the center of the trap. c) Level diagram showing the experimentally implemented CB MOT scheme in SrOH.

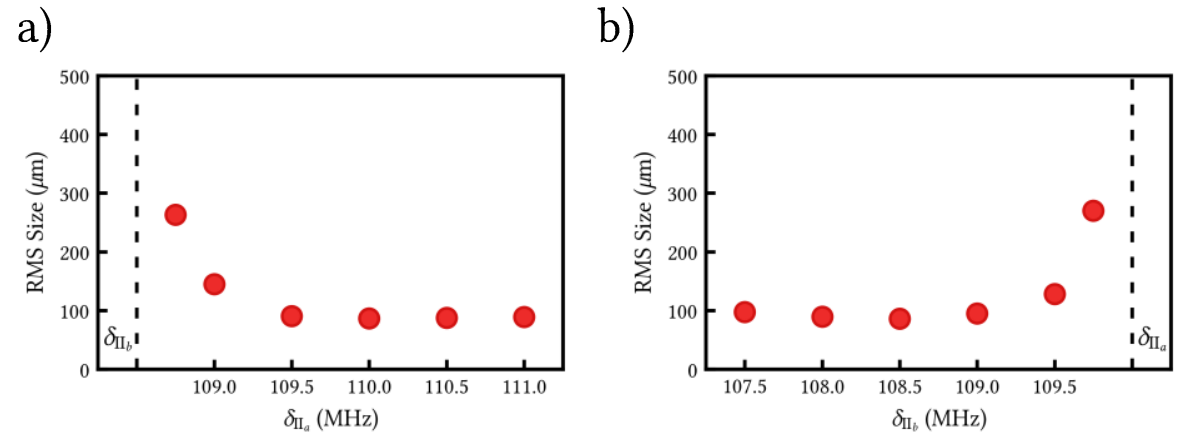

Figure 5.7: CB MOT two-photon detuning scans. a) RMS width σ_{CB} as a function of δ_{II_a}. b) RMS width as a function of δ_{II_b}.

5.2 a) Principles of a Conveyor Belt MOT

To describe the principles of a CB MOT, it is useful to picture a simple $J'' = 1 \rightarrow J' = 0$ system as shown in Fig. 5.6 a). We illustrate the cooling below, closely following Ref. [115]:

1. Take two closely spaced frequency components $\omega_I = \omega_0 + \Delta$ and $\omega_{II} + \omega_0 + \Delta + \delta$ with opposite

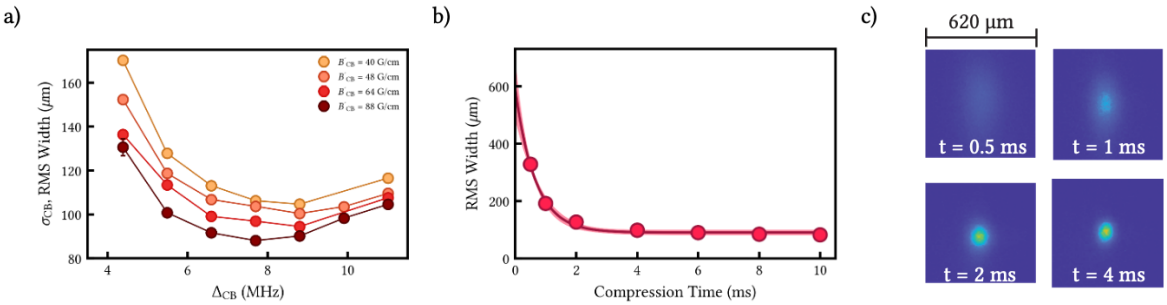

Figure 5.8: CB MOT compression as a function of experimental parameters. a) Size as a function of overall detuning Δ_{CB}. b) CB MOT images as a function of magnetic field gradient ramp time. c) CB MOT images as a function of magnetic field gradient ramp time.

circular polarizations.

2. The two σ^- lasers form a σ^- standing wave that travels at a velocity $+v_{CB} = \frac{\delta}{2\omega_l}c$ where c is the speed of light and the two σ^+ lasers form a standing wave traveling in the opposite direction with velocity $-v_{CB}$ shown in Fig. 5.6 b).

3. Due to the presence of a magnetic field gradient, the molecules preferentially scatter from one of the standing waves depending on their position relative to the center of the trap to provide a strong restoring force.

4. For a molecule with $z > 0$ and a positive magnetic field gradient, molecules are shifted closer to resonance with the σ^+ light and are sub-Doppler cooled into the frame of the moving lattice. This is the conveyor belt.

5. The molecules are dropped off at the center of the trap where no preferential scattering occurs, and are cooled further via gray molasses.

As a result of these steps, which are illustrated in Fig. 5.6, the molecular cloud is rapidly compressed while maintaining low, sub-Doppler temperatures.

5.2 b) Conveyor Belt MOT of SrOH

To implement the CB MOT, the molecules are cooled via Λ-GM after the initial capture of molecules into the MOT using the frequency configuration shown in Fig. 5.6c). Following this, the magnetic field gradient is switched from RF to DC using a solid-state relay (Crydom D1D40). Rather than driving the relay directly from the experimental control system (Cicero), a signal generator (Siglent SDG2122X) operating in burst mode is used as an intermediary: Cicero sends a trigger pulse to the signal generator, which in turn outputs a 100 ms gate signal to switch on the DC current. This scheme serves as a safety interlock, ensuring that if the control system restarts unexpectedly, the DC current is not left on indefinitely. At the same time, the frequency components are added by switching to the CB MOT configuration on the AOD board in conjunction with all the repumpers to provide the maximum photon budget. To compress the molecules, the DC magnetic field is ramped via a high bandwidth DC power supply (Delta Elektronika SM120-50) while the MOT beam intensity is decreased for reasons identical to what was discussed in Chapter 4 regarding the RF MOT. These parameters are ramped in a time ≈ 10 ms where ∼50% of the molecules survive (the rest are lost due to loss to vibrational dark states) where

$$\frac{N_t}{N_0} = e^{-\frac{\Gamma_{\text{Scatter}} t}{\bar{\gamma}}}, \tag{5.17}$$

$$0.5 = e^{-\frac{\Gamma_{\text{Scatter}} * 10\ \text{ms}}{14600}}, \tag{5.18}$$

$$\Gamma_{\text{Scatter}} = \frac{\ln(2) * 14600}{10\ \text{ms}}, \tag{5.19}$$

$$\Gamma_{\text{Scatter}} \approx 1\ \text{MHz}. \tag{5.20}$$

This is consistent with measured scattering rates during slowing and trapping with all repumps present. The frequency component detunings δ_{II_a} and δ_{II_b}, overall detuning Δ_{CB}, magnetic field gradient dependence $\mathscr{B}_{\text{CB}}$, and the starting and ending intensities $I_{\text{CB}_{\text{initial}}}$ and $I_{\text{CB}_{\text{final}}}$ were scanned. Setting $\delta_{II_a} = -0.9$ MHz,

$\delta_{II_b} = 0.1$ MHz, $\Delta_{\mathrm{CB}} = 7.7$ MHz, a starting intensity $I_{\mathrm{CB}_{\mathrm{initial}}} = 14.0$ MHz and a final intensity of $I_{\mathrm{CB}_{\mathrm{final}}} = 8.9$ MHz, we measure an optimal size $\sigma_{\mathrm{CB}} = 83(1)$ μm and a temperature $T_{\mathrm{CB}} = 91(4)$ μK. These results are summarized in Figs. 5.7 and 5.8.

5.2 c) AOD Board

The AOD board is the optics setup that deals with switching between the various frequency configurations for the different trapping and cooling stages. The overall frequency of the MOT laser is swept by a double pass AOD setup whose alignment procedure is described in Appendix A. Below in Figs. 5.9-5.12, we show the configurations corresponding to the different trapping and cooling techniques.

5.3 Conclusion

We have demonstrated the cooling of a cloud of SrOH to sub-Doppler temperatures, as well as the compression of the cloud to achieve better spatial overlap with a tightly focused ODT laser. These techniques circumvent the issues of the relatively high temperature and large trap sizes of RF red-MOTs. As such, these efforts are vital to efficiently loading an ODT, as discussed in the next Chapter, toward the ultimate goal of conducting a precision measurement with SrOH.

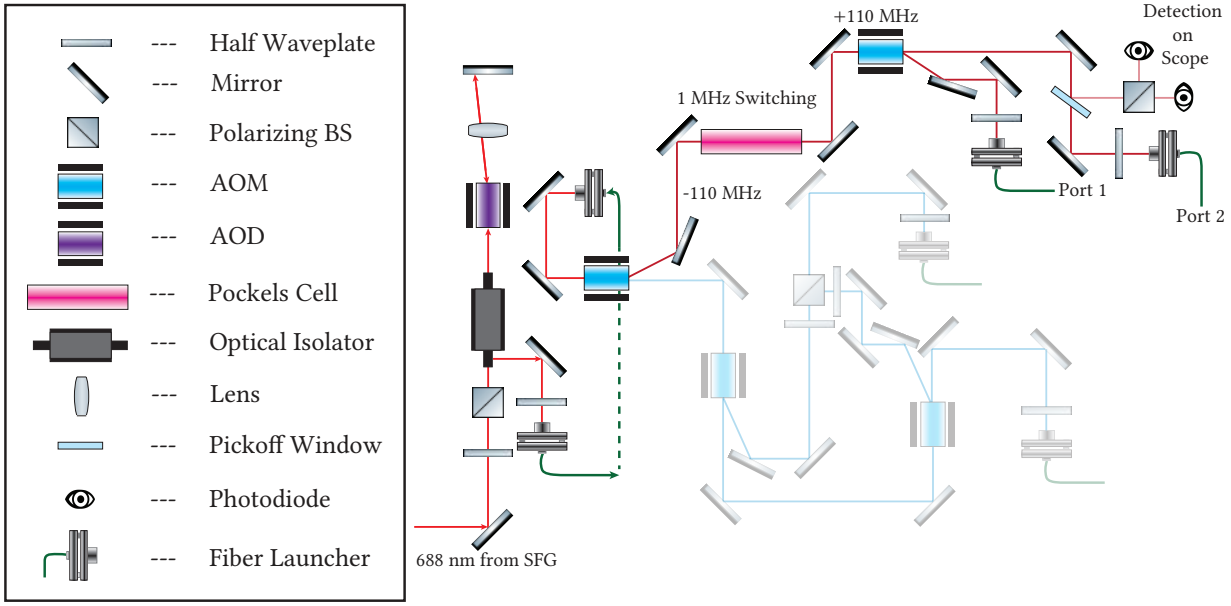

Figure 5.9: Red MOT setup.

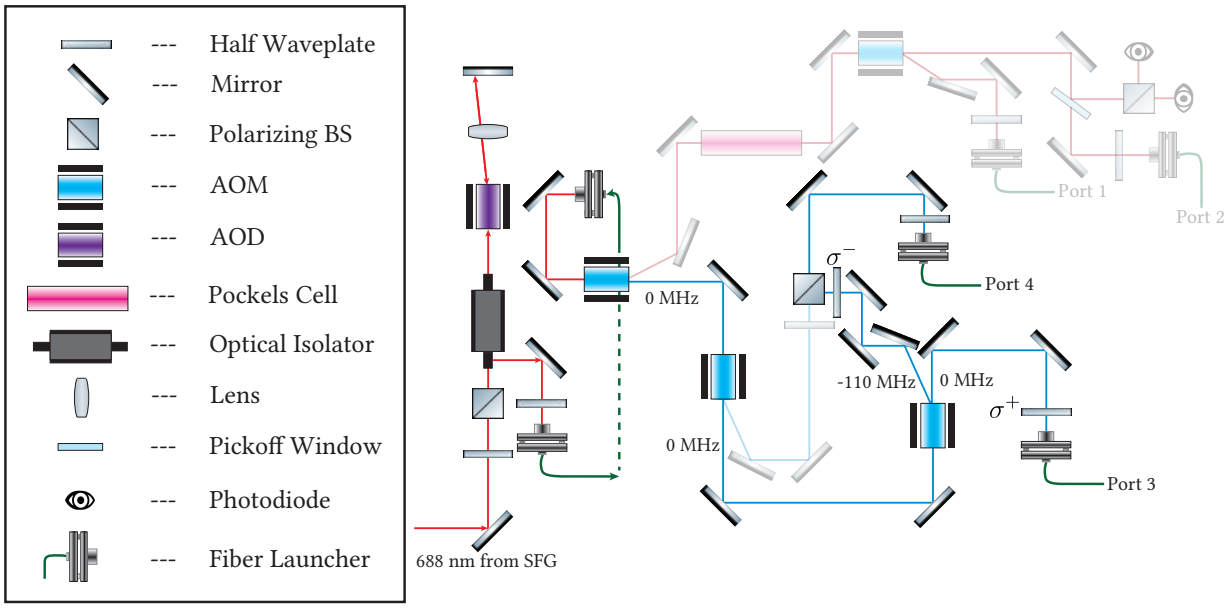

Figure 5.10: Λ-GM setup.

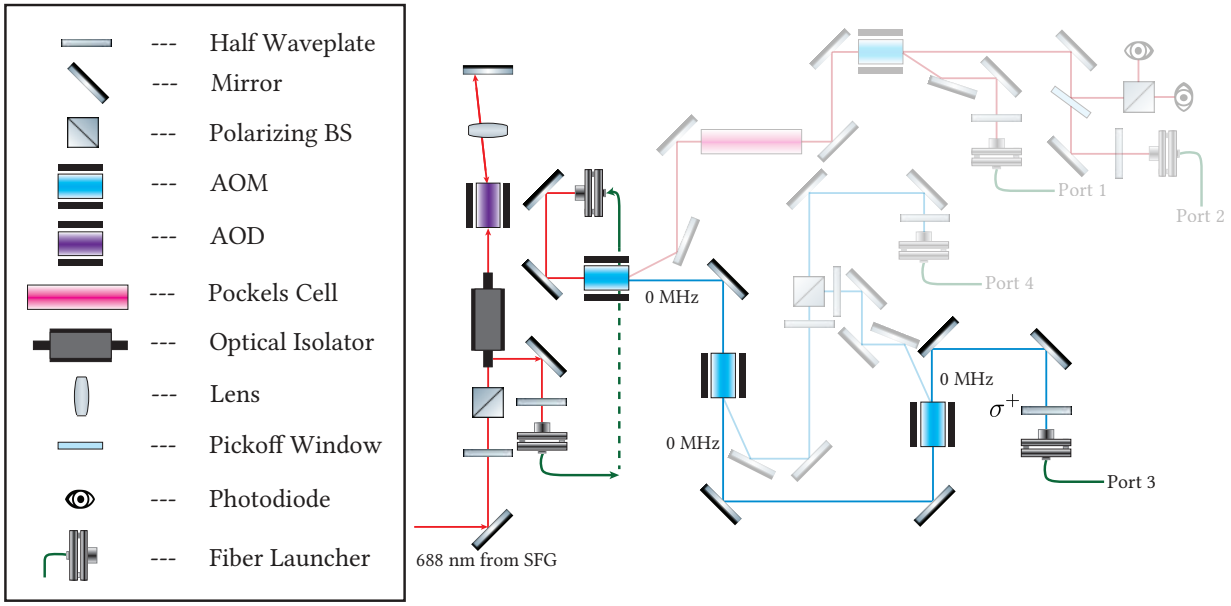

Figure 5.11: SF cooling setup.

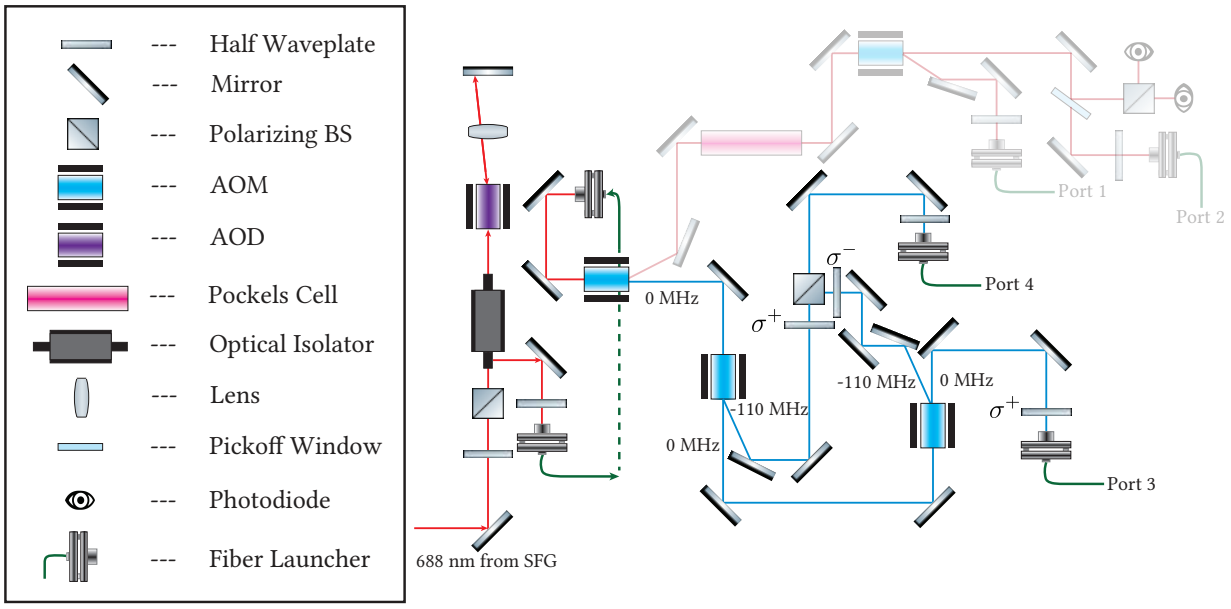

Figure 5.12: CB MOT setup.

Water, fire, air and dirt,

***[Redacted]** magnets, how do they work?*

And I don't wanna talk to a scientist

Y'all [people] lying, and getting me [upset]

Insane Clown Posse [Altered]

6

An Optical Dipole Trap of SrOH

Rapid growth in the field of molecular laser cooling has resulted in several optically trapped molecular species [8, 9, 11, 12]. Subsequent demonstrations of loading lattices and tweezer arrays [13–15, 109] have turned aspirations of harnessing the "rich internal structure" of molecular systems for quantum science into a reality. Several key results, including demonstrations of dipolar spin-exchange and entanglement [16, 116, 117], collisional shielding [118, 119], measurements of internal state dynamics and long qubit coherence times [120], and the development of precision measurement methods [18], have advanced the field of quantum science with molecules. An ODT is an ideal environment to eventually conduct such a measurement, allowing for large numbers of trapped neutral molecules compared to beam or trapped

ion experiments, long science state lifetimes, and a small volume over which to control systematic effects.

Having described the sub-Doppler cooling and CB MOT of SrOH in the previous Chapter, we now discuss an ODT of SrOH starting with its foundational principles in Sec. 6.1 after which we describe the ODT setup and report our experimental results in Sec. 6.2. Finally, we discuss collisions in a highly dense ODT in Sec. 6.3.

6.1 Principles of Optical Dipole Trapping

Optical dipole traps are composed of tightly focused, far-detuned light and rely on the electric dipole force to provide trapping. This results in weaker traps compared to MOTs or magnetic traps, but with confinement that does not depend on specifics of the ground state energy structure. As such, the molecular energy levels can be measured and manipulated over timescales ranging from 100s of milliseconds to several seconds. This is vital for conducting a wide range of science applications including precision measurements between the ground vibrational states in SrOH, i.e. the dark matter search described within the pages of this thesis. Derivations of the trapping force in an ODT can be found in Refs. [100]. Below we discuss some important parameters that are visualized in Fig. 6.1. Assuming a Gaussian beam, the intensity is given by

$$I(r,z) = I_0 \left(\frac{w_0}{w(z)}\right)^2 \exp\left(\frac{-2r^2}{w^3}\right), \tag{6.1}$$

where z is the distance from the center of the beam along its central axis, r is the distance away from this axis, and I_0 is the intensity of the beam at its waist w_0. In particular, w_0 is the width of the beam at its focus, and $w(z)$ is the size of the beam along its axis at some distance from the focus. The Rayleigh range for the beam is given by

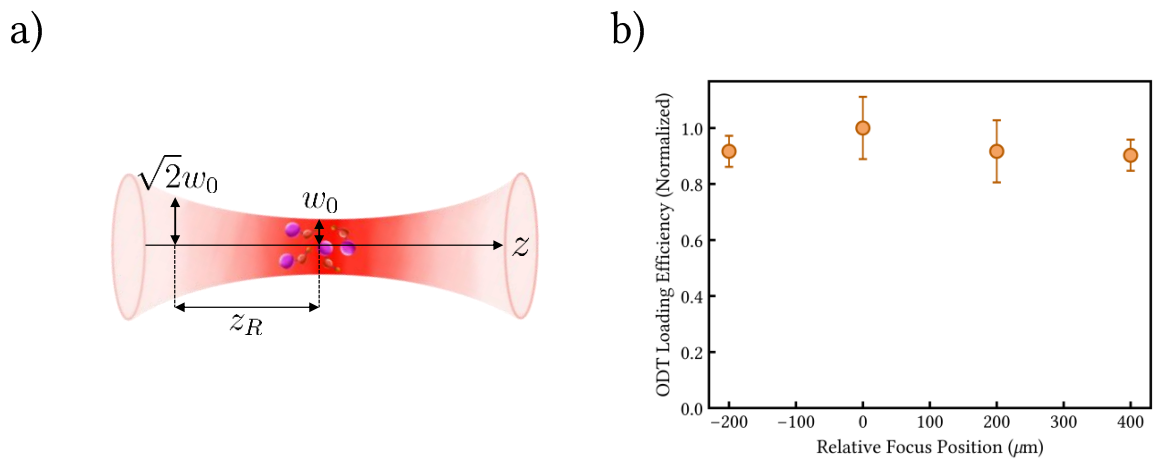

Figure 6.1: ODT parameters. a) Schematic of a Gaussian beam with the Rayleigh range z_R and beam waist w_0 labeled. b) Measurement of normalized ODT loading efficiency as a function of focus position in the axial direction, where the efficiency is uniform within a Rayleigh range. The y-axis represents the loading efficiency from the CB MOT which is normalized to the peak value.

$$z_R = \frac{\pi w_0^2}{\lambda}, \tag{6.2}$$

and depends on the beam waist and the wavelength of light λ. It is defined as the distance along the beam axis over which the beam intensity drops by a factor of 2 and the beam size increases by a factor of $\sqrt{2}$, such that we can write the spot size

$$w(z) = w_0\sqrt{1 + \left(\frac{z}{z_R}\right)}. \tag{6.3}$$

For example, a 1064 nm beam with a waist of ~50 μm has a Rayleigh range of ~1 cm. This is a useful metric as it determines the precision tolerance when aligning the trap in the axial direction by moving its focus; within a Rayleigh range, the beam looks roughly "cigar shaped", so that overlapping the molecules within this region yields roughly the same trapping as shown in Fig. 6.1 b) where the loading efficiency was taken while the focus of the ODT was tuned by moving a lens on a micrometer translation stage.

In the approximation of a harmonic potential, the trap depth and scattering rate are given by

$$U_{\text{Dipole}} \propto \frac{\Gamma}{\Delta} I, \tag{6.4}$$

$$\Gamma_{\text{Dipole}} \propto \left(\frac{\Gamma}{\Delta}\right)^2 I, \tag{6.5}$$

where Δ is the detuning between the trap light and the internal molecular states, and Γ is the natural linewidth of the available transitions. We can write

$$\Gamma_{\text{Dipole}} \propto \frac{U_{\text{Dipole}}}{\Delta}. \tag{6.6}$$

In order to have a high enough trap depths to efficiently load molecules, and low scattering rates to realize high trap lifetimes, it is important to maintain a high detuning and intensity. For SrOH, 1064 nm is an ideal choice as systems with 50 W are readily available and it is far detuned from any allowed optical transitions.

6.2 ODT Experimental Results

The ODT light is generated by a 1064 nm seed (RIO ORION, Luna Innovations) input to a 50 W Ytterbium fiber amplifier (YFA-SF-1064-50-CW) to finally produce ~18 W of power in the vacuum chamber. The ODT setup is shown in Fig. 6.2, where the light is fiber coupled into a PCF after which it is expanded and focused into the MOT chamber. A small fraction of the beam is picked off to be monitored to provide power stabilization using a PID control loop.

To load the ODT, we first start with a red MOT that is captured and ramped for 15 ms each as described in Chapter 4. Following this, Λ−GM cooling is applied for 2 ms after which the molecules are compressed for 16 ms in the CB MOT and held for an additional 2 ms. The DC magnetic field is ramped down for 1 ms during which the ODT light is turned on. This is followed by 5 ms of GM cooling after which the trap is held with no repumps on for an additional 30 ms to allow for any untrapped molecules to fall, after which the molecules in the ODT are imaged with Λ-GM cooling light. So far, we have demonstrated traps with up

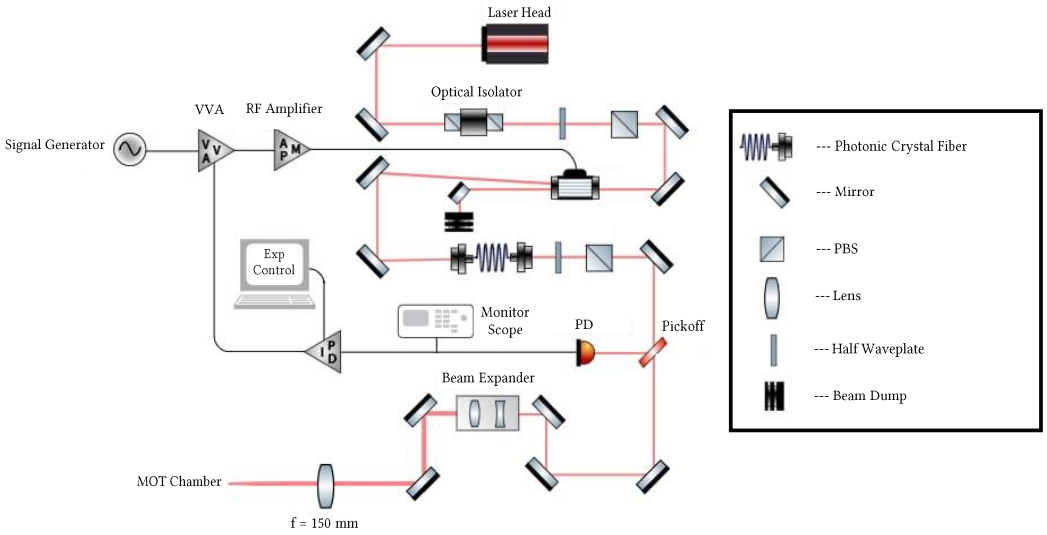

Figure 6.2: Schematic of the ODT optics and PID setup.

to ~22,000(3000) molecules with the help of transverse cooling (Chapter 7). We expect this to improve by an order of unity with optimization of the current experimental setup, without adding any new hardware or methods.

6.2 a) Science State Lifetimes

We measure the lifetimes of molecules in the ODT for the vibrational ground state as well as the vibrationally excited "science states" including $\tilde{X}^2\Sigma^+(010)$, $\tilde{X}^2\Sigma^+(200)$ and $\tilde{X}^2\Sigma^+(03^10)$. The $\tilde{X}^2\Sigma^+(010)$ state is proposed as an eEDM science state candidate [71] due to its closely spaced parity doublet structure, while the latter two are what will be used for the SrOH UDM measurement [25] due to their differential sensitivity to the oscillation of μ as described in Chapter 1.

ODT Lifetime Experimental Data

When molecules are initially loaded into the ODT, they predominantly occupy the $\tilde{X}^2\Sigma^+(000)$. After loading, we can then move molecules to other states of interest. Following this, the trap is held for variable periods of time (up to 2 s) after which the trap number is recorded. The number as a function of time is plotted and a decaying exponential is fit where the characteristic time is extracted to provide the lifetime. The lifetimes for all four states are shown in Fig. 6.3. First, the lifetime of $\tilde{X}^2\Sigma^+(000)$ is measured to be $\tau_{(000)} = 1.5(1)$ s, predominantly limited by blackbody radiation (BBR) excitations out of the ground state which also limits the science state lifetimes reported below. This lifetime was taken before the ODT waist was increased from $w_0 \sim 23$ μm to $w_0 \sim 39$ μm and is limited by two-body loss via collisions, which is discussed in Sec. 6.3.

The $\tilde{X}^2\Sigma^+(010)$ state resides in the optical cycle, and can thus be prepared by turning off the repump laser addressing the $\tilde{X}^2\Sigma^+(010) \rightarrow \tilde{B}^2\Sigma^+(000)$ transition for 60 ms, where the molecule population piles up in this now "dark" vibrational state. The $\tilde{X}^2\Sigma^+(200)$ state is similarly prepared but by turning off the $\tilde{X}^2\Sigma^+(200) \rightarrow \tilde{B}^2\Sigma^+(100)$ repump. After state preparation, the main slowing light as well as every repump besides the one addressing the science state is turned on for 6 ms to push away any molecules occupying other ground states. The ODT is then held for a variable amount of time with no repumps on after which it is imaged for 100 ms using Λ−GM imaging. We measure lifetimes of $\tau_{(010)} = 320(30)$ ms and $\tau_{(200)} = 135(17)$ ms as shown in Fig. 6.3.

For the $\tilde{X}^2\Sigma^+(03^10)$ state, a separate optical pumping step is needed as it does not reside in our photon cycling scheme. Following the work done in [12], the molecules are first prepared in the $\tilde{X}^2\Sigma^+(010)$ state as described above, but for 200 ms. During this time the $\tilde{X}^2\Sigma^+(010) \rightarrow \tilde{A}(030)\kappa^2\Sigma_{1/2}$ transition is simultaneously driven using a tunable CW ring dye laser (Coherent 899) delivering 50 mW of power, after which the slowing light and every repump laser are turned on for 6 ms. This results in the molecules predomi-

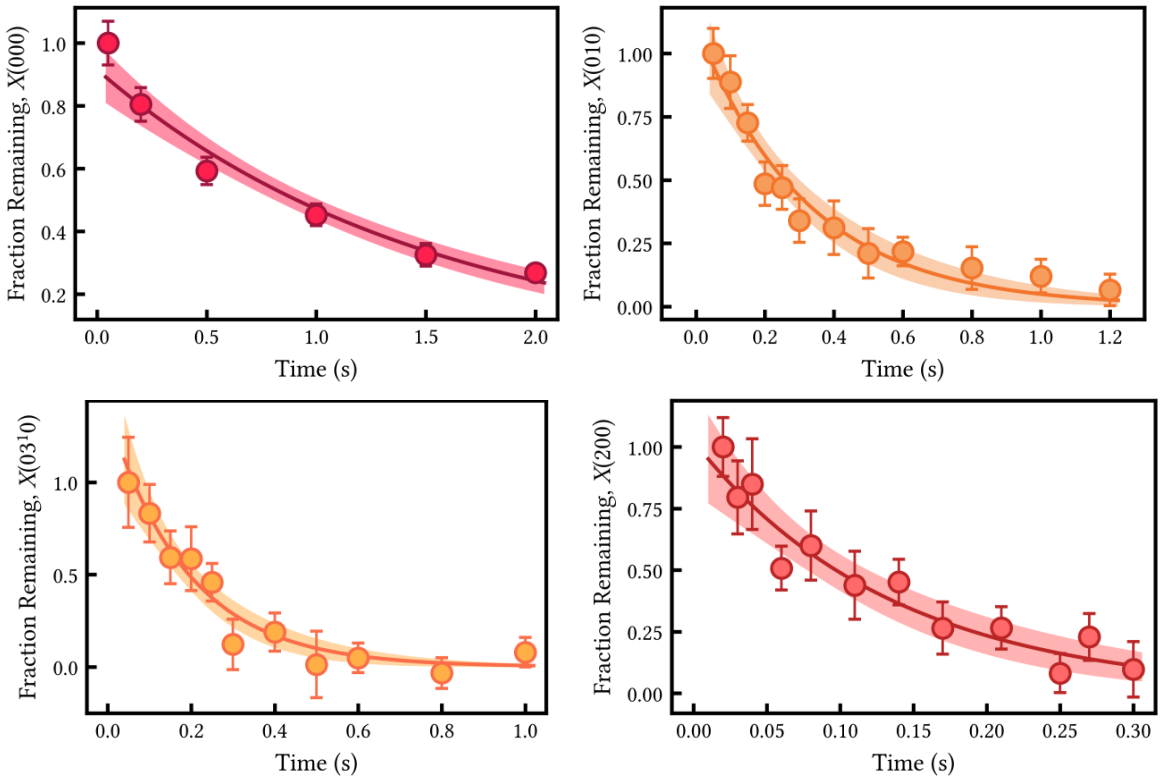

Figure 6.3: Vibrational state lifetimes in the ODT.

nantly occupying $\tilde{X}^2\Sigma^+(03^10)$, which is the main decay from $\tilde{A}(030)\kappa^2\Sigma_{1/2}$. Following this, the molecules are again held for variable times without repumps on, after which they are imaged in a similar way as above, but this time with the inclusion of a single-frequency tunable Ti:Sapphire ring laser (Sirah Matisse) delivering 100 mW of power to drive the $\tilde{X}^2\Sigma^+(03^10) \rightarrow \tilde{A}(010)\kappa^2\Sigma_{1/2}$ transition and bring the molecules back into the optical cycle. The lifetime is measured to be $\tau_{(03^10)} = 190$ ms as shown in Fig. 6.3.

ODT Lifetime Theory

As previously mentioned, the ODT lifetimes are primarily limited by excitations due to blackbody photons, where the BBR depends on the environmental temperature. Following Ref. [121, 122], the spontaneous decay rate between states i and j can be written as

$$\Gamma_{\text{Decay},ij} = \frac{\omega_{ij}^3}{3\pi\epsilon_0\hbar c^3}\langle i|\mu|j\rangle,$$

where ω_{ij} are the frequencies between states i, j with transition dipole moment $\langle i|\mu|j\rangle$ which can be determined through theoretical calculations of the potential energy surfaces for the relevant vibrational modes. Given the level of mathematical rigor in this thesis, such a calculation is clearly out of the scope and has been done by our talented theory collaborators and presented in [123]. The spontaneous decay rate generally describes the decay between two states; this is then weighed by the blackbody occupation number

$$f(\omega, t) = \frac{1}{e^{\hbar\omega_{i,j}/k_B T} - 1}, \tag{6.7}$$

which describes the average number of black body photons which occupy a mode with energy $\omega_{i,j}$ at some temperature T. To get the BBR loss rate, we weight the spontaneous decay by this occupation for a given temperature, such that

$$\Gamma_{\text{BBR}} = \sum_{i\neq j} \Gamma_{\text{Decay}} \frac{1}{e^{\hbar\omega_{i,j}/k_B T} - 1}. \tag{6.8}$$

The transition dipole matrix elements have contributions from both vibrational and rotational transitions. Based on theory, the rotational contributions are calculated to be constant for all transitions and thus only vibrational contributions are considered. We can then express

$$\begin{aligned}\langle i|\mu|j\rangle &= |\langle v_{1i}, v_{2i}, \ell_i, 0|\vec{\mu}|v_{1j}, v_{2j}, \ell_j, 0\rangle|^2 \\ &\approx \left|\frac{d\vec{\mu}}{dQ_1}\langle v_{1i}|Q_1|v_{1j}\rangle + \frac{d\vec{\mu}}{dQ_2}\langle v_{2i}, \ell_i|Q_2|v_{2j}, \ell_j\rangle\right|^2,\end{aligned} \tag{6.9}$$

where $Q_{1,2}$ are the vibrational normal coordinates for $v_{1,2}$, respectively. Approximating the system as a 2D harmonic oscillator, we can rewrite

Table 6.1: Lifetimes for different vibrational states including spontaneous decay, blackbody radiation (BBR), and measured values [12].

State	τ_{decay} (ms)	τ_{BBR} (ms)	τ_{Theory} (ms)	τ_{Exp} (ms)
$\tilde{X}^2\Sigma^+(200)$	178	699	135	135(17)
$\tilde{X}^2\Sigma^+(010)$	1117	896	427	320(30)
$\tilde{X}^2\Sigma^+(03^10)$	408	528	214	190(30)

$$|\langle v_1+1|Q_1|v_1\rangle|^2 = \tfrac{1}{2}(v_1+1) \tag{6.10}$$

$$|\langle v_2+1,\ell\pm1|Q_2|v_2,\ell\rangle|^2 = \tfrac{1}{4}\big(1+\delta_{\ell,0}+\delta_{\ell\pm1,0}-\delta_{\ell,0}\delta_{\ell\pm1,0}\big) \tag{6.11}$$

$$\times\Big(\tfrac{v_2\pm\ell}{2}+1\Big). \tag{6.12}$$

where the remaining unknowns $\frac{d\vec{\mu}}{dQ_1}$ and $\frac{d\vec{\mu}}{dQ_2}$ have been calculated by the aforementioned talented collaborators Lan Cheng and Chaoqun Zhang of Johns Hopkins University. The overall lifetime can be written as

$$\frac{1}{\tau} = \frac{1}{\tau_{\text{Decay}}} + \frac{1}{\tau_{\text{BBR}}} + \frac{1}{\tau_{\text{Vacuum}}}. \tag{6.13}$$

The first two terms are what we can calculate using the aforementioned derivation, and the vacuum lifetime $\frac{1}{\tau_{\text{Vacuum}}}$ is estimated to be 3 s based on the mean free path of gas particles in a $10^{-10}-10^{-9}$ Torr environment. As this lifetime is the largest, any uncertainty in it does not greatly affect the final calculation. From Table 6.1, we compare the predicted lifetimes with what was measured in the experiment. The $\tilde{X}^2\Sigma^+(200)$ and $\tilde{X}^2\Sigma^+(03^10)$ measurements agree to within 1σ, whereas the measured $\tilde{X}^2\Sigma^+(010)$ lifetime is 3σ away from the theory due to the large uncertainty of $10\%-30\%$ on the calculated values of $\frac{d\vec{\mu}}{dQ_1}$ and $\frac{d\vec{\mu}}{dQ_2}$.

6.3 Two-Body Loss Through Collisions

Transverse cooling of the molecular beam results in an ODT with $> 10^4$ molecules, representing an order of magnitude increase. This results in large enough densities to observe collisional loss in the trap, reducing the effective lifetime of the molecules. The loss can be circumvented by increasing the trap waist and volume, but would require more power in order to maintain a high enough trap depth U_0 to sufficiently load the ODT.

6.3 a) ODT Volume and Temperature

In order to investigate the effect of collisions in the ODT, we must measure the lifetime of the trap. In the case of two-body loss via collisions between molecules, quantifying this process and extracting a value for the two-body loss rate coefficient β requires knowing the density of the trap. As such, we must characterize the ODT trap volume as we already have a calibrated measurement of the trap number. The effective trap volume can be written as:

$$V_{\text{eff}} = \left(\frac{4\pi k_B T}{m}\right)^{3/2} \frac{1}{\omega_r^2 \omega_z}, \tag{6.14}$$

where k_B is the Boltzmann constant, T is the trap temperature, m is the mass of SrOH, and ω_r and ω_z are the radial and axial trap frequencies, respectively. We can rewrite the trap frequencies in terms of the trap waist w_0, Rayleigh range z_R, and trap depth $T_{\text{depth}} = U_0/k_B$ such that

$$V_{\text{eff}} = \left(\frac{4\pi k_B T}{m}\right)^{3/2} \frac{m w_0^2}{4U_0} \sqrt{\frac{m z_R^2}{2U_0}}. \tag{6.15}$$

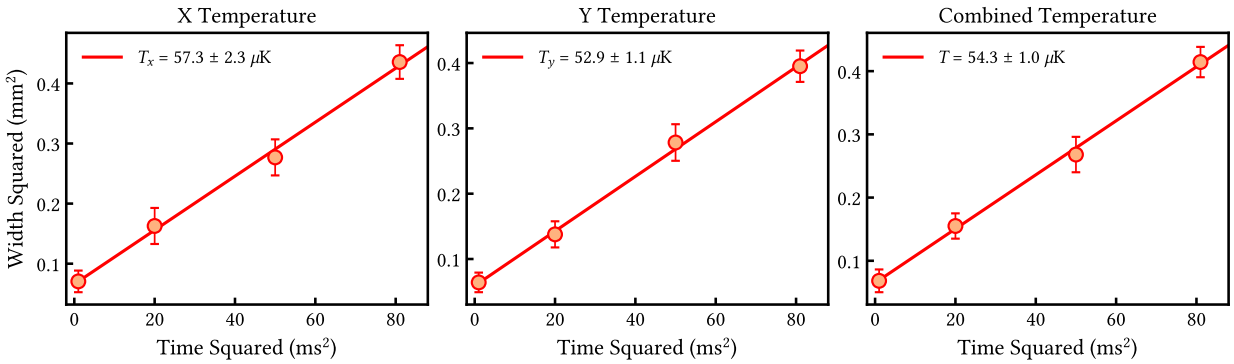

Figure 6.4: Time-of-flight data to measure the temperature of the trapped molecules in the ODT.

With an ODT laser power of $P_{\mathrm{ODT}} \sim 18.4$ W and a trap waist of $w_0 \sim 39$ μm, the trap depth is calculated to be $U_0/k_B \sim 0.5$ mK based on estimations of the polarizability at the trapping light wavelength of $\lambda = 1064$ nm. The expression then simplifies to

$$V_{\mathrm{eff}} = \sqrt{2}\,\pi^{5/2}\frac{(k_B T)^{3/2} w_0^4}{\lambda U_0^{3/2}}. \tag{6.16}$$

To measure the temperature, we employ the same time-of-flight technique as discussed in the previous chapter when investigating sub-Doppler cooling. This results in $T \sim 54$ μK as shown in Fig. 6.4. Plugging in all known values, the effective trap volume as a function of power and beam waist (assuming the temperature remains constant) is

$$V_{\mathrm{eff}} = 1.0255 \times 10^{27}\frac{w_0^7}{P^{3/2}}, \tag{6.17}$$

which gives $V_{\mathrm{eff}} = 2.1 \times 10^{-6}$ cm^{-3}.

6.3 b) Measuring Trapped Molecule Numbers

Measuring the collision rates relies on measuring the lifetime of the trapped molecules in the ODT, similar to what was done in the MOT as described in Chapter 4 and demonstrated in previous collisional studies

with other molecules [124, 125].

In order to measure the trap density, we measure the ODT molecule number by holding the molecules in the ODT (with only the optical trapping light on) for $\tau_{\text{hold}} = 150$ ms, then turning on the RF red-MOT to recapture and image them for 100 ms, which we refer to as RRI. To confirm that any molecules that were not trapped in the ODT completely leave the RF MOT recapture region, we measure the molecule number after loading the ODT for a fixed time, after which we turn off the trap light for some time τ_{hold} and image the leftover molecules. Varying τ_{hold} subsequently informs us about how long the untrapped molecules take to exit the RF MOT recapture region. Setting $\tau_{\text{hold}} = 150$ ms ensures that these molecules have fully fallen out of the region such that the background signal is consistent with zero molecules in the RF MOT at this hold time. Previous work calculated the conversion from the camera fluorescence to the trapped molecule number in the red-MOT [77, 96], and the same calibration can be used to report the ODT number using RRI. Moreover, we measure the recaptured molecule lifetime to be 37(1) ms, which is set by the known finite photon budget and scattering rate of the RF MOT beams. A 100 ms imaging window therefore collects $1-e^{-100/37} = 93\%$ of this budget, resulting in a small correction of 1.07× on the calibrated ODT number to account for loss during imaging due to the finite molecular lifetime. In this work, we report the number of molecules trapped at the time the image is taken as opposed to the extrapolated peak trapped molecule number as was done in previous work.

It is important to image the trapped molecules after short hold times starting at $\tau_{\text{hold}} < 150$ ms to fit the relevant decay curves and observe signs of collisions. RRI is not suitable for a short τ_{hold} as it takes 150 ms for the molecules to escape the MOT region. Instead, we employ gray-molasses imaging (GMI), whereby the light is blue-detuned in the Λ-enhanced GMI configuration as described in [12]. It is sufficient to wait for the untrapped molecules to diffuse out of the imaging region as the sub-Doppler cooling does not provide a restoring force. This is achieved with $\tau_{\text{hold}} = 30$ ms while the region of interest (ROI) is selected to maximally zoom in on the trapped molecules in the ODT. For lifetime scans, GMI is turned on for 2 ms

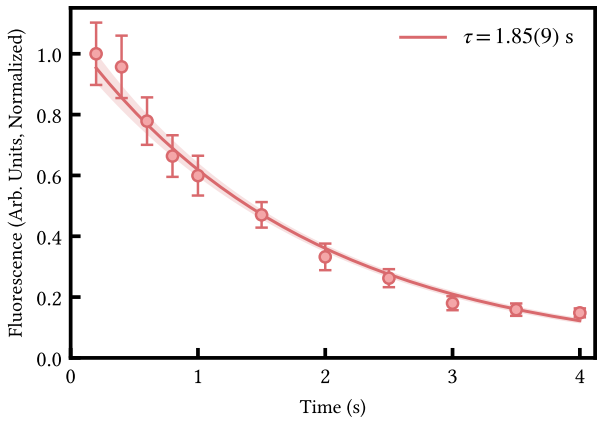

Figure 6.5: Dilute trap lifetime showing single body loss with a characteristic time of $\tau = 1.85(9)$ s.

and the trap is imaged for various values of τ_{hold}.

In order to determine the molecule number density, the absolute molecule number must be measured. To do this, the ODT fluorescence is measured by switching between GMI for 2 ms and RRI for 100 ms with $\tau_{\text{hold}} = 150$ ms, the latter of which is calibrated to give the molecule number as described above. The ratio between these two imaging methods gives the relevant conversion factor for the molecule number measured with GMI.

6.3 c) Measuring the Two-Body Rate Constant

Once we measure the trap lifetime, we fit it to the relevant decay model that characterizes the molecular loss. We can write the rate of change of density n as a function of time as

$$\frac{dn}{dt} = -\Gamma n - \beta n^2, \tag{6.18}$$

where the first term represents one-body loss with some characteristic loss rate Γ which was described in Sec. 6.2 a), and the second term represents two-body loss with loss rate β. Then, n as a function of time t

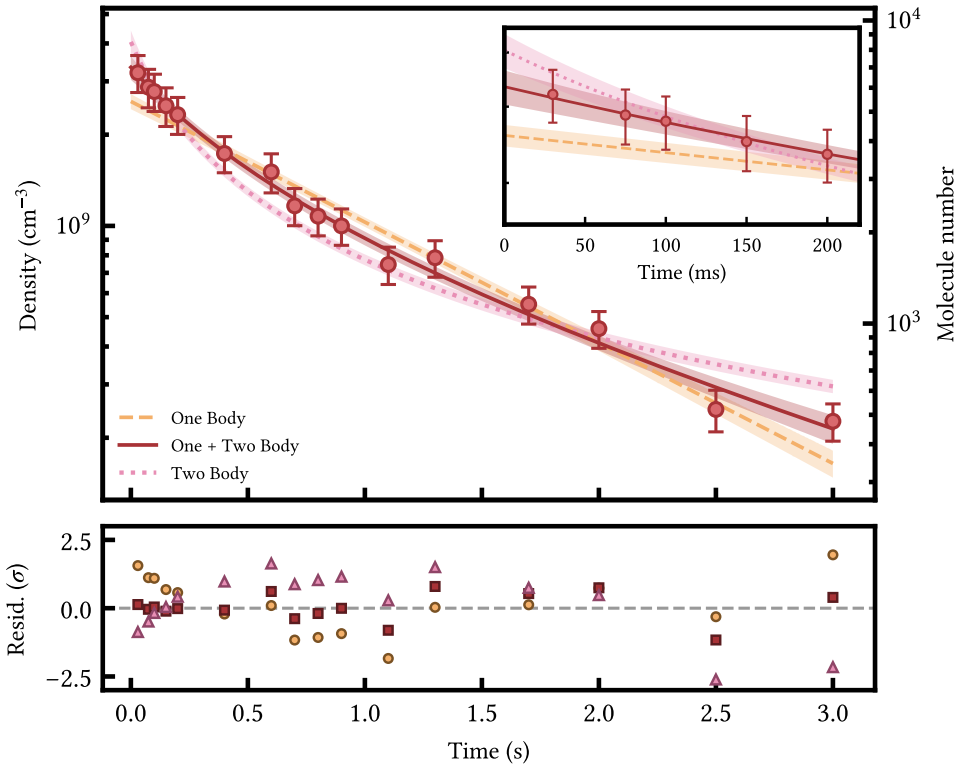

Figure 6.6: Measured number of molecules in the ODT as a function of time, fit to a one body, one plus two body, and two body functions, with all parameters free. The one plus two body curve fits best to the data and has a characteristic decay time of $\tau = 1.9$ s, consistent with the one-body lifetime measured in a dilute sample, where collisions are negligible. This fit results in a two-body rate constant of $\beta \sim \mathrm{B} \times 10^{-10}$ cm^3/s with an estimated systematic uncertainty of a factor of ~ 2, surmised from variations in fit β values as described in the text. The normalized residuals for the three fits are shown, where the circles represent the one body fit, the squares the one plus two body fit, and the triangles the two body only fit. The structure of the residuals show that the fit is best for the one plus two body case. Fitting to one plus two body with the one body rate constant set to that measured with dilute samples yields the same β within error.

is given by

$$n(t) = \frac{n_0 e^{-\Gamma t}}{1 + \frac{\beta n_0}{\Gamma}\left(1 - e^{-\Gamma t}\right)}, \tag{6.19}$$

where we fit the rate constants Γ and β, as well as the initial trap density n_0. In a dilute trap, Fig. 6.5 shows single-body loss corresponding to $\Gamma \sim 1.9$ s. Here, the trap number was made worse by changing the ablation spot. This lifetime is higher than what was reported in Sec. 6.2 a) which was likely limited by collisions in the smaller trap. Figs. 6.6 and 6.7 show lifetime measurements at higher densities with

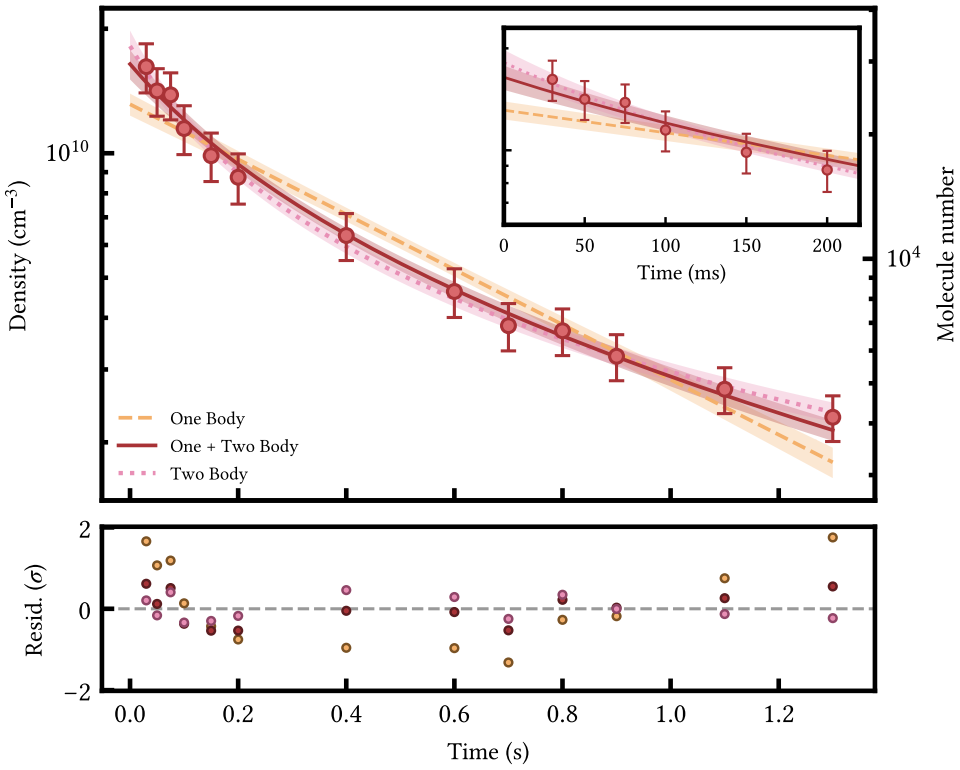

Figure 6.7: Similar lifetime measurement of trapped molecules in the ODT to Fig. 6.6 with a higher trap density further indicating two body loss.

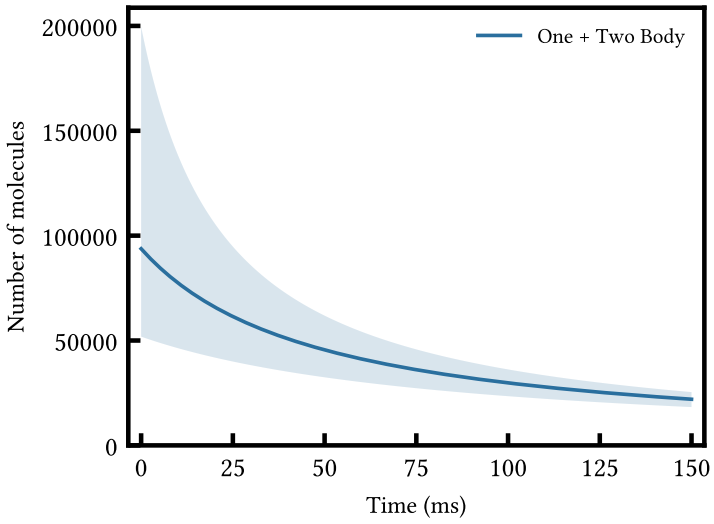

Figure 6.8: Extrapolated ODT number at short ODT hold times taking into account the two-body loss due to collisions.

Table 6.2: Trapped molecule number as a function of ODT hold time accounting for the measured value of β.

ODT Hold Time (ms)	Trapped Molecule Number	Lower Bound	Upper Bound
0	93,758	51,844	199,613
10	77,505	46,361	138,557
20	66,004	41,906	105,975
30	57,437	38,215	85,715
40	50,808	35,107	71,899
50	45,527	32,454	61,874
60	41,220	30,163	54,269
70	37,641	28,164	48,301
80	34,619	26,406	43,493
90	32,035	24,846	39,538
100	29,798	23,454	36,226
110	27,845	22,203	33,413
120	26,123	21,074	30,994
130	24,594	20,049	28,891
140	23,228	19,114	27,047

clear indications of two-body loss. A one body, one plus two body, and two body curve are fit the to the data, where the residuals show that the one plus two body curve has the best fit. For this curve, $1/\Gamma$ fits to $\sim$ 1.9 s, in good agreement with the measured dilute trap lifetime. Moreover, we measure a value of $\beta \sim 4 \times 10^{-10}$ cm^3/s which, based on other measurements, varies by a factor of $\sim$ 2 relative to the mean value due to potential deviations in the molecule distribution in the trap from the uniform-density model employed.

Due to collisions, after holding the ODT for 150 ms the transfer efficiency from the CB MOT drops from 20% at low densities to $\sim$ 6% at high densities. As such, from this value of β we can extrapolate what the trapped molecule number in the ODT would be at early hold times given our measured number of $\sim$ 20,000 at a hold time of 150 ms as shown in Fig. 6.8 and Table 6.2. This gives us a sense of what the peak molecule number is in the absence of two-body loss. From this analysis, we see that it is possible to increase the trapped molecule number by at least a factor of two by reducing the effect of collisions. This can be done by increasing the ODT waist to reduce the density as the volume scales $V_{\text{eff}} \propto w_0^4$, while also

increasing the laser power as the ODT laser intensity $I_{\mathrm{ODT}} \propto 1/w_0^2$.

6.4 Conclusion

In conclusion, we have illustrated the optical dipole trapping of SrOH. This marks progress towards conducting a precision measurement in an optical trap toward a UDM search. We are able to capture $\sim$ 20,000 molecules where the CB MOT has allowed for up to 20% transfer efficiency from the RF MOT to the ODT at low densities, a factor of 5 improvement from previous efficiencies in earlier molecular ODT demonstrations [8, 9, 11, 12]. We have also measured the lifetimes for states sensitive to UDM and the eEDM which are currently blackbody limited, and have developed techniques to prepare molecules in these states with high efficiencies. Lastly, we have shown evidence for two-body loss due to collisions in a dense ODT when we employ transverse cooling of the molecular beam, and can increase the trapped molecule number by utilizing a trap with a larger volume.

Is somebody gonna match my [improvement to trapped molecule number by an order of magnitude]?

Tinashe [Altered]

7

Transverse Cooling of the SrOH Molecular Beam

Due to the complexity and relative inefficiency of molecular laser cooling and the low molecular flux emanating from current sources, typical trap numbers and densities remain orders of magnitude lower than those in state-of-the-art atom experiments. Quantum science with cold molecules has often been limited by these metrics. For example, precision measurements in traps with neutral molecules rely on high numbers (as well as long coherence times) to lower statistical uncertainty and quantum simulation experiments require high trap densities to enable the study of many-body physics or acquire quantum degeneracy. In

this Chapter, we demonstrate the transverse cooling (TC) of the SrOH molecular beam resulting in an order-of-magnitude improvement of the number of opticall;y trapped molecules to $N_{\mathrm{ODT}} \sim 10^4$.

7.1 Improving Trapped Molecule Numbers

In addition to enhancing the signal-to-noise ratio for data collection, improving N by an order of magnitude has the following implications:

1. **SrOH UDM:** An ODT with 10^4 SrOH molecules allows for a precise measurement of the oscillation of the proton-to-electron mass ratio $\mu = m_p/m_e$ to probe UDM This would improve the sensitivity to UDM by an order of magnitude in one day of running for one decade of mass.

2. **SrOH eEDM:** 10^4 SrOH molecules would result in an eEDM measurement that improves upon the current best sensitivity set by JILA using molecular ions [20]. For example, 10^4 trapped SrOH molecules with a coherence time of 300 ms and a week of integration time would result in a statistical uncertainty of $\sigma_{\mathrm{edm}} \approx 4.0 \times 10^{-30}$ e cm which is ~2 times better than the JILA result.

3. **Molecules for BSM Physics:** The techniques developed here improve the prospects for obtaining high enough trap numbers for heavier molecules that are more difficult to produce than SrOH. Examples include Radium containing molecules or asymmetric tops, which have greater sensitivity to BSM physics,.

4. **Quantum Degeneracy:** An order of magnitude improvement in the highest reported molecular ODT densities from $n_0 = 10^{10}$ cm^{-3} [83] to $n_0 = 10^{11} - 10^{12}$ cm^{-3} match those in early evaporative cooling experiments using atoms [126]. In conjunction with microwave shielding [127], this is a key step towards obtaining quantum degeneracy in directly cooled molecules towards a Bose-Einstein

condensate, a key milestone which has only so far been achieved with assembled molecules [128, 129].

For precision measurements in particular, recall the statistical uncertainty as shown in Chapter 1

$$d_{\text{bsm}} = \frac{1}{X_{\text{sys}}\tau\sqrt{N}} \tag{7.1}$$

where X_{sys} is the intrinsic sensitivity of the system, τ is the interaction time and N is the number of measurements corresponding to the number of trapped molecules in the case of SrOH. For a given system, N is the parameter with the highest ceiling for improvement: in CBGB experiments, up to 10^5 molecules can be optically trapped from $\sim 10^{10}$ produced. There is great potential to improve the number of trapped molecules, while the option to improve τ is not always available or can present a large technical challenge for a marginal gain. For example, blackbody loss can be mitigated through cryogenic cooling of the science chamber, but this would result in some order unity improvement in the lifetime. Below however, we discuss steps that have already been taken to improve molecule flux and trap numbers by orders of magnitude in direct laser cooling experiments from CBGBs.

7.1 a) Chemical Enhancement

When the reaction between Sr atoms and H_2O molecules occurs inside the cell following ablation, the reaction rate can be improved by exciting the intercombination line $^1S_0 \rightarrow {}^3P_1$ in Strontium. The increase in energy of the Sr atoms from this excitation results in a more favorable exothermic reaction to produce SrOH. The discovery of this technique as first demonstrated in YbOH [130] greatly improves molecular yield by a factor of ~10 for the SrOH experiment where 800 mW of laser light with a wavelength of 689 nm is used to drive the atomic transition.

7.1 b) Blue-Detuned Conveyor Belt MOT

As described in Chapter 6, loading an optical dipole trap for a red MOT is inefficient due to the mode mismatch between the ODT light and the size of the trapped molecule cloud. The advent of the Conveyor Belt (CB) MOT allows for rapid compression of the cloud [82], increasing the density by close to two orders of magnitude. This has resulted in $5-10$x improvements in ODT loading efficiencies. Moreover, the CB MOT is one of the first examples of a novel laser cooling technique being first discovered and demonstrated using molecules instead of atoms.

7.1 c) In-MOT Repumper Spectroscopy

Improving the available photon budget helps circumvent loss to vibrational dark states during photon cycling in the slowing and trapping steps. This can be done by identifying and adding repump lasers to address additional loss channels. On the SrOH experiment, work was done to use the MOT as a highly sensitive spectroscopy tool to identify these repumping transitions [96]. The low temperature and confinement of molecules in the MOT allows for long interaction times between the molecules and spectroscopy lasers, resulting in wide features which are easier to identify. Moreover, depletion/revival spectroscopy using the trapped molecules as the signal is a robust technique due to the high SNR available. This work resulted in the addition of two new repumpers addressing the $\tilde{X}^2\Sigma^+(12^00)$ and $\tilde{X}^2\Sigma^+(12^20)$ ground states, improving the photon budget from 9800(400) to 14500(700). This in conjunction with various technical upgrades improved the initially reported number of magneto-optically trapped molecules from $\sim$ 7,000 to $\sim$ 32,000.

7.2 Collimating the Molecular Beam

The predominant loss mechanism in a CBGB laser cooling experiment is due to geometry. For example, an SrOH beam with a divergence of 1 STR propagating a distance of 1.4 m will result in only 1 in 10^4 molecules intersecting with a MOT of capture radius 1 cm. This effect is exacerbated for heavier molecules which require longer slowing distance. The trapped fraction can be improved through effectively "collimating" the beam by applying 2D transverse cooling after the beam box, as shown in Fig. 7.5. Magnetically assisted Sisyphus transverse cooling in particular allows for the realization of colder transverse temperatures in the sub-Doppler regime [6], results in minimal transverse velocity spreads, and is often proposed as a viable technique to circumvent this large loss mechanism [106]. Before discussing how this is achieved on the SrOH experiment, we provide some background and describe experiments in which this technique has been demonstrated on molecular beams.

7.2 a) Magnetically Assisted Sisyphus Cooling

The mechanism by which magnetically assisted Sisyphus cooling reduces the temperature of the molecular beam is identical to the Sisyphus processes that were described in Chapter 6. To recap, a standing wave of light is created in a direction orthogonal to the molecular beam. In a type-II system, this results in a spatially evolving bright state and a coherent dark state. For blue-detuned light, the molecules ride up the hill of this bright state and are optically pumped at the top into the dark state, preventing them from recovering their kinetic energy. The bright and dark states are then remixed by the applied magnetic field to allow the process to continue. Transverse cooling has played an important role in molecular laser cooling. It is often used a proof-of-principle technique to demonstrate photon cycling in various molecular species. In fact, the transverse cooling of SrOH in 2015 [6] was a milestone result as it made it the first laser cooled polyatomic molecule. Additionally, transverse cooling in two dimensions for YbF [131] and

BaF [132] beams have improved beam fluxes to aid in precision measurements.

Despite being well understood, transverse cooling has not been successful in enhancing trap numbers for laser cooling experiments. In fact, while prior studies involving Doppler transverse cooling have shown order unity improvements in MOT number [133], the same work shows a reduction in trapped molecule number through sub-Doppler transverse cooling. Below, we discuss key simulations of the molecular beam that provided us with a benchmark for improving the MOT, after which we describe some key issues that need addressing in order to see an enhancement in MOT and ODT numbers.

7.3 Trajectory Simulations

To understand the potential gains from transverse cooling, simulations can provide some guidance to inform the viability of such a technique. They provided a benchmark which ended up being close to what was experimentally realized. These simulations are done in Julia using the ordinary differential equation (ODE) package and are entirely classical, dealing with kinematic forces on a forward propagating molecular beam.

7.3 a) Molecular Beam Propagation

The simulations begin with producing the molecular beam. The forward and transverse velocities are simulated via Monte Carlo methods from a Gaussian probability distribution with centers and widths matching experimental data. The forward velocity of the beam is taken to be centered at 100 m/s with a 1σ width of ~30 m/s, and the transverse velocity is centered at 0 m/s with a width of 25 m/s. The transverse velocity spread is selected to match the angular spread of the molecular beam as discussed in [72]. The molecules are allowed to propagate, where their positions and velocities are recorded at various time increments. The beam encounters various apertures defined by the beam box radiation shields, as well

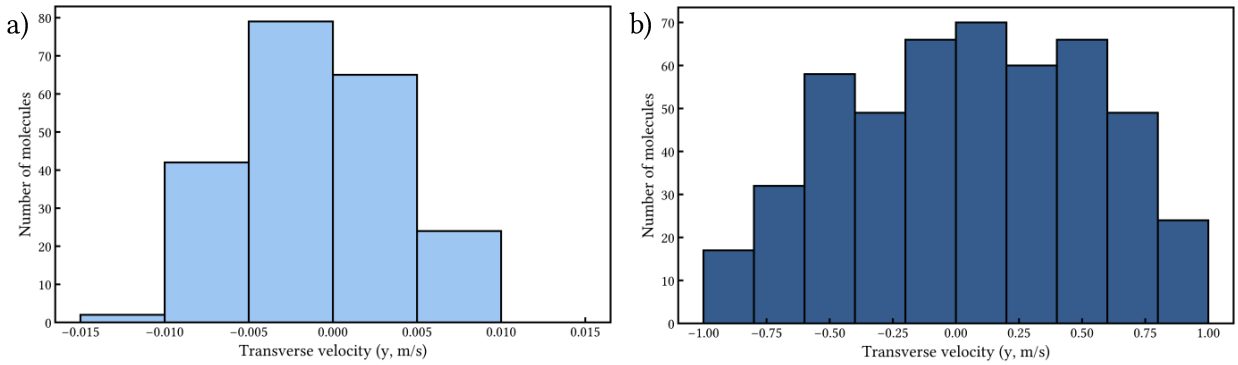

Figure 7.1: Transverse velocity distributions of eventually trapped molecules. a) No transverse cooling applied where the transverse velocity distribution spread is very close to 0 m/s. b) Transverse cooling applied with a capture velocity of 1 m/s.

as the UHV shutter, which are accounted for via callbacks which terminate a molecule trajectory if it encounters a solid wall. The size of each aperture, as well as their distance from the cell, is taken to match the experiment.

7.3 b) Baseline MOT Condition

Before adding transverse cooling (TC), the reliability of the simulation was tested to ensure that it could reasonably replicate what is observed in the lab before TC was added. This is done by simulating the SrOH MOT in the presence of slowing and seeing if the results match what is seen on the experiment. The slowing light is defined as a cone of light to match the focused laser in the experiment, where molecules are decelerated at a scattering rate of ~600 kHz while they see the light until they reach a velocity of 10 m/s. The positions and velocities of each molecule are calculated at each time increment using kinematic equations with a constant acceleration. The scattering rate is a free parameter and was tuned to match experimental observations. The force vectors in the slowing beam are calculated to reflect the inward slope to simulate the focusing effect. Additionally, the molecules experience a photon kick in some random direction at some defined increment of time to replicate the heating due to photon emission.

Once the slowing concludes, the decelerated molecules propagate towards the MOT. This trapping re-

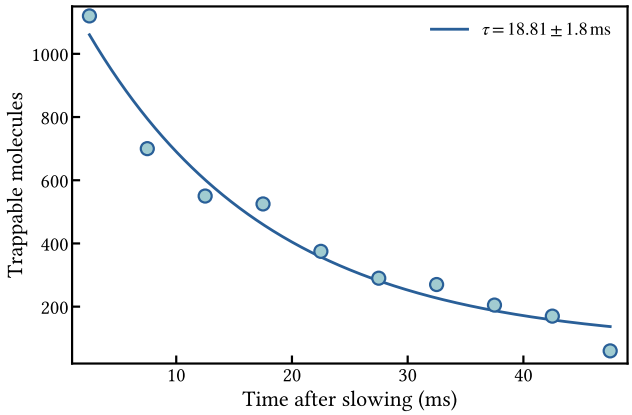

Figure 7.2: Simulated extended loading curve of SrOH, where the MOT is captured at some variable amount of time following slowing. The exponential decay curve fit to this simulated data agrees well with the experiment.

gion is defined as some sphere with fixed radius, where molecules whose trajectories intersect this volume and are slower than the MOT capture velocity are considered trapped. The simulations show that 1 in 10^5 molecules are trapped in the MOT, an order of magnitude larger than what is observed on the experiment without accounting for losses due to the finite photon budget. The rest of the loss is strictly geometric, which agrees with the simple calculation we made previously. Additionally, the "extended loading" curve for the molecular beam is simulated as shown in Fig. 7.2. Here, the slowed molecules are captured in the MOT at some time after slowing ends. The number of trapped molecules is plotted as a function of this wait time, where the points fit to a decaying exponential with a characteristic time of ~18 ms which matches the experimentally obtained value [77]. The fact that these two simulated results agree with the experimental variables gives us confidence in the reliability of the simulation.

7.3 c) Transverse Cooling

Transverse cooling is treated very simply in the simulations, once the molecules propagate 30 cm from the cell, their transverse velocities are set to 0 m/s if they are below the set capture velocity of the TC. Following this, the molecules are slowed in the same way as described above after which they are trapped in the MOT. The transverse velocity distribution of the molecules that are captured in the MOT is shown

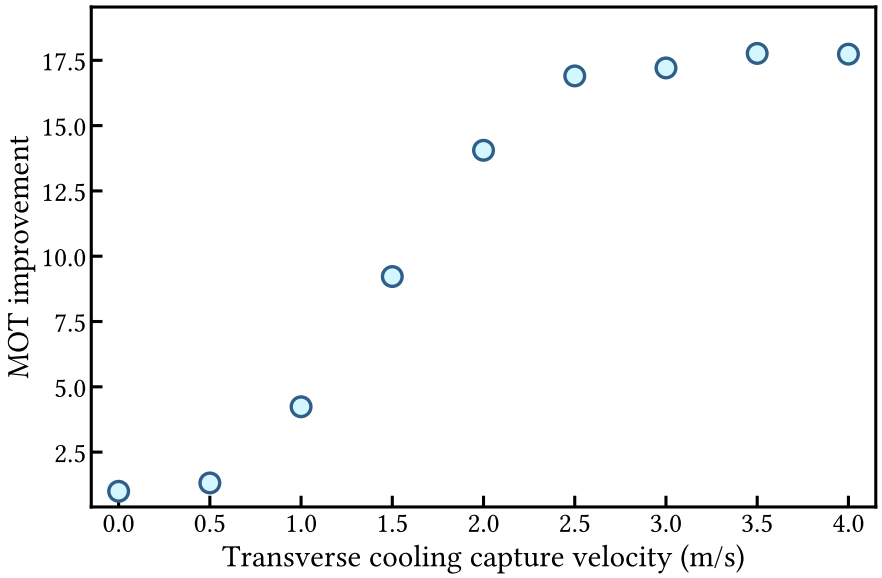

Figure 7.3: Simulated MOT number improvement as a function of transverse cooling capture velocity.

in Fig. 7.1a) in the absence of transverse cooling where the spread is very close to 0 m/s. Fig. 7.1b) shows the distribution with a transverse cooling capture velocity of 1 m/s resulting in a much broader velocity profile. Moreover, Fig. 7.3 shows the multiplicative improvement in the trapped molecule number as a function of capture velocity. The sharp plateau is due to the 17 mm diameter UHV shutter acting as a limiting aperture, as it is smaller than the MOT capture radius. Thus, increasing this aperture size could lead to order unity improvements in the transverse cooling gain. The increase in MOT number from the simulations is within a factor of 2 of what is experimentally measured, as described below.

7.3 d) Magnetic Lens and Telescope

One of the initial ideas to collimate the SrOH molecular beam was to use a magnetic lens and telescope in conjunction with transverse cooling. In the simulation, the molecules first pass through the lens to initially collimate them. The conservation of etendue dictates that compressing the beam radius increases its angular spread, which defeats the purpose of collimating it. As such, a dissipative transverse cooling step is implemented after the initial lens to compress the phase space distribution of the beam. Following

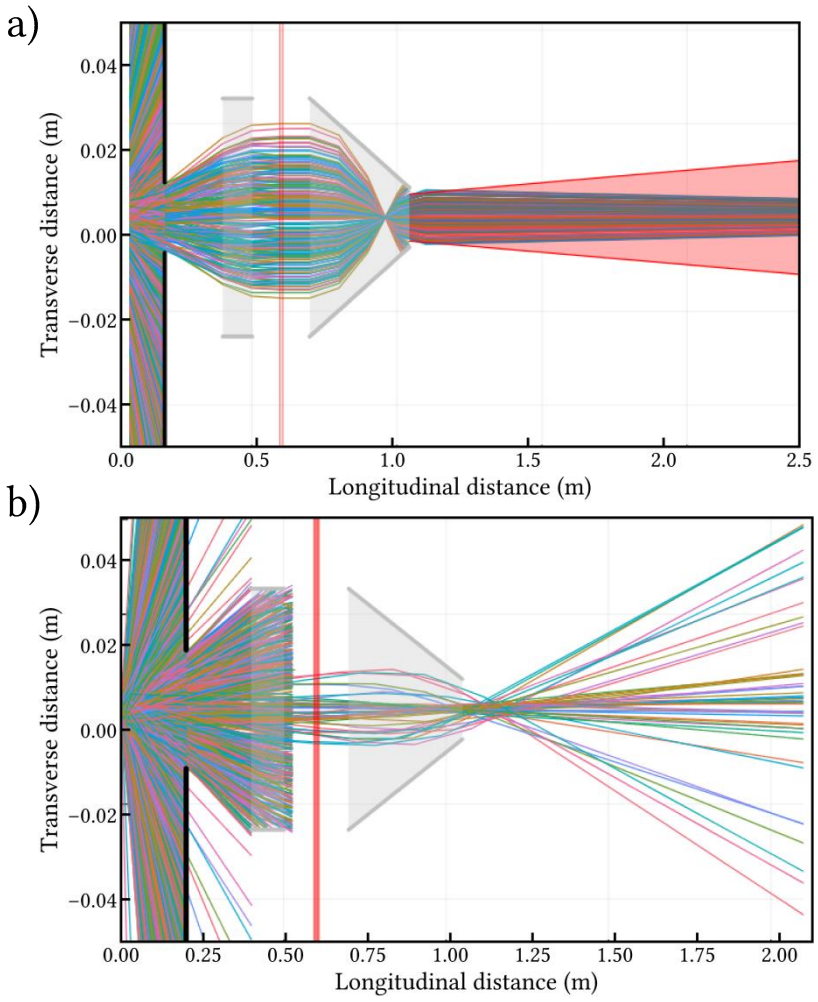

Figure 7.4: Trajectory simulations in the presence of a magnetic lens followed by transverse cooling and a magnetic telescope. a) Ideal collimation of a monochromatic molecular beam. b) Divergence of a molecular beam with a finite velocity distribution.

this, the beam is shrunk through a reverse telescope comprising a tapered solenoid before it is slowed and trapped. The simulation results for this technique are shown in Fig. 7.4. In Fig. 7.4a), the molecular beam is simulated to be monochromatic and is thus collimated extremely well after the magnetic lensing elements. In reality, the beam has a finite velocity spread reflected in Fig. 7.4b) resulting in a large degree of divergence after the magnetic telescope. This additional spread ends up resulting in a decrease of the trapped molecule number in the MOT. As such, the simulations suggested that transverse cooling alone was a viable option to circumvent the loss due to the angular spread of the molecular beam.

7.4 2D Transverse Cooling of the SrOH Molecular Beam

The transverse cooling (TC) we describe is in a different regime to many of the previous demonstrations. In particular, each TC laser arm for each axis consists of light generated by an SFG laser capable of producing 5 W of power, whereas prior work has been limited to $10 - 100$ mW, with the aforementioned YbF experiment using up to 850 mW. We found that this level of power results in comparatively higher detunings for optimal cooling. Additionally, considerations must be made for interactions between the transverse cooling and slowing light, as well as interactions between the two cooling axes themselves. In this section, we will tackle each of these aspects where our figure of merit for the performance of cooling is given by η_{TC}, which we define as the multiplicative gain in the trapped molecule number in the MOT due to TC.

7.4 a) Evolution of the Laser Configurations

In order to make clear the conditions with which the data were taken in this chapter, we distinguish the different laser configurations that were used for this work. The cooling transition used here is the same as for radiative slowing and the MOT, namely $\tilde{X}^2\Sigma^+(000) \rightarrow \tilde{A}^2\Pi_{1/2}(000)$ at 688 nm. The laser configurations (LCs) are discussed below and referred to throughout this chapter.

LC a) Initially, the light for both TC axes was supplied by one Precilasers SFG (FL-SF-687-5-CW) which produces 5 W of power. This light was aligned through an AOM to generate a 110 MHz to address the spin rotation splitting. These sidebands were aligned on a polarizing beam splitter (PBS) and delivered to the cooling region through a PCF. This resulted in a total of ~2.4 W total which was then split between both axes on a 50/50 beamsplitter. This resulted in a max $\eta_{\mathrm{TC}} \sim 5$.

LC b) The results from the previous condition were limited by the power of the cooling light. To increase

the overall power, we used two lasers to generate the cooling light instead of one. In this particular condition, each spin-rotation component was generated by a different laser: one was the same standalone SFG system used in condition a), and the other was supplied from the SFG responsible for the slowing light. The light was then combined on a PBS and aligned through an AOM switch before being coupled into a PCF and again split via a 50/50 beamsplitter to address both cooling axes. This resulted in ~2.4 W per axis corresponding to $\eta_{\mathrm{TC}} \sim 10$, but as discussed below, the upper frequency component saturated at a much lower power than the lower component. As they were supplied by different lasers, there was no way to move the power from one into the other. The data presented in this Chapter was taken in this configuration.

LC c) This is the current configuration that we are working towards optimizing. Instead of being responsible for the spin-rotation components, each laser is now responsible for each cooling axis. The spin-rotation splitting is addressed in the same way as for LC a), and each axis is individually coupled via PCF to the cooling region. The relative power between the sidebands can be tuned via the AOM RF drive power. Work is ongoing to optimize this setup, where the powers in the vertical and horizontal axes are 3.2 W and 2 W respectively. So far, values of $\eta_{\mathrm{TC}} \sim 10$ have been achieved due to the increased power in the power-starved frequency component with potential for further improvement.

7.4 b) Experimental Setup

In the experiment, the TC light is applied 30 cm downstream of the end of the cell and is turned on simultaneously with ablation for 13 ms thereafter, until the slowing light is applied. The laser configurations described in Sec. 5.3 a) determine how much power is delivered to each cooling axis. Once the light is brought to the cooling region, it propagates through a 3x beam expander, followed by a 10x cylindrical

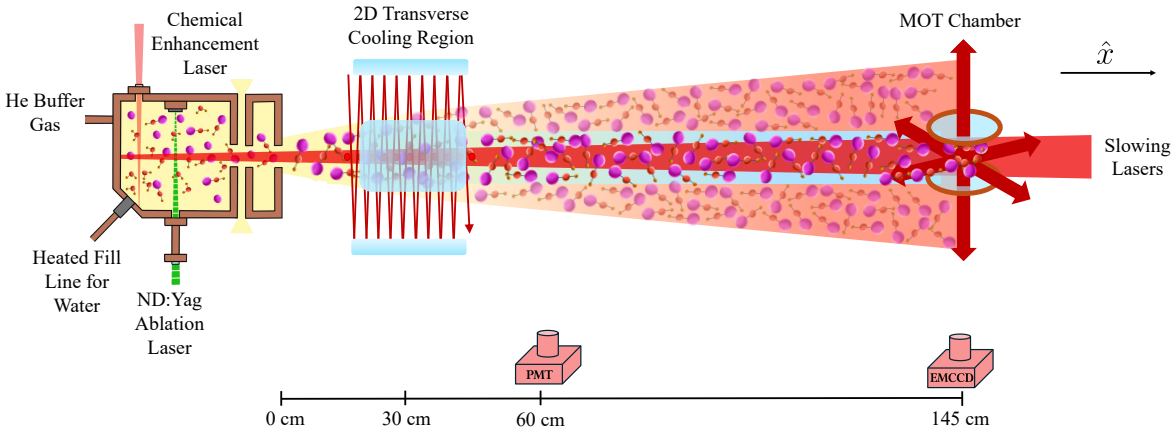

Figure 7.5: Experimental sequence, starting with SrOH production in a cryogenic buffer gas cell. The molecules propagate 30 cm before they encounter the 2D transverse cooling region, after which they are collimated and laser slowed before being trapped. The beam is monitored with a photomultiplier tube (PMT) 60 cm downstream of the cell to benchmark molecular production and measure the arrival time after the Nd:Yag is fired. The MOT and ODT are then imaged on an EMCCD through a viewport on the MOT vacuum chamber. The faded molecules in the orange cone represent the spread of the beam without TC applied, where the vast majority of them end up missing the capture region. The opaque molecules in the blue region represent the collimated beam after TC is applied, showing an increase in on axis density and subsequent enhancement of captured population in the MOT.

telescope comprising a -19 mm and 200 mm focal length lens resulting in expansion in the direction orthogonal to the propagation of the molecular beam to increase the cooling volume. The light starts with a Gaussian width of 3 mm and is expanded to measure 3×30 mm. The expanded beams now propagate through the TC region, which comprises of a custom made vacuum chamber with a square cross-section. Optical access in both TC dimensions is provided through four anti-reflection (AR) coated windows optimized for 688 nm light. Each window is made of ultraviolet (UV) fused silica and measures 3.25" x 3.65" x 0.625". The light is multi-passed ~20 times over a distance of 50 mm between two mirrors to create a standing wave at the geometric center between the mirrors, which is also the geometric center of both the vacuum chamber and the molecular beam.

In addition to the main cooling light, three additional lasers are added in the TC region to address the most predominant decays to unaddressed vibrational ground states, specifically the $\tilde{X}^2\Sigma^+(100)$, $\tilde{X}^2\Sigma^+(200)$

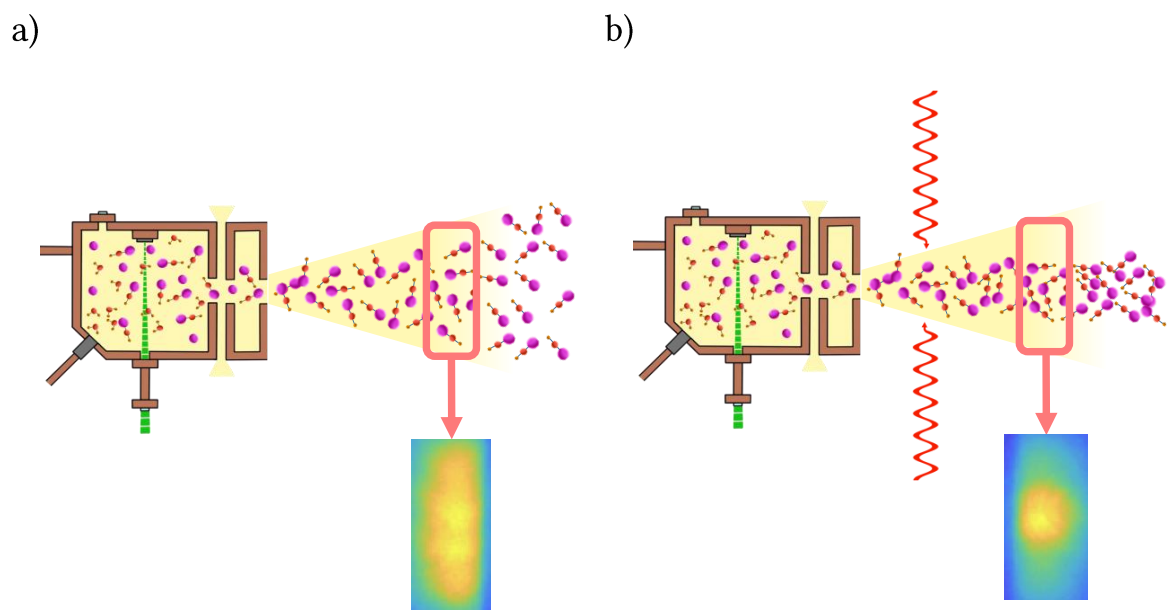

Figure 7.6: Schematic of the SrOH beam measured on a PMT at a distance of 60 cm from the exit aperture of the cell. a) Fluorescence signal of the uncooled SrOH beam. b) Compression and collimation of the transversely cooled SrOH beam in one dimension.

and $\tilde{X}^2\Sigma^+(010, N = 1)$ states. This is achieved through the following repumping transitions: $\tilde{X}^2\Sigma^+(100) \rightarrow \tilde{B}^2\Sigma^+(000)$ and $\tilde{X}^2\Sigma^+(200) \rightarrow \tilde{B}^2\Sigma^+(100)$ at 631 nm, and $\tilde{X}^2\Sigma^+(010, N = 1) \rightarrow \tilde{B}^2\Sigma^+(000)$ at 624 nm. The repumping lasers are combined with the main TC laser on a long pass dichroic mirror before the expanding optics in each axis, resulting in the ability to scatter ~900 photons before appreciable loss to vibrational dark states.

Before we observed the effect of TC on the MOT and ODT, we recreated the results from Ref. [6] to demonstrate compression of the SrOH molecular beam. Fig. 7.6 shows this compression in the presence of transverse cooling light in one dimension as measured in a region 60 cm downstream from the exit aperture of the cell using an EMCCD camera.

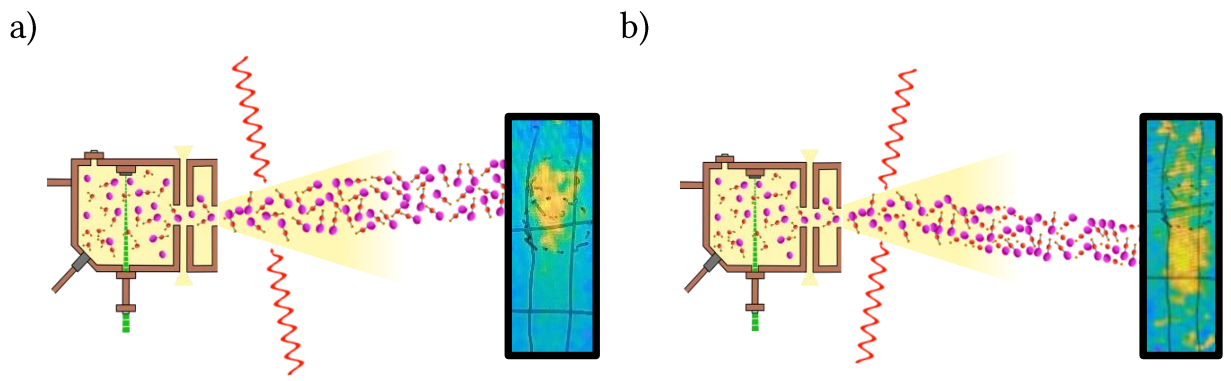

Figure 7.7: Tilting of the transverse cooled molecular beam in one dimension. The beam image on the EMCCD can move based on a change of tilt angle of the standing wave.

7.4 c) Pointing the Collimated Beam

As mentioned previously, a potential key issue in previous TC attempts is the pointing of the collimated beam. For example, having the beam be cooled but tilted such that it is aimed away from the MOT would result in a decrease in trapped molecule number as was reported in Ref. [133]. While looking at the SrOH molecular beam, we imaged its final position on an EMCCD and moved it in one dimension by "tilting" the overall standing wave in the transverse cooling region. This is shown schematically in Fig. 7.7.

7.4 d) Interaction with the Slowing Beam

Although previous simulations [106] have shown that the performance of the TC is in fact enhanced by the presence of the slowing laser, this is not what was observed on the experiment. Having both lasers on simultaneously results in no TC when looking at the beam downstream, and so the timing of these various techniques becomes important. One potential way to explain this effect is that the slowing beam which addresses the same cooling transition is pumping molecules out of the dark states which are vital for the sub-Doppler mechanism.

Due to the length of the beamline, there exists a buffer time in between when ablation occurs and

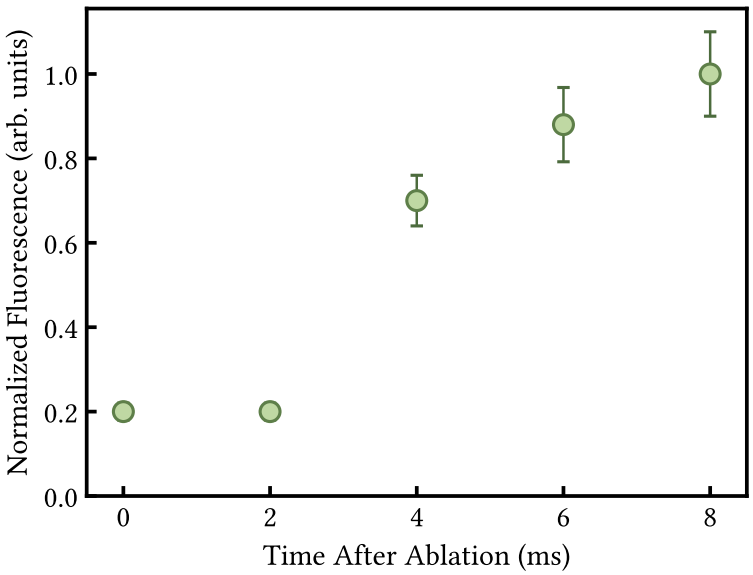

Figure 7.8: Transverse cooling performance as a function of varying buffer time before slowing and after ablation.

when the slowing light is turned on. Depending on the speed of the beam and power in the slowing lasers, this time can be 6-10 ms long. As shown in Fig. 7.8, this is enough time for the beam to propagate and pass through the TC region to provide the desired transverse compression.

7.5 MOT and ODT Number Enhancement

Once the beam was overlapped with the MOT light, the trapped molecule number was measured with TC on versus off, where the ratio η_{TC} between the two conditions was maximized by tuning various parameters, including powers and frequencies of the TC lasers as well as the alignment of the standing wave described earlier. Following this optimization, the improvement in the number of molecules trapped in the ODT due to TC was measured. For both the MOT and ODT, $\eta_{\mathrm{TC}} \sim 12$, resulting in a trapped molecule number in the ODT $N_{\mathrm{ODT}} \sim 20{,}000$.

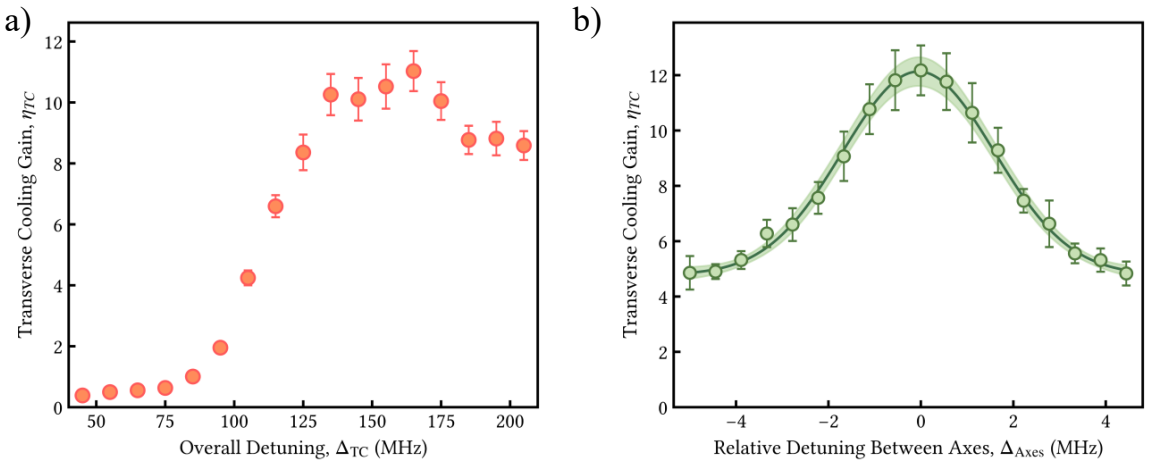

Figure 7.9: Multiplicative increase in trapped molecule number, η_{TC}, as a function of laser detuning. (a) Overall detuning of the TC lasers relative to the $J = 1/2$ spin-rotation level, with each cooling-axis frequency held fixed. A maximum occurs near $\Gamma_{TC} \sim 20$ which corresponds to a frequency of 140 MHz, where the curve exhibits a less steep drop-off toward blue detuning. Around $\Gamma_{TC} \sim 10$, cooling becomes ineffective because the lower-frequency component approaches resonance with the $J = 3/2$ level, disrupting the Sisyphus cooling mechanism. (b) η_{TC} as a function of the relative detuning between the two cooling-axis frequencies, Δ_{Axes}. The dashed line shows η_{TC} for a single axis: when the laser frequencies are well separated, they are incoherent and the total gain is additive. The peak occurs at zero relative detuning, where coherence enhances the intensity in regions of overlap between the orthogonal axes, leading to an increase in η_{TC}.

7.5 a) Overall and Two-Photon Detunings

The dependence of TC on the overall detuning of the light Γ_{TC} is shown in 7.9 a), where $\Gamma_{TC} = \Delta_{TC}/\Gamma_{SrOH}$, where Δ_{TC} is the detuning relative to resonance on the main slowing transition and $\Gamma_{SrOH} = 2\pi \times 7$ MHz is the natural linewidth of SrOH. The laser frequencies for both TC axes are scanned while maintaining their relative frequency Δ_{Axes}, where η_{TC} is maximized at $\Gamma_{TC} \sim 20$.

Figure 7.10a) shows a two-dimensional scan where both Δ_{TC}, the overall detuning of the TC lasers and δ_{SR}, the relative detuning between the frequency components present in each cooling arm, is changed and η_{TC} is measured while keeping Δ_{Axes} fixed. This data was taken in LC b). This structure in figure 7.10a) provides some insight into the underlying sub-Doppler cooling mechanism: in the configuration shown in figure 7.10b), there is a region of high η_{TC} compared to its surroundings within the dashed blue ellipse.

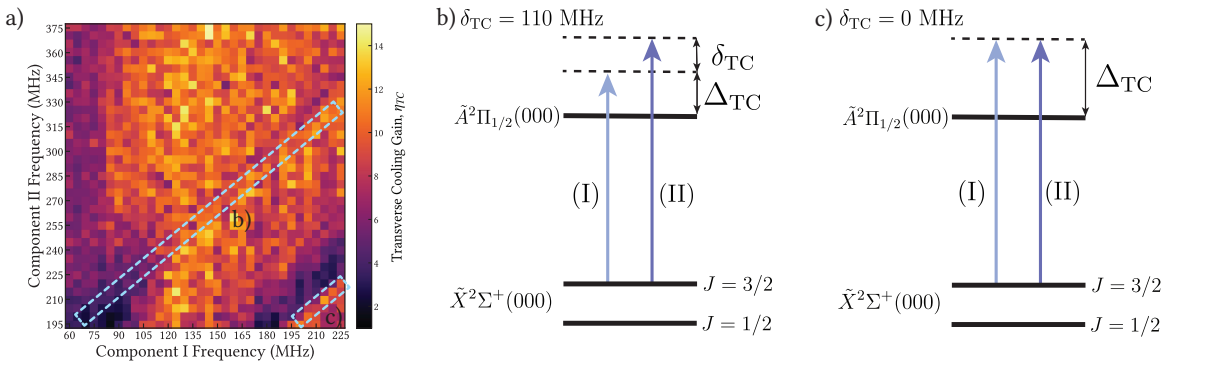

Figure 7.10: 2-D scan varying the δ_{SR}, the spacing between frequency components in each axis, while maintaining $\Delta_{Axes} = 0$. The overall structure demonstrates the characteristic blue-detuned sub-Doppler cooling mechanism. (i) A slice showing a region of high η_{TC} with $\delta_{SR} = 110$ MHz, which equals the ground state spin-rotation splitting, characteristic of gray molasses cooling. (ii) A similar slice showing a region of high η_{TC}, with $\delta_{SR} = 0$ MHz, characteristic of single-frequency cooling.

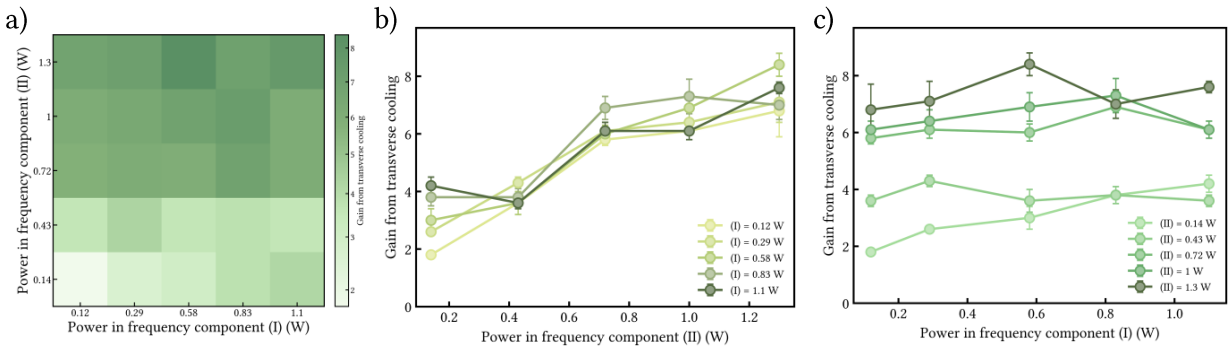

Figure 7.11: Standing wave intensity profiles for different conditions. a) A single axis formed of a retroreflecting beam of light. b) Two incoherent, orthogonal axes. c) Two coherent, orthogonal axes.

This region corresponds to $\delta_{SR} \approx 110$ MHz, which matches the splitting between the ground state spin-rotation levels very closely. Given that the overall detuning of the lasers is blue, this configuration is analogous to gray molasses (GM) cooling using a lambda system. Figure 7.10c) shows a similar region of high η_{TC}, but at a condition where $\delta_{SR} = 0$, analogous to single-frequency (SF) sub-Doppler cooling: both of these cooling techniques are well understood and have been demonstrated in several laser cooling experiments [11, 134–138].

7.5 b) Power Scans

A key improvement made on this experiment is how much power each TC beam can have. In Fig. 7.11, the powers for each frequency component (I) and (II) were scanned while looking at the improvement in the MOT. These powers were scanned with overall frequency $\Delta_{TC} = 150$ MHz and two-photon detuning $\delta = 110$ MHz. Overall, the power in frequency component (II) which addresses the $J = 3/2$ spin-rotation state saturates at far lower powers than (I) which addresses the lower lying $J = 1/2$ state. Thus, component I1) has detunings of 40 MHz and 150 MHz to $J = 3/2$ and $J = 1/2$ respectively, while component (II) has detunings of 150 MHz and 260 MHz to the same states. Since component (I) is much closer to one of the states, it can much easily induce AC stark shift which creates the standing wave necessary for cooling. Thus, it can be thought of as the "pump" beam in the Λ-configuration, largely responsible for increasing the height of the potential well. This means that it benefits from increasing power as opposed to component (II) whose primary role is that of the "probe" beam, which in turn closes the Λ-system and determines the motion or detuning dependence of the standing wave. Subsequently, the probe beam does not benefit from much higher power. This power scan resulted in the shuffling of laser systems to go from LC b) to LC c), since there is a large power discrepancy between components (I) and (II).

7.5 c) Repumping Lasers

We found that increasing power alone was not enough to improve the TC performance, and that introducing additional repumpers was necessary. TC performance relies on a combination of having a sufficiently long interaction length with the molecules, having a high enough scattering, and a large enough photon budget. In a low main cooling power regime, the scattering rate is lower and fewer total photons are cycled. As such, we observed that adding a repump would reduce the TC performance as the scattering rate would further decrease while the photon budget was already sufficient. When moving from LC a) to LC

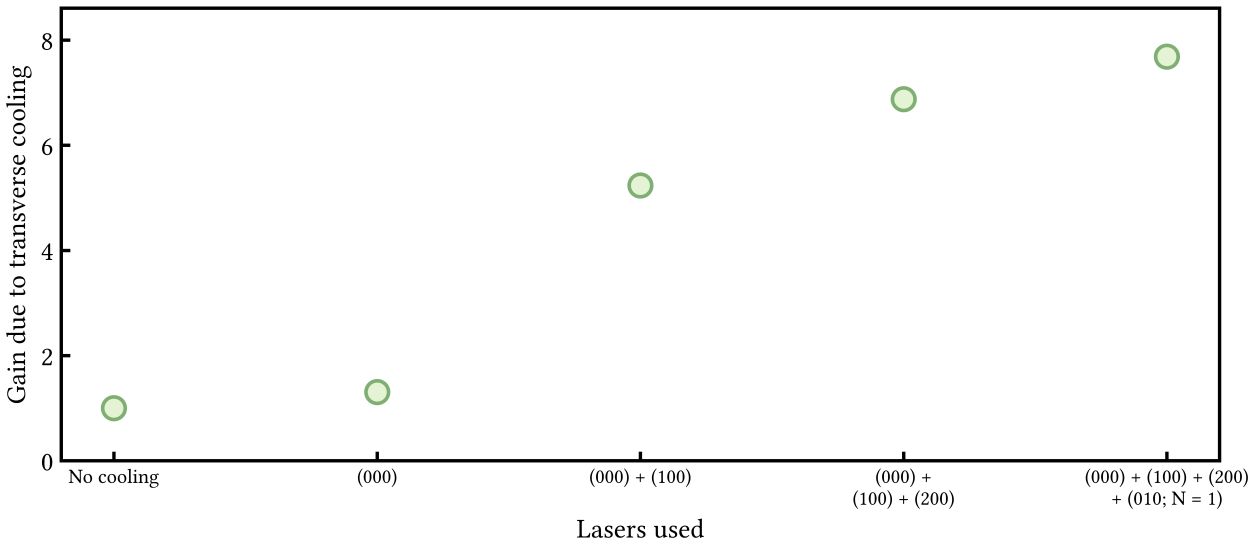

Figure 7.12: MOT improvement due to adding repumpers in the transverse cooling region.

b) and LC c), however, the increased power necessitated the introduction of more repumpers due to the increased scattering rate.

The repumpers are combined with each other first: the $\tilde{X}^2\Sigma^+(100)$ and $\tilde{X}^2\Sigma^+(200)$ repumps are combined on an Optigrate volume Bragg grating, which are then combined with the $(010; N = 1)$ light on a dichroic mirror. The repumpers are then brought to the cooling region via an optical fiber, split into both axes with a 50:50 fiber coupler, and combined with the main cooling light on another dichroic mirror. To investigate whether a repumper would help us, we first used the corresponding repumping laser through the slowing light. Although the observed gain was minimal as the size of the slowing beams did not cover the full TC region, it was an indication that combining it with the cooling path would be beneficial. Currently as mentioned above, the first three repumping lasers are used to provide a photon budget of ~1000. Since the molecular beam has a central velocity of 100 m/s traveling through a ~5 cm region, a 1 MHz would result in ~500 photons, which necessitates this photon budget. Fig. 7.12 summarizes the effects of each repumper in the TC region.

7.5 d) Relative Detuning of the Orthogonal Axes

In two dimensions, the performance of the overall cooling has a strong dependence on the relative detuning between the vertical transverse cooling (VTC) and (HTC) lasers. A potential explanation for this is that the coherence between the two axes results in a larger well depth of the standing wave. For one dimension, a standing wave of light is created by interference of the transmitted and retro-reflected beams. This results in a wave

$$\mathbf{E}_{+}(z,t) = \hat{\epsilon} E_0 \cos(kz - \omega t) \tag{7.2}$$

$$\mathbf{E}_{-}(z,t) = \hat{\epsilon} E_0 \cos(kz + \omega t) \tag{7.3}$$

$$\mathbf{E}_{\mathrm{SW}}(z,t) = \mathbf{E}_{+}(z,t) + \mathbf{E}_{-}(z,t) \tag{7.4}$$

$$= \hat{\epsilon} E_0 \left[\cos(kz - \omega t) + \cos(kz + \omega t)\right] \tag{7.5}$$

$$= 2\hat{\epsilon} E_0 \cos(kz)\cos(\omega t) \tag{7.6}$$

where E_+ and E_- are the transmitted and reflected waves which combine to form a standing wave E_{SW}. Now, we take the standing waves in orthogonal directions E_H and E_V with some phase ϕ between them such that:

$$\mathbf{E}_{\mathrm{tot}}(x,y,t) = \mathbf{E}_H(x,t) + \mathbf{E}_V(y,t), \tag{7.7}$$

$$I_{\mathrm{tot}}(x,y) \propto \left\langle \left|\mathbf{E}_{\mathrm{tot}},(x,y,t)\right|^2 \right\rangle_t \tag{7.8}$$

$$= \left\langle |\mathbf{E}_H(x,t)|^2 \right\rangle_t + \left\langle |\mathbf{E}_V(y,t)|^2 \right\rangle_t + 2\left\langle \mathbf{E}_H(x,t)\cdot\mathbf{E}_V(y,t)\right\rangle_t, \tag{7.9}$$

$$= I_H(x) + I_V(y) + 2\sqrt{I_H(x) I_V(y)}\cos\phi. \tag{7.10}$$

where I_V (I_H) is the time averaged intensity for the vertical (horizontal) axis on its own. The third term is an additional cross term which is present when ϕ is fixed. Changing the value of ϕ only serves to spatially move the standing wave pattern while preserving its overall intensity profile. If ϕ is rapidly evolving on a timescale faster than the molecule response time, this term averages out. Since $\Delta\phi \propto \omega$ where ω is the frequency difference between the VTC and HTC lasers, coherence is achieved if they are close to each other. Thus, the total maximum intensity can be written for the coherent and incoherent cases such that

$$I_{\max}^{\text{coherent}} = I_{H,\max} + I_{V,\max} + 2\sqrt{I_{H,\max} I_{V,\max}} = \left(\sqrt{I_{H,\max}} + \sqrt{I_{V,\max}}\right)^2, \tag{7.11}$$

$$I_{\max}^{\text{incoherent}} = I_{H,\max} + I_{V,\max}. \tag{7.12}$$

These results are summarized in Fig. 7.13. Assuming that η_{TC} is proportional to intensity as experimental power scans suggest, one can estimate:

$$\eta_{\text{TC}}^{\text{coherent}} = \eta_H + \eta_V + 2\sqrt{\eta_H \eta_V} = \left(\sqrt{\eta_H} + \sqrt{\eta_V}\right)^2 \tag{7.13}$$

$$\eta_{\text{TC}}^{\text{incoherent}} = \eta_H + \eta_V \tag{7.14}$$

where η_V (η_H) is the gain in trapped molecule number due to the vertical (horizontal) axis only. Fig. 7.9 b) shows the cooling performance as a function of the frequency difference between the lasers responsible for each individual axis. Each axis has $\eta_H = \eta_V \approx 2.5$, such that when the beams are separated in frequency, $\eta_{\text{TC}} \approx 2\eta_H = 5$ and when they are the same, $\eta_{\text{TC}} \approx 4\eta_H = 10$.

Although the picture of increased intensity can help shed some light on the effect of coherence, this is a simple and perhaps naive picture of what is really happening. First, the TC gain does not strongly depend on the relative polarization of the VTC and HTC lasers, which is a necessary condition for coherence. Moreover, coherence is quite difficult to achieve in systems with orthogonal lattices as shown in Ref. [139], where care must be taken to phase stabilize the lasers and ensure mechanical drifts are mini-

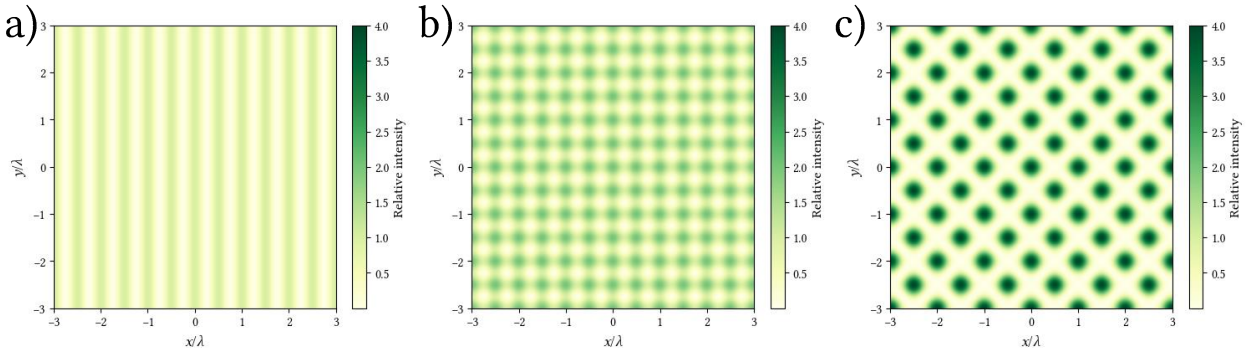

Figure 7.13: Standing wave intensity profiles for different conditions. a) A single axis formed of a retroreflecting beam of light. b) Two incoherent, orthogonal axes. c) Two coherent, orthogonal axes.

mized. Additionally, it is possible that the frequencies being similar prevents the destabilization of dark states, however, the true mechanism is still quite unknown.

Beat note Lock

The scan in Fig. 7.9 b) was done by beatnote locking the HTC and VTC cooling lasers and scanning the difference in frequency between them. A schematic of the beatnote lock is given in Fig. 7.14. The lock works in the following way: first, one of the cooling axes is aligned through an AOM to generate a +80 MHz sideband. The voltage going into the bias tee then reads

$$V_{\text{beat}} = V_{\text{DC}} + A_{\text{beat}} \left(2\pi f_{\text{beat}} t + \phi_{\text{beat}}\right), \tag{7.15}$$

where V_{DC} is the signal offset that depends on the intensity of the light, A_{beat} is the amplitude of the beatnote signal, f_{beat} corresponds to the beatnote frequency of 80 MHz which has some phase ϕ_{beat}. The bias tee then separates the DC and oscillating components such that the beatnote error signal does not change if the laser powers drift.

After this, the combination of a low-pass filter and amplifier removes any high frequency noise while amplifying the beat note signal voltage. The directional coupler then picks off 1% of this signal which

is currently monitored on a spectrum analyzer (Siglent SSA 3021X) to monitor the locking performance. Following another amplification step, a mixer combines the beatnote signal with a 290 MHz RF signal generated via a VCO which is controlled through a DC voltage output by Cicero which is user controlled. The VCO signal is put through a low-pass filter to ensure that any high frequency noise is dealt with and only the fundamental VCO frequency is present. This results in a mixed signal

$$V_{\mathrm{RF}}(t) = A_{\mathrm{beat}} \cos(2\pi f_{\mathrm{beat}} t + \phi_{\mathrm{beat}}), \tag{7.16}$$

$$V_{\mathrm{VCO}}(t) = A_{\mathrm{VCO}} \cos(2\pi f_{\mathrm{VCO}} t + \phi_{\mathrm{VCO}}), \tag{7.17}$$

$$V_{\mathrm{mix}}(t) \propto V_{\mathrm{RF}}(t) V_{\mathrm{VCO}}(t), \tag{7.18}$$

$$= A_{\mathrm{beat}} A_{\mathrm{VCO}} \cos(2\pi f_{\mathrm{beat}} t + \phi_{\mathrm{beat}}) \cos(2\pi f_{\mathrm{VCO}} t + \phi_{\mathrm{VCO}}), \tag{7.19}$$

$$= \frac{A_{\mathrm{beat}} A_{\mathrm{VCO}}}{2} \cos[2\pi (f_{\mathrm{VCO}} + f_{\mathrm{beat}}) t + \phi_{\mathrm{VCO}} + \phi_{\mathrm{beat}}] \tag{7.20}$$

$$+ \frac{A_{\mathrm{beat}} A_{\mathrm{VCO}}}{2} \cos[2\pi (f_{\mathrm{VCO}} - f_{\mathrm{beat}}) t + \phi_{\mathrm{VCO}} - \phi_{\mathrm{beat}}], \tag{7.21}$$

where A_{VCO}, f_{VCO} and ϕ_{VCO} correspond to the amplitude, frequency and phase generated by the VCO and V_{mix} is the product of the two signals. This results in the sum of two signals oscillating at the sum of the two frequencies $f_{\mathrm{sum}} = f_{\mathrm{VCO}} + f_{\mathrm{beat}} = 370$ MHz and $f_{\mathrm{diff}} = f_{\mathrm{VCO}} - f_{\mathrm{beat}} = 210$ MHz. The high pass filter following the mixer then selects the larger of the two frequencies, which is then split into another mixer which directly combines the frequency with a phase shifted version of itself after it travels through a 10 ft long BNC cable. The signal becomes

$$V_1(t) = A_1 \cos(2\pi f_{\text{sum}} t + \phi_{\text{sum}}) \tag{7.22}$$

$$V_2(t) = A_2 \cos(2\pi f_{\text{sum}}(t-\tau) + \phi_{\text{sum}}) \tag{7.23}$$

$$= A_2 \cos(2\pi f_{\text{sum}} t + \phi_{\text{sum}} - 2\pi f_{\text{sum}}\tau) \tag{7.24}$$

$$V_{\text{mix},2}(t) \propto V_1(t)V_2(t) \tag{7.25}$$

$$= \frac{A_1 A_2}{2} \cos(2\pi f_{\text{sum}}\tau) \tag{7.26}$$

$$+ \frac{A_1 A_2}{2} \cos(4\pi f_{\text{sum}} t + 2\phi_{\text{sum}} - 2\pi f_{\text{sum}}\tau)\,. \tag{7.27}$$

where V_1, V_2 correspond to the direct and delayed signals, respectively, with amplitudes A_1, A_2, and $V_{\text{mix},2}$ is the signal after the mixer. The delay due to the BNC is given by τ, which can be calculated as

$$\tau = \frac{L_{\text{BNC}}}{v_p}, \tag{7.28}$$

where the length of the BNC $L_{\text{BNC}} = 10$ m and the speed of light in the cable $v_p \sim 0.66$c. Thus, $\tau = 15$ ns and the low frequency oscillation after the mixer is

$$V_{\text{err}} \propto \cos(2\pi f_{\text{sum}}\tau) \tag{7.29}$$

$$= \cos[2\pi(f_{\text{VCO}} + f_{\text{beat}})\tau]\,. \tag{7.30}$$

The error signal V_{err} is sent to an SRS PID module (SIM960) whose setpoint is scanned such that the lock occurs at the steepest point on the slope of V_{err}. Then, while looking at the beatnote lock on a spectrum analyzer, the correct locking frequency can be obtained by tuning the VCO value or the PID offset. This beatnote lock allows the transverse cooling lasers for both axes to be very close in frequency to each other to within ~100 kHz.

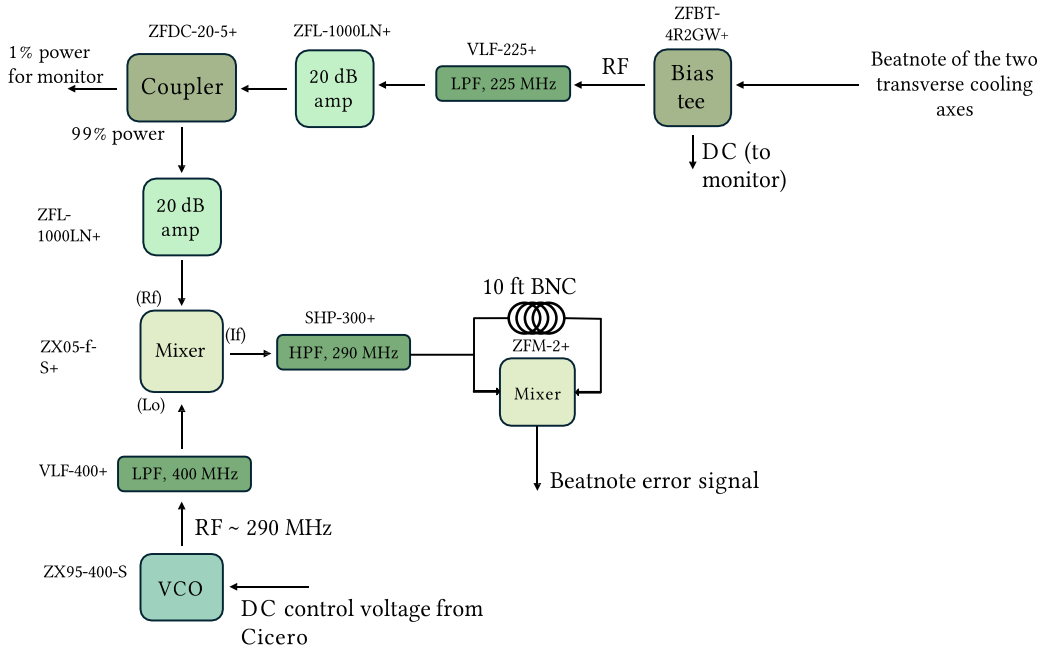

Figure 7.14: RF circuit used to beatnote lock the horizontal and vertical transverse cooling lasers. One of the lasers is aligned through an AOM generating a side band at +80 MHz which is then overlapped and beat with the other laser.

7.6 Conclusion

In conclusion, we have demonstrated the 2D transverse cooling (TC) of the SrOH molecular beam to increase the number of molecules in both the MOT and ODT by an order of magnitude. This technique, although ubiquitous in the field of molecular laser cooling, has never before been utilized to increase trap numbers. So far, TC has resulted in our experiments with an ODT having $\sim 10^4$ SrOH trapped molecules. This ODT number is currently limited by technical issues related to the RF MOT number, which we project can be improved upon by at least a factor of 2-3. As discussed in Chapter 9, this TC technique can be improved upon in a variety of ways including moving the TC region closer to the exit aperture of the cell, and moving the alignment optics in vacuum to prevent attenuation of TC light due to the finite reflectivity of the windows.

One must imagine [Abdullah] happy

Albert Camus, The Myth of [Abdullah] [Altered]

8

Challenges with Laser Cooling YbOH

The triatomic molecule YbOH has greater sensitivity to the *e*EDM than SrOH due to its higher mass leading to a larger effective electric field $\mathcal{E}_{\text{eff}}$. In fact, a trap of YbOH requires $\sim$ 100× fewer molecules for the same *e*EDM sensitivity as SrOH. Despite this promise, the complex structure of YbOH poses many challenges towards the goal of laser cooling, and SrOH was selected as a lighter but simpler system that can still effectively probe BSM physics. The purpose of this chapter is to shed light on these difficulties through some of the techniques implemented in attempting to wrangle YbOH, without going into specific experimental details which can be found in the theses of Ben Augenbraun, Alex Frenett, and Hiromitsu Sawaoka [98, 99, 140]. We first discuss in Sec. 8.1 the issue of photon scattering, after which we demonstrate

results related to the Zeeman-Sisyphus slowing of YbOH in Sec. 8.2. Lastly, we illustrate the mechanism of inner-shell excitations causing loss to "f-states" in Sec. 8.3. The YbOH molecular structure is similar to SrOH, but with a few important differences which are highlighted in this Chapter.

8.1 YbOH Photon Cycling

In the YbOH experiment, the molecule was produced in an identical way to SrOH but with a Ytterbium metal target. Various other production techniques were explored to improve beam flux and reduce its velocity as discussed in [140]. Although TC and photon cycling was demonstrated with YbOH [141], its main cooling transition has an FCF of $\sim$ 90% [142] which is considerably less diagonal than SrOH or CaOH. As a result, $\sim$19 lasers are required to scatter 20,000 photons before incurring a $1/e$ loss to unaddressed vibrational dark states. Additionally, only five repumping transitions have been studied to high resolution for YbOH, necessitating considerable time to conduct the spectroscopy to identify the rest. The VBRs of vibrational ground states in YbOH are shown in Table 8.1. An attempt to resolve the issue of needing such a high photon budget is discussed in Sec. 8.2 by utilizing a slowing method that does not rely on radiative cooling. However, even if efficiently cooled to a low enough velocity, the MOT relies on a certain number of photon scatters to establish initial trapping. The photon recoil velocity for YbOH where the $\tilde{X}^2\Sigma^+(000) \rightarrow \tilde{A}^2\Pi_{1/2}(000)$ cooling transition has a wavelength of 577 nm is

$$v_{\text{recoil}} = \frac{\hbar k}{2m} = 3.6 \text{ mm/s}. \tag{8.1}$$

For a scattering rate $R_{\text{sc}} = 1$ MHz and an initial velocity of 10 m/s, the number of photons required to turn the molecules around is given by

$$N_\gamma = \frac{\Delta v}{v_{\text{recoil}}} \approx 3000. \tag{8.2}$$

Table 8.1: Vibrational branching ratios and photon budgets in YbOH [142], where only the first five have been studied to high resolution. For the remaining states, they have either been studied in DLIF or their VBRs have been calculated.

State	VBR (%)	Cumulative Closure	Photons @ $1/e$ loss
(000)	89.3654	0.893654	9.40
(100)	9.1024	0.984677	65.26
(200)	0.9132	0.993810	161.55
$(02^{0}0)$	0.3347	0.997157	351.75
(300)	0.0669	0.997826	460.08
$(12^{0}0)$	0.0550	0.998376	615.77
(010, $N = 1$)	0.0540	0.998916	922.15
$f13(3/2)$ (000)	0.0200	0.999115	1130.21
(010; $N = 2$)	0.0180	0.999295	1418.55
$(02^{2}0)$	0.0160	0.999455	1834.60
(110; $N = 1$)	0.0100	0.999555	2246.38
$f13(3/2)$ (100)	0.0100	0.999655	2895.66
$f13(1/2)$ (000)	0.0067	0.999721	3586.79
$22^{0}0$	0.0050	0.999771	4369.82
(400)	0.0045	0.999816	5438.34
$(12^{2}0)$	0.0034	0.999850	6670.75
(110; $N = 2$)	0.0033	0.999883	8576.14
$f13(1/2)$ (100)	0.0033	0.999917	12000.42
$f13(3/2)$ (200)	0.0033	0.999950	19976.75
$03^{1}0$	0.0020	0.999970	33250.34
(210)	0.0019	0.999989	90165.35
$f13(1/2)$ (200)	0.0011	1.000000	–

Thus, without accounting for loss due to a finite photon budget, a minimum of 3,000 molecules are required to establish trapping. From Table 8.1, this requires repumping 13 states, including the f-states which are described in Sec. 8.3. As such, the laser cooling of YbOH hinges on either embarking on a years long journey to characterize and address the necessary repumps or coming up with some novel trapping scheme.

8.2 Zeeman-Sisyphus Deceleration of YbOH

For large enough energy gradients, Sisyphus cooling can result in appreciably more energy removal per photon scattered than radiative cooling. This motivated the use of a Zeeman-Sisyphus (ZS) decelerator as first proposed in Ref. [108] and initially demonstrated in CaOH [143]. Below we summarize the implementation of this technique in YbOH, where additional information can be found in Refs. [98, 99, 144].

8.2 a) Principles and Experimental Implementation

The Sisyphus technique is similar to what is described in Chapter 6 but with a few key differences. As shown in Fig. 8.1, the energy gradient is created via the application of a magnetic field gradient. Superconducting electromagnets create Tesla-scale magnetic fields that help remove a fixed amount of energy per stage where $\Delta E \approx 2\mu_B \mathscr{B}_{\max}$ where μ_B is the Bohr magneton and $\mathscr{B}_{\max}$ is the peak of the magnetic field gradient. The experiment relied on two magnet stages as shown in Fig. 8.2.

Instead of a dark state, the two spin rotation levels vary in the opposite way under an applied magnetic field. The Zeeman shift can be expressed as

$$\Delta E = g\mu_B m B, \tag{8.3}$$

for some applied magnetic field B, the state g-factor g, and spin projection along the z-direction m, where the applied magnetic field defines the quantization axis. For the ground state spin-rotation levels with

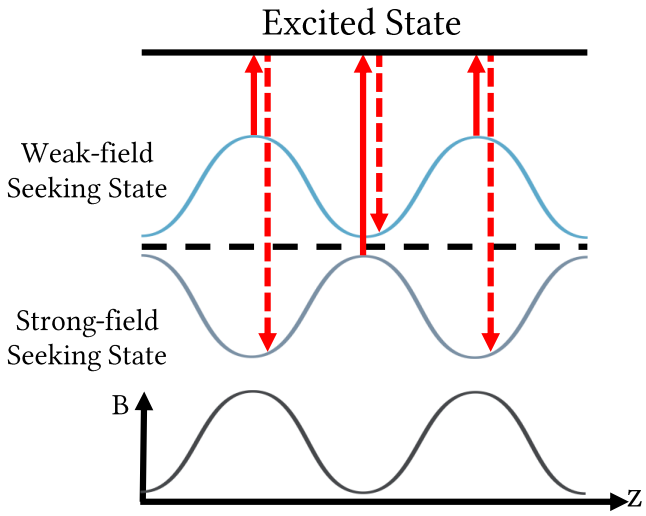

Figure 8.1: Level scheme of YbOH in the presence of a spatially varying magnetic field. Here, only two states are shown, where the weak and strong field seeking states behave opposite to each other.

labels $J = 1/2$ and $J = 3/2$, one can calculate the g-factors such that

$$g_J = g_S \frac{J(J+1) + S(S+1) - N(N+1)}{2J(J+1)}, \tag{8.4}$$

where $g_S \approx 2$. From this, $g_{J=\frac{1}{2}} \approx -2/3$ and $g_{J=\frac{3}{2}} \approx +2/3$. Then, depending on the sign of the m_J levels, the ground state energy either decreases with increasing magnetic field and is a high field seeking state (HFS), or it increases with increasing magnetic field and is a low field seeking state (LFS). The molecules are prepared in a LFS state, where they ride up the energy hill and lose kinetic energy. At the peak of the hill corresponding to the magnetic field maxima, they are optically pumped to the $\tilde{A}^2\Pi_{1/2}$ state and decay to the LFS state where they are unable to recover their lost kinetic energy and ride up another potential hill. This optical pumping step is then repeated two more times as shown in Fig. 8.2. Once molecules are produced in the cell, they undergo a state preparation stage after which they are brought to the cooling region via a 12″ octupole magnetic guide. They then undergo two cooling stages characterized by two magnetic field peaks as shown in Fig. 8.2, where three optical pumping steps result in the entropy loss needed for cooling.

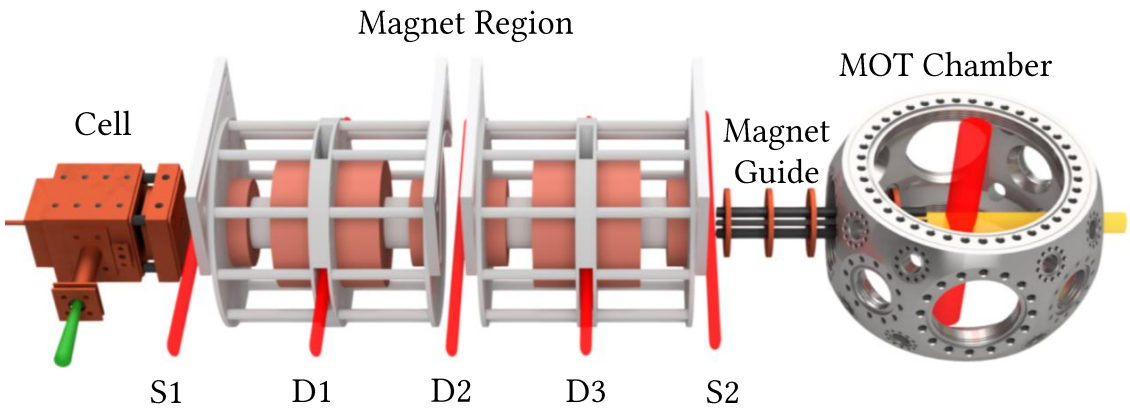

Figure 8.2: Schematic of the YbOH Zeeman-Sisyphus decelerator. The molecules are prepared in a HFS with a laser denoted by S1 after which they traverse the superconducting magnet region and undergo optical pumping steps given by D1, D2 and D3. Following this, they are state prepared using S2 in a LFS to be efficiently guided into the detection region.

The results of this slowing method are shown in Fig. 8.3. Here, we tuned the resonance of our detection laser to probe molecules at 18(3) m/s and switched the slowing on and off. As there is negligible natural population at 18 m/s in the beam, the presence of a peak in the condition that slowing is on is evidence that deceleration occurred.

8.2 b) Limitations of the ZS Deceleration of YbOH

Despite succesfully slowing the YbOH molecular beam, the ZS deceleration technique is limited in a number of ways that make it infeasible to implement in a trapped molecules experiment.

1. To slow to trappable velocities, the initial velocity of the molecular beam must be about ~35 m/s to start. Engineering a beam this slow results in much lower flux as shown in Refs. [140].

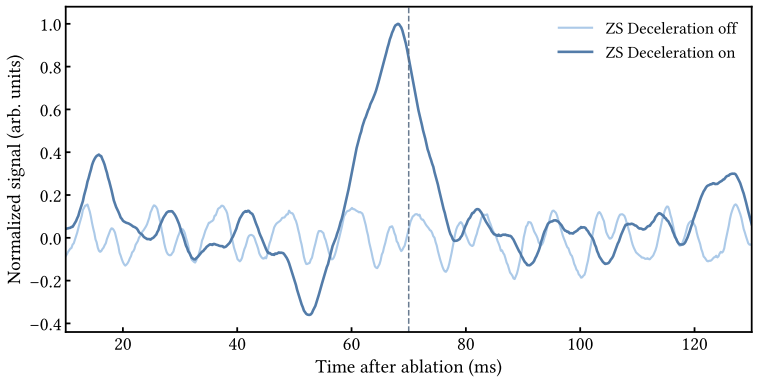

Figure 8.3: Time-of-flight data for a YbOH molecular beam looking at a velocity of 18 m/s. There is no natural population present at this velocity, meaning that the increase in signal when the deceleration is applied is due to the beam being slowed. The dashed line represents the expected arrival time of the unslowed beam, where the slowed beam arrives sooner implying a higher initial velocity.

2. Adding more magnetic field stages can result in a larger removal of energy. However, this adds technical complexity to the experiment, as well as additional loss through inefficiencies in the optical pumping steps.

3. The guide and bore size cut off much of the molecular beam. However, increasing these sizes can lead to helium build up issues in the magnet apparatus.

4. YbOH has a finite excited state g-factor. In the presence of a large magnetic field there is rotational mixing of the various sublevels which breaks rotational closure for the optical pumping steps.

This technique was first demonstrated in CaOH [143], where ZS deceleration resulted in fewer molecules trapped to MOT capture velocities compared to white light slowing due to the measures taken to ensure a slow initial beam. Consequently, such a technique needs further development to be a viable candidate for the slowing step in a molecular laser cooling experiment.

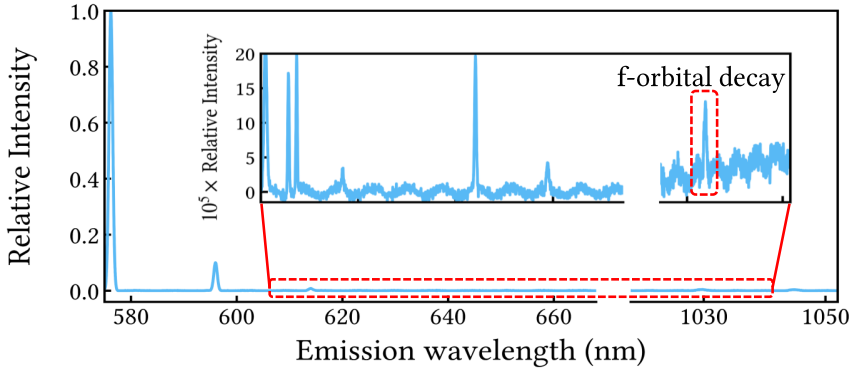

Figure 8.4: DLIF data showing decays to vibrational ground states in YbOH as well as the decay to a metastable f-state.

8.3 Inner Shell Excitations

Even if pursuing the radiative slowing and trapping of YbOH were viable, certain aspects of its molecular structure make repumping particular transitions nontrivial. Ytterbium has a ground state electronic configuration of $[\mathrm{Xe}]4f^{14}6s^2$, which after bonding to the OH results in a "hydrogen-like" configuration of $[\mathrm{Xe}]4f^{14}6s^1$ for the Yb^+ ion. The electronic states discussed in Chapter 2 are also present in YbOH, and describe the excitation of the outer s-shell electron to the $[\mathrm{Xe}]4f^{14}5d^1$ configuration. However, in YbF and YbOH, there exists a set of states corresponding to the excitation of an inner-shell electron from the f-orbital to the $[\mathrm{Xe}]4f^{13}6s^2$ configuration. Calculations done by Lan Cheng at JHU predicted a number of these states, each with their own vibrational manifold, sitting in between the $\tilde{X}^2\Sigma^+$ and $\tilde{A}^2\Pi_{1/2}$ levels. Through DLIF spectroscopy, one of these levels was observed at a wavelength of ~1030 nm at the 10^{-4} level as shown in Fig. 8.4, which is in good agreement with theory. These states have been studied in great detail in YbF, where their nature as well as spectroscopic labeling is presented in Ref. [145].

8.3 a) Repumping Challenges

The f-orbitals in YbOH are metastable states with lifetimes on the order of $\sim$ ms, which makes them quite challenging to repump. For a scattering rate of $\sim$ MHz, these states are visited every $1-5$ ms and would need to be repumped at a similar timescale, necessitating much higher powers then the mainline and first few repumpers, which require a few Watts each. In YbF, progress has been made to address this issue [145, 146], but given that there are other states of this nature at the $10^{-5}-10^{-4}$ level, it seems at present infeasible to design a laser cooling to account for these decays in YbOH.

8.4 Conclusion

To summarize, the issue of YbOH's poor FCFs as well as the existence of additional loss channels via the aforementioned f-states make it a challenging molecule to laser cool. This is in conjunction with its high mass and finite excited state g-factor which could add further complications to cooling, trapping, and conducting a precision measurement with it. Over time, perhaps with the development of more photon-efficient laser cooling schemes and novel trapping techniques, YbOH could once more become a viable candidate for a trapped molecule eEDM experiment. However, pivoting to SrOH has proven fruitful and has resulted in developments that could, in fact, be useful to YbOH in the future.

Sometimes maybe good,

Sometimes maybe [not good]

Gennaro Gattuso [Altered]

9

Conclusion and Outlook

In summary, we have demonstrated the full quantum control of SrOH and have identified the science states and have achieved improved trap numbers to enable a powerful, new search for ultralight dark matter (UDM). The proposed UDM search experiment is, at its heart, simply a measurement of μ-variation. Generally, the probing of non-trivial fundamental constants such as μ can probe a wide variety of unexpected BSM physics. With further technical upgrades to our laser cooling apparatus, as well as the implementation of proposed new techniques, even higher molecule numbers can make SrOH a potentially powerful probe of the eEDM, eventually being an order of magnitude more sensitive than the current state-of-the-art eEDM searches. Furthermore, the transverse cooling of the SrOH beam to provide an order of

magnitude improvement in the trapped molecule number makes laser cooling experiments with heavier, more complex molecules more viable. These molecules, such as Radium containing molecules like RaF or RaOH, have greater sensitivity to a wide variety of BSM physics, but sources for these molecules are very limited in flux. Thus, making use of the few molecules emanating from a CBGB source is extremely important.

9.1 Further Improvements to Molecule Numbers

One of the goals of the SrOH experiment, apart from the main focus of increasing the sensitivity to UDM, is to also test ways to improve trapped molecule numbers. While this has direct implications for the statistical uncertainty on the UDM experiment itself, such techniques can be generally applied to other direct laser cooling experiments.

9.1 a) Improved Transverse Cooling

Although demonstrating MOT and ODT number enhancements through transverse cooling is a significant improvement, its performance can be further increased, potentially resulting in an additional order of magnitude gain. Below we discuss a few key upgrades towards obtaining this goal.

Moving Closer to the Cell

For a molecular beam emerging from the cell with some finite solid angle, the width of the beam depends quadratically on how far away it is measured from the point at which it is produced. As such, moving the cooling light closer to the exit of the cell can result in a tight collimated beam with higher flux, yielding greater improvement in the trapped molecule number as shown in Fig. 9.1. From simulations (using the limiting apertures in the SrOH beamline), moving the transverse cooling region from 30 cm away from the

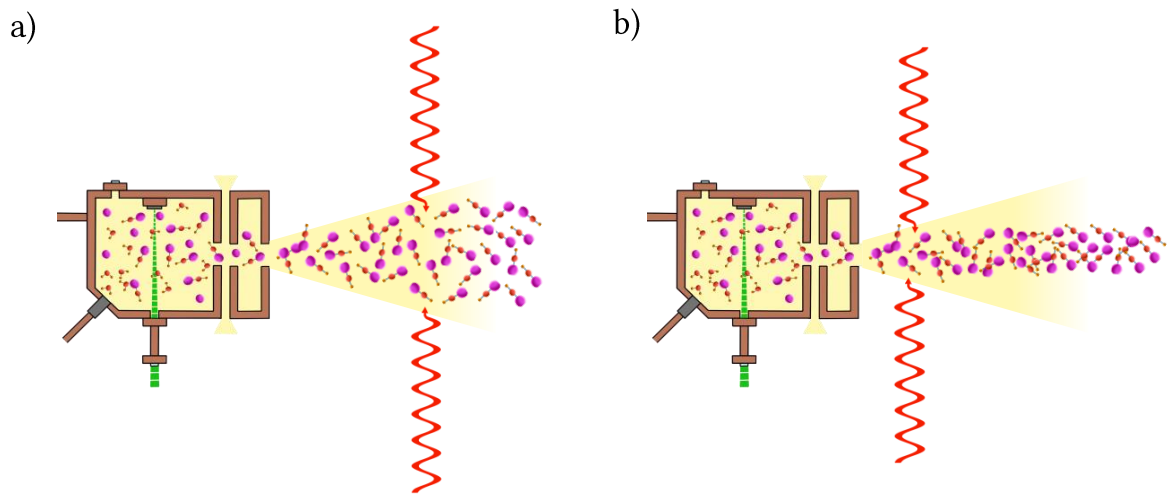

Figure 9.1: The collimated beam when transverse cooling at different distances away from the exit aperture of the cell where the schematic in b) shows a collimated beam with a smaller width when cooling closer to the cell than in a).

cell to a distance of 10 cm would increase the molecule number in the ODT by an additional factor of 10 to an overall factor of ~ 100 due to TC. Cooling very close to the cell is potentially difficult due to increased inelastic collisions with Helium atoms. As such, to fully optimize this technique, modifications of the beam box (including configuring the radiation shields to minimize these collisions), introducing optical access in both dimensions, and careful characterizations of the heat loads due to high laser powers are all crucial. Moreover, moving closer to the cell allows for molecules with higher capture velocities to be cooled and eventually trapped.

In-Vacuum Optics

On the SrOH experiment, although the transverse cooling light propagates over a distance of ~ 5 cm to produce a standing wave, blocking the light halfway along the window at 2.5 cm results in no change to the cooling performance. This can be attributed to the fact that over dozens of passes, the light is attenuated due to finite reflections from the four window surfaces. This effect is significant enough such that the low power towards the end of the cooling region leads to no appreciable additional cooling. Furthermore,

as mentioned previously, moving the cooling closer to the cell necessitates higher capture velocities and stronger cooling with longer interaction regions and higher powers. These issues can be addressed by moving the transverse cooling optics in-vacuum, using high reflectivity mirrors that lose little power even following the many reflections required to create the desired standing wave. One method is implemented by the ACME experiment [147]. Here, a state preparation laser is multi-passed via a set of in-vacuum prisms before the beam is collimated through an electrostatic lens. Implementing such a technique in the beambox can allow for the highest available power in the cooling light while being close to the exit aperture of the cell.

9.1 b) Push Beam

From simulations in Ref. [106], TC in tandem with a "push" beam has the potential to further increase MOT and ODT numbers. The push beam is characterized by light that propagates with the molecular beam at the main cooling frequency, which give the molecules a forward boost. This prevents the molecules from being over-slowed and turned around due to imprecise frequency cutoffs in white light broadening. In reality, the over-slowing effect is taken care of by chirped-slowing which allows us to carefully engineer the lowest velocity class that we laser cool. However, a push beam may help us cool slower molecules that are not trapped in the first place. For example, on the SrOH experiment, the total slowing time is $\sim$ 20 ms. This is the time it takes a molecule with an average velocity of 75 m/s to traverse the 1.5 m beamline, which means that it is likely that slower molecules present in the beam do not end up in the MOT as they take too long to arrive. As such, giving these slower molecules a boost to the MOT capture velocity can help improve MOT and ODT numbers.

9.1 c) ODT Size

As we discussed in Chapter 6, the ODT trap depth increases with the intensity of the trap light. However, in the same way that compressing the trapped cloud size via a CB MOT results in better ODT loading efficiency through improved mode-matching, increasing the ODT waist can have the same effect given enough power is present in the beam. We can change the ODT size by using a pair of liquid crystal tunable lenses which act like a telescope, where an adjustable input voltage can result in different degrees of magnification. Being able to do this dynamically also could have advantages, where the size can be ramped over time depending on the size and temperature of the molecular cloud.

9.2 Conveyor-Like Forces

The mechanism used in the conveyor-belt MOT allows for rapid compression of the molecular cloud through additional frequency components. Through simulation, we can study the effect of adding additional frequency components in other laser cooling stages in our experiment to enhance their affects. For example, work is being done currently to predict the effect of adding an additional sideband in a DC red-MOT, to see if the additional frequency can aid in the remixing of dark states and provide a conveyor effect that results in comparable or even better trapping than in an RF MOT. Ideally, it would be experimentally convenient to implement a DC MOT as the RF amplifiers and tank circuit which deliver the varying magnetic field have thus far proven to be problematic on our experiment, needing regular maintenance. Furthermore, utilizing this principle to come up with a novel frequency component scheme for TC could perhaps allow for higher capture velocities without just increasing laser power. Details of such simulations are described in Christian Hallas' thesis [148].

9.3 Technical Upgrades to the Experiment

This section serves as a checklist for potential technical upgrades which can be made to the experiment to facilitate the future precision measurement, including

1. Test ablation with a Strontium Titanate target, to avoid the issue of oxidation with the regular Strontium metal target.

2. Implement a DC MOT with additional frequency components to improve trapping.

3. Cryogenically cool the MOT chamber to improve the blackbody lifetime of bending mode science states in the ODT.

4. Chirp the main slowing laser to provide higher effective intensity per velocity class. This would require the use of Optigrate volume Bragg gratings to combine closely spaced wavelengths.

5. Use fiber EOMs on the SFG seeds to avoid aligning through the EOM crystals, helping to establish a more precise frequency cutoff and prevent power loss due to degradation of the beam shape from the additional optical element.

6. Replace the double-pass AOD with either a frequency chirp or cavity setup to prevent the power loss through the AOD and the necessary fiber coupling after. This would allow for more power for sub-Doppler cooling and a DC MOT, and it would provide us with the option of turning down the MOT laser fiber amplifiers.

7. Attempt to directly load the ODT from the CB MOT to prevent additional expansion during the sub-Doppler cooling step.

8. Utilize a crossed ODT or very weak lattice to improve capture and trapping.

9. Attempt to modify the production of the experiment and have a continuous beam source via thermal desorption.

9.4 Future Directions

The next step for the SrOH experiment is to fully characterize the UDM science states, specifically $\tilde{X}^2\Sigma^+(200)$ and $\tilde{X}^2\Sigma^+(03^10)$, by driving various rotational manifolds with microwaves. Moreover, applying electric and magnetic fields will allow for Zeeman and Stark spectroscopy of these levels to help narrow down the set of rotational levels to be used in the dark matter measurement. Following this, the experiment will possess all the ingredients necessary to conduct the measurement and carry out a rigorous systematic survey to probe theories of UDM. The experiment can then take various directions following the dark matter measurement, including preparation to measure the *e*EDM or development of novel techniques to improve molecular flux and trap numbers.

A

Double-Pass AOD

When aligning the double-pass acousto-optic deflector, there are a few considerations. First, it is aligned so that the first-order efficiency is optimal. To do this, the VCO frequency is set to a central value, and the laser is carefully aligned through the AOD to maximize the single-pass transmission. Following this, the efficiencies are checked at the other frequencies. If the efficiency curve is skewed too far one way, the setup is reoptimized for a central frequency in the opposite direction.

Once the single-pass efficiency is optimized, the cat's eye is set up to have good double-pass fiber-coupling efficiency downstream over a wide range of frequencies. The way a cat's eye works is as follows: a lens "collimates" the diffracted beams, which are then retro-reflected. The key principle is that, if the lens is placed a focal length away, the rays of light will always be perpendicular to the surface of the mirror,

and thus perfectly retro-reflected back regardless of the diffraction angle that the first-order ray makes with the zeroth order. The alignment procedure is as follows:

1. Place a 100 mm lens a focal length away from the center of the AOD crystal. This will not be precise. Lens tubes before and after the AOD can be used as stoppers; this will be made clear later. A tip to ensure the lens is roughly in the right place is to measure the distance between the zeroth- and first-order beams on the lens, propagate it a very far distance, and make sure that the distance between those beams remains relatively constant. Lock down this lens.

2. Place a mirror a focal length away from the lens. To ensure that this is the case, coarsely adjust the mirror to retro-reflect the light back through the AOD and have it propagate somewhere far away. Make small adjustments to the mirror's position relative to the lens, and make sure that the light is collimated far away by tracking its size at different distances. This positioning can be done quite well by hand.

3. Once all this is done, set up fiber coupling as close as possible to the output of the double-pass AOD. Using the mirror, and setting the VCO voltage to 3 V, corresponding to a frequency of 110 MHz somewhere in the middle of the range, retro-reflect the first-order beam back on itself. Take an efficiency curve of the second-order/first-order efficiency and ensure it is as flat as possible.

4. Fiber-couple the light, and take a fiber-coupling efficiency curve as a function of the AOD frequency. At this point, it is likely that the double-pass setup is not perfectly aligned, which will mean that the curve will not look flat. In Fig. A.1(a), the coupling efficiency drops off more steeply at higher frequencies and higher deflection angles. When the actual center distance of the crystal to the lens was measured, it was too small relative to the focal length.

5. A lens tube can be used as a spacer, or the AOD can be placed on a translation stage. The spacer

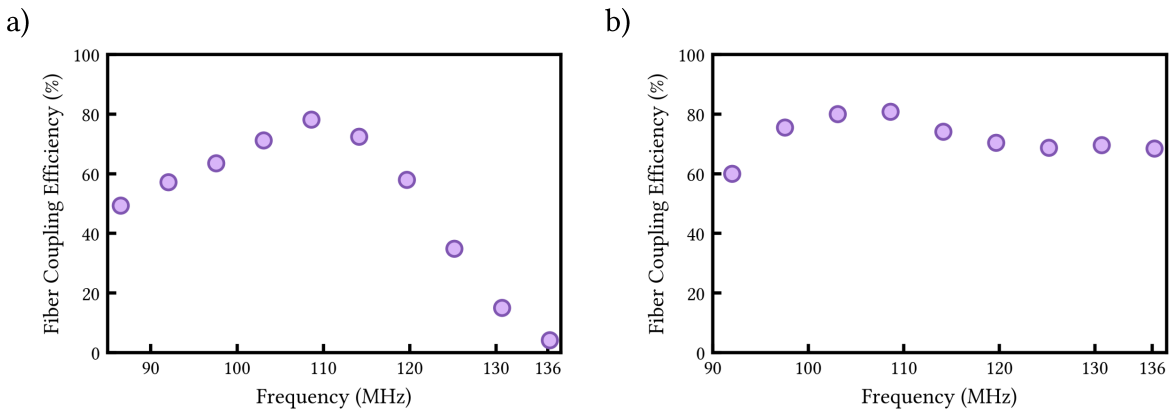

Figure A.1: Fiber coupling efficiencies after a double-pass AOD for a range of drive frequencies. a) The cats-eye configuration was not perfect, leading to poor efficiencies for high frequencies. b) Adjusting the collimating lens to improve the cats-eye and get better all efficiency.

is placed 1 mm away from the AOD, and the AOD is then shifted until it hits the lens tube. The AOD is then slightly tilted to recover the first-order efficiency. Repeating steps 1–4 gives a flatter efficiency curve, as shown in Fig. A.1(b).

B

Polarization Gradient Cooling

As discussed in [149], polarization gradient cooling (PGC) Polarization gradient cooling, specifically with circularly polarized light, requires more formal treatment to understand. It is often described as "Sisyphus-like", but does not quite possess the simplicity of balls rolling up and down hills or in fact, a mythological Greek figure subject to eternal punishment in the underworld. Despite being more complicated, it is still useful to describe as its polarization configuration is what is implemented in most molecular laser cooling experiments. As shown in Fig. B.1, two counter-propagating beams of orthogonal, circular polarization combine to form a beam with linear polarization that rotates in space. To see this, following Ref. [149] we take the electromagnetic fields such that

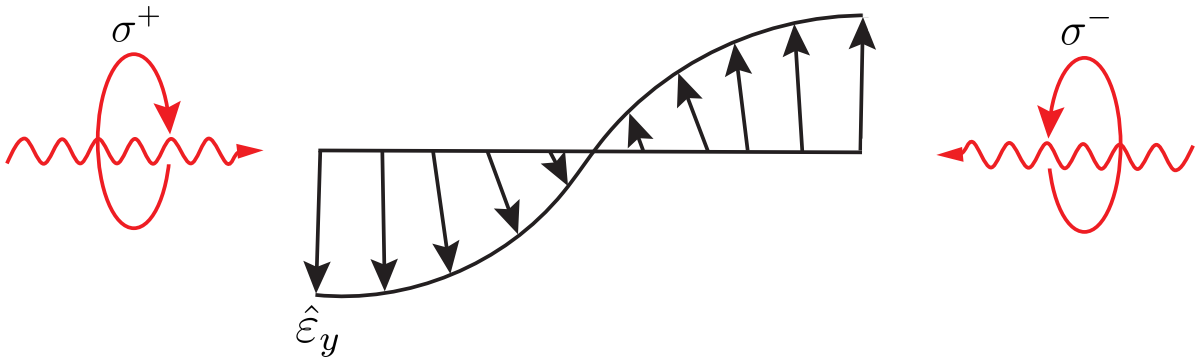

Figure B.1: $\sigma^+\sigma^-$ light counter-propagating relative to each other to form a "corkscrew", or a spatially rotating linear polarization.

$$\vec{E}_{\sigma^+}^{(+z)} = \frac{E_0}{\sqrt{2}}\left[\hat{x}\sin(kz-\omega t) + \hat{y}\cos(kz-\omega t)\right], \tag{B.1}$$

$$\vec{E}_{\sigma^-}^{(-z)} = \frac{E_0}{\sqrt{2}}\left[-\hat{x}\sin(kz+\omega t) + \hat{y}\cos(kz+\omega t)\right], \tag{B.2}$$

where $\vec{E}_{\sigma^+}^{(+z)}$ and $\vec{E}_{\sigma^-}^{(-z)}$ are the right (left) handed circularly polarized laser beams propagating in the $+z$ ($-z$) direction. When these combine, we get a field $\vec{E}(z,t)_{\text{Corkscrew}}$

$$\vec{E}(z,t) = \vec{E}_{\sigma^+}^{(+z)} + \vec{E}_{\sigma^-}^{(-z)} \tag{B.3}$$

$$= \sqrt{2}E_0\cos(\omega t)\left[\hat{x}\sin(kz) + \hat{y}\cos(kz)\right]. \tag{B.4}$$

which describes light with a linear polarization that rotates in space. Because the light twists in this way, this cooling is often described as "corkscrew" cooling.

Taking the example of a system with $J = 1 \rightarrow J = 2$ as shown in Fig. B.2, we can describe what the atom experiences in this rotating polarization. First, we define the equilibrium state for the atom at rest, where we can take the quantization axis as the local polarization which at $z = 0$ is $\hat{\varepsilon}_y$. We can change basis

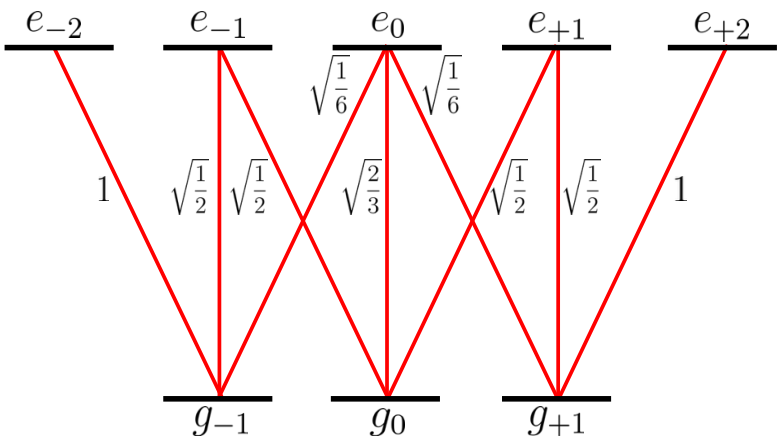

Figure B.2: Energy levels in toy model used to describe $\sigma^+\sigma^-$ polarization gradient cooling.

to obtain ground states $|g_{-1}\rangle_y$, $|g_0\rangle_y$ and $|g_{+1}\rangle_y$ as eigenstates of J_y, and calculate their optical pumping rates from the Clebsch-Gordon coefficients given in Fig. B.2 such that

$$|g_{-1}\rangle_y \to |g_0\rangle_y \;\propto\; \left(\frac{1}{\sqrt{2}}\right)^4 = \frac{1}{4}, \tag{B.5}$$

$$|g_0\rangle_y \to |g_{-1}\rangle_y \;\propto\; \left(\sqrt{\frac{2}{3}}\right)^2 \left(\frac{1}{\sqrt{6}}\right)^2 = \frac{1}{9}, \tag{B.6}$$

where the steady state populations of $|g_0\rangle_y$, $|g_{\pm1}\rangle_y$ are equal to $9/17$ and $4/17$. Moreover, since the π transition starting at $|g_0\rangle_y$ is $4/3$ as intense as the two π transitions starting from $|g_{\pm1}\rangle_y$, the light shift looks like:

$$\Delta_0' = \frac{4}{3}\Delta_1' \tag{B.7}$$

The atom at rest has its population accumulate in the $|g_0\rangle_y$ state, with no imbalance in either of the other two ground state. Suppose now that the atom is moving with some velocity v along the z-axis, such that:

$$z = vt \tag{B.8}$$

In its rest frame which moves with the same velocity v, the atom sees a linear polarization ϕ which rotates

around the z-axis

$$\phi = -kvt, \tag{B.9}$$

where k is the k-vector of the light and the atoms energy levels are light shifted as shown in Fig. B.3. Larmor's theorem tells us that in the moving rotating frame, a fictitious inertial field will appear as a result of the rotation. One way to think about this is in terms of a charged particle moving with velocity $\vec{v}$ in a magnetic field $\vec{B}$ which experiences a force

$$\vec{F} = q\vec{v} \times \vec{B}. \tag{B.10}$$

Moving into a rotating frame with rotational frequency $\vec{\omega}$ for a particle of mass m gives a Coriolis force

$$\vec{F}_{\text{Coriolis}} = -2m\vec{\omega} \times \vec{v}. \tag{B.11}$$

Now, if the frequency is selected to match the cyclotron frequency $\omega = -\frac{qB}{m}$ the Coriolis force becomes

$$\vec{F} = -q\vec{v} \times \vec{B}. \tag{B.12}$$

The Coriolis force cancels out the effect of the magnetic field, where entering the rotating frame has created a "fictitious" magnetic field in the opposite direction. The same principle applies in quantum mechanics, where the Hamiltonian gains an extra inertial term in terms of the z-component of the angular momentum operator

$$V_{\text{rot}} = kvJ_z. \tag{B.13}$$

Since J_z has nonzero matrix elements among the eigenstates of J_y, this inertial term introduces couplings proportional to kv between $|g_0\rangle_y$ and $|g_{\pm 1}\rangle_y$. These are "non-adiabatic" since they vanish when $v = 0$. To

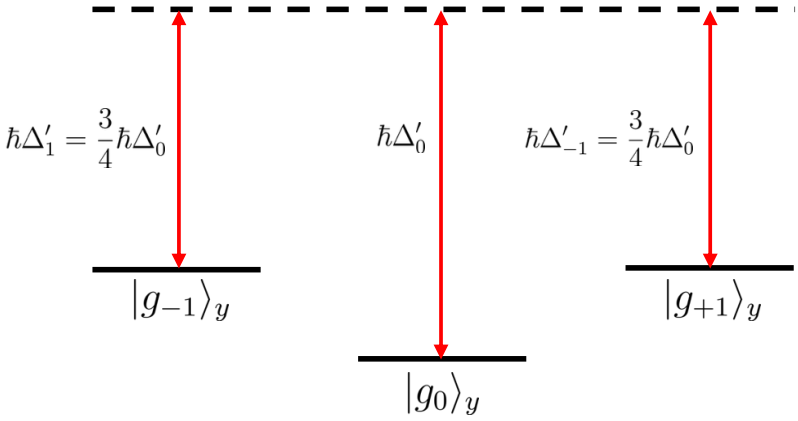

Figure B.3: Lightshifts experienced by the atom as it traverses the rotating polarization.

first order, the wavefunctions are given by

$$|g_0\rangle_y = |g_0\rangle_y + \frac{kv}{\hbar\sqrt{2}(\Delta'_0 - \Delta'_1)}\left[|g_{+1}\rangle_y + |g_{-1}\rangle_y\right], \tag{B.14}$$

$$|g_{\pm1}\rangle_y = |g_{\pm1}\rangle_y + \frac{kv}{\hbar\sqrt{2}(\Delta'_1 - \Delta'_0)}|g_0\rangle_y, \tag{B.15}$$

where the energies remain the same. Moreover, to first order, the steady state populations given by the steady state density matrix are the same. Calculating $\langle J_z\rangle$,

$${}_y\langle g_0|J_z|g_0\rangle_y = -\frac{2\hbar kv}{\Delta'_0 - \Delta'_1}, \tag{B.16}$$

$${}_y\langle g_{+1}|J_z|g_{+1}\rangle_y = \frac{\hbar kv}{\Delta'_1 - \Delta'_0}. \tag{B.17}$$

which, when weighted by the populations gives

$$\langle J_z\rangle_{\text{st}} = -\frac{2\hbar kv}{\Delta'_0 - \Delta'_1}\left(\frac{9}{17} - \frac{2}{17} - \frac{2}{17}\right) = \frac{40\hbar kv}{17\,\Delta'_0}. \tag{B.18}$$

In general, $\langle J_z\rangle_{\text{st}}$ can be thought of as a way to measure the population imbalance between states of different

angular momentum projection m, or a measure of how "oriented" the atom is along the z direction. As such, we have for a system with $J = 1$

$$\langle J_z \rangle = \mathrm{Tr}(\rho J_z) \tag{B.19}$$

where the density matrix ρ can be expressed as

$$\rho = \Sigma_j \, \rho_j |m_j\rangle\langle m_j|, \tag{B.20}$$

where ρ_j is the population in the state m_j. Substituting into Eq. (4.21), we get

$$\langle J_z \rangle = \mathrm{Tr}\left(\sum_j \rho_j |m_j\rangle\langle m_j| J_z \right), \tag{B.21}$$

$$\langle J_z \rangle = \mathrm{Tr}\left(\sum_j m_j \rho_j |m_j\rangle \right), \tag{B.22}$$

$$\langle J_z \rangle = \sum_j m_j \rho_j |m_j\rangle, \tag{B.23}$$

$$\langle J_z \rangle = \Pi_{+1} - \Pi_{+1}, \tag{B.24}$$

where the steady state populations in the $m = \pm 1$ states are written as $\Pi_{\pm 1}$. From Eq. (4.20)

$$\Pi_{+1} - \Pi_{-1} = \frac{40kv}{17\Delta_0'}. \tag{B.25}$$

Suppose the atom moves forward $z \geq 0$, $v > 0$ and $\Delta' < 0$ (red detuning), then $\Pi_{-1} > \Pi_{+1}$, and from Fig. B.2 the atom scatters σ^- light going in the $-z$ direction 6 times more than σ^+ as shown by the Clebsch-Gordan coefficients, leading to a force.

To summarize, when a moving atom is in a standing wave of light composed of counter-propagating beams of opposite circular polarization, it experiences a spatially rotating linear polarization. Due to a

finite optical pumping time, the internal state of the atom lags behind the polarization; this results in a phase accumulation which breaks the symmetry between the populations in magnetic sublevels, leading to preferential scattering from one of the beams and a force in that direction. Although the force comes from a scattering rate imbalance between the two lasers, it is still a sub-Doppler technique as the effect arises from the imbalance of populations in the ground state, and not due to the Doppler effect.

C

Molecular Constants and Frequencies

In Chapter 2, we discussed the molecular structure of SrOH and the various frequency splittings that arose. In this Appendix, we give a more comprehensive list of the molecular constants as well as relevant transition frequencies used in the laser cooling of SrOH as well as those observed during spectroscopy.

Table C.1: SrOH Molecular Constants (1/2).

State	T	B	D	γ	q
$\tilde{X}^2\Sigma^+(000)$	0	7.470822 GHz [150]	6.519 kHz [150]	72.774 MHz [150]	0
$\tilde{X}^2\Sigma^+(100)$	15.798793 THz [151]	7.426907 GHz [150]	6.538 kHz [150]	72.210 MHz [150]	0
$\tilde{X}^2\Sigma^+(200)$	31.450417 THz [151]	7.384788 GHz [151]	–	72.775 MHz [151]	0
$\tilde{X}^2\Sigma^+(300)$	–	–	–	–	0
$\tilde{X}^2\Sigma^+(010)$	10.903122 THz [152]	7.452243 GHz [150]	6.624 kHz [150]	72.240 MHz [150]	-11.855 MHz [150]
$\tilde{X}^2\Sigma^+(0200)$	21.084044 THz [152]	7.440990 GHz [150]	6.725 kHz [150]	71.736 MHz [150]	–
$\tilde{X}^2\Sigma^+(0220)$	21.991186 THz [152]	7.433287 GHz [150]	6.718 kHz [150]	71.589 MHz [150]	-11.370 MHz [150]
$\tilde{X}^2\Sigma^+(0310)$	–	7.429631 GHz [150]	6.887 kHz [150]	71.135 MHz [150]	-12.484 MHz [150]
$\tilde{X}^2\Sigma^+(0330)$	33.320073 THz [151]	7.413208 GHz [151]	–	–	–
$\tilde{X}^2\Sigma^+(110)$	26.701915 THz (est.)	7.408171 GHz (est.)	0 (est.)	71.650 MHz (est.)	-11.992 MHz (est.)
$\tilde{A}^2\Pi_{1/2}(000)$	435.975371 THz [153]	7.611350 GHz [153]	6.516 kHz [153]	–	-5.996 MHz [153]
$\tilde{A}^2\Pi_{1/2}(100)$	452.227030 THz [151]	7.566600 GHz [151]	6.486 kHz [151]	–	-5.843 MHz [151]
$\tilde{A}^2\Pi_{3/2}(000)$	443.875441 THz [153]	7.611350 GHz [153]	6.516 kHz [153]	–	-5.996 MHz [153]
$\tilde{A}^2\Pi_{3/2}(100)$	460.156960 THz [151]	7.566600 GHz [151]	6.486 kHz [151]	–	-5.843 MHz [151]
$\tilde{A}(010)\,^2\Delta_{3/2}$	447.303148 THz [154]	7.586308 GHz [154]	6.553 kHz [154]	–	-10.912 MHz [154]
$\tilde{A}(010)\,\mu^2\Sigma^+$	447.380405 THz [154]	7.589396 GHz [154]	6.676 kHz [154]	–	-10.912 MHz [154]
$\tilde{A}(010)\,^2\Delta_{5/2}$	455.217639 THz [154]	7.586308 GHz [154]	6.553 kHz [154]	–	-10.912 MHz [154]
$\tilde{A}(010)\,\kappa^2\Sigma^-$	455.413554 THz [154]	7.586128 GHz [154]	6.553 kHz [154]	–	-10.912 MHz [154]
$\tilde{B}^2\Sigma^+(000)$	490.985248 THz [155]	7.561965 GHz [155]	6.446 kHz [155]	-4.337997 GHz [155]	0
$\tilde{B}^2\Sigma^+(100)$	506.975458 THz [155]	7.514898 GHz [155]	6.535 kHz [155]	-4.263049 GHz	–
$\tilde{B}^2\Sigma^+(010)$	503.002009 THz [152]	7.534180 GHz [152]	6.884 kHz [152]	-4.211185 GHz [152]	-10.858 MHz [152]
$\tilde{B}^2\Sigma^+(0200)$	514.101405 THz [152]	7.514268 GHz [152]	7.089 kHz [152]	-4.289730 GHz [152]	-9.653 MHz [152]
$\tilde{B}^2\Sigma^+(0220)$	515.081816 THz [152]	7.506168 GHz [152]	7.008 kHz [152]	-4.202910 GHz [156]	-9.653 MHz [152]
$\tilde{B}^2\Sigma^+(200)$	522.965668 THz (est.)	7.467830 GHz (est.)	0 (est.)	-4.188101 GHz (est.)	–
$\tilde{B}'^2\Sigma^+(000)$	779.592605 THz [156]	7.977366 GHz [156]	7.102 kHz [156]	79.535 MHz [156]	0
$\tilde{C}^2\Pi_{1/2}(000)$	817.911379 THz [156]	7.634608 GHz [156]	6.364 kHz [156]	–	-17.902 MHz [156]
$\tilde{C}^2\Pi_{3/2}(000)$	819.389997 THz [156]	7.634608 GHz [156]	6.364 kHz [156]	–	-17.902 MHz [156]
$\tilde{D}^2\Sigma^+(000)$	830.474215 THz [156]	7.735845 GHz [156]	113.921 kHz [156]	585.495 MHz [156]	0
Predicted Δ	606.210329 THz [157]	–	–	–	–

Table C.2: SrOH Molecular Constants (2/2).

State	q_D	p	A_D	ϵ	b_F	c
$\tilde{X}^2\Sigma^+(000)$	–	–	–	–	1.713 MHz [158]	1.673 MHz [158]
$\tilde{X}^2\Sigma^+(100)$	–	–	–	–	–	–
$\tilde{X}^2\Sigma^+(200)$	–	–	–	–	–	–
$\tilde{X}^2\Sigma^+(300)$	–	–	–	–	–	–
$\tilde{X}^2\Sigma^+(010)$	0.025 kHz [150]	-1.030 MHz [150]	–	–	–	–
$\tilde{X}^2\Sigma^+(0200)$	–	–	–	–	–	–
$\tilde{X}^2\Sigma^+(0220)$	–	–	–	–	–	–
$\tilde{X}^2\Sigma^+(0310)$	0.034 kHz [150]	-1.670 MHz [150]	–	–	–	–
$\tilde{X}^2\Sigma^+(0330)$	–	–	–	–	–	–
$\tilde{X}^2\Sigma^+(110)$	0 (est.)	-899.377 kHz (est.)	–	–	–	–
$\tilde{A}^2\Pi_{1/2}(000)$	–	-4.293046 GHz [153]	2.100 MHz [153]	–	–	–
$\tilde{A}^2\Pi_{1/2}(100)$	–	-4.290390 GHz [151]	2.139 MHz [151]	–	–	–
$\tilde{A}^2\Pi_{3/2}(000)$	–	-4.293046 GHz [153]	2.100 MHz [153]	–	–	–
$\tilde{A}^2\Pi_{3/2}(100)$	–	-4.290390 GHz [151]	2.139 MHz [151]	–	–	–
$\tilde{A}(010)\,^2\Delta_{3/2}$	–	-4.314013 GHz [154]	1.199 MHz [154]	-2.371358 GHz [154]	–	–
$\tilde{A}(010)\,\mu^2\Sigma^+$	–	-4.314013 GHz [154]	1.199 MHz [154]	-2.371358 GHz [154]	–	–
$\tilde{A}(010)\,^2\Delta_{5/2}$	–	-4.314013 GHz [154]	1.199 MHz [154]	-2.371358 GHz [154]	–	–
$\tilde{A}(010)\,\kappa^2\Sigma^-$	–	-4.314013 GHz [154]	1.199 MHz [154]	-2.371358 GHz [154]	–	–
$\tilde{B}^2\Sigma^+(000)$	–	–	–	–	–	–
$\tilde{B}^2\Sigma^+(100)$	–	–	–	–	–	–
$\tilde{B}^2\Sigma^+(010)$	-0.021 kHz [152]	–	–	–	–	–
$\tilde{B}^2\Sigma^+(0200)$	-0.354 kHz [152]	–	–	–	–	–
$\tilde{B}^2\Sigma^+(0220)$	-0.354 kHz [152]	–	–	–	–	–
$\tilde{B}^2\Sigma^+(200)$	–	–	–	–	–	–
$\tilde{B}'^2\Sigma^+(000)$	–	–	–	–	–	–
$\tilde{C}^2\Pi_{1/2}(000)$	–	-1.221444 GHz [156]	-6.850 MHz [156]	–	–	–
$\tilde{C}^2\Pi_{3/2}(000)$	–	-1.221444 GHz [156]	-6.850 MHz [156]	–	–	–
$\tilde{D}^2\Sigma^+(000)$	–	–	–	–	–	–
Predicted Δ	–	–	–	–	–	–

Table C.3: SrOH Repumping Transitions

Transition	Frequency (THz)	Wavelength (nm)
$\tilde{X}^2\Sigma^+(000), N=1 \rightarrow \tilde{A}^2\Pi_{1/2}(000), J=1/2$	435.968228	688
$\tilde{X}^2\Sigma^+(100), N=1 \rightarrow \tilde{B}^2\Sigma^+(000), N=0$	475.171831	631
$\tilde{X}^2\Sigma^+(200), N=1 \rightarrow \tilde{B}^2\Sigma^+(100), N=0$	475.508818	630
$\tilde{X}^2\Sigma^+(010), N=1 \rightarrow \tilde{B}^2\Sigma^+(000), N=0$	480.074325	624
$\tilde{X}^2\Sigma^+(010), N=2 \rightarrow \tilde{B}^2\Sigma^+(000), N=0$	480.044615	624
$\tilde{X}^2\Sigma^+(010), N=2 \rightarrow \tilde{A}(010)\kappa^2\Sigma^-$	444.478795	675
$\tilde{X}^2\Sigma^+(02^00), N=1 \rightarrow \tilde{B}^2\Sigma^+(000), N=0$	469.887153	638
$\tilde{X}^2\Sigma^+(02^20), N=2 \rightarrow \tilde{A}^2\Pi_{1/2}(0200), J=1/2$	435.952910	688
$\tilde{X}^2\Sigma^+(300), N=1 \rightarrow \tilde{A}^2\Pi_{1/2}(200), J=1/2$	421.360628	711
$\tilde{X}^2\Sigma^+(110), N=1 \rightarrow \tilde{B}^2\Sigma^+(010), J=1/2$	476.519898	629
$\tilde{X}^2\Sigma^+(110), N=2 \rightarrow \tilde{B}^2\Sigma^+(010), J=1/2$	476.490362	629
$\tilde{X}^2\Sigma^+(1200), N=1 \rightarrow \tilde{B}^2\Sigma^+(0200), J=1/2$	477.614315	628
$\tilde{X}^2\Sigma^+(200), N=1 \rightarrow \tilde{A}^2\Pi_{1/2}(100), J=1/2$	420.768345	713

References

[1] E. S. Shuman, J. F. Barry, and D. DeMille, "Laser cooling of a diatomic molecule", Nature **467**, 820–823 (2010).

[2] E. L. Raab, M. Prentiss, A. Cable, S. Chu, and D. E. Pritchard, "Trapping of neutral sodium atoms with radiation pressure", Phys. Rev. Lett. **59**, 2631–2634 (1987).

[3] J. F. Barry, D. J. McCarron, E. B. Norrgard, M. H. Steinecker, and D. DeMille, "Magneto-optical trapping of a diatomic molecule", Nature **512**, 286–289 (2014).

[4] S. Truppe, H. J. Williams, N. J. Fitch, M. Hambach, T. E. Wall, E. A. Hinds, B. E. Sauer, and M. R. Tarbutt, "An intense, cold, velocity-controlled molecular beam by frequency-chirped laser slowing", New Journal of Physics **19**, 022001 (2017).

[5] S. Truppe, H. J. Williams, M. Hambach, L. Caldwell, N. J. Fitch, E. A. Hinds, B. E. Sauer, and M. R. Tarbutt, "Molecules cooled below the doppler limit", Nature Physics **13**, 1173–1176 (2017).

[6] I. Kozyryev, L. Baum, K. Matsuda, B. L. Augenbraun, L. Anderegg, A. P. Sedlack, and J. M. Doyle, "Sisyphus laser cooling of a polyatomic molecule", Phys. Rev. Lett. **118**, 173201 (2017).

[7] D. J. McCarron, M. H. Steinecker, Y. Zhu, and D. DeMille, "Magnetic trapping of an ultracold gas of polar molecules", Phys. Rev. Lett. **121**, 013202 (2018).

[8] T. K. Langin, V. Jorapur, Y. Zhu, Q. Wang, and D. DeMille, "Polarization enhanced deep optical dipole trapping of Λ-cooled polar molecules", Phys. Rev. Lett. **127**, 163201 (2021).

[9] L. Anderegg, B. L. Augenbraun, Y. Bao, S. Burchesky, L. W. Cheuk, W. Ketterle, and J. M. Doyle, "Laser cooling of optically trapped molecules", Nat. Phys. **14**, 890–893 (2018).

[10] S. Ding, Y. Wu, I. A. Finneran, J. J. Burau, and J. Ye, "Sub-doppler cooling and compressed trapping of YO molecules at μK temperatures", Phys. Rev. X **10**, 021049 (2020).

[11] C. Hallas, N. B. Vilas, L. Anderegg, P. Robichaud, A. Winnicki, C. Zhang, L. Cheng, and J. M. Doyle, "Optical trapping of a polyatomic molecule in an ℓ-type parity doublet state", Phys. Rev. Lett. **130**, 153202 (2022).

[12] H. Sawaoka, A. Nasir, A. Lunstad, M. Li, J. Mango, Z. D. Lasner, and J. M. Doyle, "Optical trapping of SrOH molecules for dark matter and T-violation searches", Phys. Rev. Research **8**, 013100 (2026).

[13] C. Ospelkaus, S. Ospelkaus, L. Humbert, P. Ernst, K. Sengstock, and K. Bongs, "Ultracold heteronuclear molecules in a 3D optical lattice", Phys. Rev. Lett. **97**, 120402 (2006).

[14] L. Christakis, J. S. Rosenberg, R. Raj, S. Chi, A. Morningstar, D. A. Huse, Z. Z. Yan, and W. S. Bakr, "Probing site-resolved correlations in a spin system of ultracold molecules", Nature **614**, 64–69 (2023).

[15] L. Anderegg, L. W. Cheuk, Y. Bao, S. Burchesky, W. Ketterle, K.-K. Ni, and J. M. Doyle, "An optical tweezer array of ultracold molecules", Science **365**, 1156–1158 (2019).

[16] Y. Bao, S. S. Yu, L. Anderegg, E. Chae, W. Ketterle, K.-K. Ni, and J. M. Doyle, "Dipolar spin-exchange and entanglement between molecules in an optical tweezer array", Science **382**, 1138–1143 (2023).

[17] N. R. Hutzler, "Polyatomic molecules as quantum sensors for fundamental physics", Quantum Sci. Technol. **5**, 044011 (2020).

[18] L. Anderegg, N. B. Vilas, C. Hallas, P. Robichaud, A. Jadbabaie, J. M. Doyle, and N. R. Hutzler, "Quantum control of trapped polyatomic molecules for *e*EDM searches", Science 10.1126/science.adg8155 (2023).

[19] A. Collaboration, "Improved limit on the electric dipole moment of the electron", Nature **562**, 355–360 (2018).

[20] T. S. Roussy, L. Caldwell, T. Wright, W. B. Cairncross, Y. Shagam, K. B. Ng, N. Schlossberger, S. Y. Park, A. Wang, J. Ye, and E. A. Cornell, "An improved bound on the electron's electric dipole moment", Science **381**, 46–50 (2023).

[21] L. Essen and J. V. L. Parry, "An atomic standard of frequency and time interval: A caesium resonator", Nature **176**, 280–282 (1955).

[22] 13th General Conference on Weights and Measures, "Resolution 1: SI unit of time, second" (1967), definition of the second based on the caesium-133 transition.

[23] A. D. Ludlow, M. M. Boyd, J. Ye, E. Peik, and P. O. Schmidt, "Optical atomic clocks", Rev. Mod. Phys. **87**, 637–701 (2015).

[24] B. J. Bloom, T. L. Nicholson, J. R. Williams, S. L. Campbell, M. Bishof, X. Zhang, W. Zhang, S. L. Bromley, and J. Ye, "An optical lattice clock with accuracy and stability at the 10^{-18} level", Nature **506**, 71–75 (2014).

[25] I. Kozyryev, Z. Lasner, and J. M. Doyle, "Enhanced sensitivity to ultralight bosonic dark matter in the spectra of the linear radical SrOH", Phys. Rev. A **103**, 10.1103/PhysRevA.103.043313 (2021).

[26] D. Hanneke, B. Kuzhan, and A. Lunstad, "Optical clocks based on molecular vibrations as probes of variation of the proton-to-electron mass ratio", Quantum Sci. Technol. **6**, 014005 (2021).

[27] J.-P. Uzan, "Varying constants, gravitation and cosmology", Living Rev. Relativ. **14**, 2 (2011).

[28] T. Damour and J. F. Donoghue, "Equivalence principle violations and couplings of a light dilaton", Phys. Rev. D **82**, 084033 (2010).

[29] A. Derevianko and M. Pospelov, "Hunting for topological dark matter with atomic clocks", Nat. Phys. **10**, 933–936 (2014).

[30] D. J. Griffiths, *"Introduction to Elementary Particles"*, 2nd ed. (Wiley-VCH, 2008).

[31] X. Fan, T. G. Myers, B. A. D. Sukra, and G. Gabrielse, "Measurement of the electron magnetic moment", Phys. Rev. Lett. **130**, 071801 (2023).

[32] Y. Fukuda *et al.* (Super-Kamiokande Collaboration), "Evidence for oscillation of atmospheric neutrinos", Phys. Rev. Lett. **81**, 1562–1567 (1998).

[33] J. Aalbers *et al.* (LUX-ZEPLIN Collaboration), "First dark matter search results from the LUX-ZEPLIN (LZ) experiment", Phys. Rev. Lett. **131**, 041002 (2023).

[34] ATLAS Collaboration, "Observation of a new particle in the search for the Standard Model Higgs boson with the ATLAS detector at the LHC", Phys. Lett. B **716**, 1–29 (2012).

[35] CMS Collaboration, "Observation of a new boson at a mass of 125 GeV with the CMS experiment at the LHC", Phys. Lett. B **716**, 30–61 (2012).

[36] V. Shiltsev, "High-energy particle colliders: Past 20 years, next 20 years, and beyond", Uspekhi Fizicheskikh Nauk , 965–976 (2012).

[37] J. J. Hudson, D. M. Kara, I. J. Smallman, B. E. Sauer, M. R. Tarbutt, and E. A. Hinds, "Improved measurement of the shape of the electron", Nature **473**, 493–496 (2011).

[38] D. F. Jackson Kimball and K. van Bibber, eds., *"The Search for Ultralight Bosonic Dark Matter"* (Springer, 2022).

[39] F. Zwicky, "Die rotverschiebung von extragalaktischen nebeln", Helv. Phys. Acta **6**, 110–127 (1933).

[40] V. C. Rubin and W. K. J. Ford, "Rotation of the Andromeda nebula from a spectroscopic survey of emission regions", Astrophys. J. **159**, 379–403 (1970).

[41] J. Binney and S. Tremaine, *"Galactic Dynamics"*, 2nd ed. (Princeton University Press, 2008).

[42] D. Clowe, M. Bradac, A. H. Gonzalez, M. Markevitch, S. W. Randall, C. Jones, and D. Zaritsky, "A direct empirical proof of the existence of dark matter", Astrophys. J. Lett. **648**, L109–L113 (2006).

[43] M. Battaglieri *et al.*, "US cosmic visions: New ideas in dark matter 2017: Community report", arXiv (2017), arXiv:1707.04591 [hep-ph] .

[44] R. D. Peccei and H. R. Quinn, "CP conservation in the presence of pseudoparticles", Phys. Rev. Lett. **38**, 1440–1443 (1977).

[45] S. Weinberg, "A new light boson?", Phys. Rev. Lett. **40**, 223–226 (1978).

[46] F. Wilczek, "Problem of strong P and T invariance in the presence of instantons", Phys. Rev. Lett. **40**, 279–282 (1978).

[47] R. J. Crewther, P. Di Vecchia, G. Veneziano, and E. Witten, "Chiral estimate of the electric dipole moment of the neutron in quantum chromodynamics", Phys. Lett. B **88**, 123–127 (1979).

[48] C. Abel *et al.*, "Measurement of the permanent electric dipole moment of the neutron", Phys. Rev. Lett. **124**, 081803 (2020).

[49] J. E. Kim and G. Carosi, "Axions and the strong cp problem", Rev. Mod. Phys. **82**, 557–601 (2010).

[50] I. G. Irastorza and J. Redondo, "New experimental approaches in the search for axion-like particles", Prog. Part. Nucl. Phys. **102**, 89–159 (2018).

[51] I. M. Bloch, R. Shaham, Y. Hochberg, E. Kuflik, T. Volansky, and O. Katz, "Constraints on axion-like dark matter from a serf comagnetometer", Nature Communications **14**, 5784 (2023).

[52] Particle Data Group, "Axions and other similar particles", Prog. Theor. Exp. Phys. **2020**, 083C01 (2020).

[53] A. Banerjee, C. Csaki, M. Geller, Z. Heller-Algazi, and A. Ismail, "Ultralight dilatonic dark matter", JHEP **2026**, 158.

[54] A. Jordan *et al.*, "Dilatonic couplings and the relic abundance of ultralight dark matter", Phys. Rev. Lett. **134**, 191003 (2025).

[55] A. Banerjee, C. Csáki, M. Geller, Z. Heller-Algazi, and A. Ismail, "Ultralight dilatonic dark matter", Journal of High Energy Physics **2026**, 158 (2026).

[56] C. J. Kennedy, E. Oelker, J. M. Robinson, T. Bothwell, D. Kedar, W. R. Milner, G. E. Marti, A. Derevianko, and J. Ye, "Precision metrology meets cosmology: Improved constraints on ultralight dark matter from atom-cavity frequency comparisons", Phys. Rev. Lett. **125**, 201302 (2020).

[57] N. Sherrill, A. O. Parsons, C. F. A. Baynham, W. Bowden, E. A. Curtis, R. Hendricks, I. R. Hill, R. Hobson, H. S. Margolis, B. I. Robertson, M. Schioppo, K. Szymaniec, A. Tofful, J. Tunesi, R. M. Godun, and X. Calmet, "Analysis of atomic-clock data to constrain variations of fundamental constants", New J. Phys. **25**, 093012 (2023).

[58] T. Kobayashi, A. Takamizawa, D. Akamatsu, A. Kawasaki, A. Nishiyama, K. Hosaka, Y. Hisai, M. Wada, H. Inaba, T. Tanabe, and M. Yasuda, "Search for ultralight dark matter from long-term frequency comparisons of optical and microwave atomic clocks", Phys. Rev. Lett. **129**, 241301 (2022).

[59] P. Touboul, G. Métris, M. Rodrigues, J. Bergé, A. Robert, Q. Baghi, Y. André, J. Bedouet, D. Boulanger, S. Bremer, P. Carle, R. Chhun, B. Christophe, V. Cipolla, T. Damour, P. Danto, L. Demange, H. Dittus, O. Dhuicque, P. Fayet, B. Foulon, P.-Y. Guidotti, D. Hagedorn, E. Hardy, P.-A. Huynh, P. Kayser, S. Lala, C. Lämmerzahl, V. Lebat, F. Liorzou, M. List, F. Löffler, I. Panet, M. Pernot-Borràs, L. Perraud,

S. Pires, B. Pouilloux, P. Prieur, A. Rebray, S. Reynaud, B. Rievers, H. Selig, L. Serron, T. Sumner, N. Tanguy, P. Torresi, and P. Visser, "MICROSCOPE mission: Final results of the test of the equivalence principle", Phys. Rev. Lett. **129**, 121102 (2022).

[60] Z. Lasner, *"Order-of-Magnitude-Tighter Bound on the Electron Electric Dipole Moment"*, Phd thesis, Yale University (2019).

[61] N. R. Hutzler, *"A New Limit on the Electron Electric Dipole Moment: Beam Production, Data Interpretation, and Systematics"*, Phd thesis, Harvard University (2014).

[62] A. D. Sakharov, "Violation of CP invariance, C asymmetry, and baryon asymmetry of the universe", JETP Lett. **5**, 24–27 (1967).

[63] G. Lüders, "On the equivalence of invariance under time reversal and under particle-antiparticle conjugation for relativistic field theories", K. Dan. Vidensk. Selsk. Mat. Fys. Medd. **28** (1954).

[64] J. Engel, M. J. Ramsey-Musolf, and U. van Kolck, "Electric dipole moments of nucleons, nuclei, and atoms: The Standard Model and beyond", Prog. Part. Nucl. Phys. **71**, 21–74 (2013).

[65] M. Pospelov and A. Ritz, "Electric dipole moments as probes of new physics", Ann. Phys. **318**, 119–169 (2005).

[66] T. Ibrahim and P. Nath, "The neutron and the electron electric dipole moment in N=1 supergravity unification", Phys. Rev. D **57**, 478–488 (1998).

[67] W. Gerlach and O. Stern, "Der experimentelle nachweis der richtungsquantelung im magnetfeld", Z. Phys. **9**, 349–352 (1922).

[68] E. Ramberg and G. A. Snow, "Experimental limit on a small violation of the Pauli principle", Phys. Lett. B **238**, 438–441 (1990).

[69] L. I. Schiff, "Measurability of nuclear electric dipole moments", Phys. Rev. **132**, 2194–2200 (1963).

[70] P. G. H. Sandars, "The electric dipole moment of an atom", Phys. Lett. **14**, 194–196 (1965).

[71] I. Kozyryev and N. R. Hutzler, "Precision measurement of time-reversal symmetry violation with laser-cooled polyatomic molecules", Phys. Rev. Lett. **119**, 133002 (2017).

[72] N. R. Hutzler, H.-I. Lu, and J. M. Doyle, "The buffer gas beam: An intense, cold, and slow source for atoms and molecules", Chem. Rev. **112**, 4803–4827 (2012).

[73] N. B. Vilas, C. Hallas, L. Anderegg, P. Robichaud, A. Winnicki, D. Mitra, and J. M. Doyle, "Magneto-optical trapping and sub-Doppler cooling of a polyatomic molecule", Nature **606**, 70–74 (2022).

[74] L. Anderegg, B. L. Augenbraun, E. Chae, B. Hemmerling, N. R. Hutzler, A. Ravi, A. L. Collopy, J. Ye, W. Ketterle, and J. M. Doyle, "Radio-frequency magneto-optical trapping of CaF with high density", Phys. Rev. Lett. **119**, 103201 (2017).

[75] A. L. Collopy, S. Ding, Y. Wu, I. A. Finneran, L. Anderegg, B. L. Augenbraun, J. M. Doyle, and J. Ye, "3D magneto-optical trap of yttrium monoxide", Phys. Rev. Lett. **121**, 213201 (2018).

[76] Z. Zeng *et al.*, "Three-dimensional magneto-optical trapping of barium monofluoride", Phys. Rev. Lett. **133**, 143404 (2024).

[77] Z. D. Lasner, A. Frenett, H. Sawaoka, L. Anderegg, B. L. Augenbraun, H. Lampson, M. Li, A. Lunstad, J. Mango, A. Nasir, T. Ono, J. M. Doyle, and T. Sakamoto, "Magneto-optical trapping of a heavy polyatomic molecule for precision measurement", Phys. Rev. Lett. **134**, 083401 (2025).

[78] J. Dai, B. Riley, Q. Sun, D. Mitra, and T. Zelevinsky, "Magneto-optical trapping of a metal hydride molecule", Phys. Rev. Lett. (2026), accepted paper; arXiv:2512.22350.

[79] J. E. Padilla-Castillo, J. Cai, P. Agarwal, P. Kukreja, R. Thomas, B. G. Sartakov, S. Truppe, G. Meijer, and S. C. Wright, "Magneto-optical trapping of aluminum monofluoride", Phys. Rev. Lett. **135**, 243401 (2025).

[80] J. J. Burau, P. Aggarwal, K. Mehling, and J. Ye, "Blue-detuned magneto-optical trap of molecules", Phys. Rev. Lett. **130**, 193401 (2023).

[81] S. J. Li, C. M. Holland, Y. Lu, and L. W. Cheuk, "Blue-detuned magneto-optical trap of CaF molecules", Phys. Rev. Lett. **132**, 233402 (2024).

[82] C. Hallas, G. K. Li, N. B. Vilas, P. Robichaud, L. Anderegg, and J. M. Doyle, "High compression blue-detuned magneto-optical trap of polyatomic molecules", Phys. Rev. Lett. **136**, 133402 (2026).

[83] S. S. Yu, J. You, Y. Bao, L. Anderegg, C. Hallas, G. K. Li, D. Lim, E. Chae, W. Ketterle, K.-K. Ni, and J. M. Doyle, "A conveyor-belt magneto-optical trap of CaF", Nat. Commun. **17**, 83 (2026).

[84] Z. Zeng, S. Yang, S. Deng, and B. Yan, "Direct loading of BaF molecules with a conveyor-belt magneto-optical trap", Phys. Rev. Lett. **136**, 073402 (2026).

[85] P. F. Bernath, *"Spectra of atoms and molecules"*, 2nd ed. (Oxford University Press, 2005).

[86] J. M. Brown and A. Carrington, *"Rotational Spectroscopy of Diatomic Molecules"* (Cambridge University Press, 2010).

[87] E. Hirota, *"High-Resolution Spectroscopy of Transient Molecules"* (Springer-Verlag, 1985).

[88] W. Demtröder, *"Molecular Physics: Theoretical Principles and Experimental Methods"* (Wiley, 2005).

[89] M. J. Dick, *"Spectroscopy of selected calcium and strontium containing polyatomic molecules"*, Ph.D. thesis, University of Waterloo (2007).

[90] A. Allouche, G. Wannous, and M. Aubert-Frécon, "A ligand-field approach for the low-lying states of Ca, Sr and Ba monohalides", Chemical Physics **170**, 11–22 (1993).

[91] S. F. Rice, H. Martin, and R. W. Field, "The electronic structure of the calcium monohalides. a ligand field approach", The Journal of Chemical Physics **82**, 5023–5034 (1985).

[92] Z. Lasner, A. Lunstad, C. Zhang, L. Cheng, and J. M. Doyle, "Vibronic branching ratios for nearly closed rapid photon cycling of sroh", Phys. Rev. A **106**, L020801 (2022).

[93] M. D. Rosa, "Laser-cooling molecules", The European Physical Journal D **31**, 395–402 (2004).

[94] I. Kozyryev, L. Baum, K. Matsuda, and J. M. Doyle, "Proposal for laser cooling of complex polyatomic molecules", Chem. Phys. Chem. **17**, 3641–3648 (2016).

[95] D. Mitra, N. B. Vilas, C. Hallas, L. Anderegg, B. L. Augenbraun, L. Baum, C. Miller, S. Raval, and J. M. Doyle, "Direct laser cooling of a symmetric top molecule", Science **369**, 1366–1369 (2020).

[96] A. Lunstad, H. Sawaoka, Z. Lasner, A. Nasir, M. Li, J. Mango, R. Fields, and J. M. Doyle, "High-sensitivity molecular spectroscopy of sroh using magneto-optical trapping", Phys. Rev. A **113**, 042820 (2026).

[97] J. M. Brown, "The renner-teller effect: the effective hamiltonian approach", in *Computational Molecular Spectroscopy*, edited by P. Jensen and P. Bunker (John Wiley & Sons Ltd., 2000).

[98] H. Sawaoka, *"Laser cooling, optical trapping and Zeeman-Sisyphus deceleration of heavy polyatomic molecules for probing physics beyond the Standard Model"*, Ph.D. thesis, Harvard University (2025).

[99] A. Frenett, *"Motional Control of Polyatomic Molecules for Precision Measurement Citation"*, Ph.D. thesis, Harvard University (2024).

[100] C. J. Foot, *"Atomic Physics"* (Oxford University Press, Oxford, 2005).

[101] B. L. Augenbraun, L. Anderegg, C. Hallas, Z. D. Lasner, N. B. Vilas, and J. M. Doyle, "Direct laser cooling of polyatomic molecules" (2023) pp. 89–182.

[102] T. Hänsch and A. Schawlow, "Cooling of gases by laser radiation", Optics Communications **13**, 68–69 (1975).

[103] W. D. Phillips and H. Metcalf, "Laser deceleration of an atomic beam", Physical Review Letters **48**, 596–599 (1982).

[104] L. Anderegg, *"Ultracold Molecules in Optical Arrays: From Laser Cooling to Molecular Collisions"*, Ph.D. thesis, Harvard University (2019).

[105] N. B. Vilas, *"Laser Cooling, Optical Trapping, and Quantum Control of Polyatomic Molecules"*, Ph.D. thesis, Harvard University (2025).

[106] T. K. Langin and D. DeMille, "Toward improved loading, cooling, and trapping of molecules in magneto-optical traps", New Journal of Physics **25**, 043005 (2023).

[107] B. Hemmerling, E. Chae, A. Ravi, L. Anderegg, G. K. Drayna, N. R. Hutzler, A. L. Collopy, J. Ye, W. Ketterle, and J. M. Doyle, "Laser slowing of CaF molecules to near the capture velocity of a molecular MOT", J. Phys. B **49**, 174001 (2016).

[108] N. J. Fitch and M. R. Tarbutt, "Principles and design of a zeeman–sisyphus decelerator for molecular beams", Chem. Phys. Chem. **17**, 3609–3623 (2016).

[109] N. B. Vilas, P. Robichaud, C. Hallas, G. K. Li, L. Anderegg, and J. M. Doyle, "An optical tweezer array of ultracold polyatomic molecules", Nature **628**, 282–286 (2024).

[110] J. A. Devlin and M. R. Tarbutt, "Three-dimensional doppler, polarization-gradient, and magneto-optical forces for atoms and molecules with dark states", New Journal of Physics **18**, 10.1088/1367-2630/18/12/123017 (2016).

[111] W. Lunden, L. Du, M. Cantara, P. Barral, A. O. Jamison, and W. Ketterle, "Enhancing the capture velocity of a dy magneto-optical trap with two-stage slowing", Phys. Rev. A **101**, 063403 (2020).

[112] H. J. Williams, S. Truppe, M. Hambach, L. Caldwell, N. J. Fitch, E. A. Hinds, B. E. Sauer, and M. R. Tarbutt, "Characteristics of a magneto-optical trap of molecules", New Journal of Physics **19**, 10.1088/1367-2630/aa8e52 (2017).

[113] K. N. Jarvis, J. Devlin, T. Wall, B. Sauer, and M. Tarbutt, "Blue-detuned magneto-optical trap", Physical review letters **120**, 083201 (2018).

[114] S. S. Phatak, K. N. Blodgett, D. Peana, M. R. Chen, and J. D. Hood, "Generalized theory for optical cooling of a trapped atom with spin", Physical Review A **110**, 043116 (2024).

[115] G. K. Li, C. Hallas, and J. M. Doyle, "Conveyor-belt magneto-optical trapping of molecules", New Journal of Physics **27** (2025).

[116] C. M. Holland, Y. Lu, and L. W. Cheuk, "On-demand entanglement of molecules in a reconfigurable optical tweezer array", Science **382**, 1143–1147 (2023).

[117] L. R. B. Picard, A. J. Park, G. E. Patenotte, S. Gebretsadkan, D. Wellnitz, A. M. Rey, and K.-K. Ni, "Entanglement and iswap gate between molecular qubits", Nature **637**, 821–826 (2025).

[118] N. Bigagli, W. Yuan, S. Zhang, B. Bulatovic, T. Karman, I. Stevenson, and S. Will, "Observation of bose–einstein condensation of dipolar molecules", Nature **631**, 289–293 (2024).

[119] L. Anderegg, S. Burchesky, Y. Bao, S. S. Yu, T. Karman, E. Chae, K.-K. Ni, W. Ketterle, and J. M. Doyle, "Observation of microwave shielding of ultracold molecules", Science **373**, 779–782 (2021).

[120] P. Robichaud, C. Hallas, J. Tao, G. Lee, N. B. Vilas, and J. M. Doyle, "Parity-doublet coherence times in optically trapped polyatomic molecules", Nature 10.1038/s41586-026-10133-2 (2026).

[121] D. J. Griffiths and D. F. Schroeter, *"Introduction to quantum mechanics"* (Cambridge university press, 2018).

[122] R. Shankar, *"Principles of quantum mechanics"* (Springer Science & Business Media, 2012).

[123] N. B. Vilas, C. Hallas, L. Anderegg, P. Robichaud, C. Zhang, S. Dawley, L. Cheng, and J. M. Doyle, "Blackbody thermalization and vibrational lifetimes of trapped polyatomic molecules", Physical Review A **107**, 062802 (2023).

[124] N. B. Vilas, P. Robichaud, C. Hallas, J. Tao, L. Anderegg, G. K. Li, H. Lampson, L. D. Augustovičová, J. L. Bohn, and J. M. Doyle, "Quantum-state-controlled collisions of ultracold polyatomic molecules", Physical Review X **16**, 021001 (2026).

[125] V. Jorapur, T. K. Langin, Q. Wang, G. Zheng, and D. DeMille, "High density loading and collisional loss of laser-cooled molecules in an optical trap", Phys. Rev. Lett. **132**, 163403 (2024).

[126] W. Petrich, M. H. Anderson, J. R. Ensher, and E. A. Cornell, "Stable, tightly confining magnetic trap for evaporative cooling of neutral atoms", Phys. Rev. Lett. **74**, 3352–3355 (1995).

[127] L. Anderegg, S. Burchesky, Y. Bao, S. S. Yu, T. Karman, E. Chae, K.-K. Ni, W. Ketterle, and J. M. Doyle, "Observation of microwave shielding of ultracold molecules", Science **373**, 779–782 (2021).

[128] K. B. Davis, M.-O. Mewes, M. R. Andrews, N. J. van Druten, D. S. Durfee, D. M. Kurn, and W. Ketterle, "Bose–einstein condensation in a gas of sodium atoms", Phys. Rev. Lett. **75**, 3969–3973 (1995).

[129] M. H. Anderson, J. R. Ensher, M. R. Matthews, C. E. Wieman, and E. A. Cornell, "Observation of bose–einstein condensation in a dilute atomic vapor", Science **269**, 198–201 (1995).

[130] A. Jadbabaie, N. H. Pilgram, J. Kłos, S. Kotochigova, and N. R. Hutzler, "Enhanced molecular yield from a cryogenic buffer gas beam source via excited state chemistry", New Journal of Physics **22**, 022002 (2020).

[131] X. Alauze, J. Lim, M. Trigatzis, S. Swarbrick, F. Collings, N. Fitch, B. Sauer, and M. Tarbutt, "An ultracold molecular beam for testing fundamental physics", Quantum Science & Technology **6**, 044005 (2021).

[132] J. W. van Hofslot, I. E. Thompson, A. Touwen, N. Balasubramanian, R. Bause, H. L. Bethlem, A. Borschevsky, T. H. Fikkers, S. Hoekstra, S. A. Jones, *et al.*, "2d transverse laser cooling of a hexapole focused beam of cold baf molecules", Communications Physics (2026).

[133] C. J. H. Rich, *"Towards sympathetic cooling of molecules using ultracold atoms"*, Ph.D. thesis, Imperial College London (2022).

[134] L. W. Cheuk, L. Anderegg, B. L. Augenbraun, Y. Bao, S. Burchesky, W. Ketterle, and J. M. Doyle, "Lambda-enhanced imaging of molecules in an optical trap", Phys. Rev. Lett. **121**, 083201 (2018).

[135] M. R. Tarbutt and J. A. Devlin, "Engineering the sub-doppler force in magneto-optical traps", Physical Review Research **4**, L042036 (2022).

[136] S. Ding, Y. Wu, I. A. Finneran, J. J. Burau, and J. Ye, "Sub-doppler cooling and compressed trapping of yo molecules at μK temperatures", Phys. Rev. X **10**, 021049 (2020).

[137] D. Boiron, C. Triché, D. R. Meacher, P. Verkerk, and G. Grynberg, "Three-dimensional cooling of cesium atoms in four-beam gray optical molasses", Phys. Rev. A **52**, R3425–R3428 (1995).

[138] F. Sievers, N. Kretzschmar, D. R. Fernandes, D. Suchet, M. Rabinovic, S. Wu, C. V. Parker, L. Khaykovich, C. Salomon, and F. Chevy, "Simultaneous sub-doppler laser cooling of fermionic ^{6}Li and ^{40}K on the D_1 line: Theory and experiment", Phys. Rev. A **91**, 023426 (2015).

[139] M. Xu, L. H. Kendrick, A. Kale, Y. Gang, C. Feng, S. Zhang, A. W. Young, M. Lebrat, and M. Greiner, "A neutral-atom hubbard quantum simulator in the cryogenic regime", Nature **642**, 909–915 (2025).

[140] B. Augenbraun, *"Methods for Direct Laser Cooling of Polyatomic Molecules"*, Ph.D. thesis, Harvard University (2021).

[141] B. L. Augenbraun, Z. D. Lasner, A. Frenett, H. Sawaoka, C. Miller, T. C. Steimle, and J. M. Doyle, "Laser-cooled polyatomic molecules for improved electron electric dipole moment searches", New Journal of Physics **22**, 022003 (2020).

[142] E. T. Mengesha, A. T. Le, T. C. Steimle, L. Cheng, C. Zhang, B. L. Augenbraun, Z. Lasner, and J. Doyle, "Branching ratios, radiative lifetimes, and transition dipole moments for yboh", Journal of Physical Chemistry A **124**, 3135–3148 (2020).

[143] B. L. Augenbraun, A. Frenett, H. Sawaoka, C. Hallas, N. B. Vilas, A. Nasir, Z. D. Lasner, and J. M. Doyle, "Zeeman-sisyphus deceleration of molecular beams", Physical Review Letters **127**, 263002 (2021).

[144] H. Sawaoka, A. Frenett, A. Nasir, T. Ono, B. L. Augenbraun, T. C. Steimle, and J. M. Doyle, "Zeeman-sisyphus deceleration for heavy molecules with perturbed excited-state structure", Phys. Rev. A **107**, 022810 (2023).

[145] S. Popa, S. Schaller, A. Fielicke, J. Lim, B. G. Sartakov, M. R. Tarbutt, and G. Meijer, "Understanding inner-shell excitations in molecules through spectroscopy of the 4 f hole states of ybf", Physical Review X **14**, 021035 (2024).

[146] M. Athanasakis-Kaklamanakis, G. Peng, S. Li, H. Septien-Gonzalez, C. Debavelaere, A. D. White, S. Popa, J. Lim, B. E. Sauer, and M. R. Tarbutt, "Slowing YbF molecules using radiation pressure" (2025), arXiv preprint, arXiv:2508.15994 [physics.atom-ph] .

[147] X. Wu, P. Hu, Z. Han, D. G. Ang, C. Meisenhelder, G. Gabrielse, J. M. Doyle, and D. DeMille, "Electrostatic focusing of cold and heavy molecules for the acme electron edm search", New Journal of Physics **24**, 073043 (2022).

[148] C. Hallas, *"in prep."*, Ph.D. thesis, Harvard University (2026).

[149] J. Dalibard and C. Cohen-Tannoudji, "Laser cooling below the doppler limit by polarization gradients: simple theoretical models", J. Opt. Soc. Am. B **6**, 2023–2045 (1989).

[150] D. A. Fletcher, M. A. Anderson, W. L. Barclay, and L. M. Ziurys, "Millimeter-wave spectroscopy of vibrationally excited ground state alkaline-earth hydroxide radicals (X $^2\Sigma^+$)", The Journal of Chemical Physics **102**, 4334–4339 (1995).

[151] P. I. Presunka and J. A. Coxon, "Laser excitation and dispersed fluorescence investigations of the $\tilde{A}^2\Pi - \tilde{X}^2\Sigma^+$ system of SrOH", Chemical Physics **190**, 97 (1995).

[152] P. I. Presunka and J. A. Coxon, "High-resolution laser spectroscopy of excited bending vibrations", Canadian Journal of Chemistry **71**, 1689 (1993).

[153] C. R. Brazier and P. F. Bernath, "Laser and fourier transform spectroscopy of the $\tilde{A}^2\Pi - \tilde{X}^2\Sigma^+$ transition of SrOH", Journal of Molecular Spectroscopy **114**, 163 (1985).

[154] P. I. Presunka and J. A. Coxon, "Laser spectroscopy of the $\tilde{A}^2\Pi - \tilde{X}^2\Sigma^+$ transition of SrOH: Deperturbation analysis of K-resonance in the $v_2 = 1$ level of the $\tilde{A}^2\Pi$ state", The Journal of Chemical Physics **101**, 201 (1994).

[155] J. Nakagawa, R. F. Wormsbecher, and D. O. Harris, "High-resolution laser excitation spectra of linear triatomic molecules: Analysis of the $\tilde{B}^2\Sigma^+ - \tilde{X}^2\Sigma^+$ system of SrOH and SrOD", Journal of Molecular Spectroscopy **97**, 37 (1983).

[156] J.-G. Wang, M. J. Dick, P. M. Sheridan, S. Yu, and P. F. Bernath, "Further spectroscopic investigations of the high energy electronic states of SrOH: The $\tilde{B}'^2\Sigma^+(000) - \tilde{A}^2\Pi(000)$ and the $\tilde{D}^2\Sigma^+(000) - \tilde{A}^2\Pi(000)$ transitions", Journal of Molecular Spectroscopy **245**, 26–33 (2007).

[157] A. R. Allouche and M. Aubert-Frécon, "Semiempirical electrostatic polarization model of the ionic bonding in alkali and alkaline-earth hydroxides and halides", Chemical Physics 10.1016/0301-0104(91)87008-J (1991).

[158] D. A. Fletcher, K. Y. Jung, C. T. Scurlock, and T. C. Steimle, "Molecular beam pump/probe microwave-optical double resonance using a laser ablation source", The Journal of Chemical Physics **98**, 1837 (1993)


CONGRA